

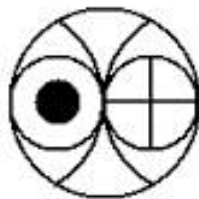
**Multiproxy-paleoclimate studies in the
Indian region for the past 200ka; A
synthesis**

Thesis submitted to
The Maharaja Sayajirao University of Baroda
Vadodara, India

For the degree of
Doctor of Philosophy in Geology
by

Shraddha Band

July, 2016



Geoscience Division
Physical Research Laboratory,
Ahmedabad - 380009, India

Dedicated to
all my mentors

Acknowledgements

Five years ago I embarked upon a journey that has reached a milestone today. The road with many twists and turns ended up in caves and began the research on speleothem science. I cannot possibly think of reaching this goal alone and have several people to acknowledge. Firstly I would like to express my gratitude to my supervisor Prof R.Ramesh for his invaluable guidance and immense patience. I have been extremely lucky to have a supervisor who emphasized greatly on maintaining good quality of work and left no stone unturned to reach perfection. I deeply acknowledge my co-guide Dr.M.G. Yadava for introducing me to the world of speleothems. His expertise in the field created a foundation on which the research could be proliferated. I also thank him for the academic freedom where I was allowed to try and fail and in turn learn a lot in the course.

I will be forever indebted to Prof. Chamyal, for not only being my co-guide at M.S.University of Baroda but also for never giving up on me and for being my constant source of encouragement. Words will fail to describe his role in molding my career and scientific aspirations. I cannot thank enough to Dr. Hrishikesh Samant from St.Xaviers college for his lion-rabbit story that kept me going through some tough times. Both of them have been my father figures and extended support in thick and thin. I could confide my deepest fears to them and come out all charged up to face new challenges.

I thank Prof.Jyotiranjana Ray for teaching me fundamentals of geochemistry and giving me freedom to learn clean chemistry procedures in his laboratory. I also thank him deeply for including me in the field trip to Amba Dongur which was in my bucket list for fluorite collection. I thank Dr.Sanjeev kumar for his constant encouraging and motivational conversations. He is one of those mentors who showed faith in my work. I would like to thank both of them for holding the stable isotope family together and helping me if the situation demanded.I thank R.A.

Jani for discussions and introducing me to the mass spectrometer analyses in the stable isotope lab. I thank N.B Vaghela Bhai for teaching me the radiocarbon dating technique with utmost patience. I also thank Manoj Tank and Ram Mhatre from the Thermo scientific for timely resolving of technical problems with the instrument.

I acknowledge the collaboration with Nikita and Gideon of the University of Oxford. Apart from providing U-Th dates for the samples, they have also given valuable suggestions which helped in improving the quality of the work. It was a great experience collaborating with Y. Asmeron from University of New Mexico and Mahjoor Lone, C.C.Shen from National Taiwan University for providing U-Th ages of the samples. I thank XRF lab from the Hyderabad University and Pawan Gautam for assistance with the mineralogy of the samples. I thank Mohammad bhai from M.S.University of Baroda for providing thin sections.

I thank Dr. R.D. Deshpande for being my thesis expert and giving his valuable suggestions. He along with his lab associates from IWIN have always helped us with eleventh hour instrument's consumable crisis. I want to express my sincere gratitude to Dr.Ravi Bhushan for being excellent mentor during my summer internship tenure. His inspiring words encouraged me to pursue research in paleoclimate. I thank Prof.Sunil Singh for trusting me with the tedious Re-Os chemistry for the two months course work project. I was first introduced to clean chemistry in his lab and developed interest in geochemistry after having scientific discussions with him.

I thank director of PRL, dean, academic committee chairman, academic committee members and registrar for their help and suggestion at different stages.

I thank Dr.Devesh Sinha and Ashutosh from Delhi University for teaching me foraminiferal species identification. I would also like to thank Alpa and Rachana

ma'm from the M.S.University of Baroda for their encouraging words and belief in me.

I thank Prof. Sarin, Dr. Arvind singh, Dr.Navin Juyal, Dr.Rengarajan, Dr. Neeraj, Dr. Shukla for their valuable suggestions. I thank Balaji for his generous help with the administrative work at the M.S.University of Baroda. I thank Prof. Srubabati Goswami for being the role model to all the women scientist in the field. I also acknowledge people from different sections of PRL: Sivdasan, Parulben, Anand Mehta, Jaldhi, Ramsha Sasi Kumar, Pragya, Dr. Nishita, Tejas, Mishraji, Jigar Raval, Hemal Shah, Sunil Bhai, Nandiniben, Pritiben, Richa, Pauline, Senthil Babu, Manan Shah, Lakhan Bhai, Pranav Bhai, Sudheer sir, Bankim Bhai, Ranganathan, Ubale, Prabha Ben, Nilesh Bhai, Jayashree, Ganesh Bhai, Shailesh Bhai, Workshop members, Sanjay Wairagade and CMD team for their helps at various stages.

Together with Lekshmy, Bhavya, Rupa, Niharika and Sangeeta I had great relaxing moments while doing lab work, cooking and indulging in art work. I experienced the joy of having sisters staying with them. Bivin, Kiran, Sachin, and Gulshan have been the best junior friends I had. I could reminisce my childhood pranks with them. Midhun and Amzad are two unseen pillars of this thesis work. They have scrutinized every scientific detail and directed me to new ideas in the field. I thank Timmy and Kaushik Sree for their assistance in the preliminary lab procedures.

I would like to thank Ikshu, Anirban, Abhaya for over-filling the jar of memories in the past five years. Without my adventure gang, life in PRL would seem very boring. I thank Naveen Negi, Arun, Girish, Tanmoy for their spontaneous bike trips to exotic places and putting me through many challenging situations. I would like to thank Chitrabhanu and Swapna for their hospitality and mouth watering Malayali food. I thank my batch mates Saweeta, Kuldeep, Gaurav, Guru, Sanjay

and Alok for sharing sorrows and happiness together. I thank Shrema, Kaki ma and Kaku for being my extended family in PRL. Apart from the love and care, they were constant source of delicious food.

I would like to thank my chemistry lab friends, Chandana, Venky, Damodar, Srinivas, Upasana, Anil, Shubhanand, Sneha, Chinmay, Nitesh for their timely help and support. I am very thankful to Vineet Bhaiyya and Dimpy Bhabhi for their hospitality. I never felt homesick in their presence. I would like thank my hostel friends Jinia, Ila, Bharti, Avadhesh, Abhishek, Vishnu, Pradeep, Aman, Bhavesh, Harsh, Harsh Vardhan, Anil, Ashimanand, Soumik, Naman, Ashish, Balbeer, Pankaj, Arvind for keeping the hostel lively and an awesome place to stay. I am also thankful to my Thaltej hostel friends Shweta, Navpreet, Priyanka, Rukmini, Kuldeep, Deepak, Dipti, Apurv, Lalit for their warm welcome to my each visit. I thank Raza and his family for the hospitality they extended towards our group.

I thank Tejal, Carlton and Akshay for continuing to be my best friends for almost nine years irrespective of my delayed responses. I thank Omkar and his family for their love and support. I thank Annapurna, Subhadeep, Archana and Siddharth for always being the best hosts ever. And special thanks to Rony for wanting to have my own canine, wherever I go there will always be place for him in my heart.

I am deeply thankful to Manu for everything good that has happened to me in the last five years. He has been my moral support and strength. He gave me new insight into life and was always there when I needed a hope. I wish he continuous to be my light in the darkness. Lastly, I thank my aai, baba, Sanket, aaji, ajoba and other family members for their great parenting and continued support. With their rising expectations after every achievement, they set a new goal to reach and kept me going. I thank all those who have directly or indirectly influenced my life

in the most positive way.

I would like to say that I have just reached a milestone, the road is long and the journey still continues and I hope there is no end to it.

Shraddha

Abstract

The Indian summer monsoon (ISM) plays a crucial role in driving the economy and societal setup of the country. The variability of monsoon is found to be modulated by the interplay between the insolation in the northern hemisphere and the northward movement of the inter-tropical convergence zone and changes in ice extent during glacial-interglacial periods. These governing factors operate on different timescales and control decadal, centennial and millennial variability of the monsoon. This thesis reports reconstruction of monsoon variability during the Holocene and the late Pleistocene. The results are based on stable oxygen and carbon measurements carried out on new stalagmites samples from the core monsoon zone of India and a sediment core raised from the Andaman Sea.

The variability of ISM during the Holocene has been studied using three new stalagmite samples from Dandak (DAN-I and DAN-II) and Kotumsar caves, central India. The record extends from ~ 10.4 ka to the present. Contrary to the earlier inference of gradual decrease in monsoon at mid-Holocene, an abrupt declining monsoon between ~ 6 to 5 ka was observed. The millennial scale monsoon variability is found to be similar to the North-Atlantic climate changes (e.g. Bond events). During the ‘Little Ice age’, when glacier advances were noticed in the Northern hemisphere, a phase of prolonged weaker monsoon, between 600 and 150 yr BP, with severe drought-like conditions at ~ 300 yr BP (1700 AD) is seen in our reconstruction. The general theory of insolation alone controlling the is debunked and instead it is observed that millennial - centennial scale changes

could have been governed by internal feedback mechanisms.

Another stalagmite from the Kailash cave was used to document the variability of monsoon during the Older Dryas period. Several episodes of decade-long mega-droughts were observed during this period. Beginning of Allerod period is marked by a sudden increase in monsoon at ~ 13.4 ka.

Monsoon between ~ 70 ka to the present was reconstructed using $\delta^{18}O$ of *G.ruber* from a sediment core from the Andaman Sea. Significant decline in ISM was observed during the Last Glacial Maximum between $\sim 20 - 18$ ka. A stalagmite sample (BLM-1) collected from the Belum cave, Kurnool district of Andhra Pradesh, India, holds the longest available monsoon record reconstructed from the core monsoon region of India. The Belum cave stalagmite, which grew between $\sim 190 - 80$, ka covers the time period of last interglacial (MIS - 5e) and the onset of the last Glacial period. A gradual decrease in monsoon was observed at the onset of glaciation. The $\delta^{18}O$ time series of early glaciation, when compared with the insolation gradient and the insolation at $30^\circ N$, shows a good coherence with the gradient. This suggests that the insolation gradient between the Mascarene high and the Indian low plays an important role in controlling the monsoon variability rather than direct influence of insolation on monsoon.

Key words : Indian Summer Monsoon, Core Monsoon Zone, Stalagmites, Holocene monsoon, Pleistocene climate, Foraminifera.

Abbreviations

| | |
|----------------|--|
| α | Isotopic fractionation factor between product and source |
| $\delta^{18}O$ | Oxygen isotopic composition of carbonate relative to VPDB standard |
| $\delta^{13}C$ | Carbon isotopic composition of carbonate relative to VPDB standard |
| δD | Deuterium isotopic composition of water relative to VSMOW standard |
| ‰ | per mil (parts per thousand) |
| AD | Anno Domini |
| BLM | Belum |
| BP | Before Present |
| CE | Common Era |
| cpm | counts per minute |
| DAN | Dandak |
| EASM | East Asian Summer Monsoon |
| ENSO | El Nino Southern Oscillation |
| GNIP | Global Network of Isotopes in Precipitation |
| GPCP | Global Precipitation Climatology Project |
| HYSPLIT | Hybrid Single-Particle Lagrangian Integrated Trajectory |
| IAEA | International Atomic Energy Agency |
| ICP-AES | Inductively Coupled Plasma Atomic Emission Spectroscopy |
| IRMS | Isotope Ratio Mass Spectrometer |
| ISM | Indian Summer Monsoon |
| ITCZ | Inter Tropical Convergence Zone |
| JJAS | June, July, August, September |
| ka | kilo annum |

| | |
|----------|--|
| LIA | Little Ice Age |
| LGM | Last Glacial Maximum |
| MIS | Marine Isotope Stage |
| m.s.l. | mean sea level |
| MWP | Medieval Warm Period |
| NARM | Narmada water standard |
| NCEP | National Centers for Environmental Prediction |
| NEM | North East Monsoon |
| NOAA | National Oceanic and Atmospheric Administration |
| PCP | Prior Calcite Precipitation |
| P-E | precipitation minus evaporation |
| PMT | Photo Multiplier Tube |
| ppb | parts per billion |
| ppl | plane polarized light |
| ppt | parts per trillion |
| PRL | Physical Research Laboratory |
| Q-ICP-MS | Quadrupole - Inductively coupled plasma |
| Tr | Trace element |
| VPDB | Vienna Pee Dee Belemnite |
| VSMOW | Vienna Standard Mean Ocean Water (IAEA water standard) |
| xpl | cross polarized light |

Contents

| | |
|---|-------------|
| Acknowledgements | i |
| Abstract | vii |
| List of Abbreviations | xi |
| Contents | xiii |
| List of Figures | xvii |
| List of Tables | xxi |
| 1 Introduction | 1 |
| 1.1 Indian Summer Monsoon | 1 |
| 1.1.1 Variability | 3 |
| 1.1.2 Paleo-monsoon reconstruction | 3 |
| 1.2 Stable isotopologues of carbon dioxide | 4 |
| 1.2.1 Notations | 5 |
| 1.2.2 Isotopic Fractionation of CO_2 in soil | 5 |
| 1.2.3 Rayleigh model for isotopic fractionation | 6 |
| 1.2.4 Observed isotopic effects | 8 |
| 1.3 Objectives | 13 |
| 1.4 Previous work | 14 |

| | | |
|----------|--|-----------|
| 2 | Paleoclimate proxies | 16 |
| 2.1 | Speleothems | 16 |
| 2.1.1 | Mineralogy | 18 |
| 2.1.2 | Isotope exchange in speleothems | 19 |
| 2.1.3 | Trace elements | 27 |
| 2.1.4 | Speleothems as paleomonsoon proxy | 30 |
| 2.1.5 | Sample locations | 31 |
| 2.2 | Foraminifera | 36 |
| 2.3 | Tree rings | 39 |
| 3 | Experimental Methods | 41 |
| 3.1 | Samples | 41 |
| 3.2 | Stable Isotope and concentration measurements | 51 |
| 3.2.1 | Isotope ratio mass spectrometer (IRMS) | 51 |
| 3.2.2 | $\delta^{18}O$ and $\delta^{13}C$ measurements | 55 |
| 3.2.3 | Trace element analysis | 60 |
| 3.3 | Additional data used | 64 |
| 3.3.1 | Global Network of Isotopes in Precipitation (GNIP) | 64 |
| 3.3.2 | Reanalysis/satellite data | 64 |
| 3.3.3 | Hybrid Single-Particle Lagrangian Integrated Trajectory (HYS- PLIT) | 65 |
| 3.4 | Radiocarbon dating | 65 |
| 3.5 | U-Th dating | 73 |
| 3.5.1 | Principles of dating | 73 |
| 3.5.2 | Preliminary procedures | 76 |
| 3.6 | Foraminifera stable isotope analysis | 78 |
| 4 | Holocene monsoon variability | 80 |
| 4.1 | The Dandak-I stalagmite | 81 |
| 4.1.1 | Mineralogy | 81 |

| | | |
|----------|--|------------|
| 4.1.2 | U-Th ages | 83 |
| 4.1.3 | Stable isotopes of oxygen and carbon | 84 |
| 4.1.4 | Trace element analysis | 85 |
| 4.2 | The Dandak-II stalagmite | 88 |
| 4.2.1 | U-Th ages | 88 |
| 4.2.2 | Stable isotopes of oxygen and carbon | 89 |
| 4.2.3 | Hendy's test | 90 |
| 4.3 | Kotumsar stalagmite | 92 |
| 4.3.1 | U-Th ages | 92 |
| 4.3.2 | Hendy test | 92 |
| 4.3.3 | Stable isotopes of oxygen and carbon | 94 |
| 4.4 | Tree Rings | 95 |
| 4.5 | Oceanic records | 96 |
| 4.6 | Discussion | 99 |
| 4.6.1 | Early Holocene climate ($\sim 10.4 - 8$ ka BP) | 100 |
| 4.6.2 | Mid- Holocene climate ($\sim 8 - 4$ ka BP) | 102 |
| 4.6.3 | Late Holocene climate ($\sim 4 -$ to the Present day) | 107 |
| 4.6.4 | Global teleconnections | 110 |
| 5 | Late Pleistocene monsoon variability | 114 |
| 5.1 | Terrestrial records | 115 |
| 5.1.1 | The Kailash cave stalagmite | 117 |
| 5.1.2 | The Belum cave stalagmite | 121 |
| 5.2 | Ocean monsoon record | 133 |
| 5.2.1 | The Andaman Sea sediment core | 135 |
| 6 | Summary and scope for future work | 140 |
| 6.1 | Reconstruction of ISM variability from stalagmites of the Kanger Valley cave complex, Chattisgarh | 140 |
| 6.2 | Impact of ISM variability on human civilization | 142 |

| | | |
|-----|---|-----|
| 6.3 | ISM variability during late Pleistocene based on Speleothem studies | 143 |
| 6.4 | ISM variability during late Pleistocene based on the Andaman Sea sediment Core | 144 |
| 6.5 | Scope for future work | 145 |

List of Figures

| | | |
|-----|--|----|
| 1.1 | Seasonal Migration of ITCZ | 2 |
| 1.2 | Schematic of fractionation of ^{13}C in soil. | 6 |
| 1.3 | Rayleigh isotopic distillation curve | 8 |
| 1.4 | Temperature- $\delta^{18}O$ relationship in precipitation | 9 |
| 1.5 | Relation between rainfall and its $\delta^{18}O$ | 10 |
| 1.6 | Schematic representation of a convective cloud system | 11 |
| 1.7 | $\delta^{18}O$ variation with altitude | 12 |
| 1.8 | Continental effect | 12 |
| 2.1 | Conceptual model explaining the formation of speleothems in a karstic cave | 17 |
| 2.2 | A schematic diagram of the role of different pathways involved in speleothem formation | 21 |
| 2.3 | Factors controlling $\delta^{13}C$ of speleothem | 24 |
| 2.4 | Map of the India showing the locations of the caves explored for paleoclimate studies | 32 |
| 2.5 | Overview of the Dandak cave | 33 |
| 2.6 | Cross sectional view of Kotumsar cave | 34 |
| 2.7 | Cross sectional view of the Belum cave | 35 |
| 2.8 | A schematic explaining Upwelling in the coast of Oman | 36 |
| 2.9 | Location of core SK-234-60 from Andaman Sea | 38 |

| | | |
|------|--|----|
| 3.1 | Dramet cutting machine at PRL | 42 |
| 3.2 | New Wave Research Micro Mill at PRL | 43 |
| 3.3 | Polished cross sectional view of the Dan-I stalagmite | 45 |
| 3.4 | Polished and schematic cross sectional view of the Dandak-II stalagmite | 46 |
| 3.5 | Polished cross sectional view of the Kotumsar cave speleothem | 47 |
| 3.6 | Schematic cross section of KOT-I stalagmite | 48 |
| 3.7 | Polished cross-section of Kailash stalagmite | 49 |
| 3.8 | Polished cross-section of Belum stalagmite | 50 |
| 3.9 | Sketch of a mass spectrometer | 52 |
| 3.10 | Working principle of quadrupole | 54 |
| 3.11 | Thermo Fisher Delta-V Plus IRMS | 54 |
| 3.12 | Kiel-carbonate device and Thermo Fisher MAT-253 IRMS | 55 |
| 3.13 | Working principle of Kiel carbonate | 57 |
| 3.14 | Thermo-scientific Quadrupole-Inductively Coupled Plasma mass spectrometer | 62 |
| 3.15 | Typical calibration curves for different trace elements generated on ICP-MS | 63 |
| 3.16 | The benzene synthesis glass line at PRL | 67 |
| 3.17 | Schematic representation showing wet and dry combustion setup for radiocarbon dating | 71 |
| 3.18 | Schematic diagram showing acetylene and benzene synthesis setup | 72 |
| 3.19 | Formation of Uranyl compound in water | 74 |
| 3.20 | Rosholt and Osmond type plots used to determine for initial activities of ^{230}Th and ^{234}U in the sample | 75 |
| 3.21 | Schematic of the Monte Carlo simulation for age model | 78 |
| 4.1 | Climatological monthly rainfall over Dandak cave | 82 |

| | | |
|------|--|-----|
| 4.2 | Plane polarized light and cross polarized light images of Dan -I stalagmite | 82 |
| 4.3 | Age model of Dan-I stalagmite | 83 |
| 4.4 | $\delta^{18}O$ and $\delta^{13}C$ profiles of the Dan-I stalagmite | 87 |
| 4.5 | Trace element variations in the Dan -I stalagmite | 88 |
| 4.6 | Age model reconstructed for Dan - II stalagmite | 89 |
| 4.7 | $\delta^{18}O$ and $\delta^{13}C$ profiles of Dan-II stalagmite | 90 |
| 4.8 | Sketch of the Dandak-II stalagmite, showing sampling the sampling sites for Hendy's test and U-Th ages | 91 |
| 4.9 | Age model for the Kotumsar stalagmite | 93 |
| 4.10 | Hendy's test results of Kotumsar stalagmite | 93 |
| 4.11 | $\delta^{18}O$ and $\delta^{13}C$ timeseries of KOT-I stalagmite | 94 |
| 4.12 | Monsoon rainfall reconstructed from Ulvi speleothem and Parambikulam teak cellulose | 95 |
| 4.13 | Locations of marine and terrestrial proxies | 97 |
| 4.14 | $\delta^{18}O$ variations of planktic foraminifera from six different cores from the eastern Arabian Sea | 98 |
| 4.15 | Combined Holocene monsoon record based on $\delta^{18}O$ of KOT-I, Dandak-I and II stalagmites | 100 |
| 4.16 | Comparison between Dandak- II stalagmite, GRIP ice core record and Qunf cave | 102 |
| 4.17 | Interproxy comparison between present study and ISM records | 106 |
| 4.18 | Charcoal layers preserved in sediments of the Kotumsar cave and the Dandak cave | 107 |
| 4.19 | The comparison between $\delta^{18}O$ time series of Jhumar speleothem, Dandak speleothem, and the present study | 109 |
| 5.1 | Locations of different terrestrial records from the core monsoon region of India | 116 |

| | | |
|------|--|-----|
| 5.2 | Age model of the Kailash stalagmite | 119 |
| 5.3 | $\delta^{18}O$ and $\delta^{13}C$ timeseries of the Kailash cave stalagmite | 120 |
| 5.4 | Climatological monthly rainfall over the Belum cave | 122 |
| 5.5 | Three day back trajectory at the Belum cave | 122 |
| 5.6 | Correlation coefficient between model simulated JJAS average rainfall $\delta^{18}O$ at the Belum cave and over surrounding grids | 123 |
| 5.7 | Plane polarized light and cross polarized light images of a thin section of the Belum stalagmite | 124 |
| 5.8 | Age model of the Belum stalagmite | 128 |
| 5.9 | $\delta^{18}O$ profile of the Belum cave stalagmite | 129 |
| 5.10 | Comparison between the $\delta^{18}O$ profile of the Belum stalagmite and trace element ratios | 130 |
| 5.11 | Interproxy comparisons of the $\delta^{18}O$ profiles of Sanbao, Xiabailong cave stalagmites with the Belum stalagmite | 132 |
| 5.13 | Locations of different cores raised from the Arabian Sea and the Bay of Bengal | 136 |
| 5.14 | Comparison between Andaman Sea sediment core $\delta^{18}O$ record of the present study with sediment cores from the Bay of Bengal and the Arabian sea | 138 |

List of Tables

| | | |
|-----|--|-----|
| 1.1 | Stable isotopes of Carbon dioxide | 4 |
| 3.1 | Sample preparation methods and mass spectrometric parameters . | 56 |
| 3.2 | IAEA standards used for carbonate and water isotope measurements | 60 |
| 3.3 | Comparison between reported and measured values of IAEA stan- dards | 60 |
| 3.4 | International standards used for trace element measurements . . . | 62 |
| 4.1 | Uranium and Thorium isotopic compositions and ^{230}Th ages of the subsamples of Dandak-I stalagmite | 84 |
| 4.2 | Uranium and Thorium isotopic compositions and ^{230}Th ages of the subsamples of Dandak- II stalagmite | 85 |
| 4.3 | Uranium and Thorium isotopic compositions and ^{230}Th ages of the subsamples of Kotumsar stalagmite | 86 |
| 5.1 | ^{230}Th ages of the Kailash cave stalagmite | 118 |
| 5.2 | ^{230}Th ages of the Belum cave stalagmite | 127 |

Chapter 1

Introduction

Economic and societal setup of India depends primarily on the crop yield, which in turn is decided by the variability in monsoon rain. Severe draught or flood events when persistent for a long period of time, may lead to country wide devastation. Since Indian Summer Monsoon (ISM) contributes to $\sim 80\%$ of the annual rainfall in India, the economy of the country critically depends upon the performance of the monsoon [[Gadgil, 2003](#)].

Understanding the causative processes affecting rainfall occurrences requires continuous instrument based monitoring and observations of meteorological parameters, and in parallel development of mathematical models validated by the observations. We also need to look into the variability and conditions of Earth's climate in the near and also distant past. This is part of a discipline known as paleoclimatology, which is the study of past or ancient climates.

1.1 Indian Summer Monsoon

The word monsoon is derived from the Arabic word “mausam” which is defined as seasonal reversal of winds. It has been suggested that monsoon system was established about 20 million years ago due to the uplift of the Tibetan plateau. Indian Summer Monsoon (ISM) is a manifestation of the seasonal migration of

the Inter-tropical Convergence Zone (ITCZ, [Gadgil, 2003]) in response to heating of the high altitude Tibetan plateau (Figure 1.1). ITCZ is the region where trade winds merge together and form a low pressure belt. During the northern summer, the Indian subcontinent gets heated up and a low pressure trough is formed. This heat induced low pressure (<999 mb) extends from northern Rajasthan to Kolkata at the surface level. Concomitantly, Austral winter causes high pressure over the southern hemispheric subtropical Indian ocean ($\sim 30^{\circ}\text{S}$), also known as the Mascarene High (>1023 mb). This pressure gradient drives cross equatorial flow of heat and moisture. On account of this, the ITCZ migrates over the Indian region causing the wind flow from the southwest leading to monsoon precipitation [Gadgil, 2003; Sikka and Gadgil, 1980]. Shift of ITCZ is a climate system behavior occurring at a global scale and hence Indian monsoon forms an interactive part of the global monsoon system. However, ITCZ behavior on local and regional scales is quite complex [Tomas and Webster, 1997], and hence unique to a particular geographic setting.

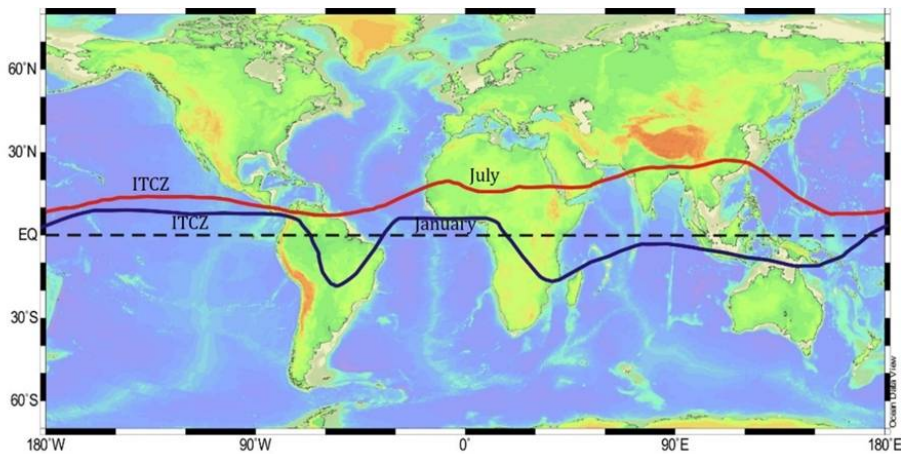


Figure 1.1: Equatorial position of ITCZ in January (blue) and its northward migration in July (red). Re-drawn from: *The Atmosphere* [Lutgens and Tarbuck, 2000], using ocean data viewer.

The Indian monsoon generally responds to interglacial/glacial events by intensification/weakening of its strength.

1.1.1 Variability

Strength of ISM varies on different timescales ranging from intraseasonal to interannual, decadal, centennial and millennial [e.g., [Gadgil, 2003](#); [Ramesh et al., 2010](#)]. The intraseasonal oscillation reflected as active and break cycles of monsoon, [[Rajeevan et al., 2010](#)] having 30-60 day oscillations, are mainly controlled by the internal dynamics. The interannual variability of monsoon rainfall is mainly governed by both the internal dynamics as well as the external controls such as El Niño Southern Oscillation (ENSO) [[Kumar et al., 1999](#)], the solar cycle etc. The longer time scale variability (decadal to millennial) is controlled by the changes in incoming solar radiation (insolation) associated with changes in the Earth's orbital parameters along with the changes in circulation pattern [[Imbrie and Imbrie, 1986](#)].

1.1.2 Paleo-monsoon reconstruction

Instrumental record of monsoon rainfall exists for the past 100 or 150 years and historical records gives qualitative estimates for a few hundred years farther back in time. Long term reconstruction of monsoon necessitates exploiting natural archives which preserve signatures of the monsoon in the form of faunal and floral counts, characteristic chemical constituents and isotopic compositions. The most widely used and accepted archives are tree rings [e.g., [Managave et al., 2011b](#); [Ramesh et al., 1989](#); [Sano et al., 2010](#)], speleothems [e.g., [Allu et al., 2015](#); [Laskar et al., 2011](#); [Ramesh et al., 2010](#); [Sinha et al., 2007](#); [Yadava and Ramesh, 1999, 2001, 2005, 2006](#); [Yadava et al., 2004](#)], lake sediments [e.g., [Enzel et al., 1999](#); [Prasad and Enzel, 2006](#)] and river sediments [e.g., [Juyal et al., 2006](#); [Khadkikar et al., 2000](#); [Sridhar et al., 2016](#)], and ocean sediments [e.g., [Gupta et al., 2003](#); [Kudrass et al., 2001](#); [Prabhu et al., 2004](#)]. Each of these archives have associated advantages and drawbacks. Tree rings with sub-annual resolution have the limitation of the extent of time to which they are available. Ocean sediments

on the other hand, preserve longer timescale climatic data but lack the ability to reconstruct annual or decadal monsoonal variability. However, in the case of speleothems using the U-Th dating technique, potential ISM variability for past 500,000 years can be reconstructed. Also, a speleothem grown under favorable conditions may offer annual resolution.

1.2 Stable isotopologues of carbon dioxide

Different combinations of the isotopes form CO_2 molecules with different masses, called CO_2 isotopologues. Carbon dioxide isotopologues constitute mainly three masses, with the most abundant mass of 44, CO_2 containing ^{13}C atom of mass 45, and additionally, CO_2 containing an ^{18}O instead of the ^{16}O oxygen isotope has mass 46. There are a few CO_2 molecules with a ^{13}C and a ^{18}O , or two atoms of ^{18}O with very low abundances. The three major isotopologues of CO_2 with their relative abundance are shown in table 1.1.

Table 1.1: *Isotopologues of carbon dioxide along with their natural abundances. Source: National Oceanic and Atmospheric Administration (NOAA)*

| Mass | Isotopologues | Abundance (%) |
|------|----------------------|---------------|
| 44 | $^{12}C^{16}O_2$ | 98.40 |
| 45 | $^{13}C^{16}O_2$ | 1.19 |
| | $^{12}C^{17}O^{16}O$ | 0.0748 |
| 46 | $^{12}C^{18}O^{16}O$ | 0.41 |
| | $^{13}C^{17}O^{16}O$ | 0.00084 |
| | $^{12}C^{17}O_2$ | 0.0000142 |

As seen above masses 45 and 46 include $^{12}C^{17}O^{16}O$ and $^{13}C^{17}O^{16}O$, $^{12}C^{17}O_2$ respectively, with very low abundances. However, for paleoclimate studies, importance is given to relative abundance of ^{13}C and ^{18}O isotopes. Hence, Craig correction is applied to negate the effect of the former low abundant masses [[Craig, 1957](#)].

1.2.1 Notations

The relative abundance of any heavier isotope is conveniently represented as it's ratio with that of the lighter one.

$$R = \frac{\text{Abundance of the heavier isotope}}{\text{Abundance of the lighter isotope}}$$

As the absolute ratios of the isotopes are difficult to measure and the relative variations are of principal interest in understanding a process, isotopic ratios are expressed as deviations (δ) from that of an international standard. Carbon dioxide isotopic compositions are reported with respect to the standard procured from International Atomic Energy Agency (IAEA): Vienna Pee Dee Belemnite (VPDB)[[Gonfiantini, 1978](#); [Gonfiantini et al., 1995](#)]. For example, carbon-13 and oxygen-18 abundances in a sample are reported respectively as

$$\delta^{13}C = \left(\frac{R_{Sample}}{R_{Standard}} - 1 \right) \times 10^3\text{‰}$$

and

$$\delta^{18}O = \left(\frac{R_{Sample}}{R_{Standard}} - 1 \right) \times 10^3\text{‰},$$

1.2.2 Isotopic Fractionation of CO_2 in soil

When the infiltrating water dissolves soil CO_2 , some of it hydrates and dissociates to form bicarbonate (HCO_3^-) and carbonate (CO_3^{2-}) ions. The concentrations of these species at any given time is controlled by the pH of the local meteoric water. At each step of ion formation different fractionation factors are involved and the largest fractionation occurs during CO_2 hydration (Figure 1.2). The rate of fractionation also depends upon closed and open system conditions (explained in detail in chapter 2), and type of parent material. In silicate bedrock terrains,

there is less presence of Dissolved Inorganic Carbon (DIC) evolution, whereas in carbonate bedrock terrains, dissolution of calcite/dolomite acts as an additional source of carbon to the DIC pool.

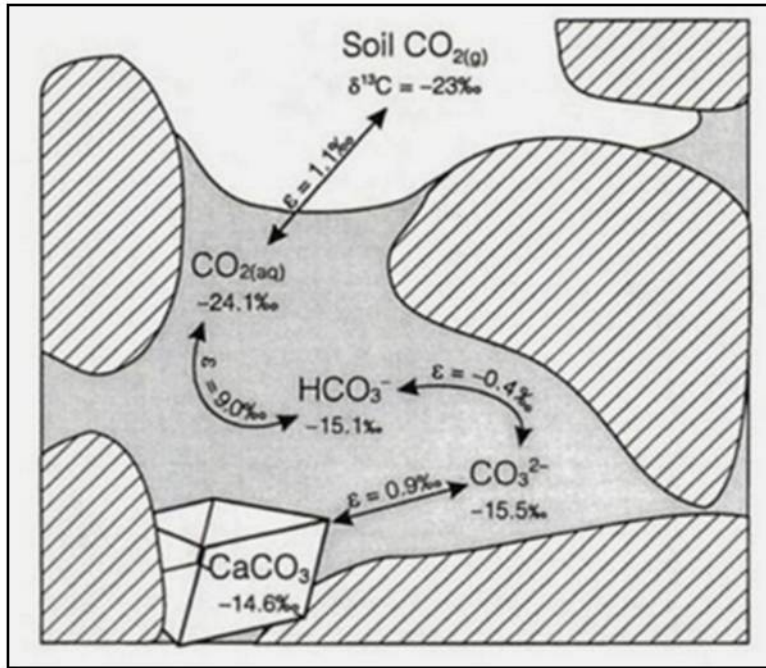


Figure 1.2: Schematic of fractionation of ^{13}C in during equilibrium exchange of carbon between CO_2 , Dissolved Inorganic Carbon and calcite at 25°C . Source: Clark and Fritz [1997]

1.2.3 Rayleigh model for isotopic fractionation

The isotopic composition of a system from which material is continuously removed can be studied using the Rayleigh model [Mook, 2006]. Consider a reservoir (vapor mass) from which rain is continuously removed by condensation. On account of isotopic fractionation, the remanant vapor gets depleted in ^{18}O and the rain is enriched in ^{18}O . The following assumptions are important, i) the abundance of heavier isotopes is much less than that of the lighter ($N^* \ll N$), ii) the isotopic fractionation occurs with instantaneous isotopic equilibrium, iii) the process is isothermal and iv) the reservoir is homogeneous (no isotopic gradient across the reservoir). At any instant, the stable isotope ratio R of the vapour is

given by

$$R = \frac{N^*}{N},$$

where N^* and N are the number of heavier and lighter isotopologues. Differentiating the equation gives,

$$dR = \frac{dN^*}{N} - \frac{RdN}{N}$$

By solving the equation with fractionation factor $\alpha = \frac{dN^*}{dN}/R$, we get

$$R = R_0 f^{\alpha-1}$$

Where, R_0 is the initial isotopic ratio of vapor and f is the fraction of substance remaining in the reservoir. In δ notations, Rayleigh equation can be expressed as

$$\delta = \delta_0 + (\alpha - 1)10^3 \ln f$$

The variation of isotopic composition of the water vapour, rain and the accumulated rain formed from the vapour at any instant according to the Rayleigh fractionation are shown in Fig 1.3 [Clark and Fritz, 1997]. In permil notation α is represented as the separation factor,

$$\epsilon = (\alpha - 1).10^3\text{‰}$$

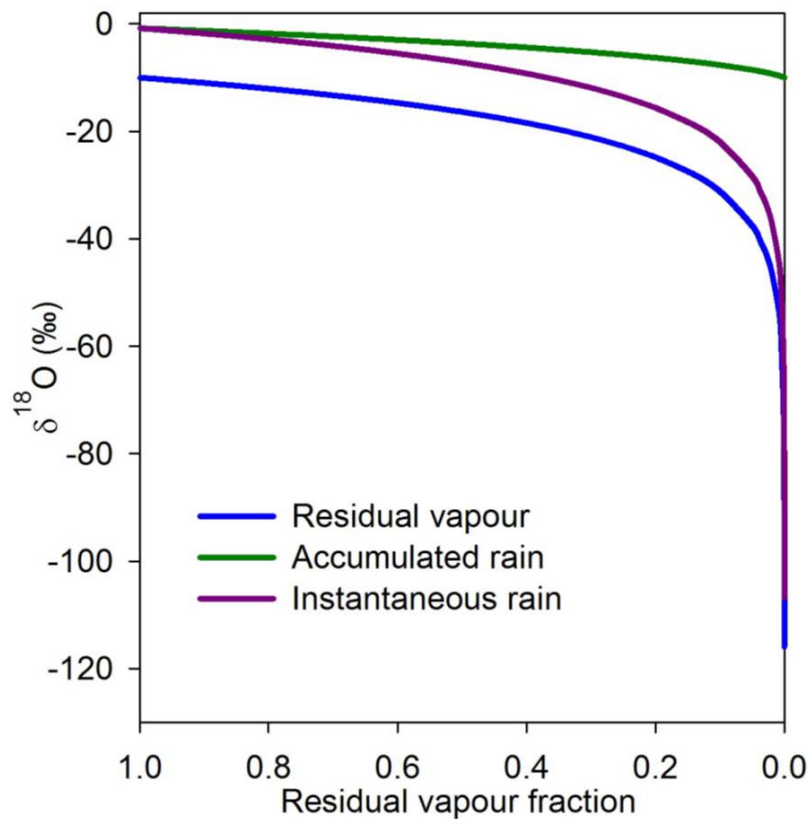


Figure 1.3: The change in the $\delta^{18}\text{O}$ of the water vapor, instantaneous rain and the accumulated rain formed from the water vapor versus the fraction of vapour remaining in the system. The process follows Rayleigh isotopic distillation. Figure redrawn from *Lekshmy [2015]*.

1.2.4 Observed isotopic effects

Stable isotopes of global precipitation shows large variations due to isotopic effects and geography.

1. **Temperature effect:** Temperature effect is the observed linear relationship between the mean annual surface air temperature and the mean annual precipitation isotopic composition (Figure 1.4). The relationship is based on the data procured from the Global Network of Isotopes in Precipitation (GNIP) and the mean annual air temperature at each station [e.g., *Dansgaard, 1964; Rozanski et al., 1993*],

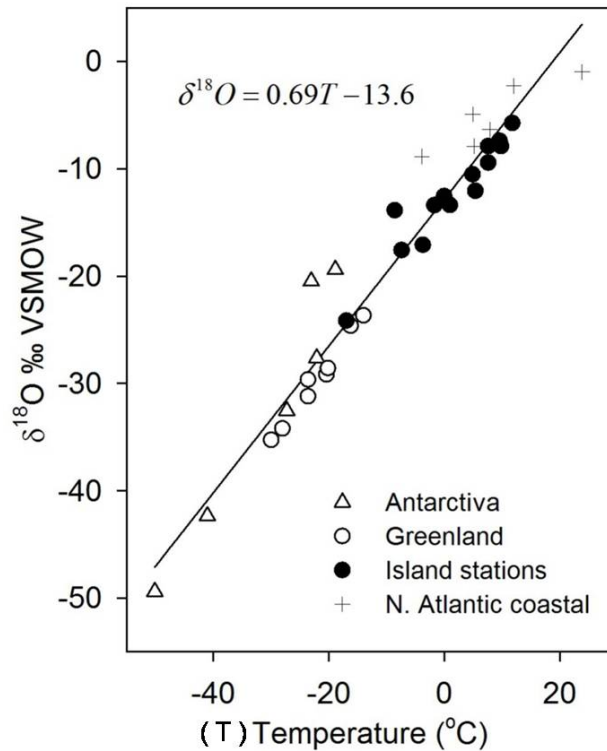


Figure 1.4: *Temperature- $\delta^{18}O$ relationship in precipitation in Antarctica, Greenland, Island stations and N. Atlantic coastal. [source: Clark and Fritz, 1997]*

$$\delta^{18}O = 0.695T_{annual} - 13.6$$

$$\text{‰}\delta D = 5.6T_{annual} - 100\text{‰}$$

This is obeyed mainly by high latitude precipitation and does not apply to tropical rain.

2. **Amount effect:** The explained temperature effect is predominately observed at high latitudes, especially where the mean annual surface air temperature is $> 15^{\circ}\text{C}$. In tropics, the isotopic composition of precipitation is controlled by the amount of rainfall. This phenomenon is known as "amount effect" [Dansgaard, 1964]. It is defined as the negative relation between the

precipitation isotopic ratio and rainfall [Fig 1.5]. [Dansgaard \[1964\]](#) observed $-1.5 \text{‰}/100 \text{ mm}$ of monthly rain on 14 islands distributed at tropical latitudes. The factors responsible for amount effect are :i) according to the Rayleigh isotopic fractionation, the newly formed condensate is enriched in ^{18}O .ii) There is re-evaporation of isotopically lighter rain at the bottom of the cloud because of lower humidity.

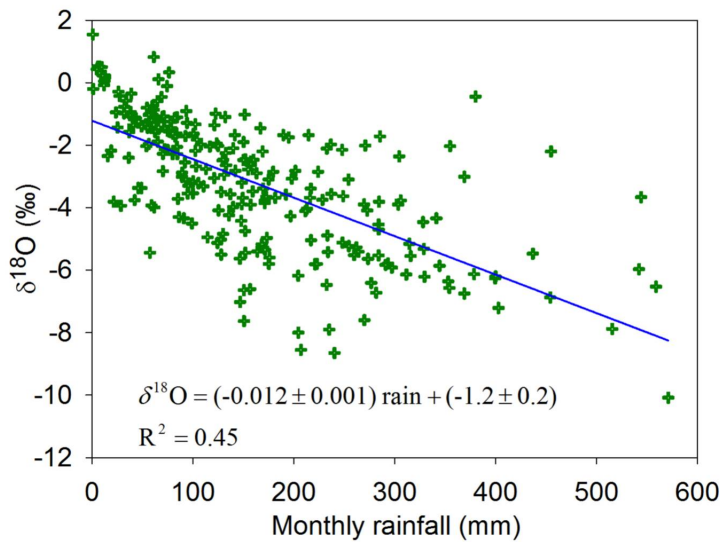


Figure 1.5: Relation between monthly rainfall and its $\delta^{18}\text{O}$ in tropical island stations around the globe [source: GNIP data, [\[Lekshmy, 2015\]](#)].

This exchanges isotopes with rain drops. So higher rainfall (high humidity) reduces the ^{18}O in rain. However, the process controlling the amount effect needs further investigation.

In the tropics, atmospheric convection is the main source of precipitation. Figure 1.6 shows a schematic representation of different components of a convective cloud system. The moisture feeding the system is derived from sub-cloud layer (SL), which consists of the surface evaporation, recycled moisture from the cloud and the entrained environmental moisture. In

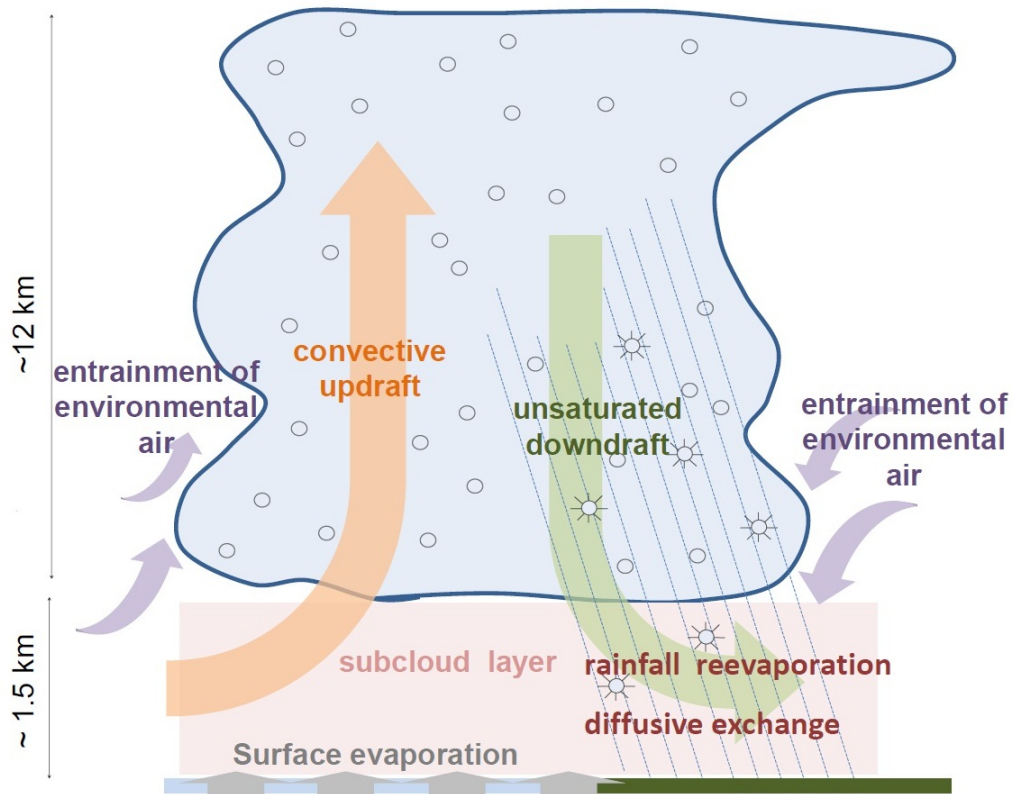


Figure 1.6: Schematic representation of a convective cloud system Source: [Lekshmy, 2015; Risi et al., 2008].

case of intense convection, high SL vapor is taken into the cloud in addition to entrained environmental air which is more depleted in the heavier isotopes. ^{18}O and D depleted water vapor (unsaturated) is formed due to condensation inside the cloud, that reaches the SL by downdraft. The re-evaporation of the rain drops also feed isotopically depleted vapor to the SL vapor. Hence, during strong convection, effective recycling of the moisture leads to depleted of ^{18}O and D of rainfall [Lekshmy, 2015; Risi et al., 2008]

- 3. The altitude effect:** As the vapor mass ascends over a mountain and cools down adiabatically, it leads to orographic precipitation. Precipitation starting at a particular height of the mountain continues till the top. Continuous precipitation leads to enriched ^{18}O and D rain at lower altitude

and depleted values at higher altitude. This process known as the altitude effect (negative relation between $\delta^{18}O$ and δD of rain and altitude) as seen in Figure 1.7.

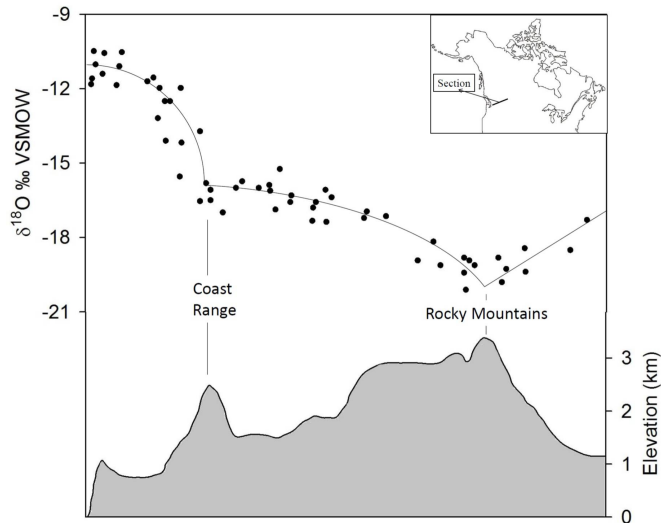


Figure 1.7: $\delta^{18}O$ variation along a high altitude mountain region [source: *Yonge et al., 1989*].

4. The continental effect:

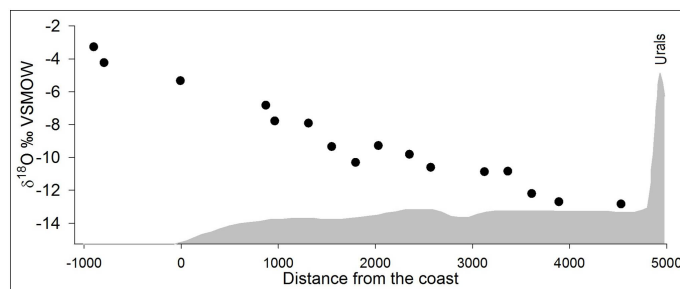


Figure 1.8: Variation of $\delta^{18}O$ from oceanic (southwest coast of Ireland) to inland region (Perm) over Europe [source: *Rozanski et al., 1993*].

The vapor mass transporting from its source region to inland, continues to rain out leading to the preferential removal of the heavier isotope in the initial rainout. The gradual depletion of the heavier isotopes is observed in

the precipitation as the vapor mass travels to the interior of the continents. This effect is known as the continental effect. Figure 1.8 shows an example of continental effect on the long term annual $\delta^{18}O$ of precipitation in Europe.

1.3 Objectives

Variability of ISM throughout the Holocene has been a debatable issue. While some workers showed that monsoon decreased in response to decline in insolation, others infer that gradual increase in its intensity from 11.7 ka to present. There is another growing consensus about the trend of decrease in monsoon during mid-Holocene which faced widespread aridification with prolonged droughts. The schools of thought are divided between abrupt or gradual decline of monsoon during mid-Holocene. Hence, the focus of the present work is to address the following issues:

1. To generate high resolution speleothem $\delta^{18}O$ record covering the entire Holocene.
2. To test the concepts of increase or decrease in monsoon throughout the Holocene.
3. To test for coherence between speleothem based monsoon reconstructions and other proxy records.
4. To assess the contributions of various internal and external driving forces in governing millennial and centennial monsoon oscillations.

Understanding the variability of monsoon on glacial-interglacial timescales is equally important as studying Holocene ISM changes. The longer records of reconstructed ISM show that it was stronger during interglacial and weaker during glacial periods [*Sirocko et al., 1993*], whereas the winter monsoon was stronger during glacial periods. Hence part of this thesis work focuses on :

1. To verify the response of ISM on glacial-interglacial timescales.
2. To study the role of insolation in driving the monsoon variability.
3. To identify the primary drivers of the monsoon system on glacial-interglacial climate oscillations.

The aforementioned issues are addressed using the five stalagmite samples and a sediment core from Andaman Sea. Three of these samples are used to study the Holocene variability of monsoon and the other two are used to reconstruct paleomonsoon during the late Pleistocene.

1.4 Previous work

Use of speleothem as a proxy to reconstruct the Indian Monsoon, is quite well established [[Kotlia et al., 2014](#); [Laskar et al., 2013](#); [Lone et al., 2014](#); [Sanwal et al., 2013](#); [Yadava and Ramesh, 2005, 2006](#); [Yadava et al., 2004](#)]. In India, speleothem formations are found where there are large outcrops of limestone bedrocks. Cluster of caves are found in Kanger valley National park, Chattisgarh. As this area falls in the core monsoon region of India, speleothems formed here represent changes in the amount of monsoon precipitation. Several studies have been carried out on speleothems from these caves [[Ramesh et al., 2010](#); [Sinha et al., 2007](#); [Yadava and Ramesh, 2006](#)]. Monsoon variability during 14th and 15th century is captured in a 900 years (600-1500 AD) old stalagmite from Dandak cave. Major famines like Durga Devi famine that lasted from 1396 -1409 AD during ‘Little Ice Age’ coincides with the enriched oxygen values of speleothem of this timespan. Higher precipitation during ‘Medieval warming’ during 900-1350 AD is also recorded in the stalagmite. Variability of monsoon during Little ice age and Medieval warming is correlated with change in the solar activity [[Sinha et al., 2007](#)].

Based on the 3400 yr BP old Gupteshar stalactite sample it was inferred that high rainfall persisted from 3400-2900 yr BP with declining monsoon intensity during 2900-1200 yr BP. Since then increase in precipitation was recorded till present [*Yadava and Ramesh, 2005, 2006; Yadava et al., 2004*]. Speleothems formed elsewhere in India are also used for monsoon reconstruction. A 331 year old stalagmite, from the Akalagavi cave of Northern Karnataka, India, revealed distinct annual layers. Variability in the monsoon rain during CE 1650-1997, with the highest precipitation at CE 1666 and the lowest around CE 1900 [*Yadava et al., 2004*] was observed. *Laskar et al. [2011, 2013]*, studied a stalagmite from Baratang cave, Andaman to assess the potential of the Andaman speleothems as monsoon recorders. Weaker ISM was observed during Roman Warm Period (2100 - 1800 cal BP) while strong ISM observed during Medieval warming. Another stalagmite sample from the Valmiki cave, southern India covering a time span of 15,700 to 14,700 a (U-Th dated) was used to infer abrupt changes in monsoon rain during the last deglaciation [*Lone et al., 2014*]. Another study from Mawmulah cave, Meghalaya records an ISM variability from 33.8 - 5.5 ka [*Dutt et al., 2015*]. Abrupt increase in rainfall during Bolling-Allerod and early Holocene and significant weakening during Younger Dryas and Heinrich cold event was observed. Solar forcing and strong ocean-atmospheric circulation were suggested as possible controllers of the ISM dynamics [*Allu et al., 2015; Asmerom et al., 2013*]. The work in this field is growing with new stalagmite studies carried across India. Many more caves are explored to assess their potential for paleoclimatic studies.

Chapter 2

Paleoclimate proxies

2.1 Speleothems

The word speleothem is derived from Greek words ‘Spelaion’ meaning cave and ‘thema’ meaning deposit [Moore, 1952; Schwarcz, 1986]. The speleothems used for paleoclimate studies are made of calcite or aragonite or a mixture of two. Speleothems are formed in karstic caves, where the water table is significantly lowered, favoring air exchange with atmosphere. A typical cross section of karstic caves can be divided to four parts, namely, soil, epikarst, vadose zone/karst and phreatic zone. A schematic representation of speleothem formation is shown in Figure 2.1. Partial pressure of carbon dioxide in rainfall is $10^{-3.5}$ bars. As rainfall percolates into the soil, it dissolves a higher amount of additional CO_2 released from microbial decay and plant root respiration. Partial pressure of CO_2 (P_{CO_2}) in soil is 10^{-1} bar. This ”corrosive” solution reacts with the host carbonate rocks in epikarst and forms HCO_3^- , CO_3^- ions [Sasowsky and Mylroie, 2007]. The degree of saturation of these ions depends upon the acidity of water and residence time of water in the passage. During the dissolution process, trace elements from the bedrock are also incorporated in dissolved, particulate or colloidal state. As the saturated water descends through the crevices and fractures into the karst, it comes in contact with cave air having lower P_{CO_2} ($10^{-2.5}$ bars) . This leads to

degassing of CO_2 from the solution and precipitation of $CaCO_3$ in the form of calcite or aragonite.

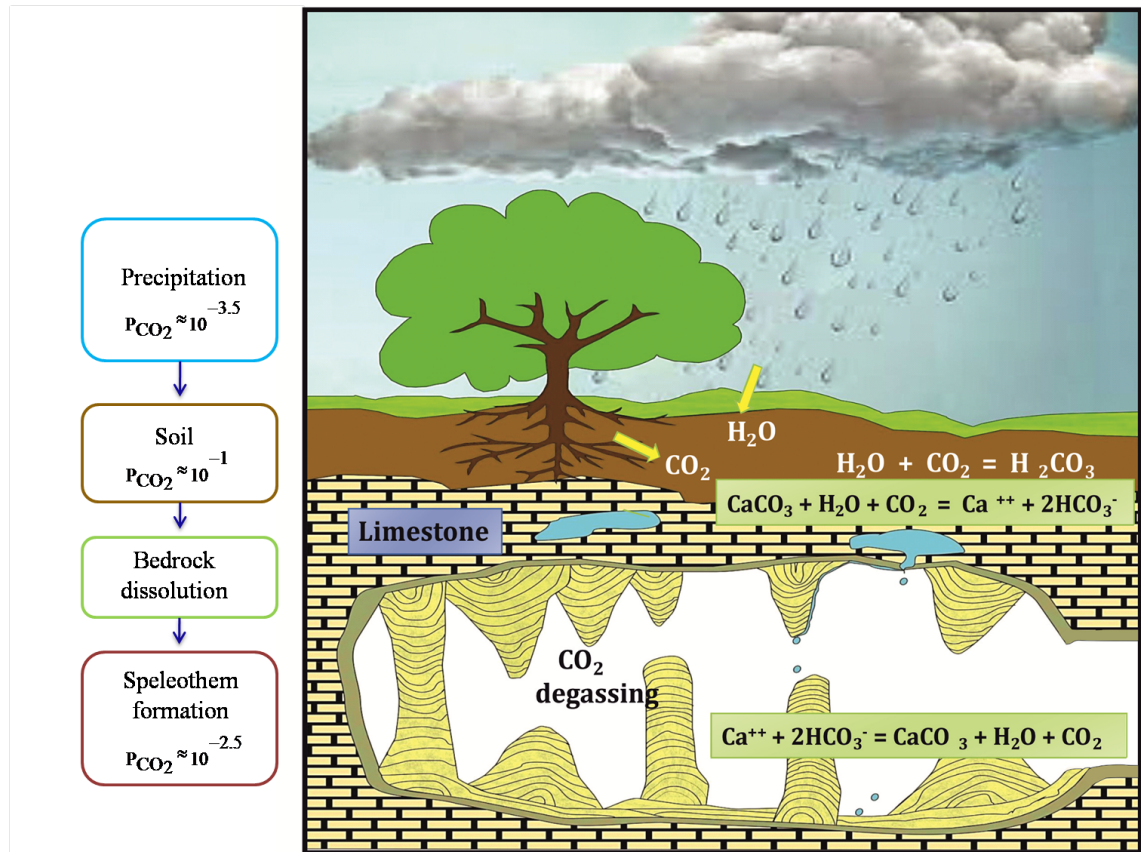


Figure 2.1: Conceptual model explaining the formation of speleothems in a karstic cave. Partial pressures of CO_2 in rainfall, soil and cave air are typical values taken from *Sasowsky and Mylroie [2007]*.

At the roof of the cave, near the exposed fractures, slow dripping of water leads to the formation of hollow cylindrical tubes known as soda straws. They are among the earliest structures to form. Ceaseless dripping along soda straws leads to precipitation of calcite on its outer margin, forming a conical structure called as Stalactite. The excess water from the stalactites drips down and forms stalagmites which grow upwards. When the rate of precipitation is high, stalactites and stalagmites grow together and merge to form columns. When the rate of drip is high, the excess water is spewed on the floor, and subsequently forms layered deposits known as flow stones. Of the following morphotypes, stalactites and

stalagmites are favored for paleoclimate studies as the layers may be unperturbed and have less detrital content. Stalagmites, are preferred over stalactites, as they are cylindrical with near flat layers. This favors sub-sampling along each layer as opposed to conical growth layers of stalactites, which may also be interrupted by soda straws in the center.

2.1.1 Mineralogy

Calcite is the most abundant mineral in speleothems. However, sometimes the calcitic fabric is intertwined with aragonite. Aragonite is metastable with respect to calcite at atmospheric pressure. Trace elements play a key role in deciding the calcite-aragonite fabric [*Sasowsky and Mylroie, 2007*]. Sr^{2+} ions favor aragonite nucleation, thereby hindering the formation of calcite crystals. Aragonite precipitation is also dominant when the host rock is dolomite, with high Mg/Ca ratios. Mg^{2+} , inhibits calcite nucleation, thereby necessitating the supersaturation required for the aragonite formation [*Berner, 1975; Bischoff, 1968*]. Calcite-Aragonite fabric also depends upon the cave setting. In poorly ventilated caves, partial pressure of water vapor is saturated and partial pressure of CO_2 may approach that of the drip water. As a result, slow deposition of calcite crystal takes place. In a dry ventilated caves, humidity is very low and P_{CO_2} may represent the values of atmosphere background [*Bar-Matthews et al., 1991; Murray, 1954; Railsback et al., 1994*]. As a result, there is rapid degassing and deposition of aragonite may be favored. A speleothem from the Sai baba cave from Nepal was used to reconstruct changes in the Indian summer monsoon during the last 2300 years based on change in calcite-aragonite fabric. Aragonite crystallization was observed during the weaker/drier phases of monsoon, whereas calcite crystallization was observed during wetter conditions [*Denniston et al., 2000*].

2.1.2 Isotope exchange in speleothems

The dissolution of bedrock and subsequent deposition of speleothem involves involved chemistry, right from the conversation of gaseous carbon oxide into dissolved aqueous state.

In the atmosphere, carbon dioxide is present as a trace species with the mixing ratio reaching up to 400 ppm. Carbon dioxide in gas phase ($CO_{2(g-soil)}$) dissolves in meteoric water to form $CO_{2(aq)}$.



$CO_{2(aq)}$ then reacts with H_2O to form carbonic acid.



Carbonic acid, being a 'weak acid', dissociates to bicarbonate ions at higher pH.



The DIC pool at neutral pH values is dominant in HCO_3^- ions, but has a small proportion of CO_3^- ions for carbonate mineral stability.



The further reactions leading to speleothem formation are



Dissolution of the bedrock carbonate can be summarized as :



Speleothems can form as a result of the interplay of various subsurface processes shown in Figure 2.2 The isotopic composition of the precipitated calcite depends upon the following cave characteristics:

- (1) The solution dissolving the limestone bedrock is always in contact with the soil carbon dioxide gas, known as 'open system'
- (2) The solution dissolving the limestone bedrock remains isolated from the gas phase until it is exposed to cave air, known as 'closed system'.

The isotopic composition of speleothems may also be influenced by changes in the cave environment. These are:

(1) When the humidity inside the cave is very high and partial pressure of carbon dioxide in cave air is close to the saturated value, the rate of loss of carbon dioxide from the solution becomes sufficiently slow. At this rate isotopes are precipitated in isotopic equilibrium. The slowest reactions within solution are dehydration of bicarbonate ions and hydration of aqueous carbon dioxide. This is the only step where there is isotopic exchange between oxygen of water and oxygen of carbon compounds in the solution [Hendy, 1971]. For calcite to be precipitated under "oxygen isotopic equilibrium" with the water, equilibrium between these species is necessary.

(2) In ventilated caves, the partial pressure of cave air may be close to the atmospheric background value. In such a scenario, when the dripping water comes in contact with cave air, there is rapid degassing of carbon dioxide, prior to achieving the state of equilibrium between aqueous carbon dioxide and bicarbonate ions. This process is called "Kinetically fractionated deposition" [Hendy, 1971].

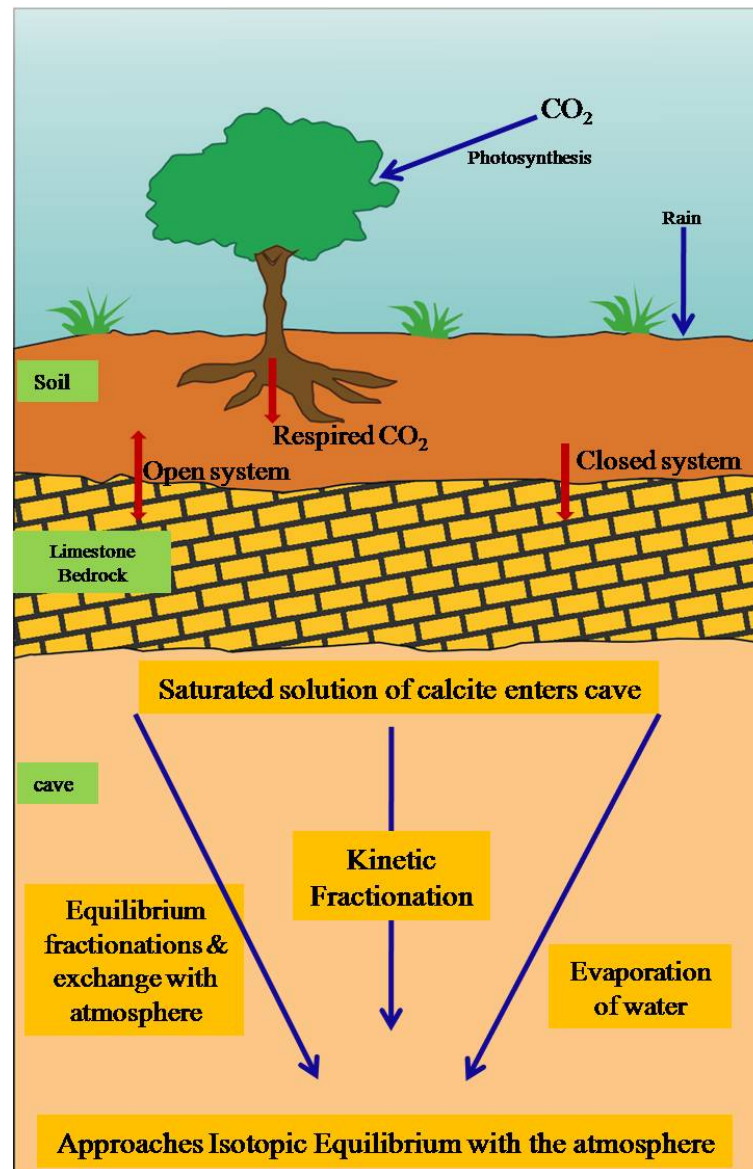


Figure 2.2: A schematic diagram of the role of different pathways involved in speleothem formation. Figure redrawn from *Hendy [1971]*.

(3) The third type of deposition occurs near the cave entrance or where the cave humidity is very low. In this case, the solution becomes supersaturated through loss of water due to evaporation.

These processes play a key role in controlling the isotopic composition in speleothems, and their effects on oxygen and carbon isotopic values will be discussed in detail below.

Carbon Isotopes

The carbon in speleothems is derived from two sources (1) Soil CO_2 which is much lighter than the atmospheric carbon dioxide, with a $\delta^{13}C$ value of -9‰ [Craig and Keeling, 1963]. And (2) Bedrock Carbon. The evolution of carbon isotopes is a complex process and depends upon several factors [Hendy, 1971; Lauritzen and Lundberg, 1999; Wigley et al., 1978] shown in Figure 2.3 . They are:

(1) The photosynthetic pathways

When carbon dioxide from atmosphere is taken by plants, it is converted to organic compound during photosynthesis, a process known as "kinetic isotopic fractionation". The plants following Calvin (normal) photosynthetic cycle (C3), produce biogenic carbon with $\delta^{13}C$ values -36‰ to -22‰ w.r.t.VPDB [Badeck et al., 2005; Cerling and Harris, 1999]. Such type of vegetation is found in humid conditions, like tropical forests. The plants following HATCH-SLACK photosynthetic cycle (C4) on the other hand, produce carbon with $\delta^{13}C$ values of about -12‰ [Bender, 1968]. Grasses in semi-arid regions follow this cycle. Hence, the $\delta^{13}C$ of deposited calcite depends upon the relative contribution from these two types of vegetation. Climate driven changes can effect the type of vegetation and in turn change the $\delta^{13}C$ of speleothems [Clark and Fritz, 1997; Gascoyne, 1992; Lauritzen, 1995]. However, change in vegetation type in response to climate change is observed on centennial timescales scales.

(2) Biological activity

Carbon dioxide in soil is derived from two sources: plant root respiration and microbial decomposition. During the wet season, intense respiration leads to high pCO_2 and lower values of $\delta^{13}C$.

(3) Closed cave system

In closed cave systems, the carbon dioxide from the solution does not interact with the gaseous phase before coming in contact with the limestone bedrock. Thus, there are two sources of carbon: the solutions that carried carbon from the

aerated zones and the carbon released during dissolution of limestone. Here the isotopically depleted carbon species from an aqueous solution with $\delta^{13}C = -24\text{‰}$ combine with the isotopically heavier carbon dioxide of $\delta^{13}C = +1\text{‰}$ to form calcite. Unless variation in climate causes changes in $\delta^{13}C$ or partial pressure of carbon dioxide in the soil, there will not be significant variation in the $\delta^{13}C$ of calcite precipitated from a closed system solutions.

(4) Open cave system

In this type of cave setting, the isotopes of carbon in solution dissolving limestone are constantly interacting with the carbon dioxide from soil atmosphere, such that, a chemical and isotopic equilibrium is maintained. The isotopic composition of carbon is give by following equation

$$\delta^{13}C_{CO_{2(aq)}} \cong \delta^{13}C_{CO_{2(g)}} + \varepsilon^{13}C_{(CO_{2(aq)}-CO_{2(g)})} \quad (2.8)$$

where $\varepsilon^{13}C_{(CO_{2(aq)}-CO_{2(g)})}$ is the isotopic enrichment factor between aqueous carbon dioxide and gaseous carbon dioxide, [[Craig, 1954](#); [Hendy, 1971](#)].

(5) Drip rate in the cave

When the saturated solution comes in contact with cave atmosphere, loss of CO_2 may take place by degassing or evaporation. If the rate of degassing is sufficiently slow then the isotopic equilibrium is maintained between degassing carbon dioxide, precipitating calcite and carbon isotopes in solution. If the equilibrium conditions are such that there is a progressive enrichment in ^{13}C of the species remaining in the solution w.r.t. carbon dioxide degassing and precipitating calcite, it is called "Rayleigh distillation" process. In this process, if rate of transport of CO_2 from the solution is close to the cave atmosphere, there will be steady exchange and isotopic equilibrium is maintained. However, $\delta^{13}C$ values may not truly represent climate variability, unless there is a systematic change in the partial pressure or $\delta^{13}C$ value of the carbon dioxide in the soil atmosphere.

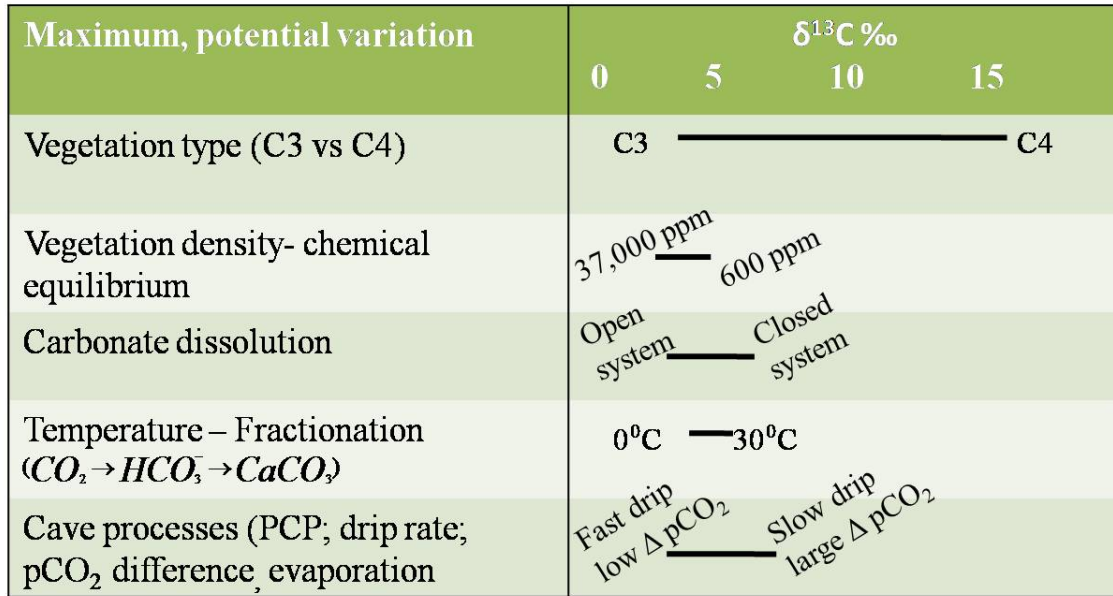


Figure 2.3: Factors controlling $\delta^{13}\text{C}$ of speleothem. Figure redrawn from the sources of carbon in speleothems, presented at the Speleothem Summer School, 2015, Oxford, Jens Fohlmeister

Oxygen Isotopes

The use of oxygen isotopes of speleothems for paleoclimate studies was first reported in the 1960's [Broecker *et al.*, 1960; Hendy and Wilson, 1968]. The stable isotopes of interest are, ^{18}O and ^{16}O and their ratios are measured relative to laboratory and international standards on a mass spectrometer. And the values are expressed as

$$\delta^{18}\text{O} = \left[\frac{\left(\frac{^{18}\text{O}}{^{16}\text{O}}\right)_{\text{Sample}}}{\left(\frac{^{18}\text{O}}{^{16}\text{O}}\right)_{\text{Standard}}} - 1 \right] \times 10^3 \text{ ‰} \quad (2.9)$$

The standard used for carbonate measurement is VPDB-Vienna Pee Dee Belemnite derived from the rostrum of Belemnitella americana from the Pee Dee Formation of South Carolina in U.S.A [Coplen *et al.*, 1983; Gonfiantini, 1978]. The standard is procured from IAEA (International Atomic Energy Agency, Vienna).

When the sample has higher $\delta^{18}O$ relative to a standard, it is referred as isotopically "enriched" or "heavier" and vice a versa. The fractionation factor α_{CW} is known for the calcite-water system and is given by the following equation [*O'Neil et al., 1969*].

$$\alpha_{CW} = \frac{\left(\frac{^{18}O}{^{16}O}\right)_{Calcite}}{\left(\frac{^{18}O}{^{16}O}\right)_{Water}} \quad (2.10)$$

$$\Delta_{cw} = (2.78 \times 10^6 / T^2) - 3.39 \quad (2.11)$$

Where, T is the ambient cave temperature in $^{\circ}K$ and $\Delta_{cw} = 10^3 \alpha_{CW}$.

The oxygen isotopes in speleothems can be traced back to the processes controlling the hydrological cycle. Evolution of oxygen isotopes precipitating in speleothems depends upon the phase changes on its course from ocean water \rightarrow vapor \rightarrow precipitation \rightarrow soil water \rightarrow epikarst solution \rightarrow karst drip water. The $\delta^{18}O$ value of the soil water is determined by the $\delta^{18}O$ value of the precipitation infiltrating the soil pores. Processes such as evaporation and transpiration play a crucial role in controlling the $\delta^{18}O$ in soil pores. In arid regions, evaporation leads to enrichment in ^{18}O , whereas in humid climates the role of evaporation is minimal [*Allison, 1982; Lachniet, 2009; Tang and Feng, 2001*]. Soil water infiltrates into the epikarst, having fissures, bedding planes and other solution features where water may get stored or mixed. Flow through the epikarst may occur through primary porosity, joints or large conduits [*Klimchouk, 2000; Williams, 2008; Yonge et al., 1985*]. The residence time of water in the epikarst also controls the $\delta^{18}O$ of water. Longer the residence time, more are the chances of mixing with ground water. Hence, a rapid flow rate leads to less alterations in the $\delta^{18}O$, making it suitable for detecting high-frequency climatic events [*McDonald et al., 2007*], whereas a slow residence time is useful for studying long term climate

changes. The $\delta^{18}O$ of the solution entering the caves later becomes functions of the degree of saturation of solution, humidity inside the cave etc. In ventilated caves, where the humidity is less than 100%, evaporation takes place and ^{18}O is further enriched.

In order for speleothems to track hydrological changes, it is important that the isotopic equilibrium is maintained between the drip water, degassing CO_2 and precipitating $CaCO_3$ [Hendy, 1971]. The only factors which affect the oxygen isotopic composition are changes in the cave air temperature and change in the mean isotopic composition of water. Both these factors change with the change in climate. The temperature inside the cave remains constant throughout the year in poorly ventilated caves because of thermal inertia [Gascoyne, 1992; Lauritzen, 1995; McDermott et al., 2006; Repinski et al., 1999]. Changes in the annual temperature affect the $\delta^{18}O$ of the precipitating calcite, where heavier $\delta^{18}O_c$ values imply lower temperatures. The degree on enrichment is given by equation: $d(\Delta_{cw})/dT = -0.21^{\circ}C^{-1}$ at $25^{\circ}C$.

The temperature interpretation based on speleothem $\delta^{18}O$ is not straight forward and depends upon many parameters. The factors controlling $\delta^{18}O$ are summarized by Lauritzen and Lundberg [1999] in an expression

$$\delta^{18}O = \exp\{a/T_1^2 - b\}[F(T_2, t, g) + 1000] - 1000 \quad (2.12)$$

same as

$$\ln\alpha = \ln\left(\frac{\delta^{18}O + 1000}{F(T_2, t, g) + 1000}\right) = \frac{a}{T_2} - b \quad (2.13)$$

where $a = 2.78 \times 10^3$, $b = 3.39 \times 10^3$ (empirical constants), T_1 is the deep cave temperature and T_2 is the surface temperature, t is the time and g is the geographical position (latitude, longitude) of the cave. The thermodynamic frac-

tionation between calcite and water inside the cave is given by the exponential part, the drip water isotopic composition ($\delta^{18}O$) is controlled by $F(T, t, g)$. In most of the cases, the cave temperature can be assumed to be equal to the surface temperature. For paleo-temperature reconstructions T derivative is expressed as

$$\mu = \frac{d\delta^{18}O_C}{dT}$$

and can be positive or negative or even zero. Hence the use of speleothem $\delta^{18}O_C$ for temperature interpretation is ambiguous [*Gascoyne, 1992; Lauritzen and Lundberg, 1999*]. However, $\delta^{18}O_C$ can be used to trace first order changes (glacial-interglacial events) in climate [*McDermott et al., 2006*].

The caves located in tropics however, show less temperature annual variability. The $\delta^{18}O_C$ of speleothems in such caves, are strongly dependent inversely on the amount of rainfall.

2.1.3 Trace elements

$CaCO_3$ while precipitating incorporates trace elements (Tr) from the solution. In the solution, various elements form divalent cations and substitute for Ca ion in the $CaCO_3$ crystal lattice [*Fairchild and Treble, 2009*]. Elements such as Mg, Sr, Ba with similar ionic radii substitute for Ca under different physical conditions [*Morse and Bender, 1990*].



A simple equation is used to define the distribution coefficient to relate solution and mineral compositions.

$$(TrCO_3/CaCO_3) = K_{Tr}(Tr/Ca)_{solution}$$

Where Tr is the trace ion and K_{Tr} is the distribution coefficient that depends on precipitation, temperature, crystal morphology. Other than substitution, trace elements come through the aqueous medium where they are adsorbed on the surface of detrital particles and hence get incorporated in speleothems. Excess

Th that gets adsorbed causes trouble in dating of the speleothem. The geological setting of karst deposits plays a major role in the trace element contribution. The primary source of calcium and other major elements come from the bedrock and overlying soil. Dissolution is maximum where pCO_2 reaches its peak. Most of the P comes from minor traces of Apatite in soil [Huang *et al.*, 2001]. Trace element concentrations also depend upon residence time of drip water. When the rock has both dolomitic and limestone composition, both will dissolve in undersaturated solutions. However, in deposited calcite Mg/Ca ratio will be lower than that of the host rock composition. The two important modes of transport of trace element to karstified bedrock are chemical mobilization and through hydrological processes [Tooth and Fairchild, 2003]. Chemical mobilization is mediated at three different rates. At rapid rates, trace elements adsorbed on organic and inorganic surfaces, preexisting dissolved species and mobilized particles are transported. At intermediate rates, there is calcite dissolution of the host rock followed by the slow process of chemical weathering of less soluble dolomite, silicates, phosphates and oxides [Fairchild and Treble, 2009]. Trace element contribution is also affected by the rate at which drip water flows. If the drip rate is slow due to low-permeable soil, the interaction time increases leading to the enrichment of trace species. High flow rate on the other hand can also be associated with trace element enrichment primarily for the species that are transported as colloids.

The infiltrating water passes from the dissolution regime to the precipitation regime, when it encounters conduits with relatively lower pCO_2 [Fairchild *et al.*, 2006]. The resultant degassing leads to supersaturation of water for $CaCO_3$ and calcite precipitation. As K_{Tr} values for the carbonate precipitated are less than one, there is larger reduction of Ca in solution than that of the trace element and hence an increase in the ratio of trace element to Ca in solution [Holland *et al.*, 1964]. Since there are gas filled conduits in the soil, leading to "Prior Calcite Precipitation" (PCP), it might suggest drier climatic conditions [Fairchild *et al.*, 2000; Johnson *et al.*, 2006; McMillan *et al.*, 2005]. PCP usually leads

to higher Mg/Ca and Sr/Ca ratios, which could also favor aragonite formation in speleothems [Frisia *et al.*, 2002; McMillan *et al.*, 2005]. Sr is incorporated in larger quantities at growth rates, where it substitutes for Ca or occupies the defect sites [Gabitov and Watson, 2006]. Other trace elements are seen associated with colloidal medium or adsorbed on organic-inorganic substrates. The elements associated with fluorescent lamina are seen in following rank order: $Y > (Cu, Zn, Pb) > Br, P$. Y is essentially transported through an organic colloidal phase [Borsato *et al.*, 2007; Fairchild and Treble, 2009]. Phosphorous binds very strongly to Calcite surfaces and if present in high concentrations may inhibit calcite growth [Huang *et al.*, 2001]. Transport of colloids is likely to increase during higher precipitation conditions where the rate of infiltration is higher. Mn is transported either as a organic complex, colloidal complexes or as a particle in groundwater [Perrette *et al.*, 2000; Richter *et al.*, 2004; Zhou *et al.*, 2008]. Mn that is present as colloidal complex may get attached to the fine detrital layers in speleothem, and it may not be associated with crystal lattice.

Mg in Speleothem Mg/Ca ratios in speleothem were considered to respond to temperature changes within caves. Gascoyne [1983] demonstrated a positive correlation between D_{mg} and the cave temperature. Fairchild *et al.* [2001] suggested that Mg in speleothems can be used to reconstruct hydrological changes. Mg/Ca ratios are found to be sensitive to amount of rainfall and can be used in conjunction with stable isotope values to assess monsoon variability. Mg/Ca ratio in drip water is influenced by PCP and is higher during low-flow conditions. A positive correlation is seen between $\delta^{13}C$ and Mg driven by the effect of PCP. In the case of $\delta^{18}C$ values, the Mg/Ca ratios show a negative correlation, as there are a few sites where PCP takes place. Sampling sites of speleothems are equally important. Baldini *et al.* [2006] argued that it is preferable to collect samples below active seepage flow, as the trace element contribution will respond to hydrological changes. Thickness of the overlying limestone bedrock is another factor affect-

ing the influx of trace elements. If the bedrock thickness is less, there are more chances of preserving the response of trace element to hydrological changes.

2.1.4 Speleothems as paleomonsoon proxy

Speleothems deposited in the karst formations of India are direct recorders of Indian summer monsoon as most of the annual precipitation is received in peninsular India during June to September [*Lone et al.*, 2014; *Sinha et al.*, 2007; *Yadava and Ramesh*, 1999, 2005, 2006, 2007]. Most of the speleothems studies so far studied ISM changes during part of the Holocene period. The Holocene marks the intensification of monsoon at around 11.7 ka. The monsoon variability during Holocene period, led to concomitant changes in different human civilizations spread across India.

There are several proxy records from east Asia and Oman that reconstructed the ISM during the Pleistocene. However, very few records exist from the core monsoon region of India covering this timespan [*Cai et al.*, 2015; *Yuan et al.*, 2004; *Zhisheng et al.*, 2011]. The importance of this period is recurring glacial-interglacial cycles. In tropical regions, the glacial-interglacial periods are interpreted in term of weakening or strengthening of monsoon respectively. Response of the ISM during these cycles is documented in the studies carried out over the Indian ocean [*Leuschner and Sirocko*, 2000; *Prabhu et al.*, 2004; *Schulz et al.*, 2002; *Sirocko et al.*, 1993; *Zorzi et al.*, 2015] and using various terrestrial proxies [*Agrawal et al.*, 2012; *Dutt et al.*, 2015; *Juyal et al.*, 2006; *Roy et al.*, 2012] . However, most of the terrestrial proxies which are direct recorders of monsoon focus on the last glacial maxima. Hence there is a lack of understanding regarding the effect of glacial millennial climate variability on ISM .With absolutely dated speleothems, in combination with high resolution stable isotope or trace element analyses, glacial-interglacial cycles can be studied in great detail.

The aim of the present study is to reconstruct high resolution monsoonal changes since the late Pleistocene period.

2.1.5 Sample locations

Most of the carbonate outcrops in India are karstified and host variety of speleothem formations. Some of these caves are explored extensively by geoscientists for paleoclimate studies. The caves which have been studied to understand the climate variability are shown in Figure 2.4 [Allu *et al.*, 2015; Sinha *et al.*, 2007; Sinha and Naik, 2004; Yadava and Ramesh, 2001, 2005, 2006; Yadava *et al.*, 2007]. Our present work is focused on three such caves in the Kanger valley cave complex, Chattisgarh and the Belum cave in Andhra Pradesh.

The Kanger valley cave complex

A vast cave complex is located in Kanger valley National Park, Chattisgarh of central India comprising of unexplored caves like Dandak, Kotumsar and Kailash 2.4. The caves are exposed in the north of the Kanger River [Biswas, 2010]. And are formed by dissolution of the Kanger limestone belonging to the Indravati group rocks of Mesoproterozoic era [Maheshwari *et al.*, 2005]. In the present study, stalagmites from all the three caves spanning different time frames are studied in detail.

The Dandak cave The Dandak cave (18°51'30" N; 81°57'00" E, 400 m.s.l) is one of the many caves located in the Kanger valley National Park, Chattisgarh (Figure 2.4) in Central India [Sinha *et al.*, 2007; Yadava and Ramesh, 2005]. The cave is situated on a hillock with scattered boulders exposed around [Biswas and Shrotriya, 2011]. The cave entrance located in the north-west direction opens up to a large hall, known as the outer chamber of the cave.

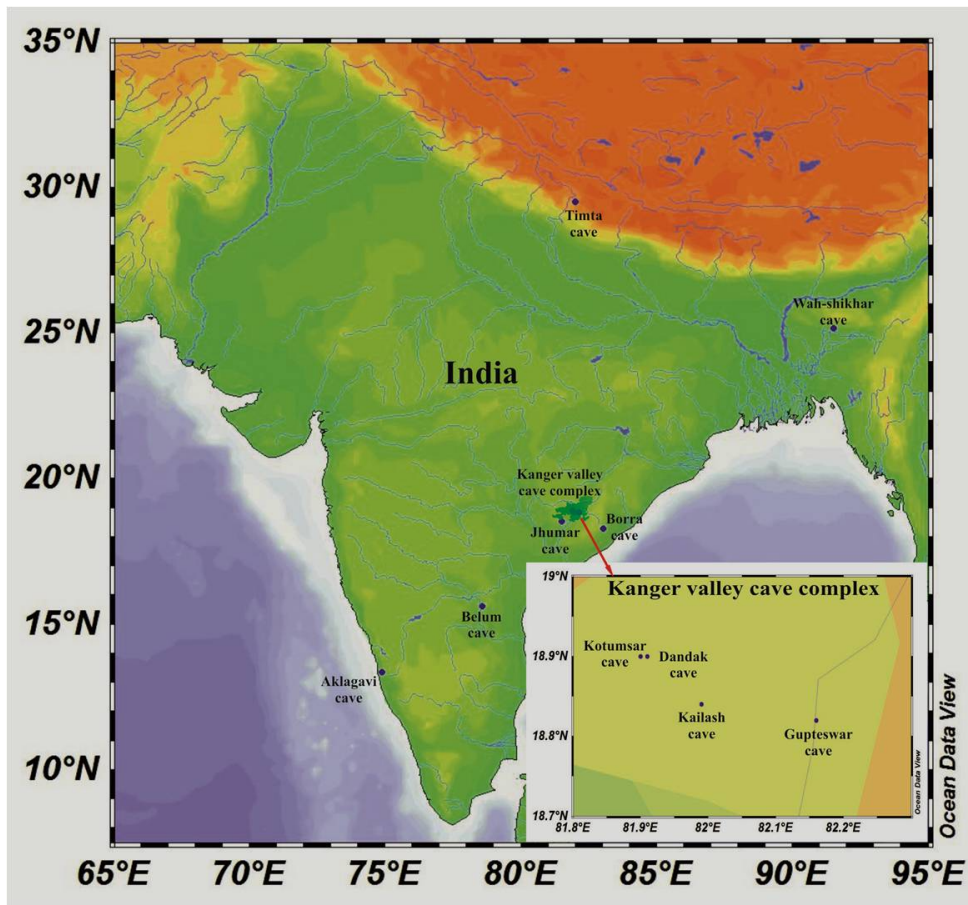


Figure 2.4: Map of the India showing the locations of the caves explored for paleoclimate studies. The box in the lower right, zooms in onto the Kanger valley cave complex, Chattisgarh.

The average length of the cave is 330 meters and it has two main chambers. The outer chamber is connected to the inner one through a narrow passage. The seasonal variability is found in the physical parameters of the cave such as, cave air temperature, relative humidity and water pH in both the chambers [Biswas and Shrotriya, 2011]. Average pH of the seepage water and drip water temperatures are (7.2-7.5) and (18-20°C), respectively, [Biswas and Shrotriya, 2011]. Tourism is exempted for the caves, and thus there is a good scope of undisturbed growth in the speleothem samples. The stalagmite samples were collected from the inner chamber, exhibiting high humidity and poor ventilation.

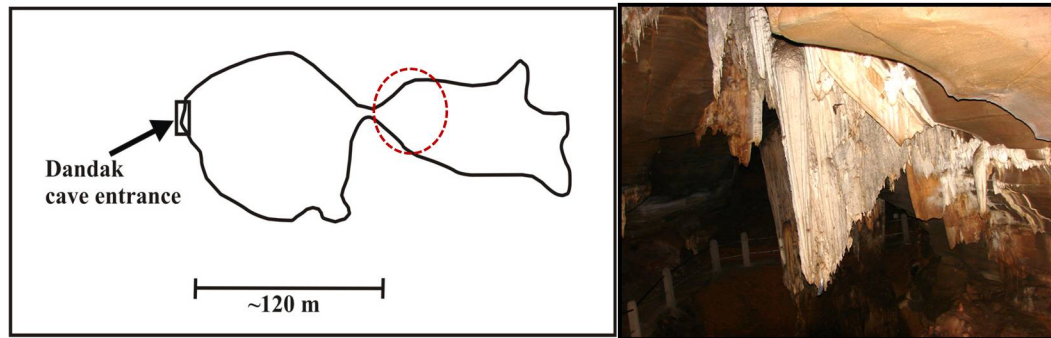


Figure 2.5: *Left: Overview of the Dandak cave, with the dashed circle indicates sampling site, Right: Photo showing Dandak stalactite. Photo source: [Biospeleologist, 2013].*

The Kotumsar cave The Kotumsar cave (19°00'N, 82°00'E, 35m below ground level) is located 5km north of the Dandak cave (Figure 2.4) in Kanger valley National Park. The lateral extent of the caves is around 330 meters with several chambers and passages around 20-70 meters wide [Yadava and Ramesh, 2007]. Cave entrance is formed by the vertical fissure in the wall of a hill [Biswas, 2010]. A narrow channel of water passes through the central part of the cave galleries which is fed at the cave entrance during the ISM season (June to September), and terminates in the middle of the cave becoming a part of the underground pathways. Small ponds are seen during the dry seasons, i.e., pre-monsoon and post-monsoon (winter), which receive cave drip water and serve as a source of life for the cave biology [Sinha and Naik, 2004]. The average pH of the pond water is 8.04 ± 0.36 . Currently the cave is open to public visit during winter. The average annual air and water temperatures within the cave are 28.25 ± 1.23 and 26.33 ± 0.96 °C respectively [Biswas, 2010]. In the far interior of this cave (Figure 2.6), a few stalagmite pieces were found lying horizontally within a narrow zone (1 to 1.5 m of vertical space between the cave roof and the surface of 1m raised bedrock). A few stalagmites were recovered from this site in June, 2006 CE. Around these stalagmites, layers of fresh carbonate deposition were seen due to which these were lying intact on the surface, although the surrounding was found

to be dry at the time of collection.

The Kailash cave Kailash cave ($18^{\circ}84'N$, $82^{\circ}00'E$, 40 m.s.l.) is located at ~ 40 km from Jagdalpur, to the south of the Kotumsar and the Dandak caves (Figure 2.4). The cave is located on a limestone hilltop in a thickly forested area of the

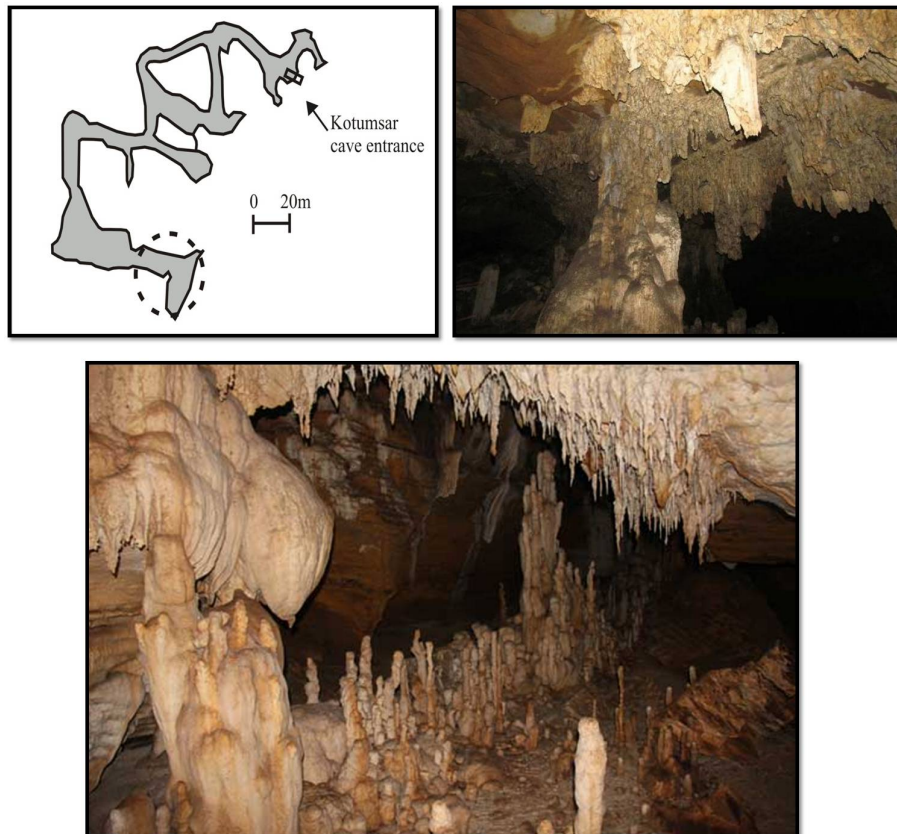


Figure 2.6: Top left: Sketch of Horizontal cross sectional view of Kotumsar cave [Yadava and Ramesh, 2007]. Dotted circle shows the site of KOT-I speleothem. Top right and Bottom: Photos showing stalactites and stalagmites exposures in cave. Photo source: [Wikipedia, 2016a].

Kanger National Park. The Kailash cave is 250 m long with only one narrow entrance at the top. The main hall of the cave follows the dip of the host rock with a very steep slope.

The Belum cave

The Belum cave ($15^{\circ}6'N$, $78^{\circ}6'E$, 367 m above m.s.l.) is situated in the southern part of India in the Kurnool district, Andhra Pradesh. Geologically the area has outcrops representing middle to upper Proterozoic rock types of the Cuddapah Basin. The caves are formed in karstified Narji Limestone series. It is the second largest cave in the Indian subcontinent and one of the longest caves in India with its galleries extending 825 m long (Narayana, et al., 2014). The deepest part of the cave is 80 m below the cave entrance. The caves have sixteen pathways including the main entrance. The cave is divided into many chambers colloquially referred as "hall". Each hall displays a magnificent formation of stalactites and stalagmites. The BLM-1 stalagmite was recovered from the inner gallery of cave having 100% humidity with a narrow channel to access.

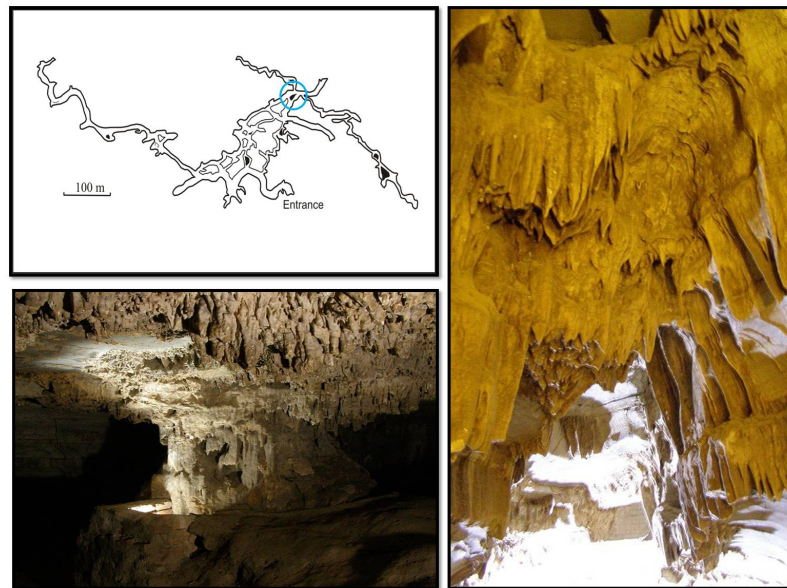


Figure 2.7: Top left: Sketch of Horizontal cross sectional view of the Belum cave. Redrawn from the sign board near the entrance of the Belum Cave. Circle over the map shows Belum stalagmite sampling site. Top right: Photo showing several stalactites famously known as "Ceiling hall of thousand hoods". Bottom: Photo showing a giant calcium carbonate column surrounded by stalactites known as "Banayan tree hall". Photo source: [Wikipedia, 2016b]

2.2 Foraminifera

Sediments in the seas around the Indian subcontinent are excellent recorders of past monsoon variability. As southwest monsoon winds flow past the Arabian Sea, warm ocean surface water gets dragged towards the western coast of India. As a result, colder deeper waters, rich in nutrients force their way to the surface (Figure 2.8) near the Oman coast [Anderson *et al.*, 1992]. Planktons such as foraminifera bloom in such conditions and hence the abundance of certain foraminiferal species (e.g., *G. bulloides*) is used as an indicator of upwelling/wind strength, which in turn is a proxy for the Indian monsoon. Higher abundance of this species has been interpreted as stronger monsoon winds [Gupta *et al.*, 2003].

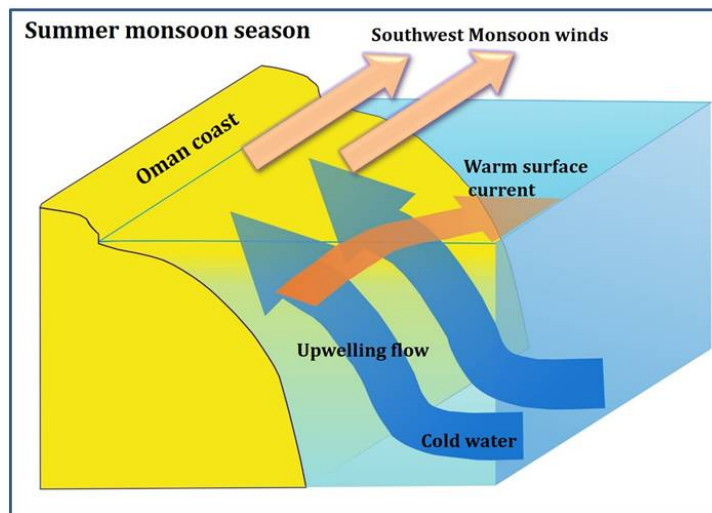


Figure 2.8: Upwelling in the coast of Oman. Colder water from the deeper ocean rises up as the warm surface water is dragged by the south-westerly winds.

During glaciations, Arabian Sea upwelling weakens in response to weakening in the monsoon wind strength. As a result, records show a lower abundance of *G. bulloides* during the glacial period and high abundance during interglacial period. Urey [1947], proposed that isotopic ratio of ^{18}O to ^{16}O (measured as deviation [$\delta^{18}\text{O}$] in parts per mille ‰ from that of a reference, Pee Dee Belemnite) of calcitic tests of marine microfossils varies depending upon the water temperature at which the test is formed; higher ratio (i.e. more positive $\delta^{18}\text{O}$) in the test

signifies a lower temperature (i.e. a temperature coefficient of $\sim -0.2 \text{ ‰}(\text{°C})^{-1}$), as later experimentally verified by [Epstein et al. \[1953\]](#). Marine Isotopic Stages (MISs) were first described based on a core raised from the Caribbean [[Emiliani, 1955](#)]. $\delta^{18}\text{O}$ fluctuations of planktonic foraminifera (marine organisms that live typically for ~ 6 weeks in the top 100 m of the ocean, on whose death, their calcareous tests settle down on the ocean floor, typically at the rate of 1 to 10 cm/ka) were used to deduce the climate variability of past ~ 280 ka as recorded by these microfossils in marine sediment. In a stratigraphic column alternate ‘warm’ and ‘cold’ stages were observed. Accordingly, the present ‘warm’ stage was designated by number 1 and the preceding ‘cold’ stage, an even number (MIS 2). Therefore, all the ‘warm’ and ‘cold’ stages are odd and even nos., respectively, giving an appearance of a sinusoidal wave where the stage boundary is marked as the midpoint between ‘temperature maximum’ and ‘minimum’. [Shackleton and Opdyke \[1976\]](#), recognized that it is not just temperature change that contributed to the observed changes in $\delta^{18}\text{O}$ of tests of the marine microfossils, but also that changes in sea level or ‘ice-volume’; thus they refined and further extended this timescale to 22 stages spanning ~ 900 ka as opposed to 16 stages originally proposed by [Emiliani \[1955\]](#). Initially researchers used planktonic foraminiferal tests for $\delta^{18}\text{O}$ measurements. Planktonic foraminifera respond to local temperature variations and may not be a suitable proxy to record global temperature variations. Deeper oceans are more uniform in temperature and salinity than the surface ocean, therefore $\delta^{18}\text{O}$ values of benthic foraminifera (foraminifera that live and die on the ocean floor) could be more reliable, as they are believed to respond mostly to global ice volume or sea level changes. Recent reconstructions of Marine Isotopic Stages are done using $\delta^{18}\text{O}$ of benthic foraminiferal tests. Climate record was improved when stacks which were averages of $\delta^{18}\text{O}$ values of benthic foraminiferal records from multiple ocean sites were correlated. A new 5.3 Myr benthic $\delta^{18}\text{O}$ stack (called “LR04”) was presented consisting of over 38,000 individual $\delta^{18}\text{O}$ measurements from 57 sites distributed globally [[Lisiecki](#)

and Raymo, 2005; Shackleton, 1987]. Most of the measurements were done on the species *Uvigerina peregrina* or *Cibicidoides wuellerstorfi*. The advantage is the elimination of “local” climate signals and generation of a smooth curve that represents “global” climate change. Two inferences are readily seen from this curve: first, a steady increasing (plotted downward) trend in the mean $\delta^{18}O$ values. This implies that the ocean water steadily became enriched in ^{18}O , signifying the formation of ice sheets (which preferentially lock in $H_2^{16}O$) and global cooling that appears to have commenced around 3 million years ago. Secondly, the amplitude of fluctuations has increased during the last one million years. This signifies that the $\delta^{18}O$ glacial and interglacial sea level changes have become higher in magnitude (100 m) with time. Equivalent, long and continuous monsoon proxy records are not available for the Indian region so far.

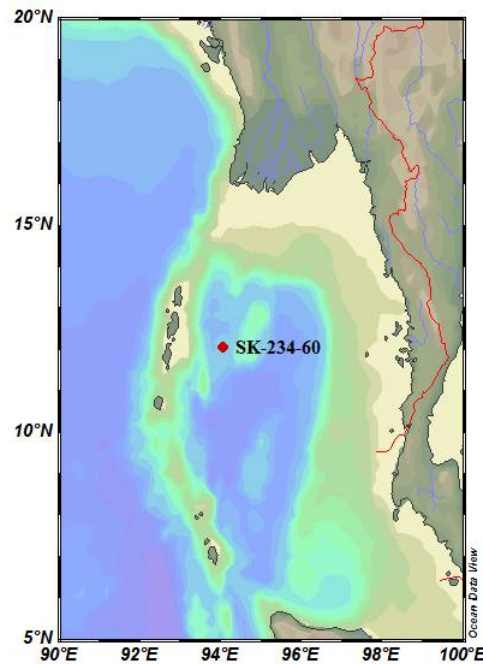


Figure 2.9: Location of core SK-234-60 from Andaman Sea.

The present study is based on a 4 m long sediment core (SK-234-60) raised from the Andaman Sea N 12°05'46" and E 94°05'18" at a depth of 2 km. Part of the work related to core SK-234-60(Figure 2.9) is covered in [Awasthi \[2012\]](#),

where geochemical studies on the sediments were carried out to understand the provenance of the deposits. The Present work is to interpret $\delta^{18}O$ timeseries to reconstruct ISM variability.

2.3 Tree rings

Climate change during the past 1000 years is important to reconstruct as it can be correlated with the historical archives and extent to which climate affected civilizations can be deduced. Of the several proxies used for paleoclimate (e.g. ice cores, lake sediments, corals and speleothems) reconstructions, tree rings have special advantages: they record seasonal monsoonal variability, they preserve continuous record and can be easily dated using ring-counting. An individual tree ring records contemporaneous climate changes in the year of formation over the life-span of the tree. Cross correlation and matching of ring patterns of different (dead, archived and growing) trees of the same climate regime can extend the climate reconstructions to past several thousands of years. Significant contributions to climate science within the last decade have firmly established tree-rings as valuable sources of proxy data for evaluating long-term climate variability/trends and as useful tools for developing long-term records of extreme climatic events [[Mann et al., 1999](#)].

Previous monsoon reconstructions using tree rings were based on ring width. The analogy used was: trees from high latitude or altitude regions, with wider (narrower) rings correspond to higher (lower) temperature/ precipitation [[Managave and Ramesh, 2012](#)]. However, the presumably simple relation between width and climate is rather complex and is influenced by non-climatic factors such as light availability, topography, soil type and forest thinning, ecological parameters and also genetic variability among trees of the same species (e.g. [Kress et al. \[2009\]](#), [Fritts \[1976\]](#)). On the other hand, isotopic composition (stable isotope ratios of carbon ($\delta^{13}C$), hydrogen (δD) and oxygen ($\delta^{18}O$)) of tree rings is believed

to be less effected by ecological parameters and considered to be better measures for climate reconstruction. Tree cellulose $\delta^{18}O$ is more sensitive to rainfall fluctuations as compared to ring-width and ring density [*Sano et al.*, 2010]. Several researches and reviews on tree rings isotopes by *Farquhar et al.* [1989], *Ramesh et al.* [1986], *Dawson et al.* [2002], *McCarroll and Loader* [2004] *Managave and Ramesh* [2012] highlight that oxygen and hydrogen of cellulose from individual growth rings can be used as proxies for climatic parameters such as rainfall, humidity and temperature. The oxygen isotope composition of plants is influenced by various physiological and climate processes. It is mainly controlled by $\delta^{18}O$ of the source water, the level of ^{18}O enrichment in leaf due to evaporation, biochemical fractionation of ^{18}O due to synthesis of sucrose in the leaf and the isotopic exchange between carbohydrate and xylem water during cellulose synthesis. The $\delta^{18}O$ of rainfall is inversely related to the amount of precipitation in the tropics [*Dansgaard*, 1964; *Rozanski et al.*, 1993; *Schmidt et al.*, 2007; *Yadava and Ramesh*, 2007] hence tree cellulose $\delta^{18}O$ is a powerful tool to reconstruct past monsoon rainfall.

In the present study, the available records of monsoon reconstruction from tree rings of the Indian peninsula are used to compare with speleothem based reconstructions to asses the coherence between the two proxies.

Chapter 3

Experimental Methods

The major focus of the present study is to reconstruct high resolution monsoon records from $\delta^{18}O$ of speleothem samples distributed across the peninsular India and compare them with available terrestrial and oceanic records for possible coherence. The work also includes analysis of planktonic foraminifera from Andaman Sea.

The following chapter describes the detailed procedures for stable isotope and trace element measurements on five stalagmite samples collected from peninsular India. The chapter is divided into six sections. Section 3.1 describes samples collected and sub-sampling. In section 3.2, analysis of stable isotope ratios of carbon and oxygen in carbonates, and trace element measurements are discussed. Section 3.3 describes the meteorological data used in the present study. Focus of sections 3.4 and 3.5 is on ^{14}C geochronology and the U/Th dating technique used to date speleothems. Section 3.6 describes the sampling and analysis of a sediment core from the Andaman Sea.

3.1 Samples

A total of five stalagmites were collected and analyzed in the present study. All were cut along their growth axes using a Dramet cutting machine (Figure 3.1)

into four slices. One slice was used for stable isotope analysis, the second slice was used for the trace element studies, the third for U-Th dating and the fourth was archived. Sub-samples for stable isotopes were extracted using a New



Figure 3.1: *Dramet cutting machine at PRL used to slice speleothems.*

Wave Research Micro Mill with the maximum possible resolution of $\sim 200 \mu\text{m}$ (Figure 3.2). The system has a video microscope coupled to a high speed drill and a set of computer controlled motorized stages. It uses a carborundum or diamond drill bit of $\sim 100 \mu\text{m}$ diameter. The sub-samples milled are stored in autoclavable polypropylene 0.2 ml tubes. The stable isotope measurements of the samples were carried out on Delta-V plus and MAT-253 Isotope Ratio Mass Spectrometers (IRMS) at the Physical Research Laboratory, Ahmedabad, India. The details of samples are discussed below.

The Dandak cave Two stalagmite samples were retrieved from the Dandak cave. Active calcium carbonate precipitation was seen on one of the samples

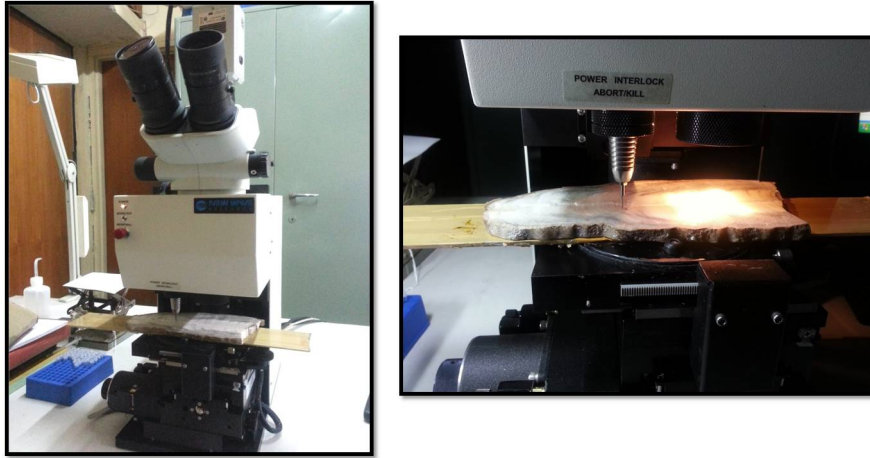


Figure 3.2: *Left: New Wave Research Micro Mill at PRL. Right: Sub-sampling of a stalagmite.*

referred to as Dan-I stalagmite. The tip of the stalagmite represents the year of its collection i.e. CE 1996. Length of the sample is ~ 29 cm and 1590 sub-samples were extracted for stable isotope measurements. The sample has a hiatus, which is seen as a discontinuity at the bottom. As shown in the figure 3.3, the layers below the hiatus are rich in detritus. The younger layers above the hiatus are made of white calcite crystals seen clearly in the thin section. The younger layers however are interrupted by thin laminations of detritus. The second stalagmite (Dan-II) has a length of 41.3 cm (Figure 3.4) and 2250 sub-samples were extracted for stable isotope analysis. The layers are made of pure calcite and show uninterrupted growth. The sample shows younger growth layers on the left side, in response to the re-activation of the drip water and shift in the drip site. Both the samples were sent to University of New Mexico, Mexico for U-Th geochronology.

The Kotumsar stalagmite The Kotumsar stalagmite (KOT-I) sample is a 29.6 cm long stalagmite (Figure 3.5), composed mostly of white calcite with its outer surface covered by gray calcitic layer (based on X-ray diffraction analyses). The sample, when cut open along its growth axis, can be divided into four bands

(I to IV, Figure 3.5) based on color and texture. All the bands show annual layers (1 mm thick in bands I, II and IV and 0.3 mm in band III) that can be viewed with the naked eye. In band III, distinct brown laminae, due to incorporation of soil impurities, are observed. High resolution sampling (Figure 3.6) was done using a micro-mill, with the spatial resolution of 200 μm ($\sim 3 - 5$ samples in a layer). Around 1277 subsamples were extracted weighing ~ 500 micro grams. Sub-samples for Hendy's test [Hendy, 1971] were extracted from four layers are shown in figure 3.6.

The Kailash cave The Kailash cave stalagmite with a length of 49 cm is the longest studied sample in the present study (Figure 3.7). The sample shows uninterrupted calcite growth layers. The thickness of the layers varies between $\sim 1 - 2$ mm and can be counted with the aid of hand-held lens. Total 146 layers were counted and 2872 subsamples were extracted for stable isotope measurements. The layers which are annual in nature have merged at some places to form thick white bands, making the counting difficult. The change in the growth axes at three different locations, point to a lateral shift of the drip site. The sample was sent to Taiwan University, Taiwan for geochronology.

The Belum cave The BLM-1 stalagmite was recovered from the inner gallery of cave having 100% humidity with a narrow channel to access. It is 31.4 cm long and shows distinct growth layers. The sample has three distinct growth zones representing the influence of different climatic regimes. The lower most section has white calcitic layers. The middle sections has high detritus with porous radial crystals and the uppermost has prominent growth layers. These three sections are separated by two hiatuses, one between the lower and the middle and other between the middle and the uppermost sections (Figure 3.8) respectively.



Figure 3.3: *Polished cross sectional view of the Dandak-I stalagmite. Planar view of the growth layers indicated constant shift in the drip direction, changing the growth axes. Near the bottom, a hiatus (Blue arrow) is observed as a distinct boundary separating two growth phases. Post hiatus, the growth axis has shifted and there is a continuous growth thereafter.*

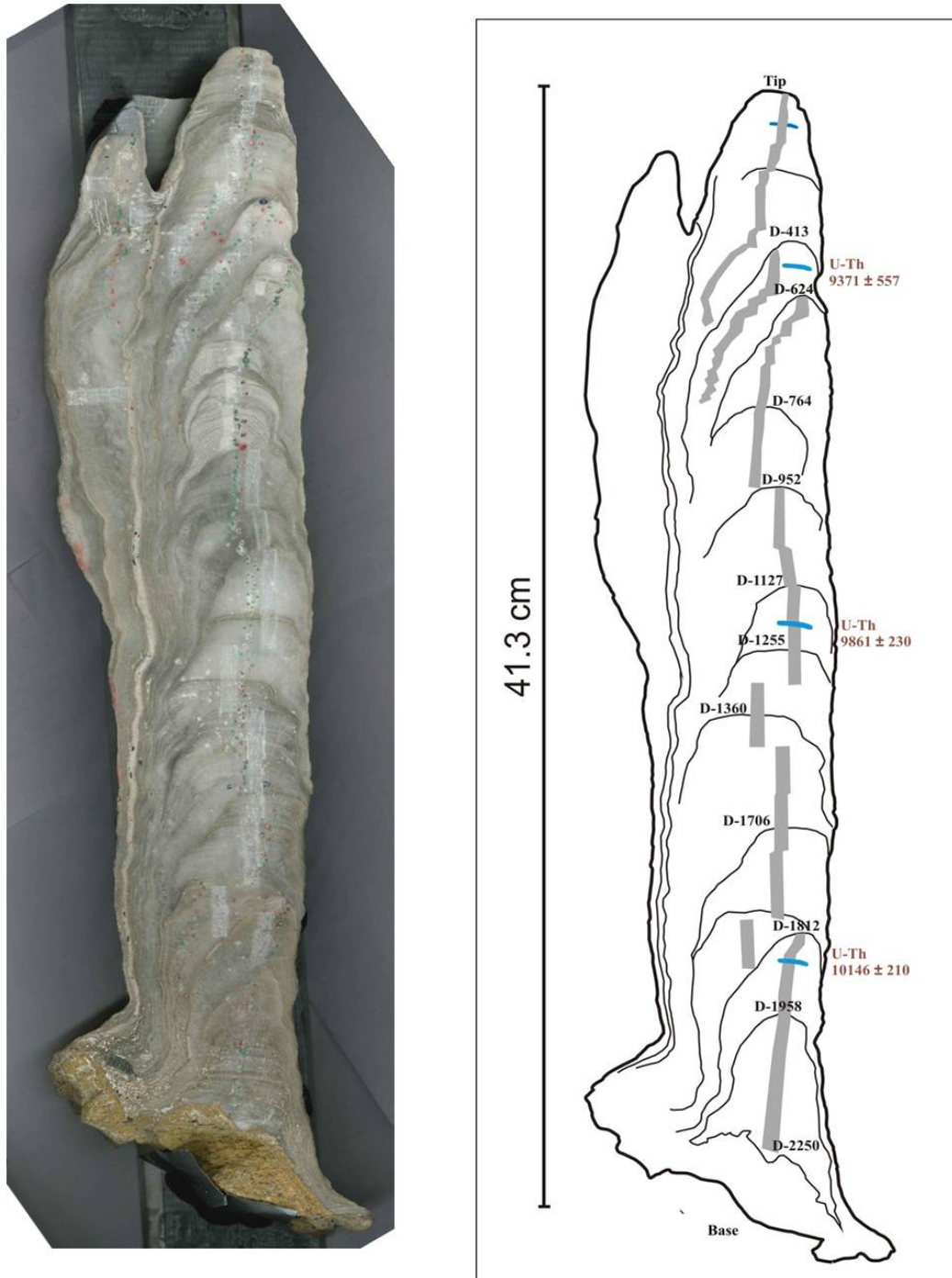


Figure 3.4: *Left: Polished cross sectional view of the Dandak-II stalagmite; .Right: Schematic cross section of Dandak-II stalagmite The gray bands represent high resolution sampling points for stable isotope analyses. Since the sampling resolution is $\sim 200 \mu\text{m}$, the band is seen as continuous. Four ^{230}Th dating points are marked by the blue lines.*

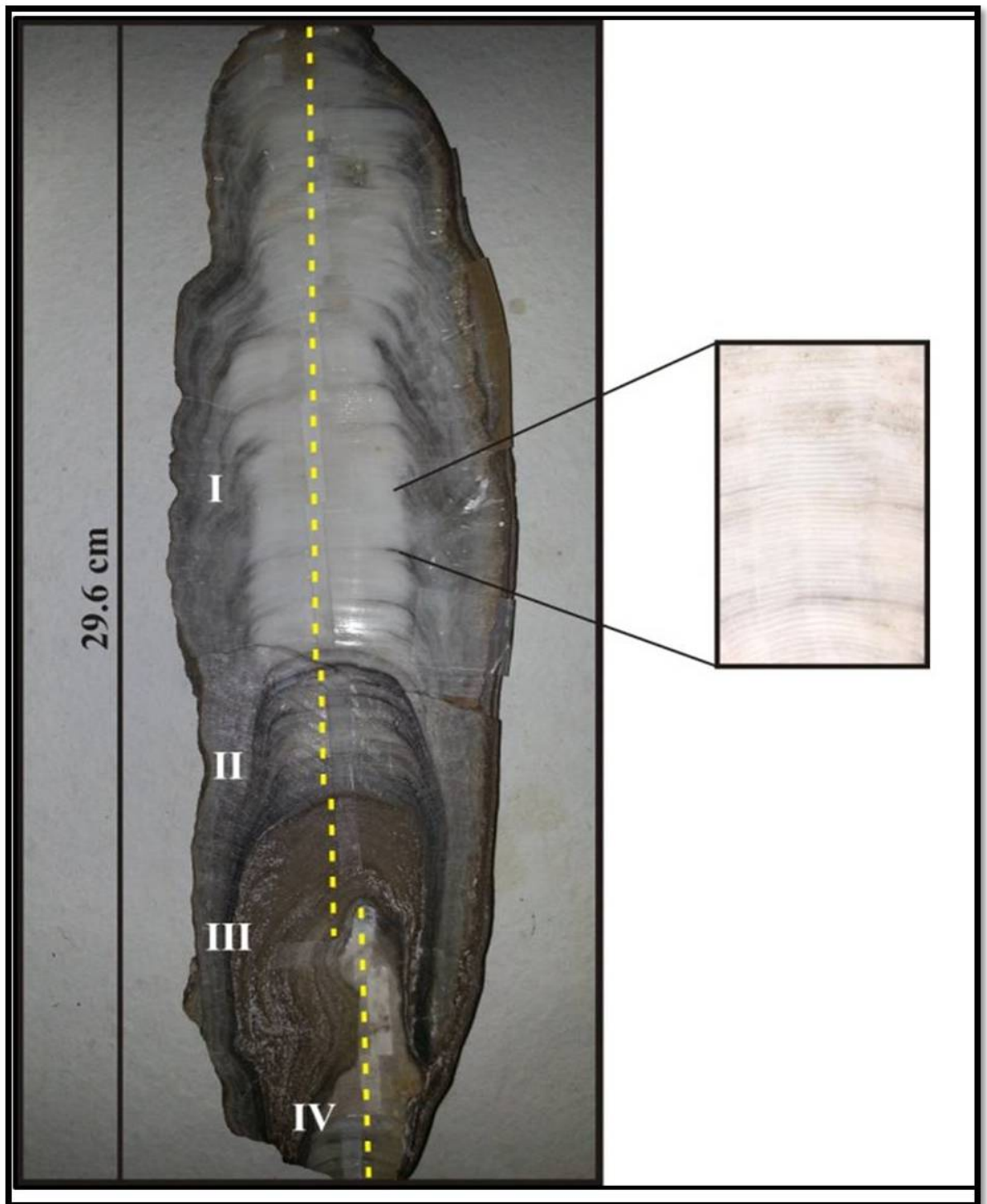


Figure 3.5: *Left: Polished cross sectional view of the KOT-I speleothem showing color bands; Right: Enlarged photo of part of the sample showing distinct layers that could be annual.*

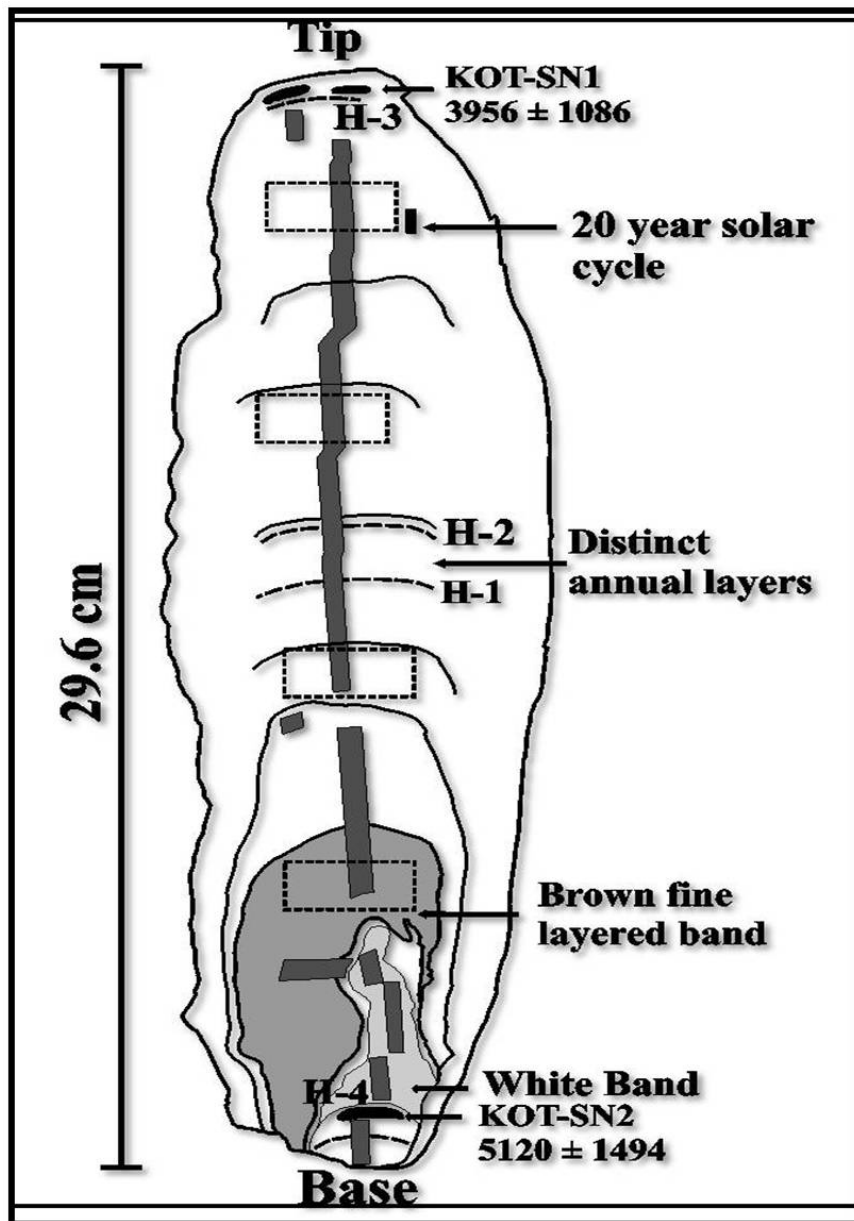


Figure 3.6: Schematic cross section of KOT-I. The dark lines indicate distinct layers that can be seen with the naked eye. Subsamples for the Hendy's test were extracted along dashed lines marked as H-1 to H-4. The dark vertical band in the middle, stretching from top to bottom, represents high resolution sampling points for stable isotope analyses. Since the sampling resolution is $\sim 200 \mu\text{m}$, the band is seen as continuous. Two ^{230}Th dates at the bottom and top are 5100 ± 1500 (SN-2) and 4000 ± 1100 (SN-1) years (errors at 2σ level), respectively. ^{14}C dating positions are shown as dashed rectangles.

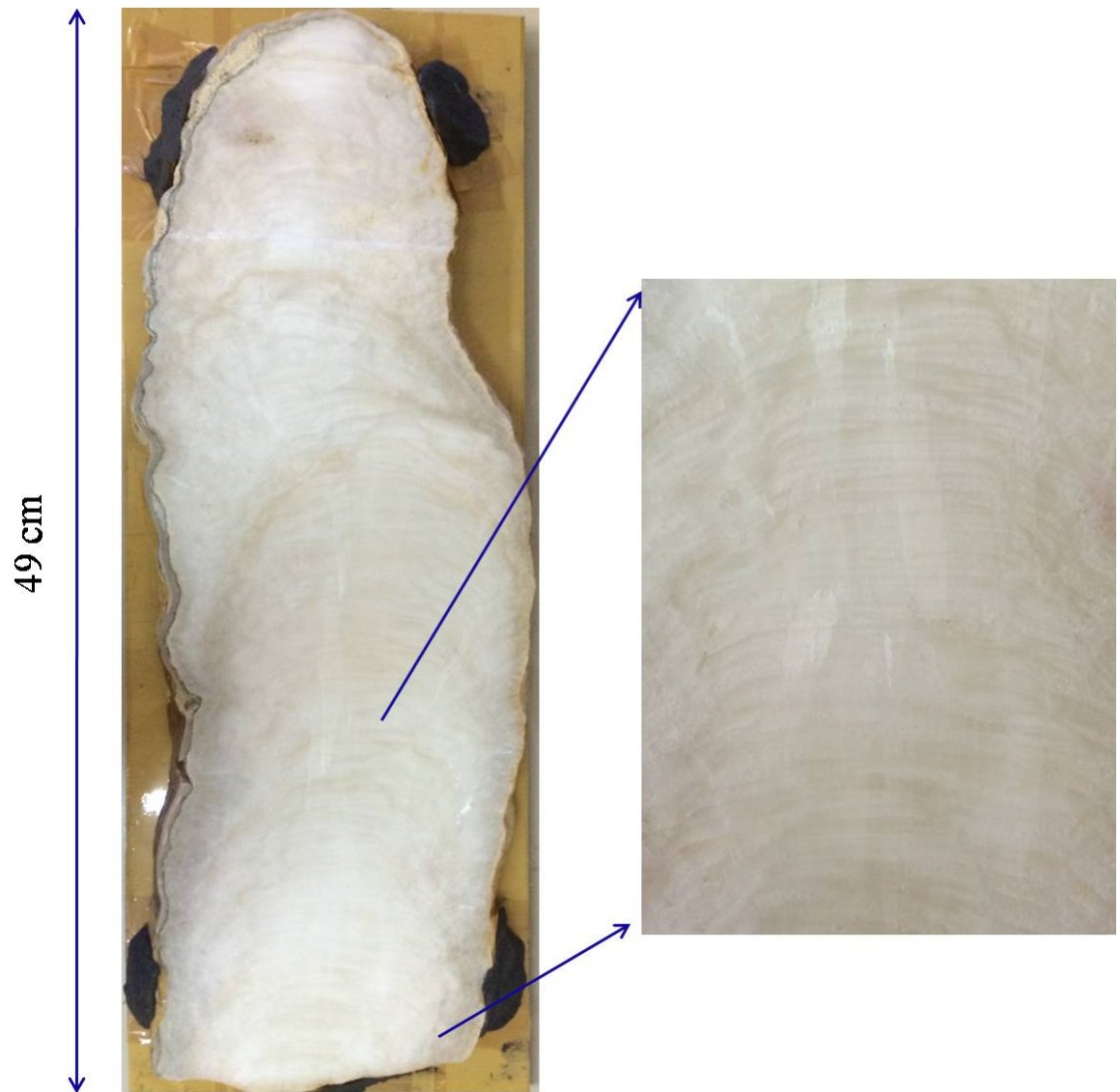


Figure 3.7: *Left: Photo shows the polished cross-section of Kailash stalagmite. The stalagmite growth is continuous and is made of calcite. The growth axis has shifted twice during deposition. Right: An enlarged view of the older section of the sample. Layers are visible to the naked eye and range from $\sim 1 - 2$ mm in thickness.*

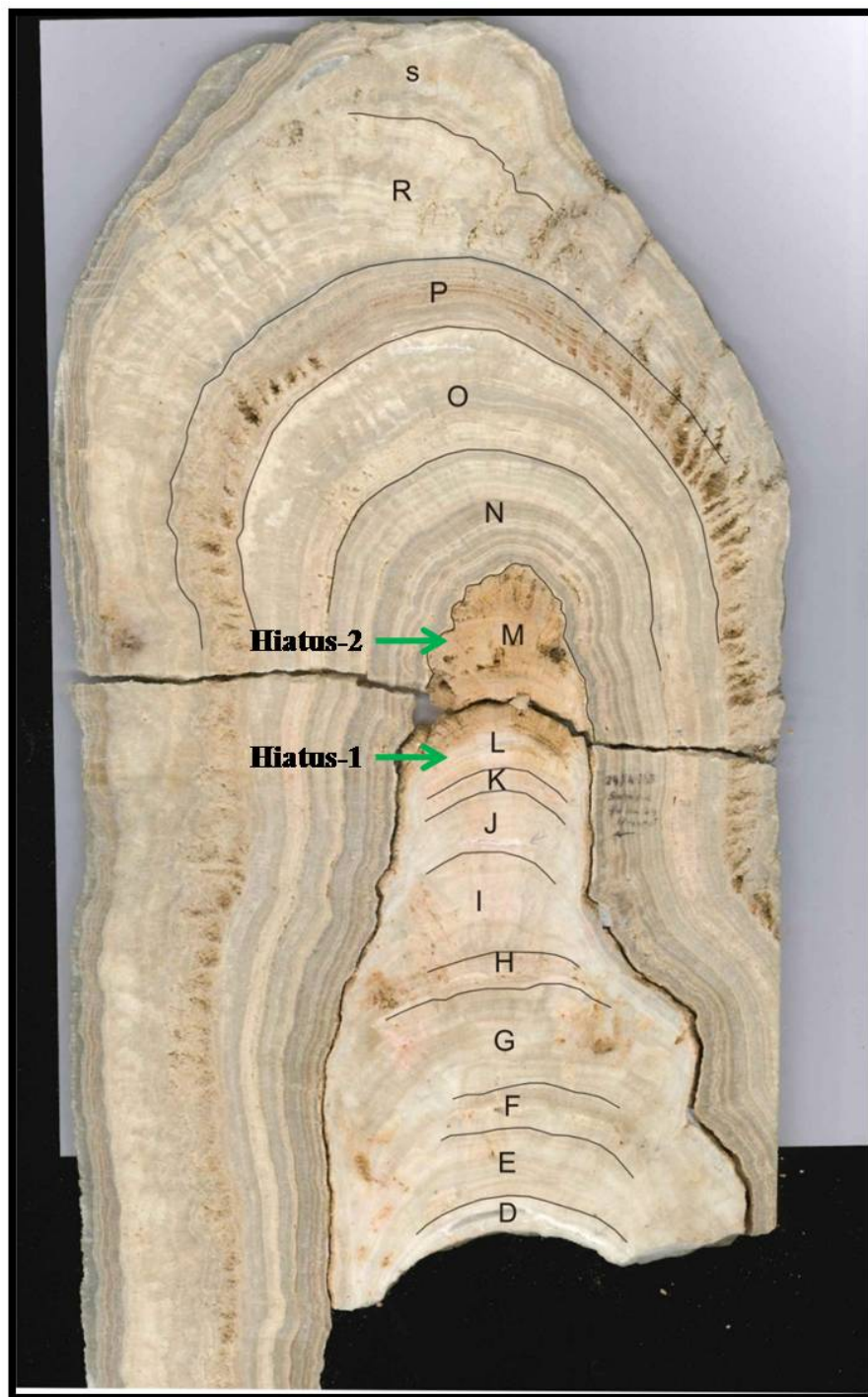


Figure 3.8: Photo shows the cross-section of the Belum stalagmite (BLM-1). The sample was divided into various bands based on the compositional changes, and for the ease of sampling. The green arrows show two distinct hiatuses, along the growth layers.

3.2 Stable Isotope and concentration measurements

3.2.1 Isotope ratio mass spectrometer (IRMS)

Analysis in the present study is by the use of two stable isotope mass spectrometers for isotopes of oxygen and carbon and a Q-ICP-MS (see below) for trace elements. The working principle of all the three mass-spectrometers is explained below.

Mass spectrometry is a technique of where ions are separated based on the mass to charge ratio. Mass spectrometer has three main components namely, the source, the analyzer and the detector (Figure 3.9). The roles of all the three parts are explained below.

1. **The source:** The source is the most diverse component of an instrument. In stable isotope mass spectrometry, electrons emitted from a filament are used to ionize the gaseous samples, whereas in an ICP-MS, the sample is injected in an aqueous medium and an argon plasma is used to ionize the sample.

The stable isotope mass spectrometer uses a thorium coated tungsten filament, to produce electrons (accelerated to ~ 70 eV energy) by passing ~ 3.5 A current through it. Upon entering the source, the gas (CO_2) gets ionized with the an efficiency of 0.1%. A low magnetic field is applied to increase the ionization efficiency, wherein the electron move in spiral motion along the magnetic field. The ion beam is focused using collimating plates and a high voltage (~ 2.5 kV) accelerates the positively ionized gas molecules into the analyzer (Figure 3.9).

The Quadrupole- Inductively coupled plasma mass spectrometer (Q-ICP-MS) has a radio frequency inductively coupled argon plasma as an ion source. The aqueous samples are introduced to a nebulizer which converts

them to small aerosol droplets. A spray chamber transfers these aerosol droplets to a plasma torch, which is at a temperature of 6000°C. Here the sample in gaseous form is stripped of an electron and the ionized gas enters the interface. As the plasma operates at air pressure while the quadrupole operates at a very low pressure, an interface between them is required to reduce the pressure. The sample ions in the interface are directed through cones and skimmer into the quadrupole.

A charged (q) molecule in an accelerating voltage (V) obtains a kinetic energy.

$$qV = \frac{1}{2}mv^2$$

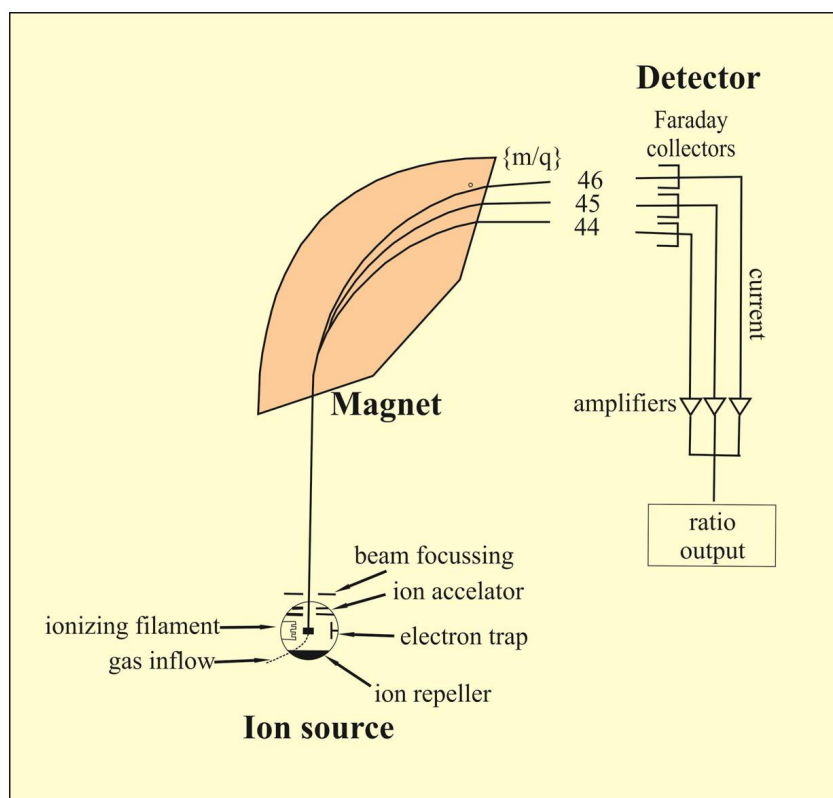


Figure 3.9: Sketch of a mass spectrometer with the three key components : source, analyzer and detector. Source: [Clark and Fritz \[1997\]](#)

2. **The analyzer:** For the analysis of carbon and oxygen isotopes of CO_2 prepared from the sample is introduced in the IRMS. A magnetic field of ~ 3.8 kG is applied perpendicular to the ion beam across the flight tube. The CO_2 ions are split based on the mass to charge ratio. In this case, three beams are produced. The motion of the ions is deflected and they follow curvilinear paths owing to the Lorentz force. This force imparts a centripetal acceleration to the ion beam entering perpendicular to the magnetic field.

$$q(\mathbf{v} \times \mathbf{B}) = \frac{mv^2}{r}$$

Hence the radius of curvature of the ion is,

$$r = \sqrt{\frac{2Vm}{\mathbf{B}^2 q}}$$

When V , B and q are constant, the radius of curvature of singly charged ion is directly proportional to the square root of its mass [Faure, 1977; Potts, 2012]. Hence, ions of heavier mass ($CO_2 = 46$) are deflected into a path of higher radius compared to the lighter ions ($CO_2 = 44$).

In Q-ICP-MS, the voltages and radio frequencies are managed so that at a given time, ions with a specific mass by charge ratio remain stable within the rods and pass through to the detector. The ions with different mass by charge ratio are rejected (Figure 3.10). To cover the mass range of interest, the electronics rapidly changes the quadrupole settings to allow different mass-to charge- ratios to pass through. The quadrupole has a capacity of scanning at a rate of 5000 atomic mass units (amu) per second [Elmer, 2001].

3. **The detector:** The currents due to ion beams are measured using Faraday cups, which are attached to very high resistances $\sim 10^9 \Omega$. In IRMS,

ions produce a voltage across the resistance, which is measured. This is proportional to the number of ions entering into the cup per unit time.

In Q-ICP-MS, the ions exiting the mass spectrometer, strike the surface of an detector (dynode), releasing an electron each time an ion strikes it. The series of dynodes generate a cascading stream of electrons until a measurable pulse is generated. The system counts the ions that hit the first dynode converting it to a signal.

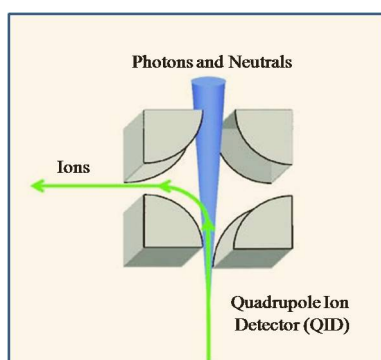


Figure 3.10: Schematic showing the working principle of quadrupole. The beam carries ions, photons, unionized particles and neutrals. The ions of selected mass pass through the detector, while photons and neutral particles are ejected out.



Figure 3.11: Photo shows Thermo Fisher Delta-V Plus IRMS on the left and Pal Gas-bench to the right at PRL.

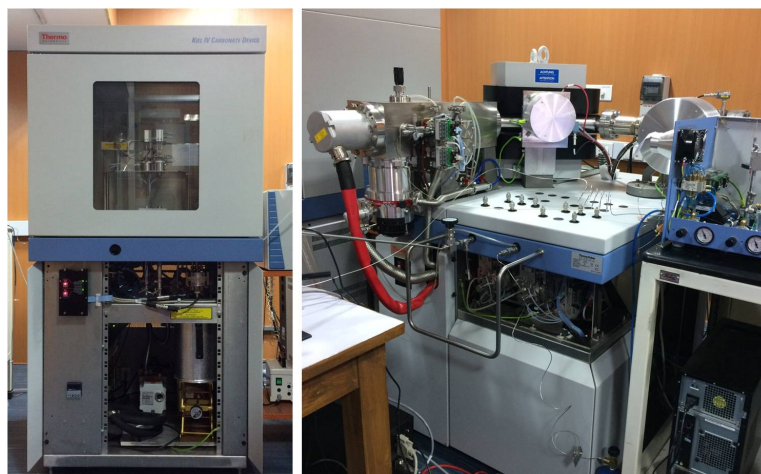


Figure 3.12: Photo shows Kiel-carbonate device to the left and Thermo Fisher MAT-253 IRMS to the right at PRL.

3.2.2 $\delta^{18}\text{O}$ and $\delta^{13}\text{C}$ measurements

Carbonate samples are converted to CO_2 by reacting the sample with 100% H_3PO_4 (Ortho-phosphoric acid), where the liberated CO_2 is directed to the mass spectrometer. Use of 100% H_3PO_4 is highly recommended as it is devoid of water and hence there is no variable contribution of oxygen isotopes from the water molecules. 100% H_3PO_4 acid is made by heating it at 120°C and slowly adding phosphorus pentoxide (P_2O_5), a dehydrating agent. The detailed procedure of preparing the acid is given by [Coplen *et al.* \[1983\]](#) and [Wachter and Hayes \[1985\]](#). Samples were measured on two mass spectrometers, namely, Delta V-plus IRMS (Figure 3.11) aided with Gas bench and MAT-253 aided with Kiel Carbonate device (Figure 3.12). The differences in components of both the IRMS are given in Table 3.1.

For the measurements in Delta v-plus, powdered carbonate samples were taken in 12 ml glass vials and tightly capped. The vials were then loaded onto the Gas Bench and flushed with He gas. Vials containing a laboratory carbonate standard, Makrana Marble (MMB), was placed in between the

Table 3.1: Sample preparation methods and mass spectrometric parameters used in the measurement of $\delta^{18}\text{O}$ and $\delta^{13}\text{C}$ in Delta V-plus and MAT-253 mass spectrometers.

| | $\delta^{18}\text{O}/\delta^{13}\text{C}$ | |
|---|--|-----------------------|
| | Delta V ⁺ | MAT-253 |
| Peripheral | Gas bench | Kiel carbonate device |
| Sample amount | 500 μg | 100 μg |
| Vial volume | 12 ml | 5.9 ml |
| Flushing gas | He (99.999 %) | He (99 %)/Ar |
| Flush time | 12 minutes | - |
| CO_2 liberation time | 1 hour | 400 seconds |
| temperature | 72°C | 72°C |
| Electron energy | 110 eV | 110 eV |
| Faraday cups | 5 | 10 |
| High voltage | 3 kV | 10 kV |
| Separated ion beams | $^{12}\text{C}_{16}\text{O}_{16}\text{O}$ (44), $^{13}\text{C}_{16}\text{O}_{16}\text{O} + ^{12}\text{C}_{16}\text{O}_{17}\text{O}$ (45) $^{12}\text{C}_{16}\text{O}_{18}\text{O} + ^{13}\text{C}_{16}\text{O}_{17}\text{O} + ^{12}\text{C}_{17}\text{O}_{17}\text{O}$ (46) | |
| Correction | Craig correction | |
| Internal precision | 0.06‰ | 0.04‰ |

sample vials at regular intervals. The needle used for flushing has two openings, one of the opening forces He gas into the vial, and the air within is flushed out through the other hole, which is then released out through the fused-silica capillary. After flushing, ~ 0.1 ml of ortho-phosphoric acid is injected manually using 1ml syringe. The samples are kept at 72°C for an hour to ensure complete the liberation of CO_2 gas. The CO_2 gas is then directed to the mass-spectrometer through the analysis needle. Figure 3.11 shows the photo of gas bench connected to Delta-V plus IRMS.

In the Kiel carbonate device, the sample powder is placed in vials and loaded onto a magazine(turret) with 44 slots. Ar/He is used as a carrier gas. The device has an automated acid injection system. After injecting the acid, the gas is carried through sample purification system comprising of two cold traps. The electronics attached to the traps ensures temperature changes from 0 to -190°C. The gas is trapped in liquid nitrogen at -190°C in the form of dry ice. At -80°C, pure CO_2 is liberated, whereas the moisture remains

in the traps. From the second trap, the purified CO_2 gas is transferred to the Dual inlet system of the mass spectrometer. The working principle of Kiel carbonate with MAT-253 IRMS is shown in Figure 3.13.

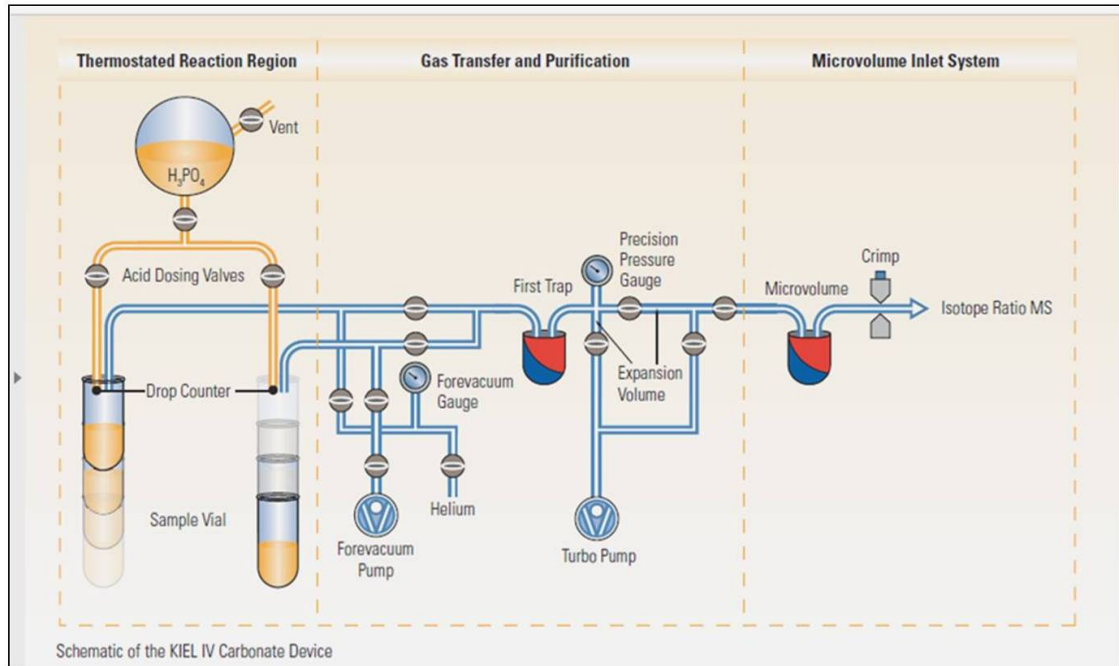


Figure 3.13: Working principle of Kiel carbonate connected to MAT-253 IRMS. Source: Instrument manual, Thermo Scientific

For the present measurements, continuous flow mode of Delta V-Plus and dual inlet mode of MAT-253 IRMS were used. In dual inlet there is alternation between a "reference" gas (of known isotopic composition) and a sample gas, whereas in the continuous flow, Helium is used as a carrier gas to carry sample to the source chamber. The details of sample preparation, equilibration and mass spectrometric conditions are listed in Table 3.1.

The sample isotopic abundances are reported with respect to VPDB (Vienna Pee Dee Belemnite) using the following conversion equation [Clark and

Fritz, 1997].

$$\delta^{18}O_{VPDB}^{Sample} = \delta^{18}O_{VPDB}^{MMB} + \delta^{18}O_{MMB}^{Sample} + (\delta^{18}O_{VPDB}^{MMB} \times \delta^{18}O_{MMB}^{Sample} \times 10^{-3}\text{‰}) \quad (3.1)$$

$$\delta^{13}C_{VPDB}^{Sample} = \delta^{13}C_{VPDB}^{MMB} + \delta^{13}C_{MMB}^{Sample} + (\delta^{13}C_{VPDB}^{MMB} \times \delta^{13}C_{MMB}^{Sample} \times 10^{-3}\text{‰}) \quad (3.2)$$

Here, MMB is the laboratory standard and stands for Makrana marble with 99.99% pure $CaCO_3$. MMB has been calibrated with respect to International standard (VPDB) and the values are:

$$\delta^{18}O_{VPDB}^{MMB} = -10.7\text{‰} \quad (3.3)$$

$$\delta^{13}C_{VPDB}^{MMB} = 3.9\text{‰} \quad (3.4)$$

Since the mass spectrometer measures the values of $\delta^{18}O_{ref}^{sample}$ and $\delta^{18}O_{ref}^{MMB}$ (ref=reference gas), the $\delta^{18}O_{MMB}^{Sample}$ is calculated from the following equation

$$\delta^{18}O_{MMB}^{Sample} = \delta^{18}O_{ref}^{sample} + \delta^{18}O_{MMB}^{ref} + (\delta^{18}O_{ref}^{sample} \times \delta^{18}O_{MMB}^{ref} \times 10^{-3}\text{‰}) \quad (3.5)$$

where $\delta^{18}O_{MMB}^{ref}$ is,

$$\delta^{18}O_{MMB}^{ref} = \frac{-\delta^{18}O_{ref}^{MMB}}{\left(\frac{\delta^{18}O_{ref}^{MMB}}{1000}\right) + 1} \quad (3.6)$$

Using equations(1.3,1.5 and 1.6) the values of $\delta^{18}O_{VPDB}^{Sample}$ are calculated. Similarly, calculations were done to derive $\delta^{13}C$ values of carbonate samples. The mass spectrometer measures ratios of 44/46 and 45/46 for $\delta^{18}O$ and $\delta^{13}C$ respectively. The corrections applied to remove isobaric interferences are explained below.

Craig correction: The masses 45 and 46 have small contribution from very low abundant isotopes of ^{13}C and ^{17}O . When these molecular ratios are converted into atomic ratios, a correction is required to eliminate the effect of $^{13}\text{C}^{16}\text{O}^{17}\text{O}$ from $^{12}\text{C}^{16}\text{O}^{18}\text{O}$ ($\delta^{18}\text{O}$), which is called Craig correction [*Craig, 1957*].

$$\delta^{13}\text{C} = 1.0676\delta_{45} - 0.0338\delta_{46}$$

$$\delta^{18}\text{O} = 1.0010\delta_{46} - 0.0021\delta_{45}$$

The accuracy and precision of the measurement were checked time to time using the international standards procured from IAEA. The reported isotopic values of the different standards procured from IAEA are given in Table 3.2. Of these standards, NBS-19 and IAEA-CO-1 were used for cross-checking the values of laboratory standard MMB. Table 3.3, shows the comparison between reported and measured values of IAEA standards. The measured values are averages of 20 analyses of each of the standards.

Table 3.2: IAEA standards used for carbonate and water isotope measurements.

| IAEA primary standards | | | | |
|----------------------------------|---------|-------------------------------|---------------------|--------------------|
| Name | Nature | | $\delta\text{‰}$ | Reference standard |
| V-SMOW | water | $^2\text{H}/^1\text{H}$ | 0 | V-SMOW |
| | | $^{18}\text{O}/^{16}\text{O}$ | 0 | V-SMOW |
| SLAP | water | $^2\text{H}/^1\text{H}$ | -428.0 | V-SMOW |
| | | $^{18}\text{O}/^{16}\text{O}$ | -55.50 | V-SMOW |
| NBS-19 | calcite | $^{13}\text{C}/^{12}\text{C}$ | 1.95 | V-PDB |
| | | $^{18}\text{O}/^{16}\text{O}$ | -2.20 | V-PDB |
| Intercomparison materials | | | | |
| GISP | water | ^2H | -189.73 ± 0.87 | V-SMOW |
| | | $^{18}\text{O}/^{16}\text{O}$ | -24.784 ± 0.075 | V-SMOW |
| NBS-18 | calcite | ^{13}C | -5.029 ± 0.049 | V-PDB |
| | | ^{18}O | -23.035 ± 0.172 | V-PDB |
| IAEA-CO-1 | calcite | ^{13}C | 2.48 ± 0.025 | V-PDB |
| | | ^{18}O | -2.437 ± 0.073 | V-PDB |
| IAEA-CO-8 | calcite | ^{13}C | -5.749 ± 0.063 | V-PDB |
| | | ^{18}O | -22.667 ± 0.187 | V-PDB |

Table 3.3: Comparison between reported (above) and measured (present work) values of IAEA standards

| Delta-vplus/Mat-253 | | | | |
|----------------------------|-----------------------------------|-----------------------------------|-----------------------------------|-----------------------------------|
| Standard | $\delta^{18}\text{O}$ reported | $\delta^{18}\text{O}$ Measured | $\delta^{13}\text{C}$ reported | $\delta^{13}\text{C}$ reported |
| NBS-19 | -2.20 | -2.22 ± 0.08 | 1.95 | 2.1 ± 0.07 |
| IAEA-CO-1 | -2.44 | -2.49 ± 0.03 | 2.48 | 2.42 ± 0.072 |

3.2.3 Trace element analysis

Trace element studies of the Belum and the Kailash stalagmites were carried out on a Q-ICP-MS at PRL (Figure 3.14). 100 subsamples from the Belum

stalagmite were milled using a dentist drill at the resolution of 3 mm for major and trace element analyses. Around 200 subsamples of Kailash stalagmite were prepared, each by clubbing 15 subsamples milled for stable isotope analysis. Each of subsamples weighed 6 to 10 mg. For trace element measurements the procedure described by [Eggins *et al.*, 1997] and modified by [Zhou *et al.*, 2008] was used. Samples were milled in a clean environment and ~ 6 mg was dissolved in 10 ml 2% nitric acid. The 10 ml solution with a dilution factor of 1666 is used as a stock solution. Sensitivity of the machine lies between 1 ppb to 1 ppt. Hence, major elements like Ca and Mg need significant factors of dilution. Two sets of dilutions were made; one for high weight percentages of Ca and the other for low concentrations of Mg, Sr and Mn. The aliquots used for Ca measurement was diluted 400 times and the aliquots prepared for trace element measurements were diluted only 4 times the volume. Since the solution had no residue, no further processing was required and they were measured directly on the Q-ICP-MS. For internal standardization, multiple enriched isotopes of ^{69}Ga – ^{115}In – ^{209}Bi were used. A synthetic limestone standard, JLS-1 was used for external calibration. The concentrations of elements of interest in the standard are shown in Table 3.4. External calibration is done using known dilutions of the standard and plotting a linear diagram of concentrations versus the counts. Once the calibration curve is ready, counts of a sample with unknown concentration can be mapped on the calibration curve and its respective concentration can be estimated. The calibration curves for the elements measured are shown in figure 3.15. The concentrations of Mg, Sr and Mn were normalized with that of Ca. Samples were altered with blank solutions to check the consistency of measurements. For cross-calibration of the measurements, JDo-1, an artificial Dolomite rock standard was run as an unknown.



Figure 3.14: *Thermo-scientific Quadrupole-Inductively Coupled Plasma mass spectrometer at PRL, Ahmedabad.*

Table 3.4: *International standards used for trace element measurements. * marks the major elements in % and minor and trace elements are reported in ppm.*

GSJ Geochemical Reference Standards

| Element | JLs-1 | JDo-1 |
|---------|---------|---------|
| Cao* | 55.09 | 33.96 |
| MgO* | 0.606 | 18.47 |
| MnO* | 0.00209 | 0.00657 |
| Sr | 295 | 116 |
| Ba | 476 | 6.14 |
| U | 1.75 | 0.858 |
| Th | 0.0287 | 0.0429 |
| Zn | 3.19 | 35.4 |

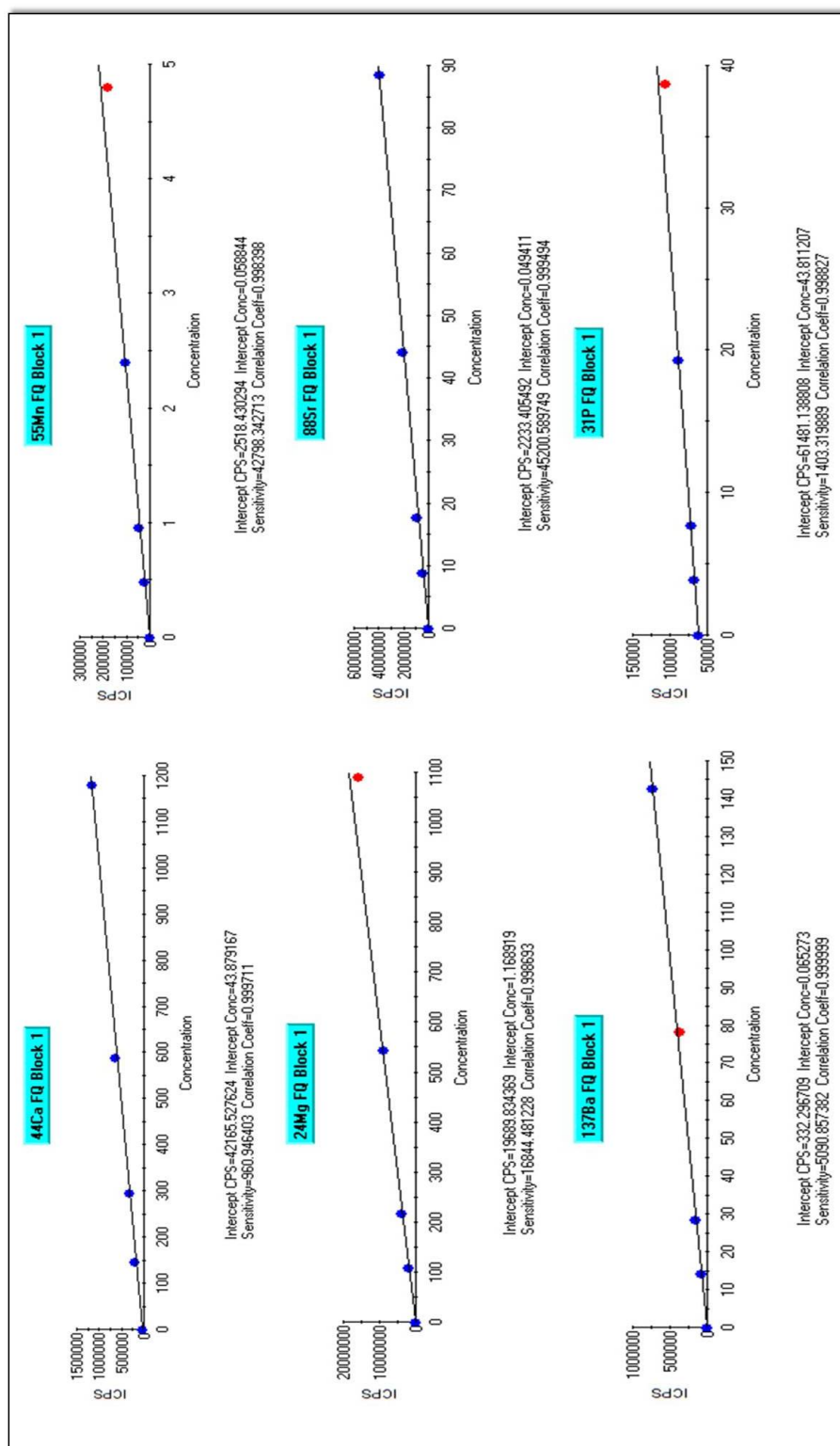


Figure 3.15: Typical calibration curves for different trace elements generated on ICP-MS using various dilutions of JLS-1.

3.3 Additional data used

To reconstruct monsoon from $\delta^{18}O$ of stalagmites, it is first essential to establish the existence of "amount effect" in the sampling region. The isotope values of rainwater samples for a long duration of time were taken from the Global Network of Isotopes in Precipitation (www.iaea.org).

3.3.1 Global Network of Isotopes in Precipitation (GNIP)

The IAEA's Water Resources Programme and the World Meteorological Organization (WMO) has established a global network for surveying the stable $\delta^{18}O$ and δD and tritium concentrations in the worldwide precipitation since 1961 CE. The data is archived at www.iaea.org/water/. In the present study, $\delta^{18}O$ and the corresponding rainfall amount over the study region is used from the GNIP data.

3.3.2 Reanalysis/satellite data

Wind field and specific humidity data were taken from the National center for Environmental Prediction reanalysis-1 [NCEP, [Kalnay et al. \[1996\]](#)]. And the monthly rainfall data were taken from Global Precipitation Climatological Project[GPCP, [Adler et al. \[2003\]](#)].

Along with the "amount effect", it is also important to know the source of precipitation over a region. This is verified using HYSPLIT models explained below.

3.3.3 Hybrid Single-Particle Lagrangian Integrated Trajectory (HYSPLIT)

HYSPLIT model is used to understand the trajectories of an air parcel reaching the sampling region. The model is forced using data from Global Data Assimilation System (GDAS). The advection of the air parcel is calculated from the position (grid point) and 3D wind field (V). At each time step, the model calculates a guess position and the velocity vectors are linearly interpolated in both space and time. The first guess position is

$$P'_{t+\Delta t} = P_t + V_{P,t}\Delta t$$

and the final position is,

$$P'_{t+\Delta t} = P_t + 0.5(V_{P,t} + V_{P',t+\Delta t})\Delta t$$

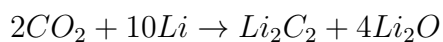
The integration time Δt varies from 1 hour to 1 minute depending upon the prevailing wind speed. The model also provides meteorological parameters such as temperature, potential temperature, relative humidity and height of the parcel above the mean sea level along the trajectory. In the present study back trajectory at 1500 m above ground level was calculated by the HYSPLIT.

3.4 Radiocarbon dating

Radiocarbon dating was used to assign ages to the KOT-I stalagmite. The sample was converted to benzene and liquid scintillation counter was used to measure the residual ^{14}C activity. The detailed procedure of benzene synthesis is explained below.

1. **Wet combustion** Four subsamples from the KOT-I stalagmite were extracted using dentist drill. Each subsample covering many growth laminae and weighing $\sim 5 - 8g$, were taken in round bottom flask connected to the vacuum line, pumped by a rotary pump. To ensure minimum loss of sediments, the powder was wetted with distilled water and evacuated. Dilute H_3PO_4 acid was added slowly to the flask and the solution was churned with magnetic stirrer to confirm complete liberation of CO_2 [Agrawal and Yadava, 1995; Gupta and Polach, 1985; Yadava and Ramesh, 1999]. The gas was then passed through two subsequent moisture traps maintained at $-80^\circ C$ using a slush(ethanol + liquid nitrogen) for water vapor trapping. The purified CO_2 was trapped in liquid nitrogen (LN_2) at $-190^\circ C$. With additional trapping and purification, CO_2 was then stored in glass flasks for acetylene preparation. The CO_2 extraction and purification glass line are shown in Figures 3.16 and 3.17 .

2. **Acetylene Preparation** In this step, CO_2 from the sample was converted to Acetylene. For this purpose, 6g of pure lithium metal is melted at $750^\circ C$ in an evacuated reaction chamber (Figure 3.18). 6 g of lithium is required for CO_2 equivalent to 1 g of carbon. At $550^\circ C$, CO_2 is passed to reaction chamber(Figure 3.16), where it reacts to form Lithium carbide (Li_2C_2). The reaction should be carried out very slowly to ensure no elemental carbon is formed. The reaction proceeds as follows:



After reaction the vessel is cooled to room temperature for hydrolysis.

3. **Hydrolysis** The process of hydrolysis involves reaction of distilled ground water with Lithium carbide. Ground water is used as there is no tritium activity and hence no interference is observed while counting. The reaction is exothermic, and hence should be carried out very slowly. The reaction proceeds as follows

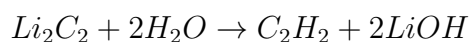


Figure 3.16: Photo shows the benzene synthesis glass line at PRL on the left and reaction chamber on the right.

The acetylene is removed by cryogenic pumping. It is passed through moisture trap at -80°C to remove traces of water vapor. As shown in the figure 3.18, the gas passes through the a trap filled with glass beads coated with NaOH and H_3PO_4 and subsequently through the trap filled with sodalime. They are used to remove the trace gases from the acetylene. The acetylene is collected using two traps, maintained at -190°C using liquid nitrogen. The gas is slowly passed to a column containing a catalyst, vanadium pentoxide (V_2O_5) pellets. The process is exothermic, and hence the column is cooled for a long time.

- 4. Benzene synthesis** The catalyst helps in polymerization of acetylene (C_2H_2) to Benzene (C_6H_6). Benzene is recovered from the column by heating it to 110°C [Polach et al., 1972] and trapping it in a vial at -190°C using

liquid nitrogen. The catalyst is reactivated at about 300°C by periodically passing dry air (through molecular sieve) into the column. The overall chemical yield is between 90-94% [Yadava, 2002].

Conversion to benzene is important for two reasons. The first reason is that benzene is a molecule with very small atomic structure containing the maximum number of carbon atoms. And the second is that the benzene solution has high transmission and low absorption for scintillation. As a result very little counts are lost.

The benzene thus obtained was made up to 1 ml and an organic scintillator (Butyl-PBD, 0.015 g per ml) is added to it for converting the β particle to photons and assayed to a low background Liquid Scintillation Counter (LSC) in a teflon vial.

The schematic of benzene synthesis line is shown in figure 3.18.

To estimate the background activity, an anthracite sample with no radiocarbon activity is used. The modern reference activity is periodically calculated from Oxalic acid-I and Oxalic acid-II provided by the U.S. National Bureau of Standards by converting them to benzene. As these compounds are organic in nature, CO_2 is produced from them using dry combustion. The samples were heated in a quartz tube to produce carbon dioxide under continuous flow of oxygen. Carbon monoxide present in trace amounts was removed by oxidizing it using CuO mesh heated at 550°C. The carbon dioxide was purified by passing it through the chemical traps filled with the solutions of KI/I_2 , $AgNO_3$ and $H_2SO_4/K_2Cr_2O_7$. The procedure for acetylene and Benzene preparation follows the same protocol as described above.

Liquid Scintillation counter(LKB-QUANTULUS) ^{14}C decays by the emission of β^- particles. The energy levels of these particles range from 0 to 156 keV.

These particles have kinetic energy which is transferred to the solvent molecules of the scintillator. These excited solvent molecules then transfer their energy to the scintillator molecules. A stable energy state leads to emission of photons proportional to energy of the emitted particle. Scintillation solutions comprise of primary and secondary scintillators. Primary scintillator is a solution which converts excitation energy into photons. The important function of the secondary scintillators is to shift the wavelengths of the photons emitted from 370 nm to 420 nm. Thus they act as wavelength shifters. The most widely used secondary scintillator is POPOP [1,4 – bis-(2-(5-Phenyl-oxazolyl))-benzene].

In order to detect the photons efficiently photosensitive device is used. Scintillation counter has two photo multiplier tubes (PMTs) which collect the total light produced in the scintillation vial and convert the absorbed photon energy into electrical energy by the release of photoelectrons. Thus the PMT amplifies the signal such that the amplitude of the pulse is directly proportional to the number of photons detected by the photo cathode. The counting period is set to 85 minutes duration and 30 repeat runs are done for statistically sound results. The average background for 1ml of benzene 0.30 ± 0.03 cpm and the modern reference is 9.36 ± 0.13 cpm per ml of benzene measured (over a period of a year) with an overall precision of 1.5% Modern [Yadava, 2002]. The laboratory dating limit is 40 kyr [Yadava, 2002]. The isotopic fractionation associated with CO_2 to C_6H_6 conversion is minimal; depletion of $1.7 \pm 1\%$ is observed [Panarello et al., 1983; Yadava, 2002]. These values correspond to age overestimation by only 10-45 years. Radiocarbon age (T) equation is given as:

$$T = (1/\lambda).ln(A_{abs}/A) \tag{3.7}$$

A = net activity of the sample

A_{abs} = original equilibrium ^{14}C activity of the reservoir that supplied the sample.

This is obtained using reference materials e.g. oxalic-I and oxalic-II.

$\lambda = 1.21 \times 10^{-4} \text{yr}^{-1}$ is the ^{14}C decay constant (half-life of 5730 years)

The results of the Kotumsar caves are discussed in chapter 4. In the case of speleothems, a discrepancy exists as there are two sources of carbon to the precipitating calcite; modern CO_2 and the carbon from limestone rock (dead carbon). The contribution from each of these sources may vary and the resultant calcite may overestimate the age if it has excess carbon from the limestone. Hence, recourse is taken to the more precise ^{230}Th dating technique.

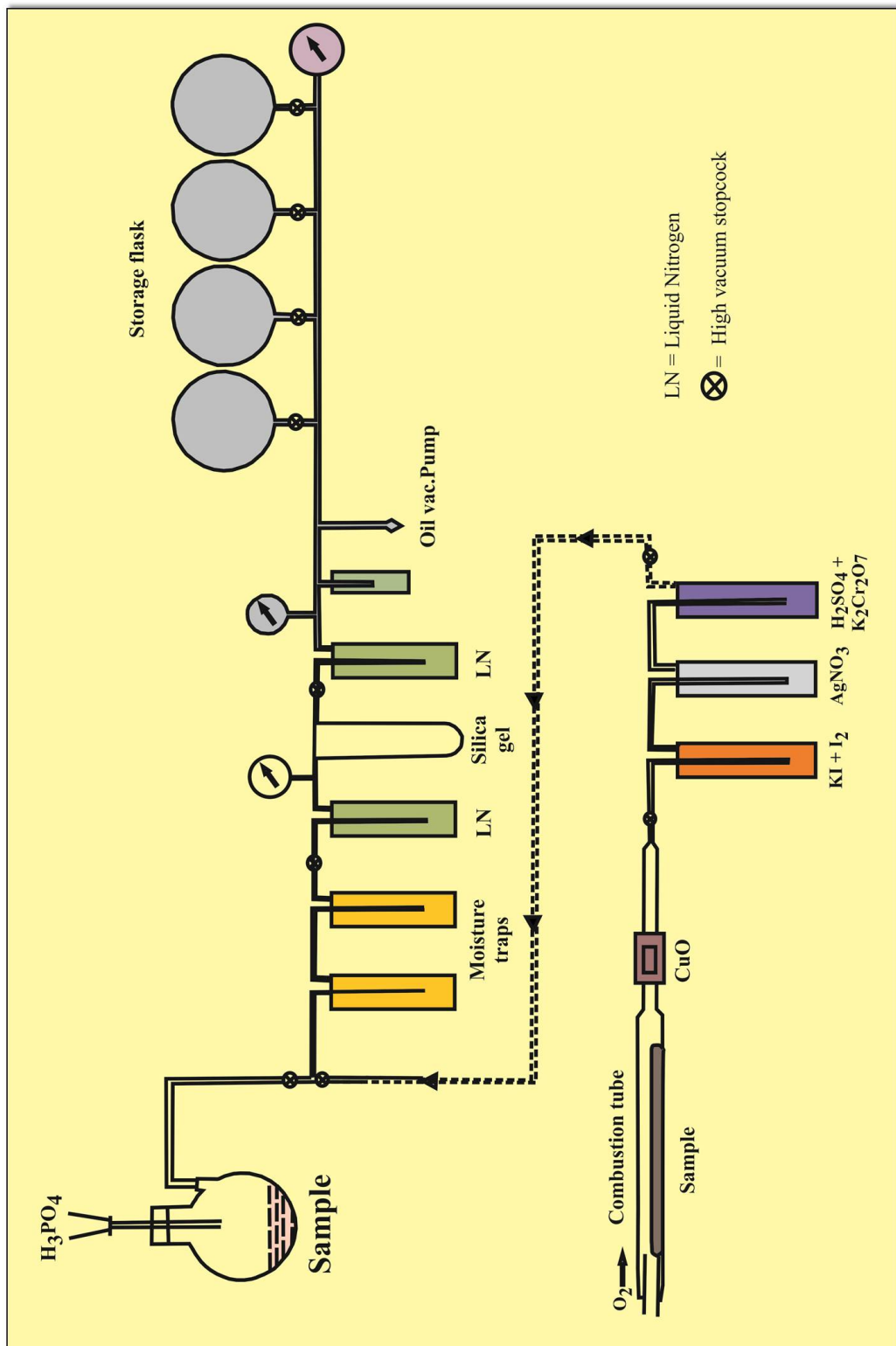


Figure 3.17: Schematic representation showing Wet and dry combustion setup for radiocarbon dating.

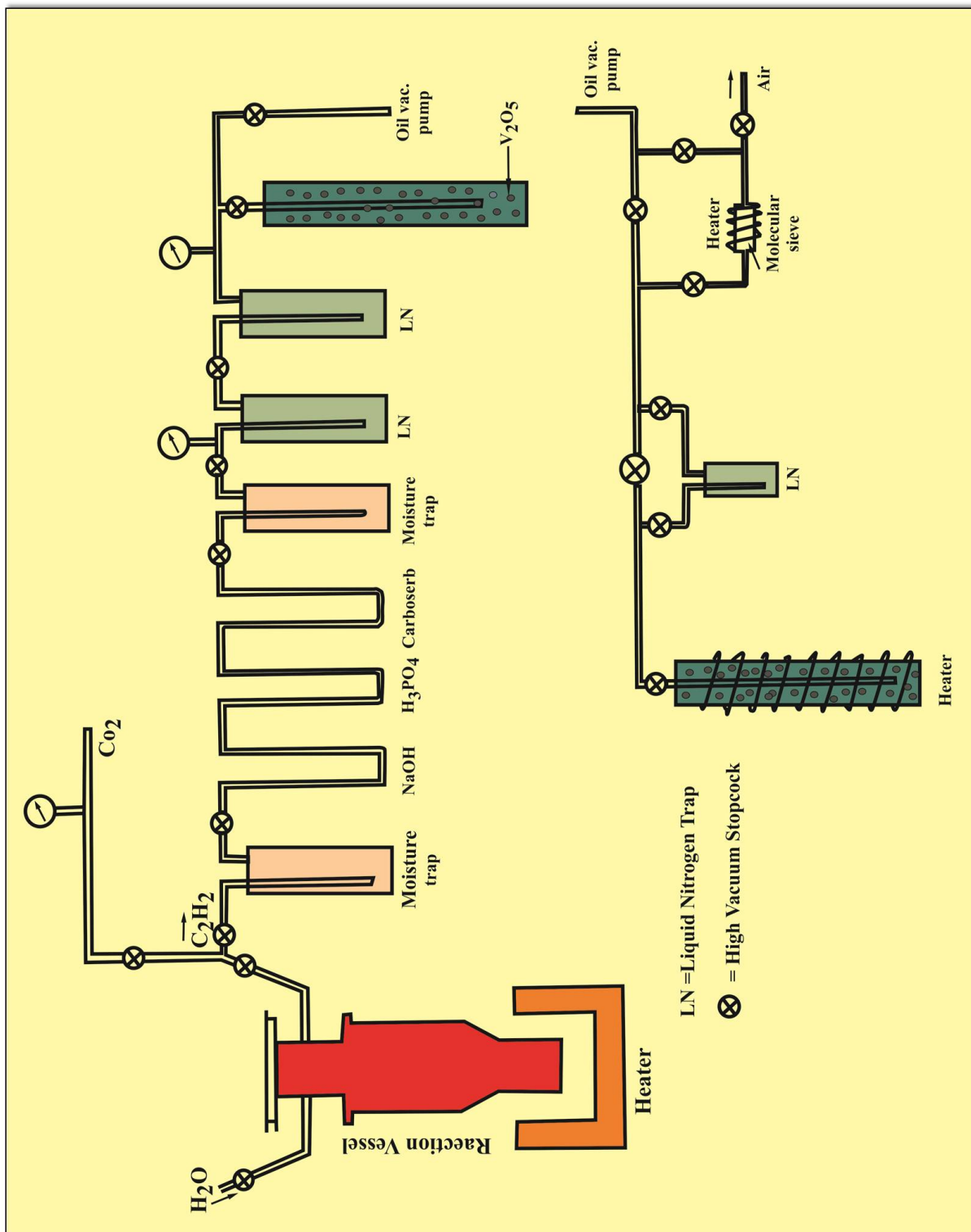


Figure 3.18: Schematic diagram showing acetylene and benzene synthesis setup.

3.5 U-Th dating

All the samples including KOT-I, were dated using the uranium-thorium dating technique. An overview of the systematics is given below.

3.5.1 Principles of dating

U-Th dating systematics is used on carbonates with accretionary growth (corals and speleothems) and deposited as a closed system. Precise age estimation can span from hundreds to over 500,000 years [[Edwards et al., 1987](#); [Henderson, 2006](#); [Scholz and Hoffmann, 2008](#)]. The technique does not rely upon the long decay series of ^{238}U to ^{206}Pb , instead it is based on the decay of its daughter product ^{234}U to ^{230}Th . U-Pb systematics under a closed system assumptions are in secular equilibrium, as the half-life of the parent nuclide is much greater than the intermediate daughter nuclide [[Faure, 1977](#)]. The secondary carbonate formed from dissolution and subsequent-precipitation, such as speleothems, however, is in disequilibrium due to incorporation of excess daughter nuclide or its deficiency as a result of nuclear or physical fractionation. Time required for the system to attain secular equilibrium is used to determine the ages of the sample.

The average continental abundance of U and Th are 1.7 and 8.5 $\mu\text{g g}^{-1}$ respectively [[Richards and Dorale, 2003](#); [Wedepohl, 1995](#)]. However, their abundances in the aquatic system vary significantly, because of the different solubility indices of U and Th. Uranium mobilizes quickly in contact with water and gets oxidized from +4 to +6 oxidation state and forms Uranyl ion (UO_2^{2+}) and its complexes as seen in figure 3.19 [[Faure, 1977](#)]. Uranyl ion co-precipitates with carbonates to form a complex ($\text{UO}_2(\text{CO}_3)^{-3}$) and gets incorporated into the system. Whereas, Th remains in the reduced +4 state and instead adsorbs or precipitates on the sediments. Hence, the speleothems precipitating under clean environments are devoid of initial Th activity.

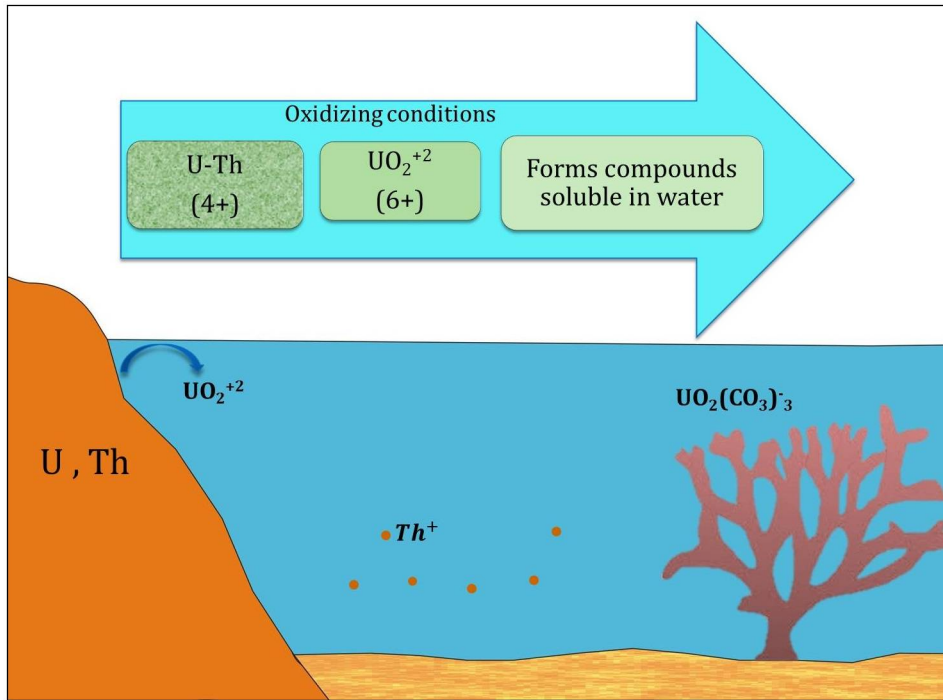


Figure 3.19: The schematic diagram explaining oxidation of uranium ion to form uranyl ion. Thorium adsorbs on the sediments and settles in water.

Hence, the $^{234}\text{U}/^{238}\text{U}$ activity is used to calculate the age of a speleothem, provided it's initial ratio while getting incorporated is known and the sample remained as a closed system. The final age equation, originally from Broecker (1963), was re-expressed by Haase-Schramm et al. (2004) as:

$$\left[\frac{^{230}\text{Th}}{^{238}\text{U}} \right] = (1 - e^{-\lambda_{230}t}) + \left(\left[\frac{^{234}\text{U}}{^{238}\text{U}} \right] - 1 \right) \times \left(\frac{\lambda_{230}}{\lambda_{230} - \lambda_{234}} \right) \times (e^{-\lambda_{234}t} - e^{-\lambda_{230}t}) \quad (3.8)$$

where, the square brackets imply the activity ratios, λ stands for decay constant and $t = \text{age}$. As the equation is transcendental, the age can be found out iteratively or graphically. The sample may have initial Th content adhering to the detrital particles, which is accounted by its measuring ^{232}Th activity. Higher ^{232}Th concentration implies higher amount of ^{230}Th . Corrections are made for the detrital ^{230}Th based on ^{232}Th concentration, used as a measure of contami-

nation and assuming appropriate $^{230}\text{Th}/^{232}\text{Th}$ ratio [Richards and Dorale, 2003]. The another approach to deduce the initial activities of Th and ^{234}U is to employ isochron technique. Isochrons can be plotted in two steps as given by Ludwig [2003].

1. $^{230}\text{Th}/^{232}\text{Th} - ^{238}\text{U}/^{232}\text{Th}$ and $^{234}\text{U}/^{232}\text{Th} - ^{238}\text{U}/^{232}\text{Th}$ referred as Rosholt type-II diagrams. The slope of the plots give the initial ^{230}Th and ^{234}U activities (Figure 3.20).
2. $^{230}\text{Th}/^{238}\text{U} - ^{232}\text{Th}/^{238}\text{U}$ and $^{234}\text{U}/^{238}\text{U} - ^{232}\text{Th}/^{238}\text{U}$ referred as Osmond type-II diagrams. The intercept of the plots give the initial ^{230}Th and ^{234}U activities (Figure 3.20).

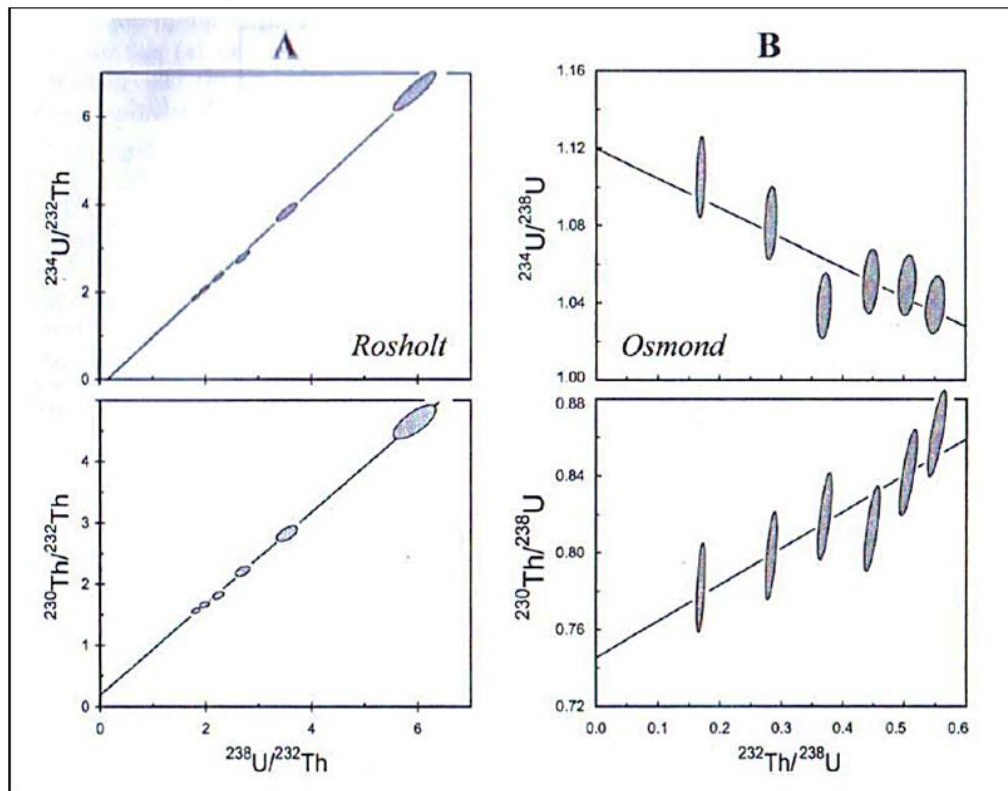


Figure 3.20: Rosholt and Osmond type plots used to determine for initial activities of ^{230}Th and ^{234}U in the sample [Ludwig, 2003].

3.5.2 Preliminary procedures

Since U-Th dating technique is crucial for speleothem based paleoclimate studies, an attempt was made to setup the technique at PRL. Much of the work is still under progress and the preliminary steps are discussed in brief.

Pre-concentration process Bulk carbonate sample consists of various trace elements, hence preferential removal of U and Th with maximum yield is important. Since the sample has trace amounts of U-Th, aerial contamination during extraction should be minimized. Hence, the pre-concentration procedures are carried out in a clean lab with class 1000 Hepa filters. U-Th separation from the matrix can be done using two types of Resins, namely, ion-exchange resin and chelating resin (UTEVA). In our work, we have used UTEVA resin, for removal of U and Th [Carter *et al.*, 1999; Horwitz *et al.*, 1992]. The maximum concentration of Uranium in speleothems can go up to is $170 \mu\text{g g}^{-1}$. For this reason, optimum carbonate sample quantity is 200 mg.

Resins are made of three main components: (a) the inner support, which is porous silica or organic polymer with size range of 50-150 μm (b) a stationary phase, which is liquid extractant and (c) a mobile phase, an acid solution. By changing the strength of the acids, different elements are leached out. In UTEVA (Uranium tetravalent Actinide) resin, the extractant is diamyl, amyl-phosphate (DAAP), which forms nitrate complexes with the actinide elements, which includes uranium and thorium. The formation of these complexes is driven by the concentration of nitrate in the sample solution. Therefore, at a higher strength of the acid (3M HNO_3) U(VI) and Th(IV) are retained by the resin, and the matrix elements(alkali earth) are separated out. In the next step, U-Th elution from the actinides is provoked by changing 3M HNO_3 to 3M HCl or changing the strength of 3N HNO_3 to 0.01M HNO_3 [Horwitz *et al.*, 1992]. In such conditions, the retention coefficient of thorium in HCl is less than that of uranium, favoring a good separation between the two elements. The protocol will be re-

fined by the measuring the concentration of elements collected in each elute and thereby changing the acid strength till the maximum recovery of U-Th. ^{229}Th and ^{236}U double spikes will be used to correct for the instrument introduced mass fractionation [Rudge *et al.*, 2009]. The final aliquots will be measured on a multi-collector-ICP-MS, using the procedures given by [Seth *et al.*, 2003; Shen *et al.*, 2002].

Age model After obtaining the U-Th ages, it is important to construct a reliable age model. Previously, most scientists opted for a linear interpolation between two-subsample distances. At present, speleologists use various age models like StalAge, COPRA, OXCAL, to name a few [Scholz *et al.*, 2012]. Each model comes with its own advantages and drawbacks. Our work is based on using the free software package COPRA 1.0, which is an interactive software that runs on the MATLAB interface [Breitenbach *et al.*, 2012]. Prerequisites to using this model is monotonicity i.e. the older deposition is at the bottom and younger at the top. Based on the ages and errors associated with them, a normal distribution is built around the age and proxy data points. The software uses 2000 Monte-Carlo simulations to interpolate between two data points. Age reversals and outliers can be identified and removed from the data set. The model also incorporates and interpolates ages between the hiatuses. The median of the distribution and the 95% confidence limits represent the final age model. The schematic of typical age model derived from COPRA is shown in figure 3.21.

For the speleothems reported in this study, the U-Th ages were obtained from the Oxford University, the University of New Mexico and the National Taiwan University. The results will be discussed in chapter 4.

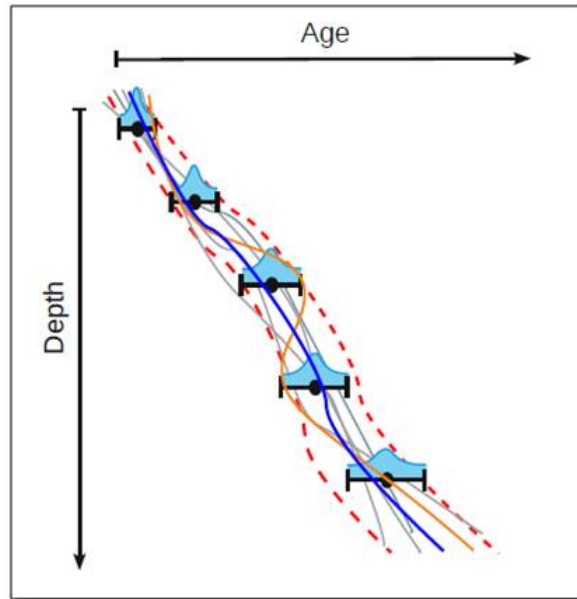


Figure 3.21: Schematic of the Monte Carlo model. The data points are plotted with the normal distribution (Cyan shaded area). The Standard deviation is equal to measurement error. The gray and brown curves indicate several realizations of the Monte Carlo simulation. The median blue curve and the 95% confidence limits (red dashed curves) represent the final age model resulting from the distribution of 2000 simulations. The image is taken from [Breitenbach et al. \[2012\]](#).

3.6 Foraminifera stable isotope analysis

The 4 m sediment core raised from the Andaman sea was composed of gray to very dark gray silty clay and seven discrete layers of tephra. After retrieval, it was divided into two parts, one for dating and stable isotope measurements and the other for geochemical and radiogenic isotope studies [[Awasthi et al., 2014](#)]. Planktic foraminifera were separated from the sediment core at intervals of 2 cm. The top 2 m of the core was dated using Accelerator Mass Spectrometer (AMS) radiocarbon dating of mixed planktic foraminiferal samples (collected from 10 different depths) at the AMS laboratory of University of Arizona, USA. The dates were converted into calendar ages using Marine-09 calibration curve [[Reimer et al., 2009](#)] and Calib 6.0 [[Stuiver and Reimer, 1993](#)]. A reservoir age

correction of ΔR (i.e., the difference between the regional marine ^{14}C age and the global model marine ^{14}C age) = $11 \pm 35(1\sigma)$ yr was assumed for the Andaman Sea [Awasthi *et al.*, 2014; Dutta *et al.*, 2001]. The bottom 2 m of the core was dated based on five sediment samples using ^{230}Th -excess dating at PRL. Samples collected at 2 cm interval were sent to Delhi university for identification and separation of foraminiferal species. The $\delta^{18}O$ composition of *Globigerinoides ruber* (white) was measured on Delta V-Plus IRMS and the values are reported with respect to VPDB.

Chapter 4

Holocene monsoon variability

The Holocene (Greek meaning = entirely new) period beginning at 11,700 yr BP, is the most recent interglacial period and is also known as the Marine Isotope stage -1(MIS-1). Climatic fluctuations within the Holocene were presumed to be less significant compared to the major glacial-interglacial variations. However, Holocene paleoclimate reconstructions have gained more importance with the discovery of oscillations with a pacing similar to the climatic events during the glacial periods (~ 1500 year cycle) [*Bond et al., 1997, 2001; Bond and Lotti, 1995; Broecker and Hemming, 2001; O'brien et al., 1995*]. These cycles are considered to be Holocene extensions of Dansgaard-Oeschger oscillations which are recorders of THE North-Atlantic climate changes during the last glacial period. Since these oscillations occurred in similar climatic conditions as today (warmer, and absence of large Hemispheric ice sheets), they are directly related to the understanding of the contemporary climate change rather than the glacial climate change. The discussions about the cyclic nature of these changes gained momentum after observing transitions from the Medieval warm period (MWP) to Little Ice Age(LIA), which is the most recent advance of glaciers in the Holocene [*Wanner et al., 2008*]. These abrupt climatic changes also have had a large impact on rise and fall of human civilizations [*Enzel et al., 1999*]. In response to interglacial warming, the Indian monsoon steadily increased at the beginning

of Holocene, as shown by several comprehensive studies [*Mayewski et al., 2004; Tiwari et al., 2011*]. However, some consensus still exists that the Holocene experienced a countrywide aridification [*Ponton et al., 2012*]. To test both these hypotheses it's important to generate high resolution records of ISM from the core monsoon region of India. The focus of this chapter is on climate variability during the Holocene and establish the link between global climate events and the Indian summer monsoon.

4.1 The Dandak-I stalagmite

The stalagmite sample was collected in February 1996, 220 m inside the cave. The temperature and humidity of the cave atmosphere were 27°C and 92%, respectively. To determine the moisture sources contributing to rainfall during the wet season (June to October), we carried out a Lagrangian back trajectory analysis using the HYSPLIT model [*Stein et al., 2015*] with NCEP Reanalysis-1 [*Kalnay et al., 1996*] as input to the model. We chose all the days with daily rain above 2 mm during 5 years (1980 to 2009 CE) for the analysis. During ISM, trajectories suggest that the Arabian Sea is the major source of moisture and its isotopic composition is likely to reflect the rainout over the Western Ghat region Figure (4.1).

4.1.1 Mineralogy

The mineralogical composition of the stalagmite was studied based on thin sections prepared at the M.S. University of Baroda, Vadodara. The sections were analyzed under a camera aided petrological microscope Leica DM EP. A section was also prepared across the hiatus boundary to check for the textural changes prior to the subsequent deposition. The stalagmite sample is composed of calcite. Figure 4.2 (a) and (b) show one such section where the layers are made up of columnar calcite fabric. Thin laminations are seen as altered dark layers. The

hiatus as shown in Figure 4.2 is an erosional boundary, with the growth of calcite crystals occurred on both the sides.

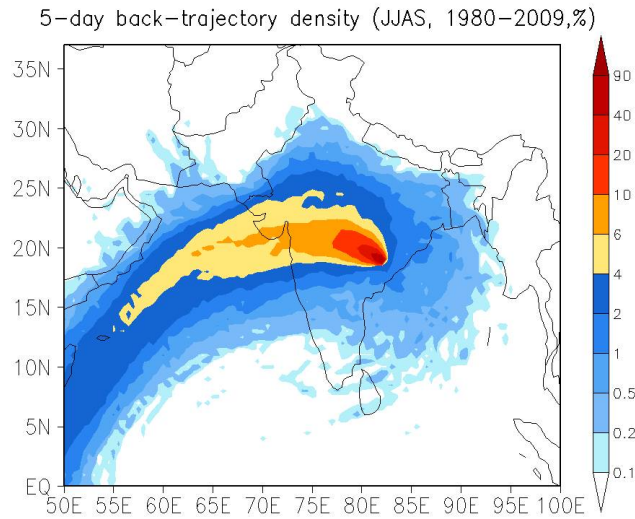


Figure 4.1: Climatological monthly rainfall in a 0.5×0.5 grid over the Dandak cave. Climatology is calculated using Asian Precipitation-Highly-Resolved Observational Data Integration Towards Evaluation (APHRODITE) data from CE 1980-2009 [Yatagai et al., 2012].

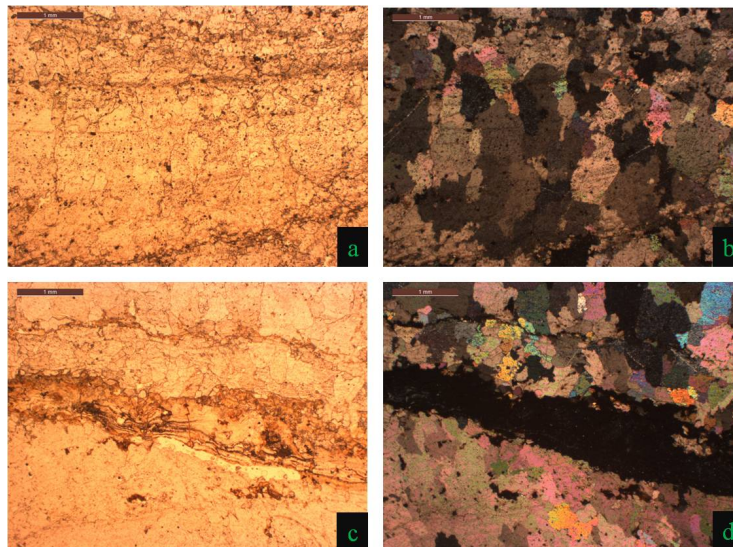


Figure 4.2: a) and b) are plane polarized light (ppl) and cross polarized light (xpl) images of DAN-I stalagmite, respectively. The entire sample is composed of columnar calcite fabric. c) and d) are ppl and xpl images of the sample across the hiatus. The hiatus is seen as a dark opaque band, with no deposition. Euhedral crystals of calcite are seen on both sides of the hiatus.

4.1.2 U-Th ages

Fourteen U-Th ages were obtained from the ~ 29 cm long Dan-I stalagmite. The sample was dated in the University of New Mexico, and the U-Th ages are shown in Table 4.1. Corrected ages use an initial $^{230}\text{Th}/^{232}\text{Th}$ atomic ratio = $0.0012 \times ^{232}\text{Th}^{-0.6386}$ where, ^{232}Th is concentration in parts per million (ppt), with the supposition that lower concentration of ^{232}Th equates with higher $^{230}\text{Th}/^{232}\text{Th}$ ratios. Years before present = yr BP, where present is AD 2007. Sub-samples weighing $\sim 90 - 408$ mg were used. The ages have five distinct tractable reversals, superimposing at 1σ error limit. An interactive tool, COPRA, was used to generate an age model shown in Figure 4.3. Since the sample was active (dripping on the stalagmite) during its collection, age zero was introduced in the model at the tip of the sample. The sample shows a brief hiatus at the depth of 21.7 cm, post which, the growth layers are continuous. Based on the age model, the stalagmite growth began at ~ 6.5 ka BP, with a cessation at ~ 2.2 ka BP. After the hiatus of 200 years, the sample growth resumed at ~ 2.0 ka BP to the present.

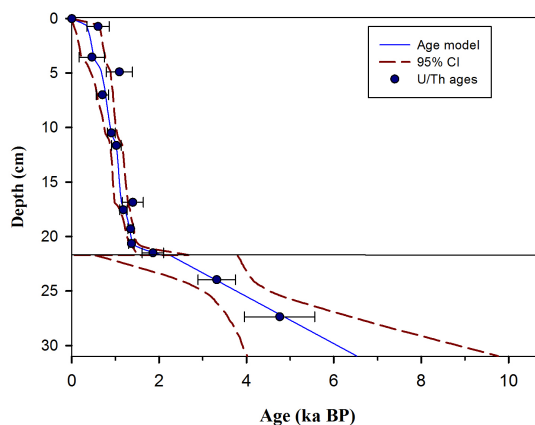


Figure 4.3: Age model reconstructed using COPRA- an interactive program on MATLAB [Breitenbach et al., 2012]. The filled blue circles are ^{230}Th ages used in the age model. The errors are reported as 2σ . The dashed lines show 95% confidence intervals and the blue line is the median through which the age model passes.

Table 4.1: Uranium and Thorium isotopic compositions and ^{230}Th ages of the subsamples of Dandak-I stalagmite. All the errors are reported in 2σ .

| Sample | ^{238}U (ppb) | ^{232}Th (ppt) | $^{230}\text{Th}/^{232}\text{Th}$ activity ratio | $^{230}\text{Th}/^{238}\text{U}$ activity ratio | measured $\delta^{234}\text{U}$ (‰) | initial $\delta^{234}\text{U}$ (‰) | uncorrected age Yr BP | corrected age Yr BP |
|-----------------|---------------------------|----------------------------|--|---|---|--|-----------------------------|---------------------------|
| 1M(7.4 mm) | 313.3±0.8 | 11409 ± 52 | 1.2 ± 0.0 | 0.0148 ± 0.0004 | 461 ± 2 | 461 ± 2 | 1688 ± 61 | 602 ± 509 |
| top1(34.4 mm) | 227.2 ± 1 | 10486 ± 55 | 0.9 ± 0.2 | 0.0131 ± 0.0036 | 442 ± 11 | 442 ± 12 | 993 ± 278 | 304 ± 743 |
| top1-2(34.4 mm) | 226.8±0.8 | 10884 ± 69 | 1.2 ± 0.5 | 0.0185 ± 0.0079 | 454 ± 5 | 454 ± 5 | 1400 ± 602 | 705 ± 918 |
| 40M (40.5 mm) | 141.4±0.3 | 1931 ± 39 | 5.0 ± 0.2 | 0.0223 ± 0.0008 | 451 ± 2 | 452 ± 2 | 1688 ± 61 | 1091 ± 600 |
| 63M (65.3 mm) | 193.5±0.5 | 574 ± 32 | 13.4 ± 0.9 | 0.0130 ± 0.0005 | 447 ± 1 | 448 ± 1 | 984 ± 35 | 702 ± 284 |
| 93M (95.9 mm) | 217.9±0.6 | 230 ± 41 | 41.4 ± 7.6 | 0.0143 ± 0.0005 | 444 ± 2 | 445 ± 2 | 1087 ± 39 | 907 ± 187 |
| P (106.9 mm) | 359.4±2.6 | 3763 ± 22 | 4.9 ± 0.2 | 0.0169 ± 0.0007 | 444 ± 8 | 445 ± 8 | 1285 ± 51 | 985 ± 304 |
| P2 (106.9 mm) | 358.8±2.6 | 3944 ± 30 | 5.0 ± 0.5 | 0.0180 ± 0.0017 | 439 ± 9 | 440 ± 9 | 1373 ± 128 | 1067 ± 220 |
| 126M (129.3 mm) | 330.8±0.8 | 331 ± 1 | 44.1 ± 4.9 | 0.0208 ± 0.0005 | 442 ± 1 | 444 ± 1 | 1583 ± 38 | 1428 ± 160 |
| 155M (159.9 mm) | 423.1±1.1 | 22089 ± 68 | 1.4 ± 0.0 | 0.0247 ± 0.0004 | 445 ± 1 | 447 ± 2 | 1879 ± 30 | 1397 ± 484 |
| N (164.6 mm) | 325.0±1.5 | 939 ± 12 | 20.3 ± 1 | 0.0192 ± 0.0010 | 445 ± 6 | 447 ± 6 | 1460 ± 73 | 1260 ± 213 |
| N2 (164.6 mm) | 325.2±2.2 | 973 ± 12 | 18.5 ± 0.9 | 0.0181 ± 0.0008 | 438 ± 11 | 439 ± 11 | 1381 ± 64 | 1177 ± 214 |
| 174M (180.4 mm) | 415.6 ± 1 | 535 ± 42 | 46.0 ± 3.7 | 0.0194 ± 0.0003 | 442 ± 1 | 443 ± 1 | 1477 ± 26 | 1348 ± 131 |
| 200M (204.1 mm) | 316.7±0.8 | 2821 ± 43 | 7.5 ± 0.2 | 0.0219 ± 0.0005 | 439 ± 2 | 441 ± 2 | 1675 ± 36 | 1368 ± 310 |
| G (210.0 mm) | 361.6±2.6 | 32564±131 | 1.1 ± 0.1 | 0.0312 ± 0.0020 | 442 ± 11 | 444 ± 11 | 2389 ± 158 | 1737 ± 670 |
| G2(210.0 mm) | 360.2±2.6 | 32873±132 | 1.2 ± 0.1 | 0.0347 ± 0.0038 | 443 ± 17 | 446 ± 17 | 2653 ± 298 | 1998 ± 719 |
| 213M (221.2 mm) | 284.5±0.7 | 35045 ± 90 | 1.3 ± 0.0 | 0.0538 ± 0.0007 | 0 ± 0 | 436 ± 2 | 4175 ± 58 | 3319 ± 858 |
| D (253 mm) | 136.3±0.6 | 24204 ± 70 | 1.4 ± 0.1 | 0.0808 ± 0.0053 | 433 ± 11 | 439 ± 12 | 6323 ± 430 | 4759±1621 |

Corrected ages use an initial $^{230}\text{Th}/^{232}\text{Th}$ atomic ratio = $0.0012 \times ^{232}\text{Th}^{-0.6386}$, where ^{232}Th is concentration in ppt, with the supposition that lower concentration of ^{232}Th equates with higher $^{230}\text{Th}/^{232}\text{Th}$ ratios. Years before present = yr BP, where present is AD 2007. Subsample sizes range from 90 to 408 mg. Distances from the tops of the stalagmites are incorporated into the subsample names.

4.1.3 Stable isotopes of oxygen and carbon

The $\delta^{18}\text{O}$ time series of the Dandak-I stalagmite is shown in Figure 4.4. The $\delta^{18}\text{O}$ (blue) values range from -6 to -2‰, whereas the $\delta^{13}\text{C}$ (purple) values vary between -11 to -3‰. The ages with 2σ errors are shown in orange filled circles. The $\delta^{18}\text{O}$ values show a slow decrease from 6.5 ka BP to present, with episodes of enrichment between 6-5 ka, 4.7-4.2 ka and 0.8-0.4 ka BP. The $\delta^{13}\text{C}$ data follow a similar trend, however the peak observed at 3.5-2.5 ka BP in $\delta^{18}\text{O}$ values is not seen. There is sharp enrichment in the values for the span of hundred years

Table 4.2: Uranium and Thorium isotopic compositions and ^{230}Th ages of the subsamples of Dandak- II stalagmite. All errors are absolute 2σ values.

| Sample | ^{238}U (ppb) | ^{232}Th (ppt) | $^{230}\text{Th}/^{232}\text{Th}$ activity ratio | $^{230}\text{Th}/^{238}\text{U}$ activity ratio | measured $\delta^{234}\text{U}$ (‰) | initial $\delta^{234}\text{U}$ (‰) | uncorrected age Yr BP | corrected age Yr BP |
|-----------------|---------------------------|----------------------------|--|---|---|--|-----------------------------|---------------------------|
| top2(13.5mm) | 266.7±1.7 | 2442 ± 25 | 46.9 ± 1.1 | 0.1406 ± 0.0030 | 695 ± 11 | 713 ± 11 | 9398 ± 217 | 9107 ± 363 |
| top2-2(13.5 mm) | 266.4±1.3 | 2412 ± 80 | 49.1 ± 2.2 | 0.1454 ± 0.0042 | 700 ± 13 | 709 ± 13 | 9706 ± 305 | 9417 ± 420 |
| top1-2(avg) | | | | | | | weight average age = | 9420 ± 270 |
| stest (61.0 mm) | 222.8±1.1 | 5040 ± 44 | 19.8 ± 0.6 | 0.1464 ± 0.0045 | 692 ± 11 | 711 ± 11 | 9825 ± 324 | 9371 ± 557 |
| K (189 mm) | 178.9±0.8 | 187 ± 18 | 437.1 ± 43.2 | 0.1492 ± 0.0030 | 683 ± 10 | 702 ± 10 | 10080 ± 221 | 9907 ± 280 |
| K2 (189 mm) | 179.3±0.8 | 203 ± 18 | 400.0 ± 39 | 0.1485 ± 0.0053 | 697 ± 9 | 717 ± 9 | 9983 ± 371 | 9762 ± 411 |
| K(avg) | | | | | | | weight average age = | 9861 ± 230 |
| B(319.5 mm) | 322.9±1.7 | 1343 ± 18 | 114.7 ± 3.4 | 0.1560 ± 0.0041 | 693 ± 9 | 713 ± 10 | 10492 ± 296 | 10298±353 |
| B2 (319.5 mm) | 323.6±1.4 | 1386 ± 16 | 109.2 ± 2.0 | 0.1529 ± 0.002 | 695 ± 8 | 715 ± 8 | 10262 ± 163 | 10067±254 |
| B(avg) | | | | | | | weight average age = | 10146±210 |

Corrected ages use an initial $^{230}\text{Th}/^{232}\text{Th}$ atomic ratio = $0.0012 \times ^{232}\text{Th}^{-0.6386}$, where ^{232}Th is concentration in ppt, with the supposition that lower concentration of ^{232}Th equate to higher $^{230}\text{Th}/^{232}\text{Th}$ ratios. Years before present = yr BP, where present is AD 2007. Subsample sizes range from 90 to 408 mg. Distances from the tops of the stalagmites are incorporated into the subsample names.

between 0.6 - 0.7 ka BP.

4.1.4 Trace element analysis

The interpretation of trace element data of the Dan-I stalagmite were already discussed in *Yadava [2002]*; *Yadava and Ramesh [2001]*(Figure 4.5). The trace element values in this study are useful as a supporting evidence to the $\delta^{18}\text{O}$ values, in paleomonsoon reconstruction. The variations in the trace element concentrations of Mg,Sr and Ba, were measured on ICP-AES (Inductively Coupled Plasma Atomic Emission Spectroscopy). The concentrations of the elements are reported in parts per million (ppm). Since the measurements of Ca ions were not carried out, normalization of trace elements with respect to calcium was not possible. Nevertheless, bare concentrations can be taken as indicators of PCP or high influx of meteoric water. The age model for trace elements was generated using

Table 4.3: Uranium and Thorium isotopic compositions and ^{230}Th ages of the subsamples of Kotumsar stalagmite. All errors are absolute 2σ values.

| Sample | ^{238}U (ppb) | ^{232}Th (ppt) | $^{230}\text{Th}/^{232}\text{Th}$ activity ratio | $^{230}\text{Th}/^{238}\text{U}$ activity ratio | measured $\delta^{234}\text{U}$ (‰) | initial $\delta^{234}\text{U}$ (‰) | uncorrected age Yr BP | corrected age Yr BP |
|---------------------|---------------------------|----------------------------|--|---|---|--|-----------------------------|---------------------------|
| KOT-1 (1.5 mm) | 244.34± 0.2 | 79.5 ± 4.5 | 0.08192 ± 0.000067 | 4152 ± 237 | 622.8 ± 1.4 | 632.8 ± 1.4 | 5631 ± 48 | 5626 ± 48 |
| KOT-2 (11.5 mm) | 80.531± 0.064 | 1281.3 ± 5 | 0.1386 ± 0.0012 | 143.6 ± 1.3 | 688.1 ± 1.5 | 705.9 ± 1.6 | 9287 ± 82 | 9040 ± 148 |
| KOT-3 (23 mm) | 78.246± 0.062 | 282.1 ± 4.1 | 0.2034 ± 0.0012 | 930 ± 15 | 693.1 ± 1.7 | 720.6 ± 1.7 | 13841 ± 90 | 13.785 ± 94 |
| KOT-4 (38 mm) | 73.557± 0.059 | 3142 ± 7.6 | 0.1362 ± 0.0017 | 52.5 ± 0.067 | 684.9 ± 1.8 | 701.5 ± 1.9 | 9142 ± 120 | 8476 ± 355 |
| KOT-5 (46 mm) | 84.213± 0.068 | 1402 ± 4.1 | 0.1325 ± 0.0010 | 132.2 ± 1.1 | 686.2 ± 1.7 | 703.3 ± 1.7 | 8948 ± 72 | 8690 ± 148 |
| KOT-6 (62.5 mm) | 74.826± 0.074 | 230.2 ± 4 | 0.1517 ± 0.0011 | 813 ± 15 | 696.5 ± 2.7 | 716.7 ± 2.8 | 10153 ± 81 | 10105 ± 84 |
| KOT-7 (78.5 mm) | 77.818± 0.070 | 315.1 ± 2.7 | 0.10064 ± 0.00078 | 409.7 ± 4.7 | 696 ± 2.1 | 709.1 ± 2.2 | 6644 ± 53 | 6581 ± 62 |
| KOT-8 (103 mm) | 95.443± 0.092 | 173.8 ± 1.7 | 0.10148 ± 0.00057 | 919 ± 11 | 696.9 ± 2.7 | 710.1 ± 2.8 | 6697 ± 40 | 6669 ± 43 |
| KOT-9 (124 mm) | 86.547± 0.079 | 629.8 ± 2.1 | 0.09881 ± 0.00065 | 223.9 ± 1.6 | 700.4 ± 2.2 | 713.2 ± 2.3 | 6503 ± 45 | 6391 ± 72 |
| KOT-10 (168 mm) | 101.609± 0.0.095 | 2063 ± 34 | 0.1012 ± 0.0012 | 82.2 ± 1.6 | 715.7 ± 2.3 | 728.6 ± 2.3 | 6603 ± 78 | 6292 ± 174 |
| KOT-11 (181.5mm) | 117.40± 0.13 | 2057.4 ± 4.3 | 0.1031 ± 0.0010 | 97 ± 1 | 706.7 ± 2.5 | 719.8 ± 2.6 | 6767 ± 68 | 6497 ± 151 |
| KOT-12 (201 mm) | 321.88± 0.064 | 4581 ± 73 | 0.648 ± 0.0019 | 751 ± 25 | 409.3 ± 3.7 | 491.2 ± 5.7 | 64857 ± 2545 | 64604 ± 2542 |
| KOT-13 (227 mm) | 114.50± 0.12 | 16518 ± 70 | 0.3967 ± 0.0064 | 45.3 ± 0.76 | 719.7 ± 2.8 | 774.2 ± 4 | 28072 ± 510 | 25903 ± 1206 |
| KOT-14 (274 mm) | 120.68± 0.11 | 7561 ± 20 | 0.1298 ± 0.0022 | 34.1 ± 0.59 | 674.6 ± 2.1 | 689.6 ± 2.3 | 8755 ± 156 | 7770 ± 519 |
| KOT-15 (276.5mm) | 93.198± 0.084 | 763 ± 4 | 0.1195 ± 0.0010 | 240.9 ± 2.5 | 684.8 ± 2.0 | 700.1 ± 2.0 | 7 + 87 ± 72 | 7860 ± 96 |

The degree of detrital ^{230}Th contamination is indicated by the $^{230}\text{Th}/^{232}\text{Th}$ atomic ratio instead of the activity ratio. Age corrections for samples were calculated using an estimated initial atomic $^{230}\text{Th}/^{232}\text{Th}$ ratio of 4 ± 4 ppm. Decay constants are $9.1705 \times 10^{-6}\text{yr}^{-1}$ for ^{230}Th , $2.8221 \times 10^{-6}\text{yr}^{-1}$ for ^{234}U [Cheng et al., 2013], and $1.55125 \times 10^{-10}\text{yr}^{-1}$ for ^{238}U [Mattinson, 2000].

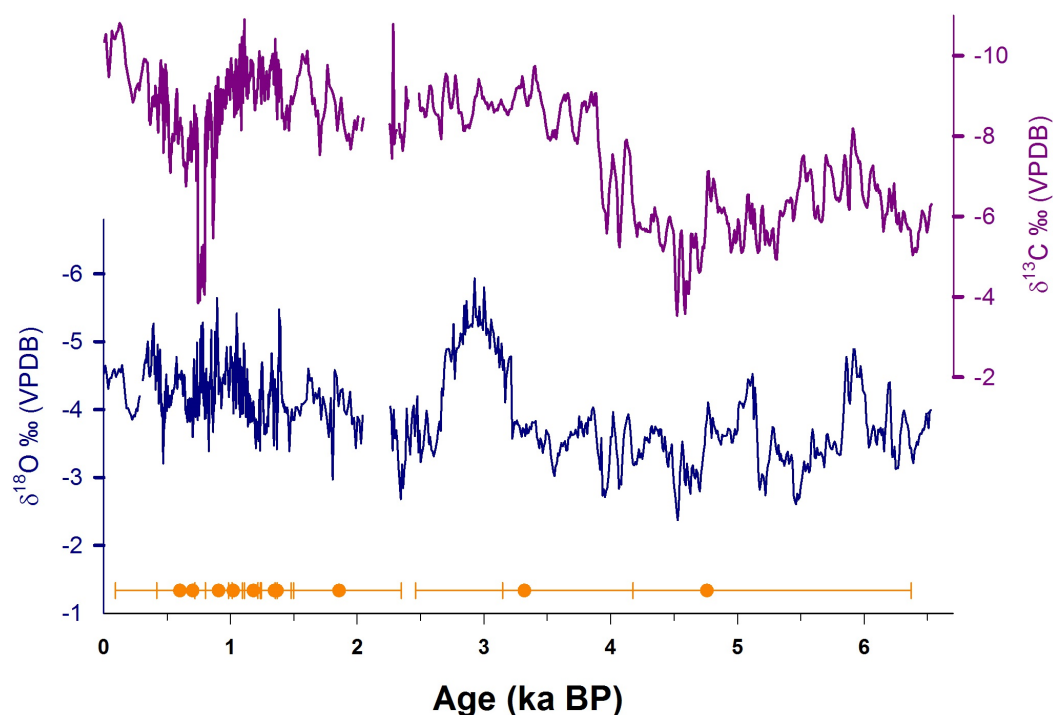


Figure 4.4: $\delta^{18}\text{O}$ (Dark blue) and $\delta^{13}\text{C}$ (Purple) profiles of the Dandak-I stalagmite. The timeseries represents the profile based on ages derived from the COPRA age model. The ages considered in the model are shown as orange filled circles. The errors are reported as 2σ .

COPRA and the timeseries is shown in Figure 4.5. Since the trace element and $\delta^{18}\text{O}$ measurements were carried out on different stalagmite slices, there is a shift in the time-series, owing to different sampling depths (indicated by the arrows). From ~ 2 ka to the present the trace element concentrations and $\delta^{18}\text{O}$ values covary. The concentrations drop abruptly between 3.5 - 2.8 ka BP, showing peak to peak matching with $\delta^{18}\text{O}$ values.

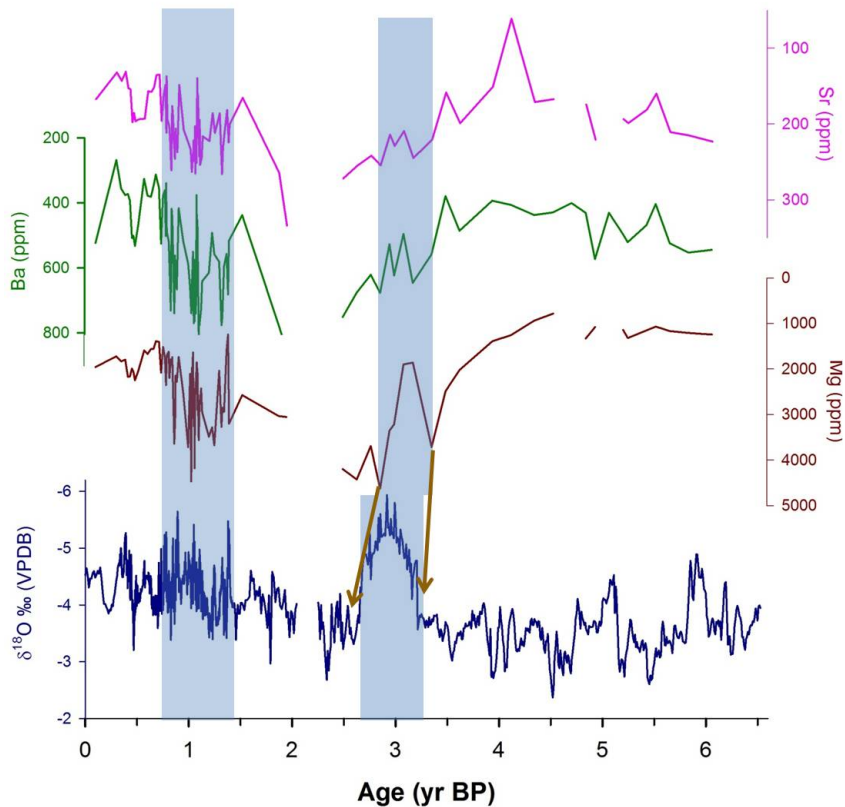


Figure 4.5: Trace element variations in the Dan-I speleothem. Concentrations of Magnesium (Mg, Red), Barium (Ba, Green) and Strontium (Sr, Pink) are reported in ppm. The trace element profiles are compared with the $\delta^{18}O$ values (blue). The arrows point to the peak in trace element with the corresponding $\delta^{18}O$ variability. Shaded regions show the zones of similar variability observed in the trace element and $\delta^{18}O$ data.

4.2 The Dandak-II stalagmite

4.2.1 U-Th ages

The timeseries of the Dandak-II stalagmite is based on four U-Th ages for a length of 41.3 cm of the sample (Table 4.2). The ages have overlapping errors, hence no outliers were detected. The age model was reconstructed using COPRA with 3000 Monte Carlo simulations (Figure 4.6). The errors are reported as 2σ values and the confidence interval of 95% is shown in red dashed lines. Corrected ages

use an initial $^{230}\text{Th}/^{232}\text{Th}$ atomic ratio = $0.0012 \times ^{232}\text{Th}^{-0.6386}$ where, ^{232}Th is concentration in parts per million (ppt), with the supposition that lower concentration of ^{232}Th equate to higher $^{230}\text{Th}/^{232}\text{Th}$ ratios. Years before present = yr BP, where present is AD 2007. Subsamples weighing $\sim 90 - 408$ mg were used. The Dandak-II stalagmite spans from 10.4 - 9 ka and shows a steady growth rate of ~ 0.4 mm/yr.

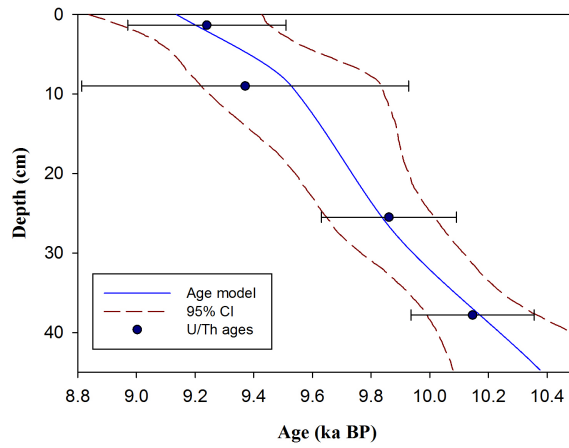


Figure 4.6: Age model for Dan- II stalagmite reconstructed using COPRA-interactive program on MATLAB [Breitenbach et al., 2012]. The filled blue circles are ^{230}Th ages taken for age model. The errors are reported in 2σ . The dashed lines show 95% confidence interval and the blue lines are the median through which the age model passes.

4.2.2 Stable isotopes of oxygen and carbon

A total of 2250 subsamples from the Dandak-II stalagmite were analyzed on a Delta-V plus IRMS. The $\delta^{18}\text{O}$ and $\delta^{13}\text{C}$ timeseries are shown in Figure 4.7. The sample shows a gradual -5% decrease in the $\delta^{18}\text{O}$ from 10.4 to 9 ka. This steady depletion is however punctuated by a cluster of sharp ^{18}O enriched peaks occurring at regular intervals. The $\delta^{13}\text{C}$ values vary between -2 to -8% , with the values fluctuating around the mean of -3.5% . The $\delta^{13}\text{C}$ data do not necessarily mimic the $\delta^{18}\text{O}$ profile. However, the peaks in the $\delta^{18}\text{O}$ values are also observed in $\delta^{13}\text{C}$ (Figure 4.7).

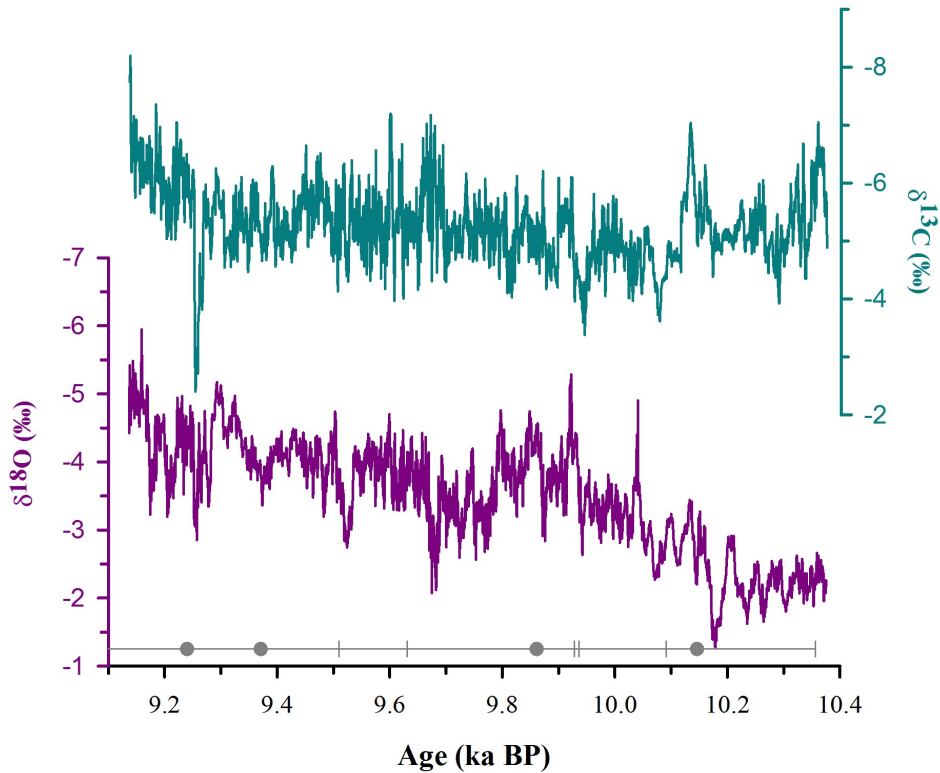


Figure 4.7: $\delta^{18}\text{O}$ (Purple) and $\delta^{13}\text{C}$ (cyan) profiles of Dandak-II stalagmite. The timeseries represents the profile based on ages derived from Copra age model. The ages considered in the model are shown as gray filled circles. The errors are reported in 2σ

4.2.3 Hendy's test

As seen in Figure 4.8, there is no significant enrichment of ^{18}O and ^{13}C along the layers. Also, there is a poor correlation between $\delta^{18}\text{O}$ and $\delta^{13}\text{C}$ values. This implies that there was minimal evaporation and slow degassing during the deposition of calcite otherwise the precipitating calcite would undergo kinetic fractionation and would show enrichment in ^{18}O along the tapering ends of a layer. This ensures that the sample was precipitated under isotopic equilibrium.

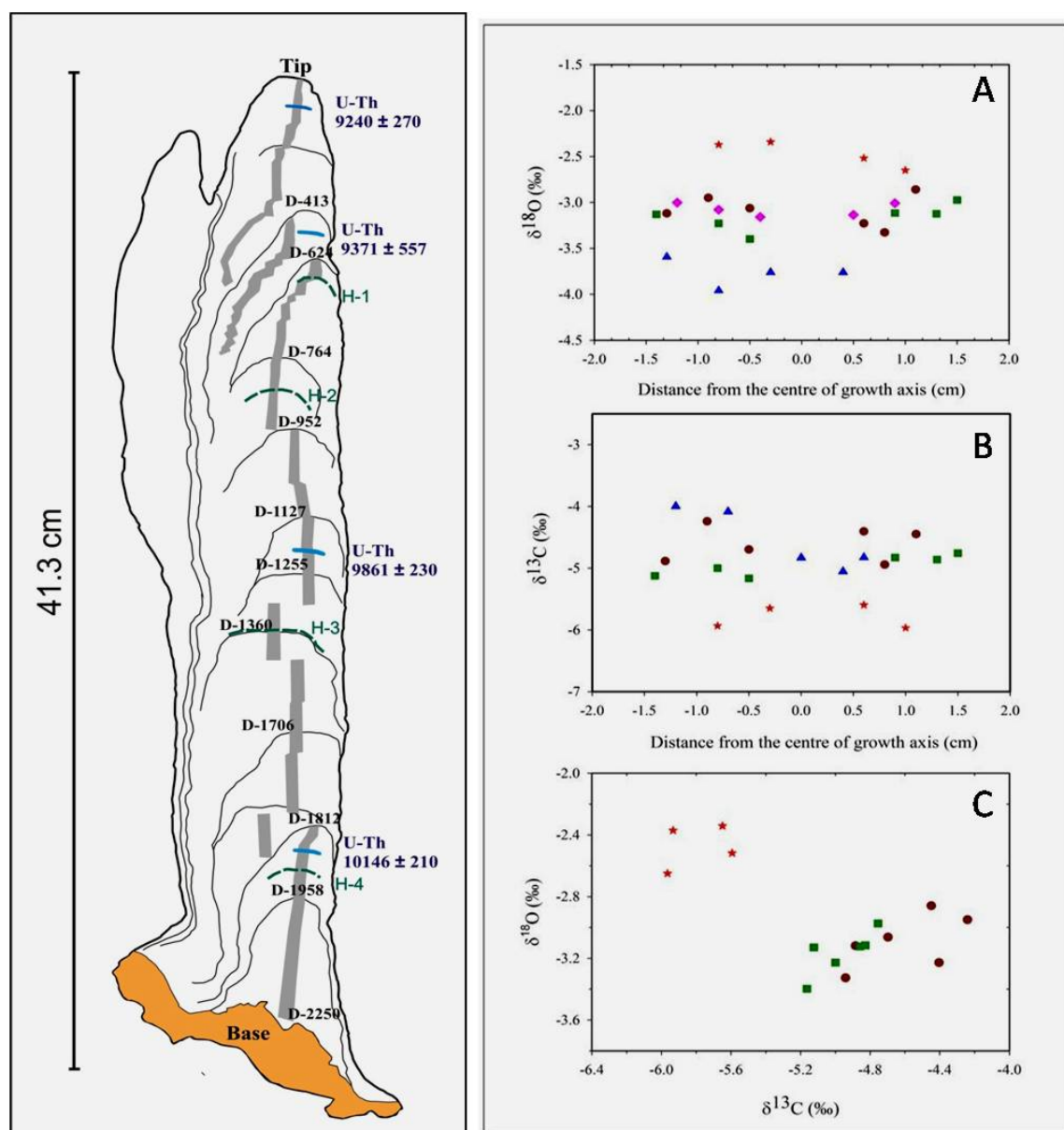


Figure 4.8: Left: Sketch of the Dandak-II stalagmite, showing sampling sites for Hendy's test (dashed green) and U-Th ages (dark blue). Right: (A) and (B) $\delta^{18}\text{O}$ and $\delta^{13}\text{C}$ variability along four layers. (C) The correlation between $\delta^{18}\text{O}$ and $\delta^{13}\text{C}$ used to indicate isotope equilibrium between precipitating calcite.

4.3 Kotumsar stalagmite

4.3.1 U-Th ages

The U-Th ages for the KOT-I stalagmite were obtained from the National Taiwan University. Table 4.3 shows the 15 ages with associated errors. The sample has many reversals and non-tractable outliers. The reversals with very old ages occur when there is a post-depositional U loss from the sample giving artificially old ages. Some reasons for the loss can be a sample that has been recrystallized from aragonite to calcite or perhaps flooding immediately after deposition (which could also cause recrystallization). These reversals were removed from the age models. The sample as seen in Figure 3.5 has a band of high detrital content and high ^{232}Th values. Thus, the ages in this band show reversals and are unreliable. The age model was then constructed based on 6 ages, and is shown in Figure 4.9. The growth of the sample is from $\sim 8.4 - 5.6$ ka BP. The rate of growth however, has varied during its course of deposition, from 8.4 -6.5 ka BP, the deposition rate was slow at ~ 0.055 mm/yr. The stalagmite growth was rapid between 6.5-5.6 ka BP, with the rate of ~ 0.23 mm/yr.

4.3.2 Hendy test

The results of Hendy test performed on four layers of KOT-I sample are shown in Figure 4.10. The $\delta^{18}\text{O}$ values along a layer do not show major fluctuations and also there is a poor correlation between $\delta^{18}\text{O}$ and $\delta^{13}\text{C}$ values. This ensures that the sample was precipitated under an isotopic equilibrium and can be used for paleomonsoon reconstructions.

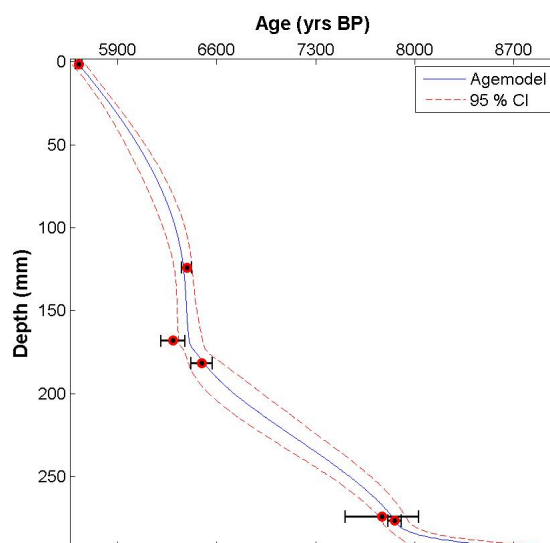


Figure 4.9: Age model for the Kotumsar stalagmite using the COPRA- interactive program on MATLAB [Breitenbach et al., 2012]. The filled blue circles are ^{230}Th ages assumed for the age model. The errors are reported in 2σ . The dashed lines show 95% confidence intervals and the blue line is the median through which the age model passes.

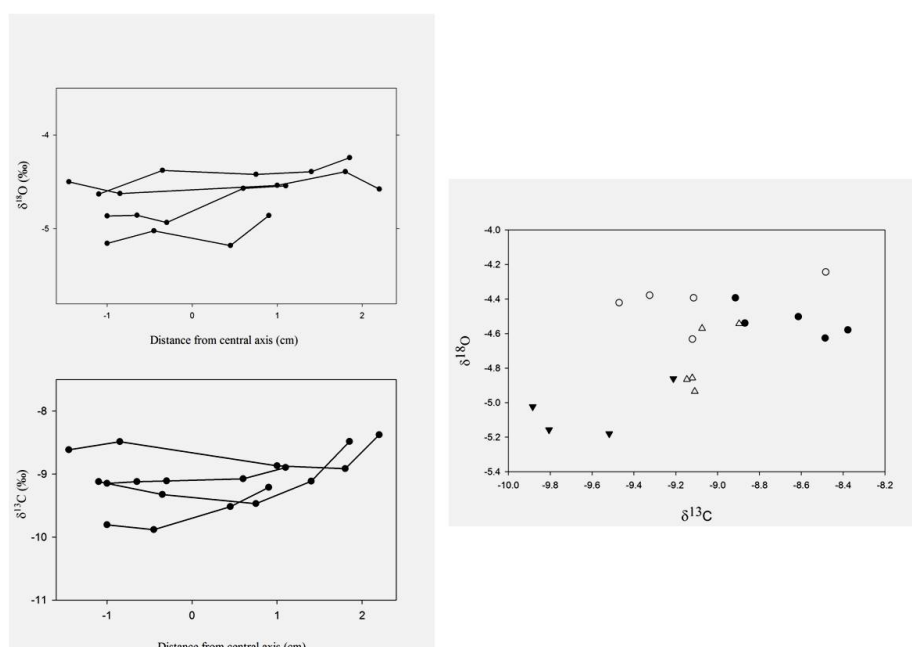


Figure 4.10: Left: Top $\delta^{18}\text{O}$ and Bottom $\delta^{13}\text{C}$ variability along four layers is plotted. Right: The correlation between $\delta^{18}\text{O}$ and $\delta^{13}\text{C}$ is used to indicate deposition of calcite under isotopic equilibrium.

4.3.3 Stable isotopes of oxygen and carbon

The stable isotope ratios of oxygen and carbon are shown in Figure 4.11. The $\delta^{18}\text{O}$ values vary between -6 to -3‰, with fluctuations around a mean of -4.5‰. The oxygen and carbon data show dense points between 7.5 - 5.6 ka BP. This is owing to the age model, where the regularly spaced proxy record has been squeezed into a precise time frame. The values show a decreasing trend from 6.5 - 5.6 ka BP. This could be attributed to an increase in rainfall, which was also seen as increased growth rates for this section of the sample. The oxygen data also shows episodes of periodic ^{18}O enrichment. The $\delta^{13}\text{C}$ profile covaries with the $\delta^{18}\text{O}$ values. The remarkable decreasing trend from 6.5 - 5.6 ka ia also observed in $\delta^{13}\text{C}$ record. The episodes of ^{13}C enrichment replicate the corresponding dips in $\delta^{18}\text{O}$ values. Hence, we can assume that, $\delta^{13}\text{C}$ values of this stalagmite, respond to climate changes, and hold a potential for paleomonsoon reconstruction.

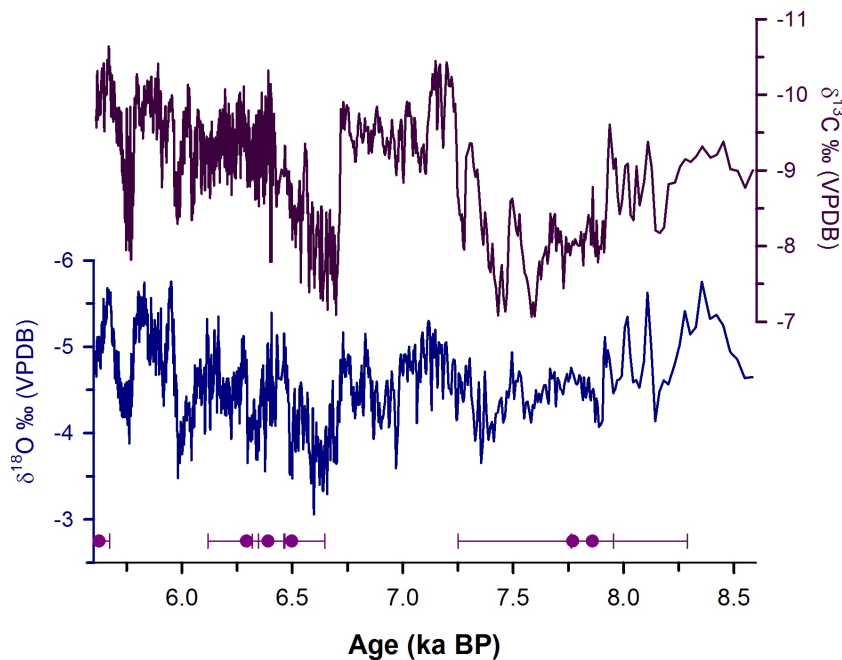


Figure 4.11: $\delta^{18}\text{O}$ (dark blue) and $\delta^{13}\text{C}$ (purple) timeseries of KOT-I stalagmite. The stalagmite was deposited between 8.4-5.6 ka BP. The ages considered in the model are shown as pink filled circles. The errors are reported as 2σ .

4.4 Tree Rings

In tropical regions of south and southwest Asia, good tree-ring data networks have been established to document monsoon variability. In this context, teak (*Tectona grandis*) from Indonesia, Thailand, Java and India have been demonstrated as a potential source for high resolution reconstruction of ISM [*Bhattacharyya et al.*, 1992; *Borgaonkar et al.*, 2010; *Buckley et al.*, 2007; *D'Arrigo et al.*, 1994; *Jacoby Jr et al.*, 1990; *Murphy et al.*, 1989; *Pant and Borgaonkar*, 1983; *Pumijumnong et al.*, 1995; *Shah et al.*, 2007].

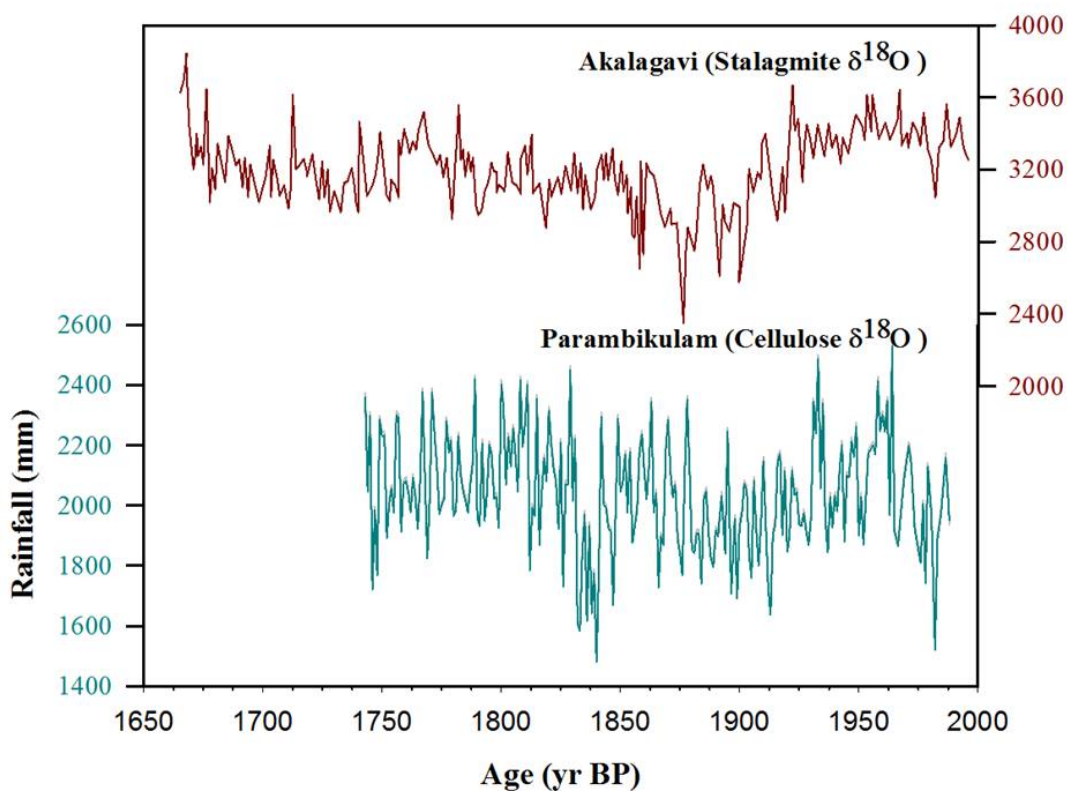


Figure 4.12: Monsoon rainfall reconstructed from Ulvi speleothem (top, *Yadava et al.* [2004]) and Parambikulam teak cellulose (bottom, *Managave et al.* [2011a]). Solid curves show the reconstructed values.

Managave et al. [2010, 2011b] showed that high resolution intra-ring analysis of $\delta^{18}O$ of cellulose from several annual growth rings of teak trees was very much useful in achieving a ~ 20 day resolution in the monsoon reconstruction. *Ramesh et al.* [1989] reported the correlation of stable isotopic ratio of hydrogen (δD) in teak with the amount of rainfall and mean maximum temperature to demonstrate its applicability for reconstruction of past climate. The lower panel of 4.12 shows the monsoon reconstruction for Parambikulam, Kerala for more than 2 centuries in the past (Managave et al., 2011). This can be compared with the three century long monsoon reconstruction for northern Karnataka (top panel of the same 4.12, locations shown in Figure 4.13) based on $\delta^{18}O$ variations in a stalagmite that had annual resolution.

4.5 Oceanic records

Contrary to terrestrial deposits, marine deposits preserve a more complete and continuous monsoon record. Extensive studies has been carried out on the evolution of the monsoon through the Holocene [*Sirocko et al.*, 1993; *Tiwari et al.*, 2011] using marine sediments. $\delta^{18}O$ variations recorded by foraminifera in marine sediment cores from the eastern Arabian Sea have shown a consistent increasing trend in the monsoon rainfall [*Sarkar et al.*, 2000] during the Holocene. Figures 4.13 and 4.14 shows locations and monsoon reconstruction from six sediment cores of Arabian sea.

All the oceanic records show consensus that there is a prominent reduction in the $\delta^{18}O$ values between $\sim 11 - 10$ ka BP. Core SK148/4 [*Rao et al.*, 2010] shows an abrupt enrichment between $\sim 8 - 4$ ka BP, while similar abrupt changes are observed in Core 3268G5 at 6 ka BP. The shaded gray regions in Figure 4.14 are Bond events in the Holocene numbered from 0 to 8. The event 3 by far is one of the most important and large event and is witnessed as a sharp enrichment in ^{18}O in 3268G5 and SK148/4 cores. In the rest of the cores, some discrepancy in

the trend exists, while event 1 famously known as the Little Ice Age is recorded in almost all the cores.

Although continuous, marine sediment cores lack the resolution to be able to distinguish small climate changes. And hence in this study the results from such sediment cores are to check for high amplitude variations in climate and study the evolution of monsoon on a millennial timescale.

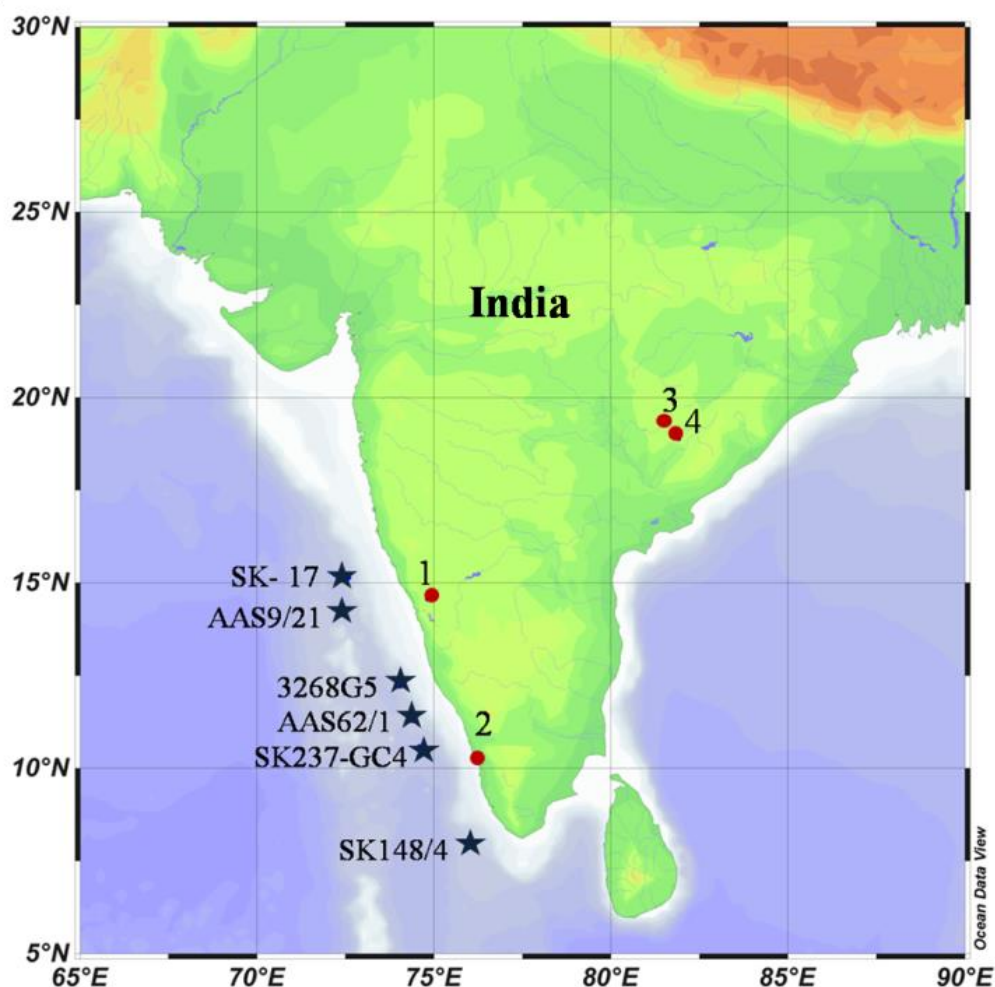


Figure 4.13: Locations of marine and terrestrial proxies. Stars are sediment cores. Core SK-17 [Singh et al., 2006], Core AAS9/21 [Govil and Naidu, 2010], Core 3268G5 [Sarkar et al., 2000], Core AAS62/1 [Kessarkar et al., 2013], Core SK237-GC4 [Saraswat et al., 2013], and Core SK148/4 [Rao et al., 2010]. Terrestrial proxies are (1) Akalagavi cave stalagmite [Yadava et al., 2004], (2) Parambikulam tree cellulose [Managave et al., 2011b], (3) and (4) are speleothems from the Dandak and Kotumsar caves [Yadava and Ramesh, 2005].

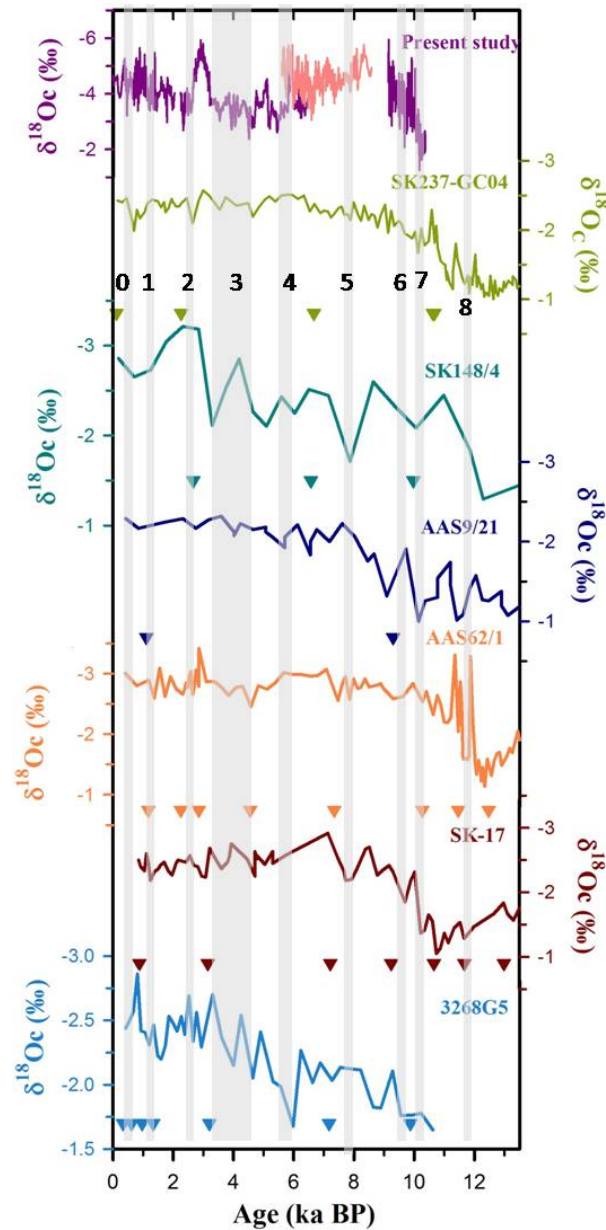


Figure 4.14: $\delta^{18}\text{O}$ variations of planktic foraminifera from six different cores from the eastern Arabian Sea (See Figure 4.13 for locations) during the Holocene, plotted with error bars (gray shaded regions). Inverted triangles represent ^{14}C ages of planktonic foraminifera from the respective cores. The sediment core records are compared with reconstructed monsoon variability from the Dandak (Pink) and the Kotumsar cave (light pink) stalagmites. Sources: (Rao et al. [2010], Cyan), (Saraswat et al. [2013], Green), (Govil and Naidu [2010], Dark blue), (Kessarkar et al. [2013], Orange), (Singh et al. [2006], Maroon), (Sarkar et al. [2000], light blue) Shaded gray regions are Bond events during the Holocene, numbered from 0 to 8 [Bond et al., 2001].

4.6 Discussion

A few speleothem studies around India vis-a-vis Qunf cave, and caves in China were used to explain the variability in ISM during the Holocene. So far, terrestrial records from the core monsoon region of India were fragmented and hence addressing the monsoon variability from the Indian region proved to be a challenge. On the other hand Chinese speleothems were used to reconstruct east Asian monsoon variability and establish a link between the climate changes at the high and low latitudes. However, more recently *Pausata et al.* [2011] based on the general circulation model postulated that chinese speleothem $\delta^{18}O$ excursions reflect changes in Indian Summer Monsoon than Heinrich events [*Johnson, 2011*]. The sensitivity test carried by *Pausata et al.* [2011] showed that Heinrich events led to cooling in northern Indian ocean and reduced the convective precipitation. As a result isotopically enriched moisture was carried across India and moisture rich in $\delta^{18}O$ were also carried over China. Accordingly, the positive excursion in the Chinese speleothems reflect variations in $\delta^{18}O$ value of moisture exported from India. *Pausata et al.* [2011], also suggests that speleothems from India are ideal for paleomonsoon reconstructions whereas, Chinese speleothems seem to record changes in the isotopic composition of the incoming water vapor. Considering that the Indian ocean plays a key role in precipitation over India and East Asia during June-August, the above postulation may hold true.

Hence it is extremely important to study Indian speleothems to reconstruct Indian monsoon and to understand the role of North-Atlantic circulation changes as one of the governing factors. With this as an objective, we have attempted to reconstruct high resolution ISM variability from CMZ of India. Our high resolution record from the Kotumsar and Dandak cave together, have provided monsoon record from ~ 10.5 ka - to the present with a brief hiatuses between $\sim 9 - 8.5$ ka BP and $\sim 2.2 - 2$ ka BP. The $\delta^{18}O$ profile is constructed using ~ 5040 subsamples and 15 U/Th ages.

The record extends from ~ 10.4 ka BP to the present. An overlap of the Kotumsar and Dandak- I profile between 7-6 ka BP. The region of overlap shows similar trend in monsoon. Our speleothem record, when compared with available monsoon records reconstructed from speleothems from Oman and China indicate, changes in Asian monsoon system comprising of ISM and EASM have similar variability. The caves which are in two separate domains of Asian monsoon, show similar trend in monsoon variability, proving it to be a robust climate signal.

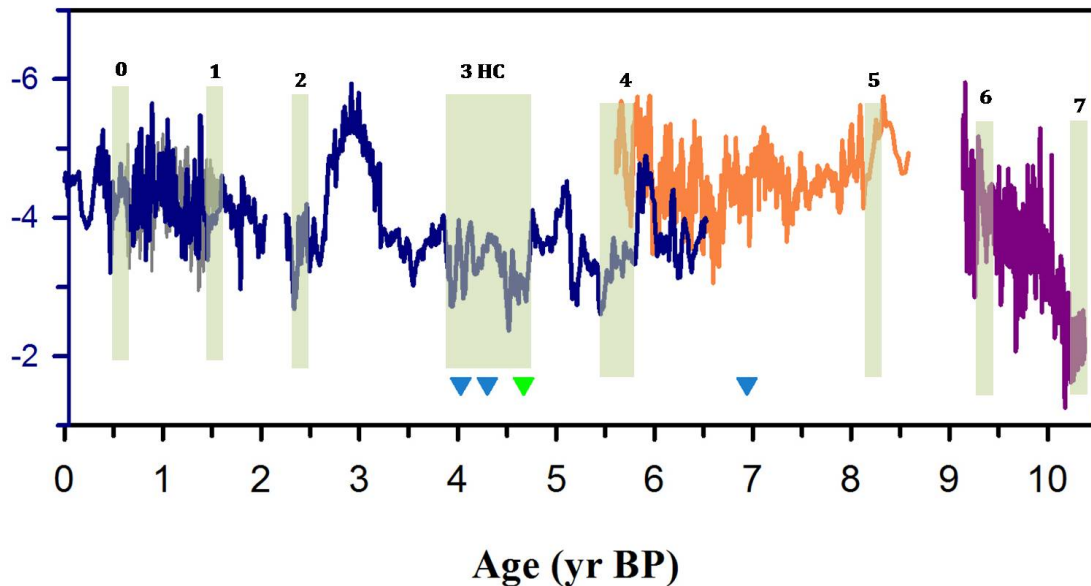


Figure 4.15: *Compiled Holocene monsoon record based on $\delta^{18}O$ variability in KOT-I, Dandak-I and II stalagmites. Blue and green triangles are the radiocarbon dates of charcoal derived from the Kotumsar and the Dandak caves, respectively. The green shaded regions are North Atlantic cooling events, known as 'Bond Cycles'. The event numbered 3, marks the culmination of the Harappan Civilization (HC)[Giosan et al., 2012].*

4.6.1 Early Holocene climate ($\sim 10.4 - 8$ ka BP)

The inception of the Holocene marks the rapid intensification of monsoon between 10.4 - 9 ka BP. Stronger monsoon is observed as a rapid decrease in $\delta^{18}O$ (around 5‰ depletion) values, and the record has a brief hiatus between $\sim 9-8.5$

ka BP (Figure 4.15). The strength of monsoon is also seen as a faster growth rate of the Dandak-II stalagmite. The increased monsoonal conditions were related to the Northward shift of ITCZ between $\sim 10.5 - 5.4$ ka BP, owing to the seasonality in the 21 ka precession cycle [Haug *et al.*, 2001]. By 11-10 ka BP, the insolation over the Northern Hemisphere rose 8% greater than today due to orbital precession that gradually aligned the boreal summer solstice with the perihelion [Ortiz *et al.*, 2000]. This early increase in the boreal summer radiation enhanced monsoonal circulation, which is also witnessed in the present study, and other available paleoclimate records (eg. [Foley *et al.*, 1994; Haug *et al.*, 2001]) also deduced from climate models [Prell and Kutzbach, 1987]. This record is in agreement with other speleothem records [Burns *et al.*, 2001; Neff *et al.*, 2001], Arabian Sea upwelling records [Overpeck *et al.*, 1996; Sirocko *et al.*, 1993] ice core data [Thompson *et al.*, 1989], and lake levels from India [Enzel *et al.*, 1999]. Comparison between the Qunf cave, Dandak-II and the GRIP ice core record (Figure 4.16) shows an increase in monsoon is in phase with the increase in the North Atlantic atmospheric temperature. Considering the error limits on the ages of the Dandak-II stalagmite, the cold events recorded in the GRIP core are witnessed as reduced monsoon precipitation at ~ 10.3 and 9.4 ka. This establishes a strong teleconnection between low and high latitude temperature changes. Contemporaneous changes in climate were observed in Africa, where the strength of eolian deposition reduced significantly [Ortiz *et al.*, 2000]. This time period is known as African Humid Period.

An abrupt increase in the monsoon was observed between $\sim 10 - 9.5$ ka BP in several other marine sediment cores (Figure 4.14) from the eastern Arabian Sea [Govil and Naidu, 2010; Kessarkar *et al.*, 2013; Overpeck *et al.*, 1996; Rao *et al.*, 2010; Saraswat *et al.*, 2013; Sarkar *et al.*, 2000; Singh *et al.*, 2006]. The increasing trend of monsoon rainfall during the Holocene is also confirmed by $\delta^{18}O$ variations in speleothems from Central India [Yadava and Ramesh, 2005]. Our record is correlatable with the Sanai lake record from Ganga plains. Both

these records agree with climatic optimum at $\sim 10.4 - 6$ ka witnessed by lake expansion and high prevalence of aquatic plants [Sharma *et al.*, 2004].

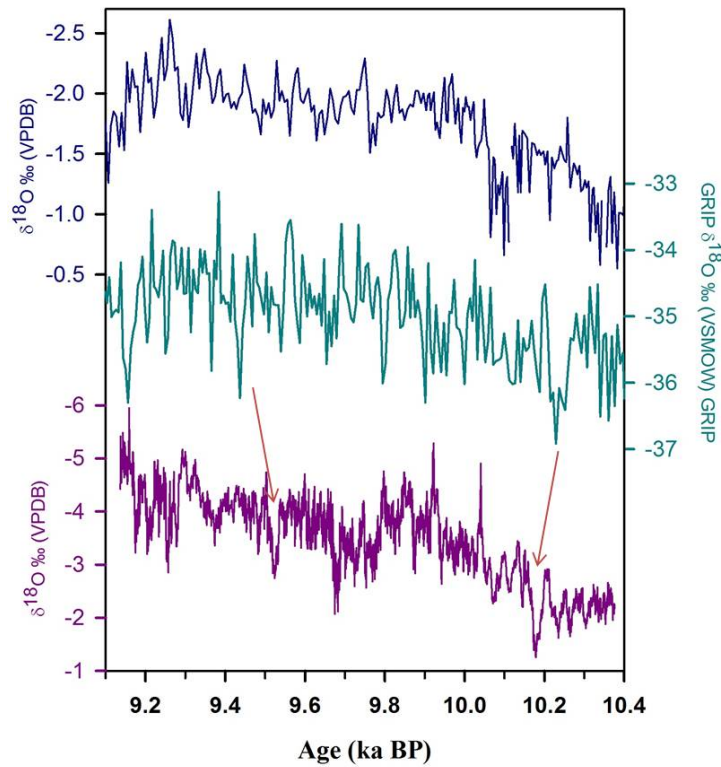


Figure 4.16: Comparison between Dandak- II stalagmite (Purple), GRIP ice core record (cyan, Dansgaard *et al.* [1993]) and Qunf cave (blue, Fleitmann *et al.* [2003].)

4.6.2 Mid- Holocene climate ($\sim 8 - 4$ ka BP)

Climate during the mid-Holocene was observed to change significantly. During this time air temperatures on land declined globally, the evidence of which is recorded clearly in ice cores (Greenland, Antarctica and eastern Canadian arctic) [Steig *et al.*, 1998]. In low latitudes the temperatures were lower or they experienced aridity. At many places, abrupt change in climate during the mid-Holocene is documented. In addition to temperature and precipitation changes, the mid-Holocene also experienced change in atmospheric and ocean circulation. To-

gether with these changes, the climate during this period was very different from the present conditions. *Steig* [1999] stated that Mid-Holocene climate changes are more complex and require high-resolution, high-quality studies from different localities. These changes are attributed to a steep decline in the Northern Hemisphere insolation at ~ 6 ka BP [*Charles et al.*, 1996; *Wright*, 1993]. Climatic events between 6000-5000, 4200–3800, 3500–2500 and 1200–1000 cal years BP were classified under "cool poles, dry tropics" pattern by *Mayewski et al.* [2004].

The monsoon intensity gradually decreased between 8 to 6 ka, the owing to southward shift of ITCZ and decreasing [*Fleitmann et al.*, 2003; *Haug et al.*, 2001; *Paillard et al.*, 1996] June-August insolation at 30°N . When the ITCZ shifts southwards, the land-sea temperature contrast decreases, leading to weakening of the monsoon. Weaker monsoon is also recorded in the Arabian Sea sediment core $\delta^{18}\text{O}$ values of *G.ruber* [*Singh et al.*, 2006] and abundances of *G.bulloides* [*Gupta et al.*, 2003] and in the lake records of Garhwal [*Srivastava et al.*, 2013]. The migration of ITCZ is also observed to affect the East Asian Summer Monsoon (EASM), the second domain of Asian monsoon, as recorded in the Dongge cave speleothem. The mid-Holocene witnessed widespread aridity in all the Asian monsoon domains [*Dykoski et al.*, 2005; *Fleitmann et al.*, 2003; *Sharma et al.*, 2004; *Wang et al.*, 2005]. A few studies report the onset of aridity as a gradual mechanism [*Fleitmann et al.*, 2003, 2007; *Gupta et al.*, 2003; *Ivanochko et al.*, 2005; *Overpeck et al.*, 1996; *Wang et al.*, 2005], while others infer it to be an abrupt event [*Anderson et al.*, 1988; *Gasse and Van Campo*, 1994; *McClure*, 1976; *Morrill et al.*, 2003; *Sarkar et al.*, 2015]. Our record shows, an abrupt decrease in the monsoon between $\sim 6 - 3.5$ ka BP, with the driest period between $\sim 4.7 - 4$ ka BP (Figure 4.15). *Fleitmann et al.* [2003], who are in favor of a gradual decline, have argued that the abrupt signal recorded in the African and Indian monsoon proxies is on account of nonlinear response of ISM. High-amplitude fluctuations in the monsoon precipitation may induce sudden negative precipitation minus evaporation(P-E) balance, leading to the drying of a lake. This argument may

hold true, for the lake records, however, speleothems from core ISM regions are less susceptible to such changes and are likely to preserve a better climate signal. [Morrill et al. \[2003\]](#), on the other hand believe that such abrupt changes in the monsoon are due to abrupt events in the external forcings or in natural or internal fluctuations of the monsoon system. External forcings including insolation and volcanic eruptions, whereas internal fluctuations include the North-Atlantic thermohaline circulation and El-Nino. During the Holocene, a gradual decrease in insolation is observed and hence can not be the sole factor in controlling the monsoon. [Turney et al. \[2005\]](#), concluded that centennial to millennial changes in the North Atlantic Climate are not solely driven by insolation. Hence the abrupt decrease in monsoon may have two possible influences. The first being the abrupt change in the North-Atlantic thermohaline circulation. The sensitivity of monsoon system to the North Atlantic changes is evidenced as effect of the short term Bond events on the weakening of the ISM. And the second plausible explanation could be sudden failure of internal feedback mechanisms governing monsoon leading to a sudden decline in the monsoon intensity. The factors governing abrupt changes in ISM in the core monsoon region of India, requires further investigation. [Ortiz et al. \[2000\]](#) and [Claussen et al. \[1999\]](#), explained such abrupt changes observed in the African monsoon as occurring due to vegetation-albedo positive feedback amplifying the insolation-driven changes in the monsoonal climate.

Our record shows a close resemblance to the High resolution Holocene precipitation from the stalagmites from the Qunf cave, Oman [[Fleitmann et al., 2003](#)], the Dongge cave, China [[Dykoski et al., 2005](#); [Wang et al., 2005](#)], titanium concentration record from the Carioaco basin [[Haug et al., 2001](#)], suggesting role of shift of ITCZ in controlling the low-latitude climate variability (Figure 4.17). The intensity of monsoon over India increased post 3.5 ka.

When sampling, evidences of controlled fire preserved as burnt earth and patches of charcoal mixed with soil and grasses in the form of three distinct layers in the Kotumsar and one layer in the Dandak cave were found [[Yadava and](#)

[Ramesh, 2007](#)]. Such deposits indicate sporadic human inhabitation. Radiocarbon dating of these layers narrow down such possible human activity to be between $\sim 6.9-4$ ka BP in the Kotumsar cave and ~ 4.6 ka BP in the Dandak cave (Figure 4.18). The samples were studied under a stereo binocular microscope and three grasses and two millet species were identified by previous workers [[Yadava et al., 2007](#)]. The grasses were *Cenchrus L.*, *Celosia argentea L.* and *Panicum L.* and the millets were identified as foxtail. By the mode of preservation, it can be inferred that millets were important for the sustenance of the Kotumsar cave-dwellers. Millets are drought tolerant crops, and suitably grow in low rainfall regions. Archaeo-biological researches carried out at 45 archaeological sites in India have revealed that millet cultivation began as early as 5.3 ka BP [[Pokharia et al., 2014](#)]. The radiocarbon ages of the charcoal deposits fall in the same range as that of the formation of KOT-I and Dandak-I stalagmites, suggesting that the caves were used as shelters during severe droughts. During one of the visits made to the Kotumsar cave in CE 2000 (wet season), it was observed that the cave entrance was inaccessible as the rain water was gushing out through the cave mouth. However, the entrance was dry and accessible during the pre-monsoon and winter. As seen in Figure 4.18, the strength of the monsoon declined between $\sim 6 - 3.5$ ka. The drought like conditions would have made caves accessible during these periods. Based on this, it can be postulated that the caves were used as a temporary dwelling and food storage site, during the weaker/drier phases of monsoon. Widespread aridity is also considered as a reason for the collapse of contemporaneous major civilizations like the Harappan, Chinese and Mesopotamian. Evidence of Indus valley suggests that, as the intensity of ISM decreased significantly, from ~ 5 to 4 ka (~ 6 to 3.5 ka, in the present study), the type of agriculture shifted towards Kharif (summer) crops, and drought tolerant crops such as millets [[Clift et al., 2012](#); [Giosan et al., 2012](#); [Weber and Belcher, 2003](#)].

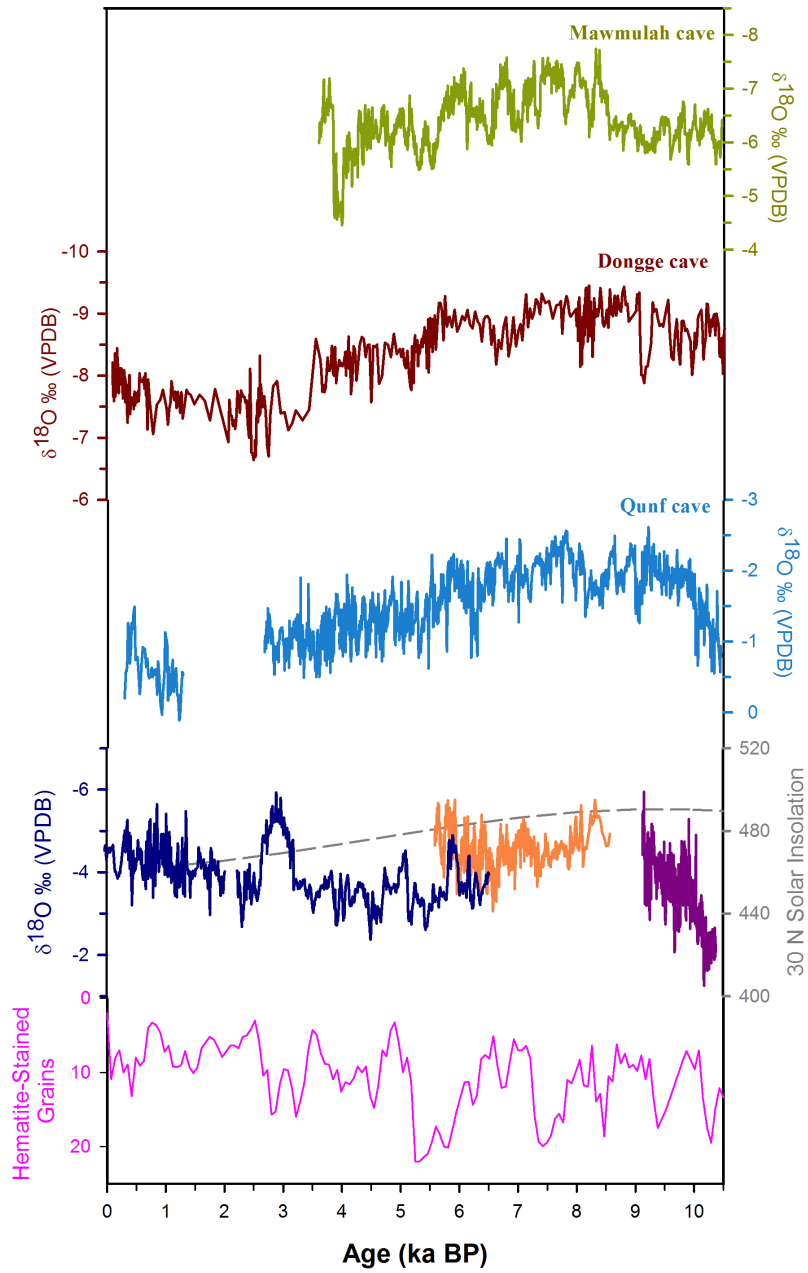


Figure 4.17: $\delta^{18}\text{O}$ records of the Mawmulah cave (Green, *Berkelhammer et al. [2012]*), the Dongge cave (red, *Dykoski et al. [2005]*), the Qunf cave (blue, *Fleitmann et al. [2003]*), the present study (Dark blue), and hematite-stained grains (pink, *Bond et al. [2001]*).

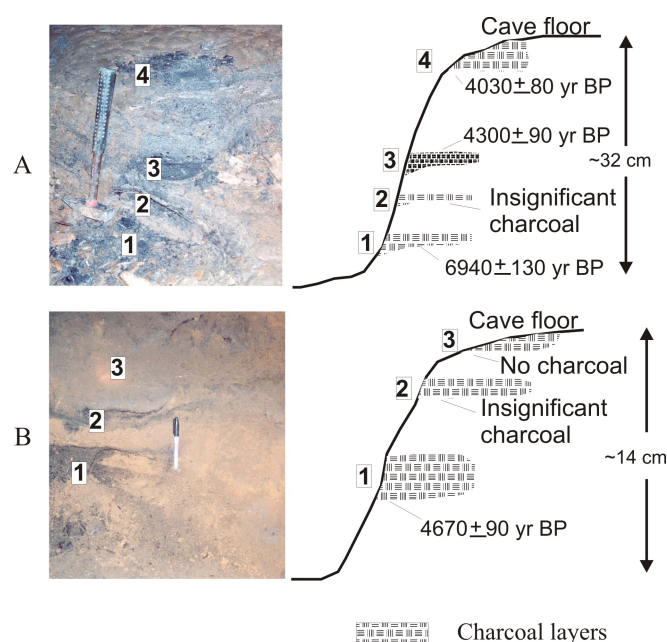


Figure 4.18: Charcoal layers preserved in sediments of Kotumsar cave (A) and Dandak cave (B) Photo taken from *Yadava and Ramesh [2007]*.

4.6.3 Late Holocene climate (~ 4 - to the Present day)

According to the observations made by *Ponton [2012]*; *Ponton et al. [2012]* and *Sarkar et al. [2015]* the monsoon intensity decreased from 4.8 ka - to the present. Their interpretation is based on $\delta^{13}C$ of leaf wax and interpreted in terms of C3/C4 type of vegetation, whereas, all other records [*Breitenbach, 2010*; *Chauhan et al., 2010*; *Fleitmann et al., 2003*; *Govil and Naidu, 2011*; *Staubwasser and Weiss, 2006*], including the present study, are based on interpreting $\delta^{18}O$ values of proxies which are direct recorders of monsoon. These records show consensus that monsoon increased post 2 ka BP. Speleothem studies from Socotra island, show a depletion of 2‰ from ~ 4 ka to the present, implying that the monsoon increased during late Holocene [*Fleitmann et al., 2007*]. As seen in Figure 4.15, $\delta^{18}O$ record between 3.8 - 2.8 ka BP is anomalously depleted, a feature not seen in other records. The effect of moisture source change from Arabian Sea to the Bay of Bengal, causes a depletion of ~ 1 ‰ and therefore is insufficient to explain

the $\sim 2.5\text{‰}$ decrease in $\delta^{18}\text{O}$ values. Hence, this can either be explained as a local intensification of monsoon or an effect of both these parameters. Figure 4.19 shows reconstructed ISM for the last 2000 years. These records are compared with annually deposited Jhumar [Sinha et al., 2011] and Dandak [Sinha et al., 2007] speleothem records. The sharp troughs recorded in our study correspond to the troughs in Jhumar speleothem at a different time interval. This shift is mainly due to the different age models used to reconstruct the data. The age model for Jhumar cave is reconstructed based on counting of annual layers, whereas our age model was reconstructed based on U-Th ages with associated errors. However, barring this small shift, the monsoonal trends in both the records covary and record major climate events.

Two most important climate events of the early Holocene were the Medieval Warm Period and the Little Ice Age, affecting most of Europe. These high latitude climate changes also affected tropical ocean surface temperature and the monsoon rainfall [Newton et al., 2006]. Based on historical records, the most recent cooling period in the Holocene known as the 'Little Ice Age' occurred as two discrete events [Jones, 1995]. High resolution Greenland ice core $\delta^{18}\text{O}$ records reconstructing surface temperatures, suggest the occurrence of these discrete events centered at ~ 1500 and 1850 A.D [Dahl-Jensen et al., 1998]. Our record shows evidence of these events as abrupt decline in monsoon between 1550-1450 AD and 1350-1250 AD (as shown in Figure 4.19 with arrows). Corresponding ^{18}O depletion is also observed in the Jhumar cave $\delta^{18}\text{O}$ record. Sinha et al. [2007] have inferred a 30% reduction in rainfall in 14th century. Historical records during this period report several famines and droughts. The major documented drought events coincide (within the dating uncertainty) with a period of reduced rainfall reconstructed from the Dandak stalagmite [Maharatna, 1996; Pant et al., 1993]. The Durga Devi famine (1396 A.D. to 1409 A.D.) [Maharashtra-Government, 1973] coincides with the first positive excursion of LIA. Multiproxy records from the Arabian Sea sediment cores [Agnihotri et al., 2002; Gupta et al., 2003; von

Rad et al., 1999], Stalagmite $\delta^{18}O$ [*Burns et al., 2002; Fleitmann et al., 2007*] records of Oman and Yemen also indicate a weaker monsoon during LIA and a stronger monsoon during MWP.

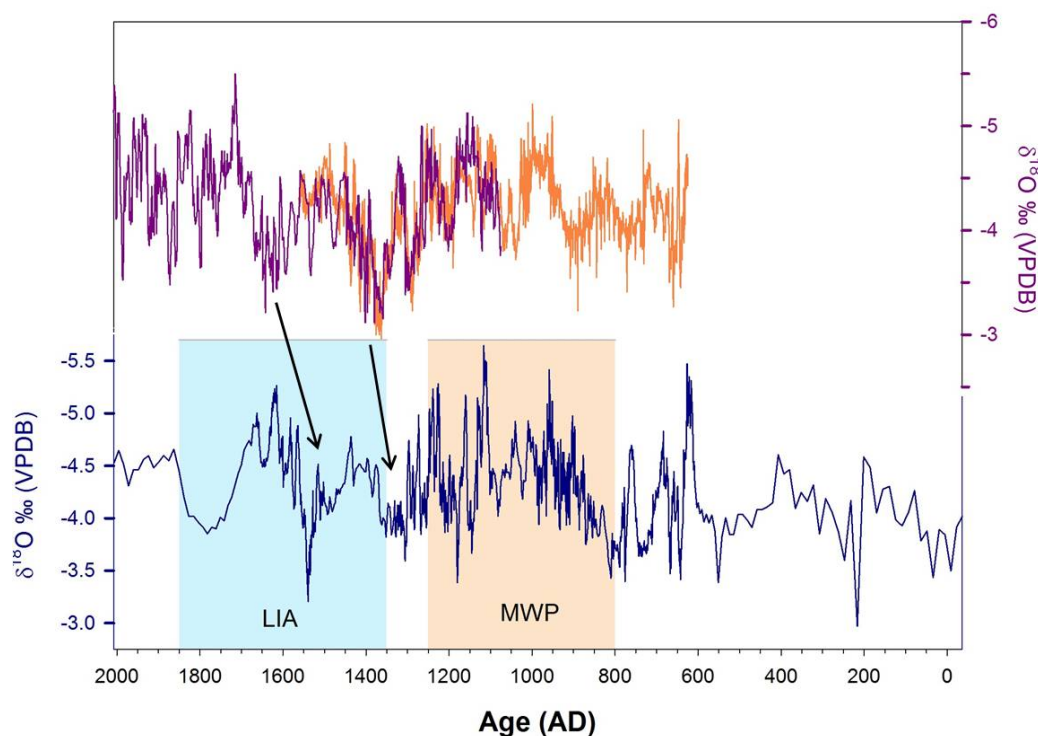


Figure 4.19: The $\delta^{18}O$ time series of Jhumar speleothem (purple, *Sinha et al. [2011]*), Dandak speleothem (Orange, *Sinha et al. [2007]*), and the present study (Blue). The shaded light blue and red blocks bracket periods of Little Ice Age and Medieval Warm Period respectively. The arrows point to the corresponding events in the Jhumar cave reconstructions. The shift in the timeseries is due to two different methods adopted to reconstruct age models.

Modern observations link weaker monsoon on land to enhanced convection in the eastern equatorial Indian Ocean (EEIO) [*Krishnan et al., 2006*]. *Sinha et al. [2011]* proposed the controlling factors of such Mega-drought events to be seasonal dynamics of the ITCZ in the EEIO. The southward migration of ITCZ in the Indian ocean prompts enhanced convection over the EEIO, which suppresses the convection and rainfall over India. Since the end of LIA, monsoon intensity has increased in 19th and 20th century, and entered an "active" phase of mon-

soon as described by *Sinha et al.* [2011]. The monsoon reconstruction based on Dandak-I stalagmite sample for 19th and 20th century is obscure and has low resolution owing to the errors in the age model. Recourse is taken to comprehensive tree ring studies to understand the climate change during this time period. *Shah et al.* [2007], based on tree ring width index of Hoshangabad observed several low rainfall years: AD 1835–1849, 1872–1896, 1908–1929, and 1952–1971. Comparison between $\delta^{18}O$ of annually resolved speleothem from Akalagavi cave and the Hoshangabad tree ring data shows that the monsoon rainfall increased from AD 1860 to 1940 reconstruction [*Shah et al.*, 2007]. Whereas tree ring studies from Parambikulam, Kerala [*Bhattacharyya et al.*, 2007] reveal there were several multi-decadal events of low and high precipitation in the last 1000 years. AD 1743–62, 1794–1806, 1815–26, 1831–51, 1856–76, 1937–56 were observed to be low rainfall events alternating with high rainfall events at AD 1763–93, 1807–14, 1827–30, 1852–55, 1877–1936, 1957–77 and 1995–98. However, most of these fluctuations were observed till the end of 19th century and the 20th century is inferred to be remarkably warm with higher rainfall [*Bhattacharyya et al.*, 2007].

4.6.4 Global teleconnections

Understanding the Holocene climate variability is of prime importance, and the teleconnection between high-latitude and low-latitude climate changes. If solar forcing is the main cause of climate change, then the tropics receiving large amount of radiation, are the hotspots for capturing the signal and communicating the amplified signal to higher latitudes through different mechanisms of heat transports [*Yin and Battisti*, 2001]. Superimposed on these long-term variations, are the millennial scale changes that can not be explained using only orbital parameters (e.g., *Gupta et al.* [2003]). Such millennial scale variations are partly attributed to abrupt changes in the North Atlantic, European and Eurasian climate, on the basis that increase in winter snowfall over Eurasia leads to a weaker monsoon over Asia the following summer [*Barnett et al.*, 1989; *Gupta et al.*, 2003;

[Meehl, 1994](#)].

The North Atlantic changes are mainly witnessed as large scale climatic events known as 'Daansgard-Oeschager' cycles during the last glacial period and 'Bond events' during the present interglacial period. The Bond events were reported in the cores raised from the North Atlantic Ocean and were observed to recur at intervals of 1470 ± 500 years. These episodes, preserved as ice rafted debris are linked to sudden cooling of ocean surface water, brought about by changes in the North Atlantic surface circulation [[Bond et al., 1997](#)]. These ice rafting deposits are related to change in the thermohaline circulation due to a southward shift of cooler ice-bearing surface water into the North Atlantic and its coupling with the Greenland atmospheric circulation changes [[Bond et al., 1997](#)]. However, the constant pacing of these events is not controlled by ice sheet oscillation directly and the forcings governing the millennial scale changes are still to be identified. The coeval increase of the North Atlantic temperature with increase in monsoon precipitation between 10.4 -9 ka (Figure 4.16), along with the evidence of Bond events (10.3 and 9.4 ka) in the core monsoon region of India, confirms the strong link between the two. The evidence of such a relation is also reported in a speleothem from the Qunf cave [[Fleitmann et al., 2003](#)] and Arabian Sea sediment cores [[Overpeck et al., 1996](#); [Schulz et al., 1998](#); [Sirocko et al., 1993](#)]. [Fleitmann et al. \[2007\]](#), relate the 9.4 ka event to the outburst of melt water, resulting in the weakening of thermohaline circulation and the subsequent cooler North Atlantic temperatures. Such temperature changes are also observed in Greenland ice core records NGRIP, GRIP [[Johnsen et al., 2001](#)]. The Greenland temperature oscillations reconstructed from ice cores, have a direct impact on the climate variability in Northern and Central Europe, with concomitant changes in ISM. The important feature of GISP-2 and GRIP $\delta^{18}O$ records is relatively smaller fluctuations during Holocene, implying no significant changes in temperature during the past 10 ka BP. However, a 300 yr running mean of bidecadal $\delta^{18}O$ values show low frequency climate changes [[Schulz and Paul,](#)

2002],

The winter cooling and concomitant increase in the Eurasian snow cover led to weakened monsoon circulation through the well-known snow cover- monsoon linkage (e.g., [Barnett *et al.*, 1988; Ye and Bao, 2001]). Due to the extensive snow cover over western Eurasia, spring heating of the landmass is reduced on account of high albedo and high energy consumed in exhumation of excess snow. The reduction in land - sea pressure gradient due to the cooling of the Tibetan plateau in summer leads to weaker summer monsoon. The reduced pressure gradient also affects the strength of cross-equatorial current, which is the predominant source of moisture and heat.

ISM not only responds to the North Atlantic changes during the glacial period, but also has a huge impact on centennial and millennial timescales. Abrupt Holocene cold spells of North Atlantic correspond to a weaker monsoon over India (Figure 4.18 [Bond *et al.*, 1997]). Bond events, in mid- and late Holocene (0 to 4) are more prominent than the events 5 - 7 (Figure 4.15). Widespread aridity is observed between 6 - 5.2 and 5 - 3.9 ka BP. The major event 3, which marked the decline of major civilizations such as the Harappan, the Neolithic culture of central China and the Akkadian empire in Mesopotamia $\sim 5-3.5$ ka BP is related to strong aridity over India [Giosan *et al.*, 2012; Kenoyer, 1998; Possehl, 2002], western china [Wenxiang and Tungsheng, 2004] and western Asia, respectively [DeMenocal, 2001]. This implies that subtle changes in North Atlantic Climate may have significant impact on ISM.

To sum up, some hypotheses proposed by previous workers about continuous increase or decrease of monsoon throughout the Holocene have failed to explain the observed variability in the present study. According to our observations, the monsoon over India increased rapidly with rising insolation followed by a gradual decrease in monsoon between 8-6 ka BP. However, post 6 ka BP, an abrupt decline in monsoon is observed possibly as the feedback mechanisms accentuated the forcing factors leading to the failure of response of the monsoon system.

Between 3.5 - 2.5 ka BP prominent increase in monsoon, comparable to present, is observed. In spite of insolation being minimum at present, strengthening of monsoon is seen from 2 ka to the present, suggesting, on a millennial timescale, the ISM intensity is controlled by other factors, along with insolation.

Chapter 5

Late Pleistocene monsoon variability

The Pleistocene epoch is known for several glacial-interglacial events and contemporaneous marine, fluvial, lacustrine deposits [*Kay, 1931*]. The Pleistocene ended with last glacial event at 11.7 ka. It is convenient to describe Pleistocene climate variability in terms of Marine Isotopic Stages (MIS) or Glacial-interglacial events. In the present study an attempt has been made to explain ISM variability during different MIS and glacial-interglacial events.

Marine isotope stages (MISs) or Oxygen isotope stages (OISs) are the alternate glacial-interglacial events marked on $\delta^{18}O$ variations observed in sediment cores from the ocean. They form the standard stratigraphic scale and are used extensively to correlate Quaternary (i.e. the last ~ 2 million years) climatic events. Seven Marine Isotopic Stages comprising of two complete glacial cycles (190-80 ka and 80 ka to present) span the past 200 ka. The Indian monsoon generally responds to interglacial/glacial events either by intensification/weakening of its strength. A majority of reconstructed monsoon records for the past 200 ka derive from marine sediment cores. They preserve the complete and continuous Quaternary monsoon records. Terrestrial records on the other hand are discontinuous, as preceding glacial evidences could be wiped out by the follow-

ing interglacial event. Although oceanic record is complete, continuous and well dated, it records the strength of the monsoon winds or ice volume rather than a direct measure of past precipitation except in the coastal regimes. Terrestrial proxies, on the other hand, record changes in monsoon precipitation. A significant amount of work has been done to reconstruct monsoon rain using aeolian, fluvial, lacustrine and peat deposits. The present study focuses on reconstructing late Pleistocene ISM variability based on a speleothem records from the Kailash and the Belum caves and a sediment core from the Andaman Sea, a literature data.

5.1 Terrestrial records

Although the oceanic record is complete, continuous and well dated, some of the proxies used record the strength of the monsoon winds rather than a direct measure of past precipitation. ISM strength is not linearly correlated with strength of wind, instead it depends upon the moisture carried by the winds depending on the SST in the southern hemisphere and rate of ascent of the parcels after they cross Indian coasts [*Rashid et al., 2007*]. Terrestrial proxies, on the other hand, record changes in monsoon precipitation. A significant amount of work has been done to reconstruct monsoon rain using aeolian, fluvial, lacustrine and peat deposits. Figure 5.1 shows such locations where extensive work has been done to reconstruct past climate. Fluvial sediments of the Sabarmati and Mahi Rivers on the southern margin of the Thar Desert are repositories of monsoon records for past 130 ka. Enhanced monsoon conditions during the MIS 5 (sub-stages e, c and a) interglacial period are seen as fine flood plain deposits on river banks. The cooler phases of MIS5-d(120-100ka) and MIS4 (74-60ka), when monsoon weakened, this signal is well represented by braided river facies [*Juyal et al., 2006*]. During Last Glacial Maximum (comprising MIS-2), extreme weakening of the monsoon is seen, where the fluvial sedimentation is replaced by aeolian (i.e.

wind-blown) deposition. The complete sequence was incised in the beginning of the Holocene, when monsoon regained its strength.

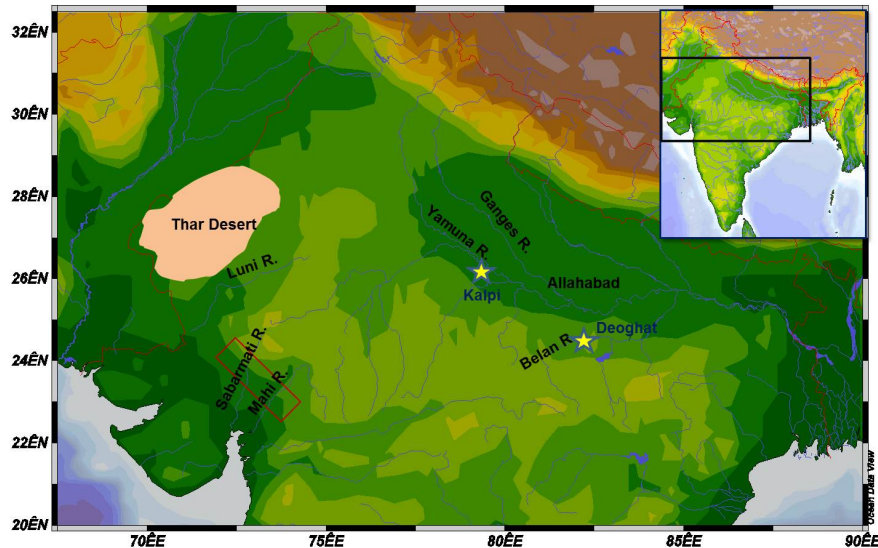


Figure 5.1: Locations of different terrestrial records from the core monsoon region of India. Image source: Ocean data viewer

Another core raised from the Luni River flowing through the Thar Desert shows that below the present aeolian sand sequence lies fluvio-aeolian deposits of the Quaternary. Sedimentary succession has recorded sequences covering duration of MIS-5 to MIS-1 and suggests a strong climatic control on the depositional environment. The glacial-interglacial cycles are in phase with the arid-humid cycles [Jain *et al.*, 2005; Kar *et al.*, 2001]. Humid phases are represented by gravel bed deposits (MIS-5 and 1) and reddening event (MIS-3). On the other hand, arid phases are represented by ephemeral sand-bed streams and aeolian deposits (MIS-2 and late MIS-3). Records from the Thar Desert and marginal areas exposed sequence of aeolian deposits covering past 200 ka. Wetter spell is recorded in the beginning of 200 ka followed by arid phase which shows extensive calcretes, sand dunes accumulation and playa formation [Dhir *et al.*, 1999, 2004]. Intense drying episodes are seen around 115 and 100 ka (colder sub-stages of MIS-5), 75 ka (MIS-4), and between 30-25 ka suggesting increase in aridity [Singhvi and

[Kar, 2004](#)]. Interesting finding by these authors is that during the LGM strong aridity was found in the Thar Desert, however aeolian activity was less. This is because even though the climate was arid, the of the strength summer monsoon wind responsible for dune building was weak and hence aeolian aggradation could not take place. This observation is also supported by studies carried out on marine sediment cores [[Sirocko et al., 1993](#)]. Intensification of monsoon is seen post LGM as stabilization of dunes and formation of paleosol layers during ‘climatic optimum’ (7-6 ka). Carbon isotopes in calcretes, soil and groundwater carbonates, derived from the Thar Desert sediments, have shown similar climatic fluctuations. C4 plants (grasses) were dominant during 70-60ka and 25ka (MIS-4 and 2) indicating weakened phase of monsoon, and their abundance reduced during enhanced phase of monsoon at around 60-25 ka, a time covering MIS-3 [[Andrews et al., 1998](#)]. Flood plain aggradation in Himalayan deposits at around 96-84 ka years (MIS-5) is an indicator of enhanced monsoon precipitation [[Sanyal and Sinha, 2010](#); [Suresh et al., 2007](#)]. Sediment core (Kalpi) along the Yamuna river channel and the Belan section, shows major floodplain aggradations in the Ganga plains during MIS 5 and 3. Relative dry phase of MIS-2 is seen as accumulation of aeolian and lacustrine deposits and by events of pedogenesis [[Gibling et al., 2005, 2008](#)]

5.1.1 The Kailash cave stalagmite

U-Th ages

$\delta^{18}O$ timeseries of Kailash cave samples is based on two U-Th ages shown in Table 5.1. Preliminary age model is constructed using ages of the top and bottom layers of the stalagmite. The sample was sent to the University of Taiwan for determining ^{230}Th ages for intermediate sampling intervals. Final age model will be constructed on procuring all the ages. However, timeseries based on a youngest and oldest ages, the sample growth is constrained between 13900 - 13400 yr BP

(Figure 5.2). The Kailash stalagmite grew at the rapid rate of ~ 1 mm/yr for ~ 500 years. The sample has several distinct growth bands, presumably annual in nature. The annual nature of the bands can be proved only after establishing the final chronology.

Stable isotopes of oxygen and carbon

The $\delta^{18}O$ values of the Kailash cave timeseries fluctuates between -3‰ to -0.5‰ from 13900 - 13450 years BP (Figure 5.3). A prominent ^{18}O depletion is observed post 13427 yr BP for only four years (13427 - 13423 yr BP) after which the sample growth had stopped. Repeat measurements were carried out for the same section twice and the analysis reproduced the same trend, hence the sudden ^{18}O depletion can not be treated as an artifact and indeed indicates a climate signal. A similar ^{13}C depletion is also observed in $\delta^{13}C$ record of the stalagmite, hinting at sudden change of climatic conditions. The record also shows periodic peaks of enriched ^{18}O values with corresponding enrichment in ^{13}C .

Table 5.1: Uranium and Thorium isotopic compositions and ^{230}Th ages of the subsamples of Kailash cave stalagmite. All errors are absolute 2σ values.

| Sample | ^{238}U (ppb) | ^{232}Th (ppt) | $^{230}Th/^{232}Th$ activity ratio | $^{230}Th/^{238}U$ activity ratio | measured $\delta^{234}U$ (‰) | initial $\delta^{234}U$ (‰) | uncorrected age Yr BP | corrected age Yr BP |
|-------------------|--------------------|---------------------|--|---|------------------------------------|-----------------------------------|-----------------------------|---------------------------|
| KLSH-1 (8.8mm) | 151.82 ± 0.16 | 515.3 ± 3.8 | 0.16985 ± 0.00090 | 825 ± 7.5 | 451.0 ± 2.3 | 468.4 ± 2.4 | 13492 ± 79 | 13430 ± 85 |
| KLSH-2 (530mm) | 899.25 ± 0.99 | 2205.3 ± 8.8 | 0.17647 ± 0.00093 | 1186.5 ± 7.7 | 459.6 ± 2.4 | 478.0 ± 2.5 | 13960 ± 82 | 13916 ± 84 |

The degree of detrital ^{230}Th contamination is indicated by the $^{230}Th/^{232}Th$ atomic ratio instead of the activity ratio. Age corrections for samples were calculated using an estimated initial atomic $^{230}Th/^{232}Th$ ratio of 4 ± 4 ppm. Decay constants are $9.1705 \times 10^{-6} yr^{-1}$ for ^{230}Th , $2.8221 \times 10^{-6} yr^{-1}$ for ^{234}U [Cheng et al., 2013], and $1.55125 \times 10^{-10} yr^{-1}$ for ^{234}U [Mattinson, 2000].

Discussion

Although several studies focus on variability of ISM since the last deglaciation, the information is poorly resolved to address centennial climate variability of a particular event. The present study is intended to focus on decadal and centennial scale variability during 'Bolling-Allerod' event. Role of the North-Atlantic climate fluctuations effecting Indian ocean circulation and thereby influencing ISM was explained in the previous chapter.

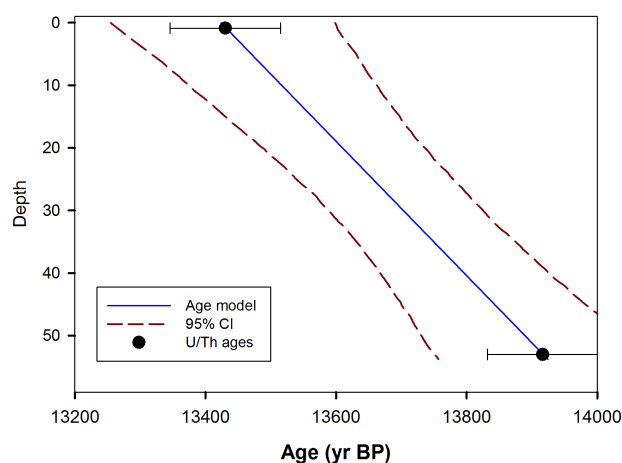


Figure 5.2: Age model of the Kailash stalagmite reconstructed using COPRA-interactive program on MATLAB [Breitenbach et al., 2012]. The filled black circles are ^{230}Th ages of topmost and bottom layers of the sample. The errors are reported in 2σ . The dashed lines show 95% confidence intervals and the blue line is the median through which the age model passes.

The sample growth is coincident with the warm and moist interstadial, known as 'Bolling-Allerod warming' in the last glacial period. Two stage oscillations are observed in this period. Bolling oscillation (peaked at 14.5 ka) and Allerod oscillation (peaked at 13 ka) were separated by older dryas. The $\delta^{18}\text{O}$ timeseries shows several fluctuations with prominent isotopic enrichment between 13.7 - 13.5 ka, indicating lower rainfall during older dryas. As in the Dandak and the Kotumsar caves, the $\delta^{13}\text{C}$ profile shows coeval changes with the $\delta^{18}\text{O}$ values implying that in extreme low precipitation conditions, even $\delta^{13}\text{C}$ values could

preserve a possible climate signal.

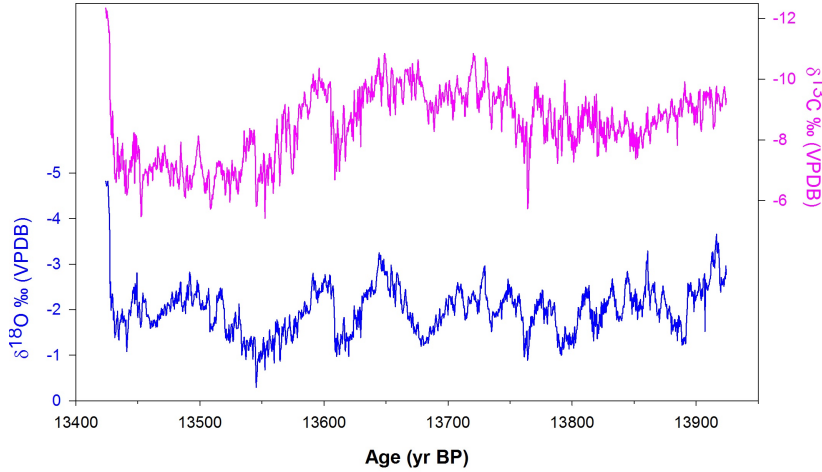


Figure 5.3: $\delta^{18}O$ and $\delta^{13}C$ timeseries of the Kailash cave stalagmite.

The abrupt depletion of $\delta^{18}O$ values at 13.3 ka followed by cessation of sample growth indicates higher precipitation coinciding with the peak of the Allerod oscillation. The sample deposition post this increase in rainfall stopped either due to the localized flooding at the sampling site or a high rate of drip water flow impeding calcite precipitation. A core raised from Bay of Bengal shows an increase in rainfall from 15.8 to 12.8 ka with concomitant increase in SST by 1.4°C [Govil and Naidu, 2011]. Kudrass *et al.* [2001]; Rashid *et al.* [2007] also observed that the Andaman Sea received more outflow from Irrawaddy river at 13.8 ka than at present. The increase in monsoon is also reported in Sanai Tal lake records from Ganga plains. The increase in monsoon around ~ 13 ka led to the expansion of lake and submergence of existing marshy lands [Sharma *et al.*, 2004].

Sinha *et al.* [2005] observed that $\delta^{18}O$ values of modern speleothem precipitate overlap with that of the deposits during the Bolling-Allerod event, implying that similar monsoon conditions prevailed during both the periods. The increase in rainfall during Bolling-Allerod is coincident with the increase in insolation after the last deglaciation. A speleothem record from the Timta cave [Sinha

et al., 2005], suggested a 60 years periodicity in ISM precipitation, during the late Bolling-early Allerod. Addressing such decadal variability in monsoon is possible only after a better chronological control is established for the sample.

5.1.2 The Belum cave stalagmite

The Belum cave receives an annual rainfall of 500 mm (Figure 5.4) of which 66% occurs during ISM (June to September) and 16% occurs during the withdrawing phase of the ISM (October). To understand the moisture sources contributing to the rainfall during the wet season (June to October), we carried out a Lagrangian back trajectory analysis using the HYSPLIT model [*Stein et al.*, 2015] with NCEP Reanalysis-1 [*Kalnay et al.*, 1996] as input to the model. We chose all the days with daily rain above 2 mm during 10 years (1998 to 2007 CE) for analysis. During ISM, trajectories suggest that the Arabian Sea is the major source of moisture, while during October, it is the mixture of the Arabian Sea and the Bay of Bengal (Figure 5.5). However, the major portion of annual rainfall is obtained from the Arabian Sea moisture, and the vapor reaching the cave is the remnant of the rainfall that occurred in the north-south oriented rainfall belt across the Western Ghats. Hence, the rainfall isotopic composition over the Belum cave is likely to reflect the rain out over the Western Ghat region. Since the actual measurement of rainfall isotopic composition from the cave is not available, we used the data from an isotope-enabled general circulation model, IsoGSM [*Yoshimura et al.*, 2008], in which the wind fields are constrained to observation (NCEP Reanalysis-2, *Kanamitsu et al.* [2002]) using the nudging technique. IsoGSM shows very good skill in predicting the spatio-temporal pattern of rainfall isotopic composition over ISM region on intra seasonal to inter-annual time scale [*Midhun and Ramesh*, 2015; *Midhun et al.*, 2016]. The inter-annual variation of the ISM rainfall $\delta^{18}O$ values at the Belum cave is well correlated with ISM rainfall over the Arabian Sea and Western Ghat region (Figure 5.6). This strengthens our hypothesis that the Belum rainfall isotopic composition is mainly controlled by the rainfall over

the Western Ghats and the Arabian Sea.

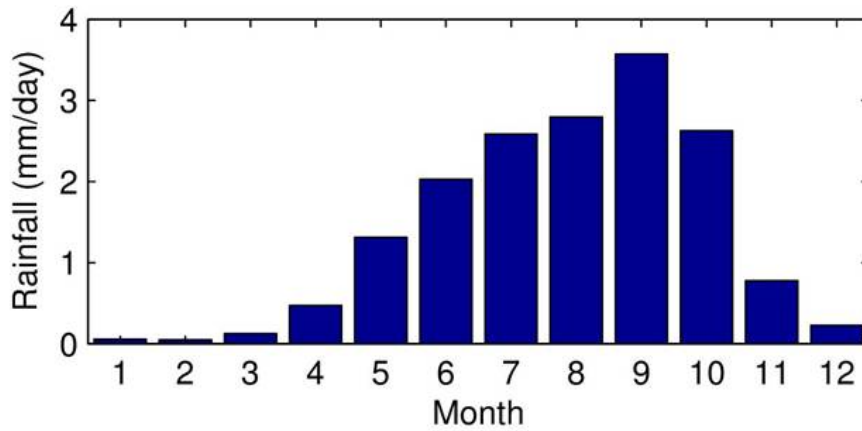


Figure 5.4: Climatological monthly rainfall at the 0.5×0.5 grid over the Belum cave. Climatology is calculated using Asian Precipitation - Highly-Resolved Observational Data Integration Towards Evaluation (APHRODITE) data from CE1951-2007 [Yatagai et al., 2012].

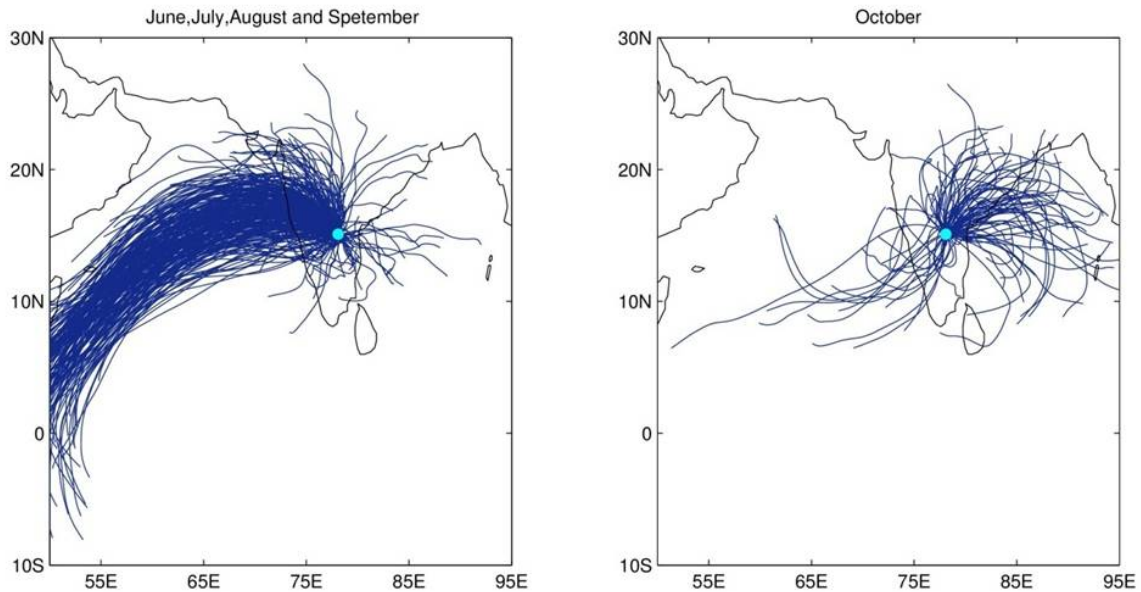


Figure 5.5: Three day back trajectory at 1500 m above ground level at the Belum cave calculated by the Hysplit [Stein et al., 2015] model using National Centre for Environmental Prediction (NCEP) reanalysis 1 dataset [Kalnay et al., 1996]. All days with rain above 2 mm during JJAS (left) and October (right) for ten years (1998-2007 CE) are used for analysis. Number of trajectories are 384 (JJAS) and 100 (October).

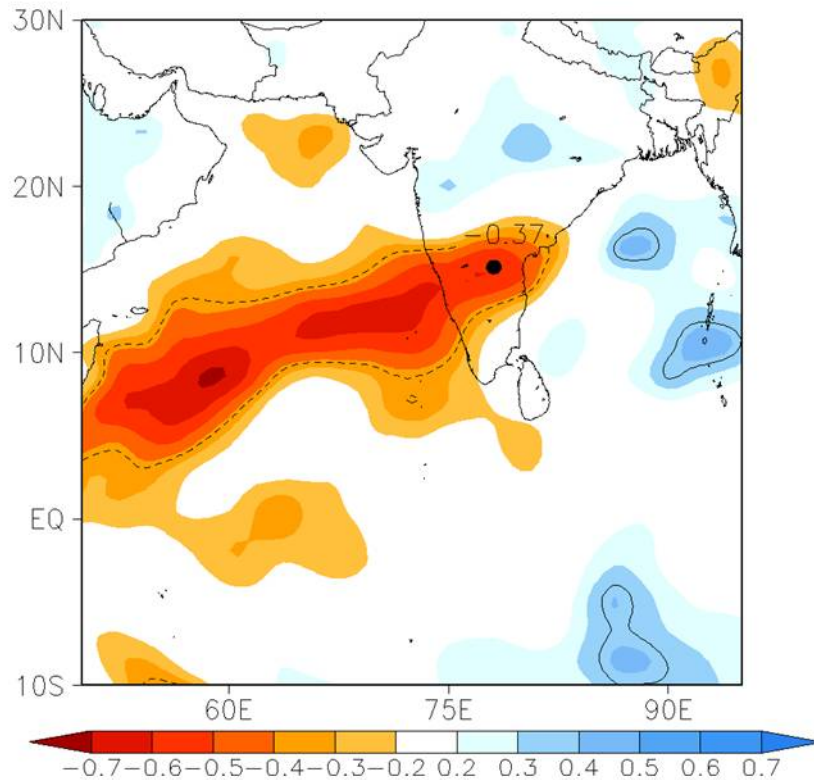


Figure 5.6: Correlation coefficient between model simulated JJAS average rainfall $\delta^{18}\text{O}$ at the Belum cave (Model resolution is $\sim 200 \times 200$ km) and model simulated JJAS average rainfall over surrounding grids, simulated by IsoGSM [Yoshimura et al., 2008]. Correlation with significance level $p = 0.05$ is marked by black dashed contour.

Minerology

The sample has three distinct growth zones representing the control of different climatic regimes. The lowermost section has white calcitic layers. The middle section has high detritus with porous radial crystals and the uppermost section has prominent growth layers. These three sections are separated by two hiatuses, one between the lower and the middle and the other between the middle and the uppermost sections (Figure 5.7), respectively. The hiatus is demarcated by a boundary of altered micro crystalline calcite with scattered inclusions of clay and Fe, evident in Figure 5.7.

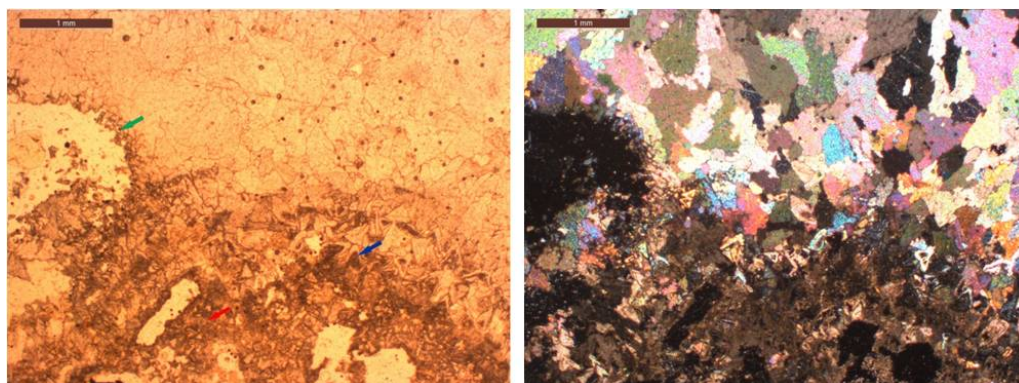


Figure 5.7: Photo taken under plane-polarized light (A) and cross-polarized light (B) shows a micro crystalline calcite layer (red arrow) below the hiatus boundary (green arrow). Calcite crystals along boundary show multiple growth zones (blue arrow) suggesting late stage precipitation. In the upper section of the photo euhedral crystals of calcite are seen post-hiatus. Micro photographs were taken using Leica DM EP microscope with attached Leica MC 120 HD camera at the M.S. University of Baroda, India.

U-Th ages

Sixteen ^{230}Th ages were obtained for the 31.4 cm long sample based on Th/U measurements (Table 5.2). The samples were analyzed by a Nu Instruments Multi-Collector Inductively Coupled Mass Spectrometer (MC-ICPMS) at the Oxford University, UK. Details of the instrument have been discussed in by *Belshaw et al.* [1998]. U concentrations were measured using a bracketing standard approach. Th was measured against in-house Th standards [*Mason and Henderson, 2010*]. Half-lives as calculated by *Cheng et al.* [2013] were used for calculations. The age data was further corrected for the presence of detrital Th using bulk detrital values of (5.38E-06, +5.38E-06, -4.84E-06) [*Hellstrom, 2006*]. From these ages, 10 subsamples have high U concentrations, for which the errors associated are less (Table-1 age). However, in the uppermost section of the sample, four ages show reversals due to low U content and relatively high ^{232}Th levels. As a result these ages are discarded. Since the Section 2 of the BLM-1 shows a high detrital content, only one age could be derived. Further dating of this section is difficult due to high ^{232}Th levels. The age model for the sample was constructed

using COPRA, an interactive age model [Breitenbach *et al.*, 2012]. A median age model with 2000 Monte-Carlo simulations and 95% confidence interval was derived. Since the section 2 is separated by two hiatuses at the top and bottom and has only one age, it was excluded from the age model. Sections 1 and 3 were modeled independently and merged together to establish a composite time series (Figure 5.8). Based on the age model, variable growth rates are observed in two sections. In section 1 growth rate increases from $1\mu\text{m}/\text{yr}$ to $5\mu\text{m}/\text{yr}$, whereas in section 3 the growth rate decreases steadily from $1\mu\text{m}/\text{yr}$ to $0.2\mu\text{m}/\text{yr}$.

Stable isotopes of oxygen and carbon

Temporal variations of $\delta^{18}\text{O}$ values are shown in Figure 5.9. The profile covers section 1 and 3 with an interval of, 183 to 173 ka and 104 to 81 ka, respectively. In section 1, the $\delta^{18}\text{O}$ values vary between -7.78‰ to -3.13‰ with an average of -4.74‰ (VPDB). In section 3, enrichment of 5‰ in ranging between -8.2‰ to -3.2‰ (VPDB) with abrupt changes was observed.

Trace element analysis

Trace element profiles of Mg/Ca, Sr/Ca, Ba/Ca and Mn/Ca are shown in Figure 5.10. Mg/Ca and Sr/Ca ratios have a good correlation ($n=101$, $r = 0.77$, significant at $p = 0.05$). All the three profiles follow the variations of the $\delta^{18}\text{O}$ trend. The major and trace element ratios increase abruptly between 85-90 ka.

Discussion

Both the sections of the sample preserve ISM variations during glacial periods, at 80-106 ka and 173-181 ka respectively. In the shorter timespan of section 1 (~ 8 ka) record, 2‰ enrichment was observed (Figure 5.9. The $\delta^{18}\text{O}$ values lie in the same range as that of the Section 3, implying both the glacial periods experienced weakening in monsoon intensity of a similar magnitude. The 5‰ stepwise enrichment in ^{18}O in section 3 during the last glacial inception can be attributed

to the declining intensity of monsoon. This, in addition with positive feedback factors such as increased evaporation from the overlying soil, could be responsible for the steep increase in $\delta^{18}\text{O}$. As a result, the infiltrating water is enriched in ^{18}O prior to precipitating in caves, and thus enhances the effect of less precipitation. The first step of 2‰ enrichment from -8‰ to -6‰ was observed from 106 – 98 ka, with a sharp increase in values at ~ 97 ka, subsequently followed by second step of 3‰ enrichment from -7 ‰ to -4‰. Interestingly, the second step is captured in the trace element record (Figure 5.10) as well. The concentrations of trace elements in speleothems depends upon various factors such as residence time in vadose zone, atmospheric dust input, temperature, and the amount of rainfall [Gascoyne, 1983; Verheyden, 2004; Verheyden et al., 2000]. However, the major climatic control of trace element concentrations in speleothems is the amount of rainfall [Verheyden, 2004]. Fairchild et al. [2000] suggested that Mg in speleothems can be used to reconstruct hydrological changes. Mg/Ca ratios are found to be sensitive to amount of rainfall and can be used in conjunction with stable isotope values to assess monsoon variability. Mg/Ca ratio in drip water is influenced by PCP and is higher during low-flow conditions. With the $\delta^{18}\text{O}$ values, the Mg/Ca and Sr/Ca ratios show negative correlations, implying higher ratios during drier conditions, favoring PCP [Cross et al., 2015]. Drier conditions prevailed during 90-85 ka, of MIS 5c seen as a sharp increase in the ratios. Mn is transported either as a organic complex, colloidal complex or as a particle in groundwater [Richter et al., 2004]. In the Belum cave stalagmite Mn could be associated with entrainment of colloidal particles adsorbed on mineral surfaces. Supporting evidence for this is seen as increased concentration of Mn where porous, impurity rich detrital layers are encountered and are significantly lower in the clear layers. Unlike what was observed by previous workers [Zhou et al., 2008], high Mn here content is not observed to be associated with an enhanced monsoon. On the contrary, it is seen when the precipitation was lower.

Table 5.2: Uranium and Thorium isotopic compositions and ^{230}Th ages of the subsamples of the Belum cave stalagmite. All errors are absolute 2σ values.

| Sample | ^{238}U (ppb) | ^{232}Th (ppt) | $^{230}\text{Th}/^{232}\text{Th}$ activity ratio | $^{230}\text{Th}/^{238}\text{U}$ activity ratio | measured $\delta^{234}\text{U}$ (‰) | initial $\delta^{234}\text{U}$ (‰) | uncorrected age Yr BP | + | - | corrected age Yr BP | + | - |
|------------------------|---------------------------|----------------------------|--|---|---|--|-----------------------------|------|------|---------------------------|-------|--------|
| BLM-1 (2 mm) | 271.51 | 8.85 | 5.19E-04 | 1.03 | 198.24 | 335.81 | 191359 | 1669 | 1668 | 190420 | 1776 | 1685 |
| BLM-1R (2 mm) | 306.99 | 9.75 | 5.27E-04 | 1.01 | 203.46 | 337.66 | 183613 | 2627 | 2460 | 182745 | 2587 | 2560 |
| B1SN2 (2 mm) | 271.8 | 9.47 | - | 1.01 | 198 | 331 | 183081 | 1998 | 1998 | 179557 † | 2615 | 2615 |
| BLM-3 (56 mm) | 427.38 | 10.15 | 6.66E-04 | 0.97 | 172.04 | 281.60 | 178930 | 2087 | 1982 | 178222 | 2277 | 2076 |
| BLM-4 (95 mm) | 424.79 | 10.61 | 6.49E-04 | 0.98 | 184.30 | 301.11 | 178150 | 2070 | 2134 | 177420 | 2124 | 2129 |
| BLM-5 (127 mm) | 163.62 | 8.34 | 3.36E-04 | 1.04 | 231.64 | 383.05 | 182662 | 1336 | 1186 | 181294 | 1645 | 1780 |
| BLM-6 (145 mm) | 500.02 | 166.68 | 4.68E-05 | 0.95 | 203.26 | 305.16 | 157084 | 1044 | 1058 | 147201 | 8559 | 9734 |
| BLM-7 (170 mm) | 396.17 | 90.37 | 5.62E-05 | 0.78 | 197.50 | 261.67 | 109933 | 622 | 558 | 103250 | 5821 | 6390 |
| BLM-8 (183 mm) | 82.76 | 59.15 | 1.77E-05 | 0.77 | 220.96 | 276.02 | 104313 | 2765 | 2726 | 81441 § | 20375 | 24614 |
| BLM-9 (191 mm) | 63.60 | 22.54 | 3.48E-05 | 0.75 | 230.73 | 293.36 | 98439 | 3013 | 2969 | 87304 § | 10446 | 10660 |
| BLM-10 (200 mm) | 97.39 | 25.68 | 4.79E-05 | 0.77 | 235.99 | 326.06 | 99099 | 893 | 1030 | 91289 § | 6795 | 7138 |
| BLM-11 (214 mm) | 63.91 | 12.21 | 6.34E-05 | 0.73 | 243.33 | 310.31 | 93879 | 3206 | 3127 | 882384 § | 6057 | 5790 |
| BLM-12 (228 mm) | 174.28 | 6.76 | 3.35E-04 | 0.79 | 286.53 | 374.84 | 99028 | 521 | 591 | 98007 | 1112 | 1185 |
| BLM-13 (250 mm) | 278.18 | 5.53 | 6.00E-04 | 0.72 | 269.09 | 342.61 | 88665 | 442 | 562 | 88089 | 683 | 767 |
| BLM-14 (280 mm) | 464.44 | 16.634 | 3.25E-04 | 0.704 | 274.284 | 344.97 | 84991 | 671 | 653 | 84023 | 1216 | 1241 |
| BLM-15 (305 mm) | 272.01 | 13.62 | 2.29E-04 | 0.69 | 270.23 | 338.11 | 83534 | 820 | 769 | 821184 | 1563 | 1478 |
| B1SN1 (305 mm) | 256.80 | 7.14 | - | 0.68 | 270.0 | 340.00 | 82615 | 676 | 676 | 82009 † | 737 | 737 |
| BLM-16 (3125 mm) | 478.55 | 383.38 | 1.45E-05 | 0.70 | 232.76 | 275.03 | 89634 | 640 | 570 | 61634 | 24809 | 286938 |

† ^{230}Th ages are discarded due to large errors. § ^{230}Th ages obtained from the University of New Mexico, New Mexico and verified by the ages obtained at the same sampling site. On comparison between ages of N2BLMS1 and N2BLMS10 with B1SN2 sampled at the same depth, N2BLMS10 was used in age model as it falls in the error limits of B1SN2. Half-lives as calculated by Cheng et al. [2013] were used for calculations. The age data was further corrected for the presence of detrital Th using bulk detrital value of ($5.38\text{E-}06$, $+5.38\text{E-}06$, $-4.84\text{E-}06$) [Hellstrom, 2006].

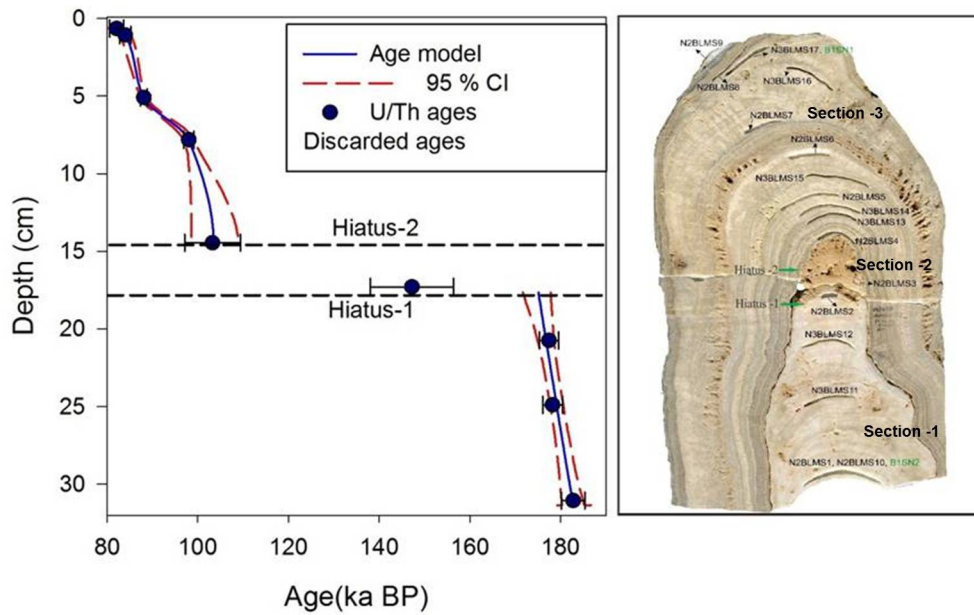


Figure 5.8: Left: Age model reconstructed using COPRA- interactive program on MATLAB [Breitenbach et al., 2012]. The filled blue circles are ^{230}Th ages taken for age model. Two separate age models were constructed for sections younger and older than the hiatuses and then merged. The errors are reported as 2σ . The dashed lines show 95% confidence interval and the blue lines are the median through which the age model passes. Right: The Belum stalagmite is displayed against the age model. Sampling intervals for ^{230}Th ages are shown. Section 1 consists of white calcitic layers, towards the end of it the boundary is marked by a prolonged hiatus 1 (green arrow). Section 2 is composed of layers rich in detrital particles. And hence only one ^{230}Th age could be derived. Section 3, succeeds the former section by a brief hiatus 2 (green arrow), that covers last interglacial period.

A possible explanation could be during enhanced monsoon, the drip rate is higher and the detrital particles accumulating at the tip of stalagmite are washed off. As a result, the calcium carbonate precipitating under high drip rate conditions has clear undisturbed growth layers. Study of seven stalagmites from the caves in Germany, show higher Mn concentrations in the autumn/winter sub annual layers. This enrichment is associated with enhanced weathering of soil cover during summer [Richter et al., 2004]. Section 3 covers the Marine isotope stages 5c to 5a. Surprisingly, there was no record of the interstadial 5e, the last inter-

glacial, during which the monsoon was stronger than the present [Burns *et al.*, 2001; Juyal *et al.*, 2006]. The lack of deposition during the last interglacial can be attributed to an enhanced monsoon which could have led to local flooding at the sampling site. The evidence of the erosional boundary are shown in the Figure 5.7. As described previously, the deeper chambers of the cave are at a lower elevation than the cave entrance, hence chances of flooding of these chambers are very high.

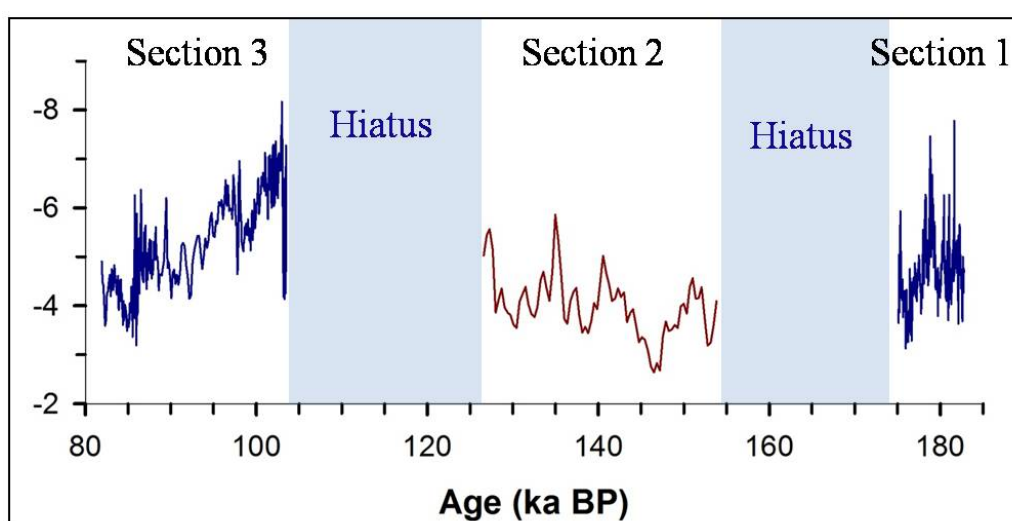


Figure 5.9: $\delta^{18}O$ profile of the Belum cave stalagmite. The blue curve represents the profile based on Copra age model. The red curve is a floating chronology based on a single U-Th date and is drawn to show the weaker monsoon phase prior to last interglacial, represented by hiatus (shaded region)

ISM has two sources for precipitation. The Arabian Sea component, ISMA mainly controls the rainfall over the Western Ghats and the region further east. And the Bay of Bengal component, ISMB, controls the rainfall over Northeastern India. Cai *et al.* [2015] presented a record from the Xiaobailong cave (XBL) located in southwestern china, representative of ISMB. Our record reflects on the ISMA branch more due to its major contribution to the sampling site (Figure 5.11). The $\delta^{18}O$ profiles of these two stalagmites from the the Belum and Xiaobailong cave representing two different sources, are comparable in the 104-80 ka timespan. Whatever could be the reason of variability during 173-180 ka, the climatic control

during last glaciation was same over both the regions.

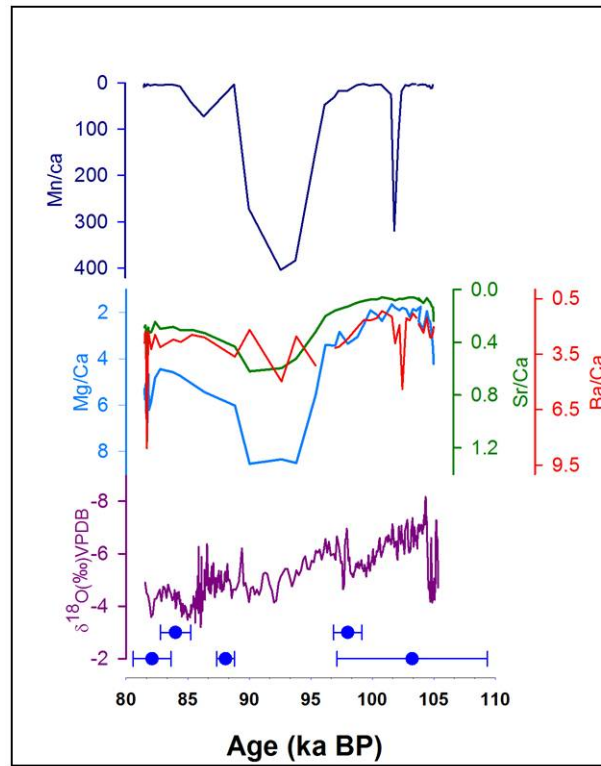


Figure 5.10: Comparison between the $\delta^{18}\text{O}$ profile of the Belum cave stalagmite (purple) and trace element ratios of Mg/Ca (light blue), Sr/Ca (green), Mn/Ca (dark blue) and Ba/Ca (red). Steep increase in ratios is seen between 90 to 85 ka, in the trace element ratios implying the role of PCP. ^{230}Th dates are shown as the blue filled circles with 2σ error bars.

Role of insolation gradient across the hemispheres in controlling monsoon

Intense heating of Indian subcontinent during the boreal summer leads to the formation of low pressure zone in north-northwestern India. As a result, there is a northward migration of the ITCZ, promoting southwesterly winds [Gadgil, 2003; Sikka and Gadgil, 1980]. The Indian monsoon system is unique in the sense that it occurs as a result of bi-hemispheric circulation. The pressure gradient between the Indian low over Central India and Mascarene high over southern Indian ocean is what drives the cross-equatorial transfer of heat [Webster et al., 1977; Zhisheng

et al., 2011]. The magnitude of this gradient determines the strength of the winds over India ocean [*Annamalai and Sperber*, 2016]. Earlier studies have shown that insolation has a direct impact on the intensity of monsoon (e.g., *Gupta et al.* [2005]). The $\delta^{18}O$ record of BLM-1 stalagmite was compared with the Northern Hemisphere insolation at 30°N. Our observation shows that there is an offset between the insolation and reconstructed monsoon profile. On the contrary the variability of the monsoon matches closely with the insolation gradient between the two hemispheres. A similar correlation was also seen in the Xiaobailong cave and the insolation gradient across the hemispheres (Figure 5.11 and 5.12). A likely explanation could be, that although insolation plays a key role in anchoring the low pressure zone over northwestern and central India, the circulation is controlled by the insolation gradient between the two hemispheres. Whenever this difference reduces the intensity of circulation reduces leading to a weaker monsoon.

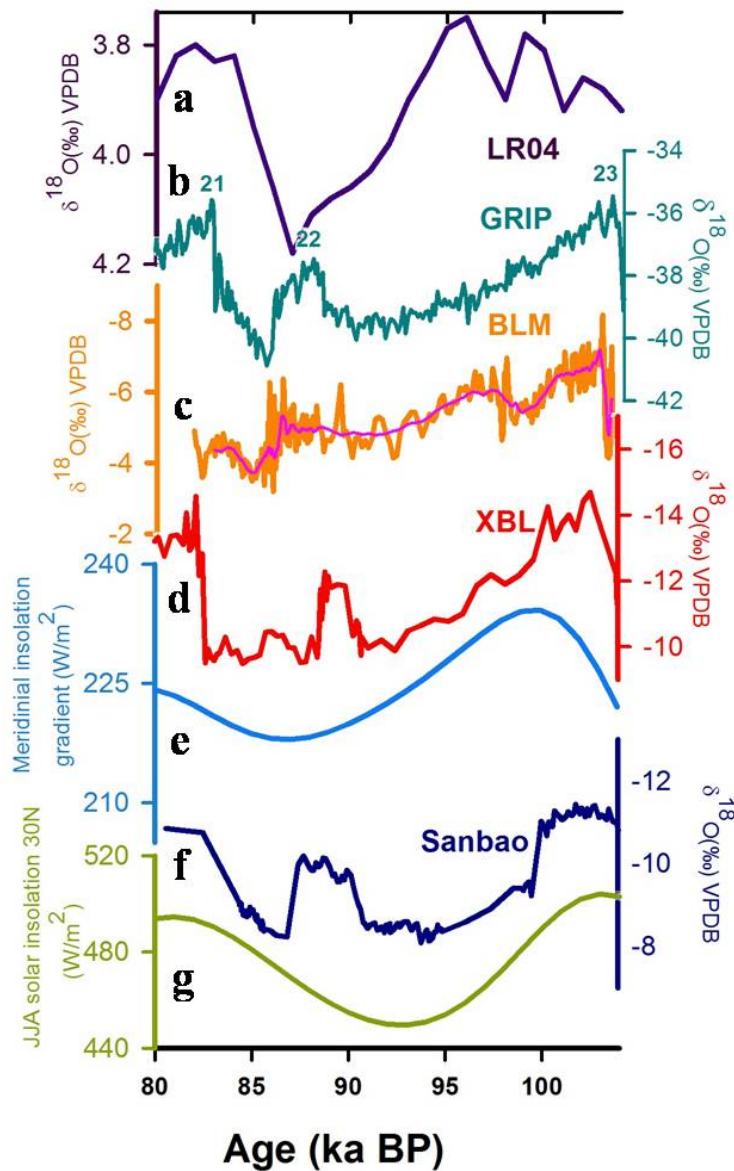


Figure 5.11: Comparison between (a) The LR04 benthic $\delta^{18}\text{O}$ stack (purple) constructed by graphic correlation of 57 globally distributed benthic $\delta^{18}\text{O}$ records [Lisiecki and Raymo, 2005] (b) fluctuations in $\delta^{18}\text{O}$ record of GRIP-2 (Greenland Ice Core Project, cyan) ice core from Greenland [Dansgaard et al., 1993; Grootes et al., 1993]. (c) The $\delta^{18}\text{O}$ values of stalagmite from the Belum cave (present study), India : BLM (orange). 25 year running average of the $\delta^{18}\text{O}$ records (pink). (d) The ISM record of a stalagmite from Xiaobailong cave: XBL (red) Cai et al. [2015] (e) meridional insolation gradient (light blue) between Northern and Southern latitudes at 30° N and 30° S [Berger, 1978; Berger A. and Loutre M.F., 1991] (f) $\delta^{18}\text{O}$ profile of a stalagmite from Sanbao cave (Blue, Wang et al. [2008]. (g) Northern Hemisphere 30° N solar insolation during JJAS.

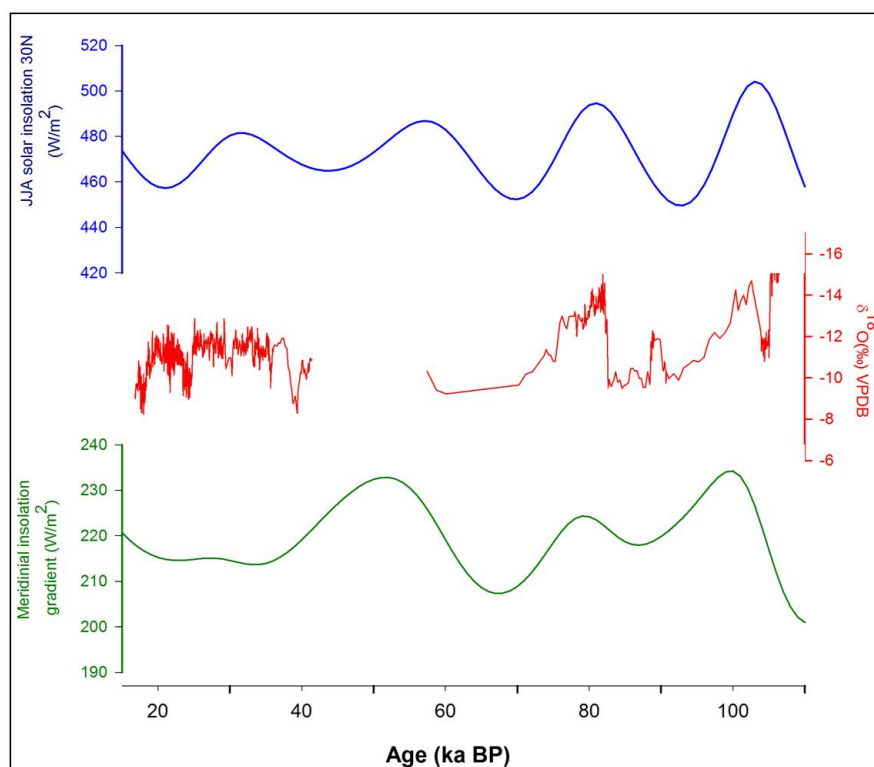


Figure 5.12: Comparison between long term composite records from the Xi-aobialong cave stalagmites (red) [Cai et al., 2015], with insolation at 30°N (blue) and inter-hemispheric insolation gradient (green) between Mascarene high over Indian ocean and tropical low over India [Berger, 1978; Berger A. and Loutre M.F., 1991].

5.2 Ocean monsoon record

Extensive work has been done on the Arabian Sea sediment cores recording monsoon variations of the past few thousand years. A complete monsoon record for the past 500 ka [Emeis et al., 1995] from a core (ODP site 723) raised near the Oman coast is in phase with major climatic boundaries. During colder phases of MIS 6, 4 and 2, abundance of *G. bulloides* was less, which in turn means a weaker upwelling and monsoonal winds in contrast to strong monsoonal winds, during MIS-5, 3 and 1. Figure 5.13 shows the locations of sediment cores from Arabian Sea and Bay of Bengal that have been investigated earlier. A detailed

study was carried out on core SO90-93KL from the Murray ridge, Arabian Sea. [Schulz et al. \[2002\]](#) studied the MIS-5/4 transition in detail. It was suggested that the well-known Toba volcanism in Indonesia that took place around 73 ka had not triggered the cooling during MIS-4, instead the climate had already begun cool prior to 73 ka. The $\delta^{18}O$ values of *G.ruber* fluctuated in accordance with Marine Isotopic Stages, with lower values during the interglacial and higher values during the glacial periods: during glacial periods much moisture from the ocean is locked into high latitudes in the form of ice which has lighter oxygen isotopic composition (i.e. more of $H_2^{16}O$ than $H_2^{18}O$ relative to ocean water), leading to less positive $\delta^{18}O$ values in ice sheets and hence more positive $\delta^{18}O$ values in the oceans, which is recorded by marine fauna. During interglacial periods, as glaciers start melting, the ocean becomes depleted in $H_2^{18}O$ and thus more negative $\delta^{18}O$ values are recorded by marine microfossils during interglacial periods. In response to such changes, lower values are observed during MIS 5, 3 and the lowest at MIS-1 (Last Glacial Maximum LGM, 21 ka). Another core from the Murray ridge (Site - NIOP4, [Reichart et al. \[1997\]](#)) covers a time span of ~ 225 ka, where $\delta^{18}O$ of *Neogloboquadrina dutertrei* was used to reconstruct climate. It is seen that during the warmer periods MIS-5, 3 and 1, primary productivity and the abundance of *G.bulloides* were in phase with strong monsoonal conditions. Sediments deposited in the Bay of Bengal by major rivers, e.g. the Ganga-Brahmaputra, and their amount varies in response to monsoon performance. [Kudrass et al. \[2001\]](#), using a core raised (SO93-126KL) from the northern Bay of Bengal, have addressed monsoon variability during past 80 ka. Here the monsoon signal is recorded as more negative $\delta^{18}O$ values corresponding to higher monsoon run-off from the Indian rivers. In this record, LGM is characterized by the highest values of $\delta^{18}O$, indicating that the freshwater flow was significantly reduced during this period. This is followed by rapid decrease in the $\delta^{18}O$ values associated with global melt water infusion and increase in sea level. Our record focuses on ISM variability from MIS-3 to 1 and is discussed below.

5.2.1 The Andaman Sea sediment core

Schulz et al. [1998] observed a correlation between the Indian Monsoon and Greenland climate oscillations on glacial-interglacial timescales. The last Glacial period (110 - 10 ka) witnessed millennial scale climate variability in terms of abrupt transitions between several cold stadials and warm interstadials. Many of these stadials were interrupted by ice-rafting events known as 'Heinrich Events'. Seven such events have been reported in the last glacial period. Climate variability associated with these cold events is not restricted to North-Atlantic basin, instead it is observed in low latitudes as well, due to rapid changes in atmospheric and ocean circulations [*Pausata et al.*, 2011].

The present study is focused on the understanding the response of the Northern Indian Ocean to such climate events and reconstruct the ISM during the last 200 ka. The objective was achieved using a core SK-234-60 raised from Andaman Sea and the Belum stalagmite (discussed in section 5.1.2) and a review of the available literature. *Awasthi et al.* [2014], identified three sources of sedimentation to the Andaman Sea: (1) the Irrawaddy catchment, (2) the western slopes of the Indo-Burman-Arakan (IBA) mountain ranges and the Andaman Islands, and (3) the catchments of Salween and Sittang and the Bay of Bengal shelf. Around 30-60% of the sediments are derived from the first two sources. The sediment flux associated with these sources depends upon the intensity of rainfall and reach their peak during the monsoon season around July-August [*Rashid et al.*, 2007].

Awasthi et al. [2014], reported the highest rate of sedimentation of 8.4 cm/ka during 52.0 – 57.5 ka and the lowest of ~ 2.4 cm/ka during the LGM, i.e., at 17.3 – 23.5 ka. The average sedimentation rate in the core was estimated to be 5.6 cm/ka. Sedimentation rate during MIS-3 was 5.5 cm/ka, followed by decreased rate of 3.0 cm/ka during the MIS-2 and rapid increase in rate of 7.7 cm/ka during the MIS-1 (Holocene).

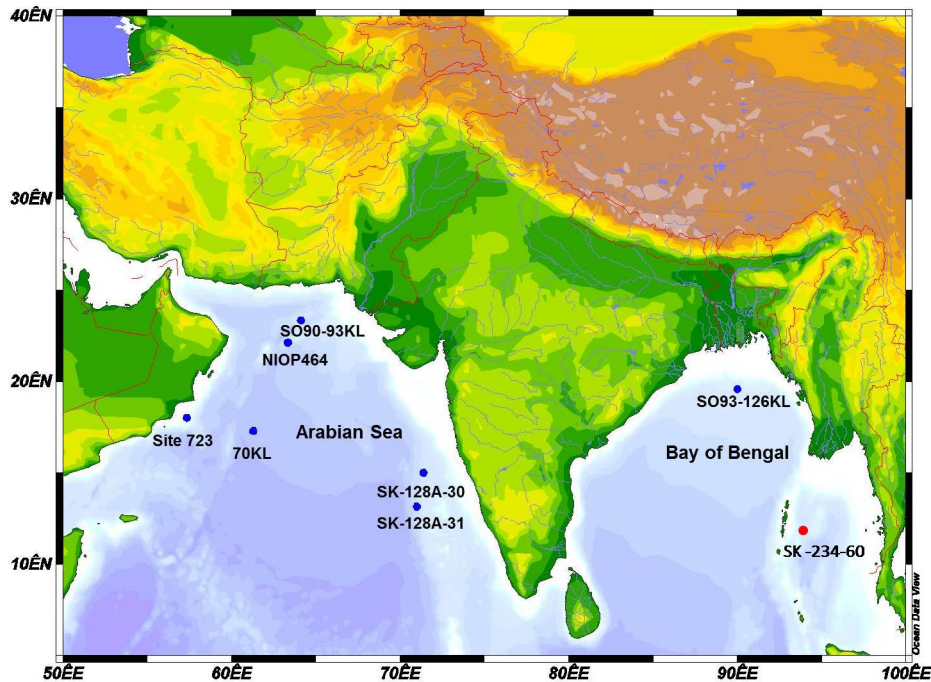


Figure 5.13: Locations of different cores raised from the Arabian Sea and the Bay of Bengal. (Site 723, [Emeis et al. \[1995\]](#)), (Site: SO90-93KL, [Schulz et al. \[2002\]](#)), (Site: NIOP464, [Reichart et al. \[1997\]](#)), (Site: SO93-126KL, [Kudrass et al. \[2001\]](#)), (Site: 70KL, [Leuschner and Sirocko \[2000\]](#)), (Site: SK-128A-30 and SK-128A-31, [Prabhu et al. \[2004\]](#), Site: SK-234-60, present study (red).

Based on the geochemical properties and hence the provenance of the sediments, [Awasthi et al. \[2014\]](#) concluded that the strength of the Indian Summer Monsoon (ISM) over western Myanmar and Andamans during the Last Glacial Maximum (LGM) was similar to the present. However, the provenance of the sedimentation can give little information about the strength of the monsoon. After reanalysis of the $\delta^{18}O$ values of *G. ruber* of the present core and comparing the record with pteropod abundances from core SK 168/GC1, a weaker ISM during the LGM is inferred. [Sijinkumar et al. \[2010\]](#) interpreted the late Quaternary climate using the abundance of pteropods in the Andaman sediment core SK 168/GC1. They observed high abundances on account of better preservation during the LGM, while lower abundance of pteropods throughout the Holocene.

Most importantly they reported high abundance of mesopelagic pteropods as

compared to epipelagic species, explaining deep water mixing, weaker Oxygen Minimum zone (OMZ) and lower Aragonite Compensation Depth (ACD). During LGM, weakening of summer monsoon reduced the ocean stratification by low influx of fresh water and strengthening of winter monsoon resulted in vertical mixing, increasing ACD favoring the pteropod preservation [Sijinkumar *et al.*, 2010]. Sarkar *et al.* [1990]; Sijinkumar *et al.* [2011] and Duplessy [1982] also pointed out that during LGM summer monsoon was weaker and there was strengthening in winter monsoon. Another study from the Andaman Sea [Rashid *et al.*, 2007] also reported a weaker summer monsoon during the LGM. Based on these evidences, we infer that the geochemical signatures of IBA as provenance during LGM to Andaman Sea reported by Awasthi *et al.* [2014] are not due to the strengthening of the summer monsoon over western Myanmar. Instead, the bulk load of sediments were transported and deposited at the core site owing to a stronger winter monsoon.

Based on Mg/Ca, Rashid *et al.* [2007], postulated that the Andaman Sea was cooler at LGM in comparison to late Holocene by 3°C. Similar cooling is also observed in the tropical Indian ocean by Bard *et al.* [1997]; Naidu and Malmgren [2005] and in the Bay of Bengal by Kudrass *et al.* [2001]. Further, Rashid *et al.* [2007] argues that late-glacial period (19-14.8 ka) was the phase of the weakest monsoon in the past 25 ka. Our records shows that LGM (25-19 ka) was the weakest monsoon period in the last 70 ka.

Existing records from the Bay of Bengal and the Andaman Sea show a strong relation between the Greenland climate oscillations and ISM variability. Most of these studies focus on migration of Ganga-Brahmaputra delta at water depths which are closer to sea level to a few tens of meters [Goodbred, 2003; Goodbred and Kuehl, 2000; Rashid *et al.*, 2007].

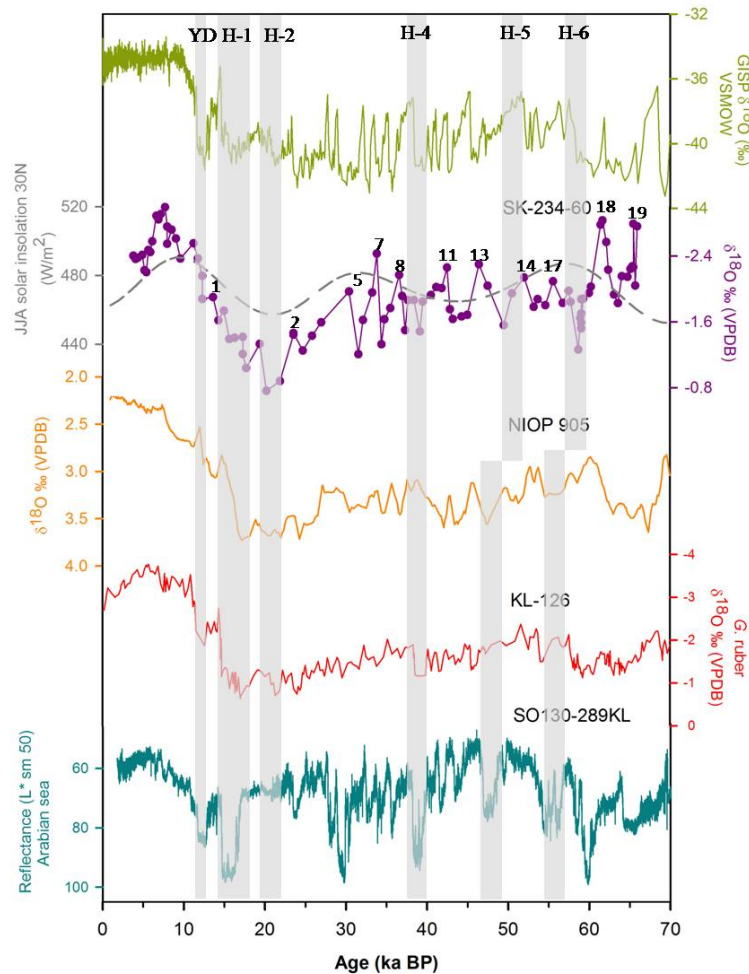


Figure 5.14: Comparison of $\delta^{18}\text{O}$ values of GRIP ice core (Green, *Grootes and Stuiver [1997]*), $\delta^{18}\text{O}$ timeseries of Andaman Sea sediment core SK (present study), the dashed gray line shows insolation at 30°N , the $\delta^{18}\text{O}$ record of the planktic foraminifera *N. dutertrei* from the Arabian Sea sediment core NIOP-905 (Yellow, *Jung et al. [2009]*), $\delta^{18}\text{O}$ values of a core from the Bay of Bengal (Red, *Kudrass et al. [2001]*) and the reflectance data from the Arabian Sea sediment core SO130-289KL, (Cyan, *Deplazes et al. [2013]*) The gray vertical bands represent ice calving events in the North-Atlantic known as Heinrich events and are shown from H-1 to H-6, the colder stadial Younger Dryas is shown as YD. The recorded Daansgard-Oeschger events are numbered from 1 to 19.

Colin et al. [1998, 1999], based on high magnetic susceptibility and increase in smectite/(illite+chlorite) ratio and $^{87}\text{Sr}/^{86}\text{Sr}$ in sediment cores raised from the Andaman Sea and Bay of Bengal showed increase in ISM during the Bolling-Allerod and the Daansgard-Oeschger events. Our record, within the age un-

certainty responds to Heinrich events by showing prominent enrichment in ^{18}O values, as shown in figure 5.14. Ice calving episodes recorded in the North-Atlantic, disrupt the ocean circulation; as a result, the Indian Ocean became more enriched during these events. The $\delta^{18}\text{O}$ profile of the present study shows coeval changes with $\delta^{18}\text{O}$ values of the sediment cores raised from the Bay of Bengal (NIOP 905) and the Arabian Sea (KL-126) implying that the records preserves changes in the Indian Ocean circulation. Moreover, the $\delta^{18}\text{O}$ timeseries is based on Dansgaard-Oeschger events (beyond the limit of radiocarbon dating) signifying the role of North-Atlantic climate changes in controlling the Indian ocean circulation, including the water currents passing through the Preparis channel. During the LGM the south Preparis current was active in spite of lowering of mean sea level by 120 m, bringing the waters enriched in ^{18}O from the Bay of Bengal. The troughs in our data correspond to the cooling events in Greenland ice core records as seen in figure 5.14.

Chapter 6

Summary and scope for future work

This thesis deals with reconstructing the variability of Indian Summer Monsoon (ISM) during the Holocene and the late Pleistocene from speleothems of Indian peninsula and Sediment core from the Andaman Sea. Such studies are important to understand the role of insolation and North-Atlantic oscillation on ISM and as yet such studies are limited over the Core Monsoon Zone (CMZ) of India. The present work has improved our understanding regarding the evolution of the monsoon during the late Pleistocene and the Holocene. The major findings of this study are summarized below :-

6.1 Reconstruction of ISM variability from stalagmites of the Kanger Valley cave complex, Chattisgarh

1. The Variability of ISM during the Holocene has been studied using three stalagmites from the Dandak (DAN-I and DAN-II) and the Kotumsar caves, central India. High resolution ISM reconstruction based on $\delta^{18}O$ ($n = 5040$)

measurements covers most of the Holocene. The record extends from 10.4 ka to the present, with brief hiatuses from 9 to 8.5 and 2.4 to 2.2 ka.BP.

2. The beginning of the Holocene between 10.4 - 9 ka is marked by amelioration of ISM . Increased monsoon was related to the Northward shift of the Intertropical Convergence Zone (ITCZ) in response to increased insolation.
3. Holocene North Atlantic oscillations known as **Bond events** are evident as abrupt decline in monsoon between 10.4 -9 ka, establishing a strong teleconnection between low and high latitudes.
4. In the past, the variability and trends in the ISM during the mid-Holocene has remained a debatable issue. While some proxy records showed changes to be gradual in response to decreasing insolation, there are observations of abrupt decline at 6 ka as well. Contrary to the consensus of gradual decrease in monsoon during the mid-Holocene, an abruptly declining monsoon between 6 and 5 ka was observed.
5. This abrupt decline in monsoon can be attributed to the external forcings or natural or internal fluctuations of the monsoon system. The external forcings include insolation and volcanic eruptions, whereas the internal fluctuations include North-Atlantic thermohaline circulation and El-Nino. The gradual decline in insolation is not sufficient to explain such a abrupt decrease. However, when superimposed with North-Atlantic climate changes, the millennial scale monsoon variability can be explained. The sensitivity of the monsoon to North Atlantic climate is also observed as Bond events leading to the weakening of monsoon in the mid-Holocene.
6. The second plausible cause behind the abrupt decrease of ISM at ~ 6 ka could be sudden failure of internal feedback mechanisms governing the monsoon, leading to a sudden decline in the monsoon intensity.

7. The Dandak -I $\delta^{18}O$ timeseries shows a decrease in the monsoon from 4.8 - 3.8 ka. Anomalously depleted $\delta^{18}O$ values are present between 3.8 - 2.8 ka, implying amelioration of monsoon during this period. Such an increase was not reported so far from any other proxy and could be related to the local intensification of the monsoon or change in the moisture source (from the Arabian sea to the Bay of Bengal).
8. Post ~ 2 ka BP, ISM strengthening is observed, consistent with previous observations. The ISM reconstruction shows abrupt decline in monsoon between 1550-1450 AD and 1350-1250 AD. Since the end of LIA, monsoon intensity has increased in 19th and 20th century, and entered an "active" phase.
9. A phase of prolonged weak monsoon, between 600 and 150 yr BP, with severe drought-like conditions at 300 yr BP (1700 AD) is seen in the reconstruction during the Little Ice Age.

6.2 Impact of ISM variability on human civilization

1. When sampling, evidences of controlled fire preserved as burnt earth and patches of charcoal mixed with soil and grasses in the form of three distinct layers in Kotumsar and one layer in Dandak cave were found, indicating sporadic human inhabitation. Based on radiocarbon dating of the charcoal deposits, human activity was observed during 6.9 - 4 ka.
2. ISM reconstruction during this time shows a decrease in monsoon from 6.5 - 4 ka. Use of caves during poorer monsoon episodes suggests that they were used as shelters during severe droughts. Also, decrease in monsoon intensity for prolonged periods must have led to stressed conditions for

agriculture. This could have forced people to store food grains for drought-like conditions.

6.3 ISM variability during late Pleistocene based on Speleothem studies

1. High resolution sampling of the **Kailash cave** stalagmite holds potential to address decadal and centennial monsoon variability during the **Bolling-Allerod event** from 13.9 - 13.4 ka.
2. Most of the sample deposited during the **Older Dryas** event separated by Bolling (peak at 14.5 ka) and Allerod oscillations (peak at 13 ka). The $\delta^{18}O$ timeseries shows multi-decadal low rainfall events throughout this period. The frequency of occurrence of these mega-droughts can be determined after establishing stronger chronological control over the sample.
3. The strength of ISM increased with the start of Allerod oscillation, resulting in plausible flooding at the sampling site and the cessation of the sample growth there after.
4. ISM variability during the inception of the **Last Glacial Period** is reconstructed using a stalagmite sample from the **Belum cave**, India. The stalagmite is used to reconstruct ISM from 181 ka to 173 ka and 104 ka to 81ka. Both the periods have $\delta^{18}O$ values in the same range, implying the factors controlling ISM during glaciations were likely the same.
5. With the onset of glaciation, stepwise decrease in monsoon was observed from 106 – 98 ka, with sharp increase in $\delta^{18}O$ values at ~ 97 ka. This was followed by second step of 3‰ enrichment.
6. Analysis of Mg/Ca, and Sr/Ca indicate the role of prior calcite precipitation during the drier glacial period and point to extended drier period

between 90-85 ka. Interestingly, this time period is recorded as layers with high detrital content, and hence high Mn/Ca ratios. Unlike the previous hypotheses of Mn precipitation associated with high rainfall episodes, we observed that, enrichment of Mn is related to decreased ISM. Thereby we postulate that higher rainfall events accelerate the drip rate, washing off accumulating detrital particles from precipitating stalagmite.

7. The sample with two distinct hiatuses has a missing monsoon record during the last interglacial at ~ 125 to 110 ka. This gap in deposition is explained as flooding of sampling site during the last interglacial period or shifting of feeding channel temporarily which resumed back in 104 ka.
8. The declining phase of monsoon during last glacial inception can not be solely attributed to changes in insolation. On comparing $\delta^{18}O$ profile with $30^{\circ}N$ insolation and the insolation gradient between Mascarene high and Tropical low over India, ISM seems closely related to the insolation gradient than insolation itself. Similar results were also reported from Xiaobialong cave, China, where the $\delta^{18}O$ profile follows the variability in the insolation gradient.

6.4 ISM variability during late Pleistocene based on the Andaman Sea sediment Core

1. The present work has correctly interpreted the Andaman Sea sediment core $\delta^{18}O$ data of *Awasthi et al.* [2014]. Evaluating the $\delta^{18}O$ values of *G.ruber*, we question the inference of the strengthening of ISM during the last Glacial Maximum based on geochemical evidences alone. The geochemical proxies are useful to determine the provenance of the sediments but can not be used to address the ISM variability.

2. Monsoon was weaker during the LGM between 20-18 ka, a finding which is supported by numerous studies carried out by several workers on different sediment cores from the Indian Ocean. Also based on the $\delta^{18}O$ record it can be inferred that strength of ISM was weakest during LGM in the past 70 ka. High influx of sediments from western Myanmar during LGM could be due to strengthening of winter monsoon.
3. The ISM variability reconstructed from the core SK-234-60 shows significant correlation with change in insolation during the past 70 ka. It can hence be said that the ISM is modulated by change in insolation to some extent.

6.5 Scope for future work

1. Although we have attempted to reconstruct ISM covering entire the Holocene, one such data set representing ISM is only indicative not complete in itself.
2. Contrary to the previous beliefs, we have shown that strength of the monsoon decreased abruptly at 6 ka. To strengthen this hypotheses, analyses of more samples from CMZ covering the Holocene need to be attempted.
3. Spectral analysis of the compiled Dandak and Kotumsar $\delta^{18}O$ timeseries is essential to address decadal and centennial variability in the monsoon.
4. Kanger valley cave complex, hosts many caves which still require detailed explorations. More speleothem studies from different caves in the same complex, will help for cross-correlation of the reconstructions.
5. There is a urgent need to set up a U-Th mass spectrometric dating facility in India so that speleothem science can be accelerated and more samples with better age models be analyzed.
6. Previous workers postulated the enrichment of trace elements in stalagmite during high rainfall events. These studies were not carried in an ISM

regime, which is in seasonal nature. Drip rates are higher during the monsoon season. We found that enrichment of trace elements in stalagmites is possible only when the rainfall is low, as high rainfall accelerates drip rate washing off the colloidal particles. However, trace element accumulation in Indian speleothems where ISM plays a key role is poorly understood and requires future investigation.

7. As previously stated, insolation is not the only governing factor for monsoon variability. Comparisons with El-Nino events, and different forcings factors are required to understand the millennial and centennial scale variability in monsoon.

Publications

1. Awasthi, N., Ray, J.S., Singh, A.K., **Band, S.T.**, Rai, V.K., 2014. Provenance of the Late Quaternary sediments in the Andaman Sea: Implications for monsoon variability and ocean circulation. *Geochemistry, Geophys. Geosystems* 15, 3890–3906. doi:10.1002/2014GC005462.
2. Sridhar, A., Bhushan, R., Balaji, D., **Band, S.**, Chamyal, L.S., 2016. Geochemical and Sr–Nd isotopic variations in palaeoflood deposits at main-stem–tributary junction, western India: Implications on late Holocene flood events. *CATENA* 139, 32–43. doi:10.1016/j.catena.2015.12.004
3. **Shraddha Band**, Madhusudan G. Yadava and Rengaswamy Ramesh, Monsoon climate and Marine Isotopic Stages over the Indian subcontinent during the last 200,000 years. *Indian History* ,Primus Publishers,New Delhi(in press)
4. R. Ramesh, H. Boragaonkar, **S. Band** and M. G. Yadava, Proxy climatic records of past monsoons. Monograph on climate variability and change, springer publications (in press)
5. **Shraddha Band**, M.G.Yadava, V. J. Polyak ,Y. Asmerom, Mahjoor lone, Chuan-Chou Shen, Kaushik Sree , Sachin Gupta, and R.Ramesh, Holocene monsoon variability and its links to Greenland climate oscillations (in preparation)
6. **Shraddha Band**, M.G.Yadava, R.Ramesh, Nikita Kaushal, M. Midhun, Timmy

Francis , Amzad Laskar, Gideon Henderson, Response of Indian Summer Monsoon during the last two Glacial periods, a study from stalagmite, Belum cave, India (in preparation).

7. **Shraddha Band**, M.G.Yadava, V. J. Polyak ,Y. Asmerom, Sachin Gupta, and R.Ramesh. Impact of mid-Holocene aridification on central Indian civilization.(in preparation)

Papers/Abstract in conference proceedings

1. **Shraddha Band**, M.G.Yadava, Kaushik Sree R. Ramesh, V. J. Polyak and Y. Asmerom, High resolution precipitation records from a stalagmite of Kotumsar cave, Chhattisgarh. 28th ISMAS symposium cum workshop on mass spectrometry, 2014, pp 264-265.
2. **S. Band**, A.H. Laskar, P. R. Lekshmy, M. Midhun, M. G. Yadava and R. Ramesh, Holocene monsoon variability derived from speleothems. Mini-symposium on reconciliation of Marine and Terrestrial records of summer monsoon variability during the Holocene, 80th INSA anniversary general meeting ,2014, page 4 .
3. **Shraddha T Band**, Madhusudan G Yadava, Kaushik Sree, R. Ramesh, Victor J Polyak and YemaneAsmerom, High-resolution monsoon reconstruction using an annually resolved stalagmite from Kotumsar cave, India, AGU fall meeting 2014.
4. **Shraddha Band**, M.G.Yadava, R.Ramesh, Sachin Gupta, V. J. Polyak and Y. Asmerom, Holocene Monsoon variability using stalagmite record from Dandak cave, India, Goldschmidt conference, Yokohama, 2016
5. Narayana Allu C, GautamPawan K, **Band Shraddha** , Yadava M G , Ramesh Rengaswamy, and Chuan-Chou Shen, High Resolution deglacial

monsoon $\delta^{18}O$ record from a new stalagmite from the Kailash Cave, Central India, Geophysical Research Abstracts Vol. 18, EGU2016-9006, 2016

Oral/ Posters presented

1. **Shraddha Band**, M.G.Yadava, Timmy Francis, Amzad Laskar, Nikita Kaushal, R.Ramesh, Gideon Henderson, High resolution precipitation records from a stalagmite of Belum Cave, India. Summer school on speleothem science. University of Oxford, 2015. (Poster presentation)
2. **Shraddha Band**, M.G.Yadava, R.Ramesh, Sachin Gupta, V. J. Polyak and Y. Asmerom, Holocene Monsoon variability using stalagmite record from Dandak cave, India. Goldschmidt conference, Yokohama, 2016. (Oral presentation).
3. **Shraddha Band**, M.G.Yadava, V. J. Polyak, Y. Asmerom, Mahjoor lone, Chuan-Chou Shen, Kaushik Sree, Sachin Gupta, and R. Ramesh, Holocene monsoon variability and its link to Greenland climate oscillations. Workshop on “Recent advances in Paleoclimate Studies”, University of Tokyo, 2016. (Oral presentation)

Bibliography

- Adler, R. F., G. J. Huffman, A. Chang, R. Ferraro, P.-P. Xie, J. Janowiak, B. Rudolf, U. Schneider, S. Curtis, D. Bolvin, et al. (2003), The version-2 global precipitation climatology project (gpcp) monthly precipitation analysis (1979-present), *Journal of hydrometeorology*, 4(6), 1147–1167.
- Agnihotri, R., K. Dutta, R. Bhushan, and B. Somayajulu (2002), Evidence for solar forcing on the indian monsoon during the last millennium, *Earth and Planetary Science Letters*, 198(3), 521–527.
- Agrawal, D. P., and M. Yadava (1995), *Dating the human past*, 1, Indian Society for Prehistoric and Quaternary Studies.
- Agrawal, S., P. Sanyal, A. Sarkar, M. K. Jaiswal, and K. Dutta (2012), Variability of indian monsoonal rainfall over the past 100ka and its implication for c 3–c 4 vegetational change, *Quaternary Research*, 77(1), 159–170.
- Allison, G. (1982), The relationship between 18o and deuterium in water in sand columns undergoing evaporation, *Journal of Hydrology*, 55(1-4), 163–169.
- Allu, N. C., M. Tiwari, M. G. Yadava, N. C. Dung, C.-C. Shen, S. P. Belgaonkar, R. Ramesh, and A. H. Laskar (2015), Stalagmite $\delta^{18}\text{O}$ variations in southern India reveal divergent trends of Indian Summer Monsoon and East Asian Summer Monsoon during the last interglacial, *Quat. Int.*, doi: 10.1016/j.quaint.2014.12.014.
- Anderson, D. M., J. C. Brock, and W. L. Prell (1992), Physical upwelling processes, upper ocean environment and the sediment record of the southwest monsoon, *Geological Society, London, Special Publications*, 64(1), 121–129.
- Anderson, P., C. Barnosky, P. Bartlein, P. Behling, L. Brubaker, E. Cushing, J. Dodson, B. Dworetsky, P. Guetter, S. Harrison, et al. (1988), Climatic changes of the last 18,000 years: Observations and model simulations., *Science*, 241, 1043–1052.

- Andrews, J. E., A. K. Singhvi, A. J. Kailath, R. Kuhn, P. F. Dennis, S. K. Tandon, and R. P. Dhir (1998), Do stable isotope data from calcrete record late pleistocene monsoonal climate variation in the thar desert of india?, *Quaternary Research*, 50(3), 240–251.
- Annamalai, H., and K. Sperber (2016), South asian summer monsoon variability in a changing climate, in *The Monsoons and Climate Change*, pp. 25–46, Springer.
- Asmerom, Y., V. J. Polyak, J. B. T. Rasmussen, S. J. Burns, and M. Lachniet (2013), Multidecadal to multicentury scale collapses of Northern Hemisphere monsoons over the past millennium., *Proc. Natl. Acad. Sci. U. S. A.*, 110(24), 9651–9656, doi:10.1073/pnas.1214870110.
- Awasthi, N. (2012), Geochemical and isotopic studies of sediments from the andaman island the andaman sea, *Unpubl. Ph. D. thesis, The Maharaja Sayajirao University of Baorda, India*, p. 181.
- Awasthi, N., J. S. Ray, A. K. Singh, S. T. Band, and V. K. Rai (2014), Provenance of the late quaternary sediments in the andaman sea: Implications for monsoon variability and ocean circulation, *Geochemistry, Geophysics, Geosystems*, 15(10), 3890–3906.
- Badeck, F.-W., G. Tcherkez, S. Nogues, C. Piel, and J. Ghashghaie (2005), Post-photosynthetic fractionation of stable carbon isotopes between plant organs—a widespread phenomenon, *Rapid communications in mass spectrometry*, 19(11), 1381–1391.
- Baldini, J., F. McDermott, and I. Fairchild (2006), Spatial variability in cave drip water hydrochemistry: Implications for stalagmite paleoclimate records, *Chemical Geology*, 235(3), 390–404.
- Bar-Matthews, M., A. Matthews, and A. Ayalon (1991), Environmental controls of speleothem mineralogy in a karstic dolomitic terrain (soreq cave, israel), *The Journal of Geology*, pp. 189–207.
- Bard, E., F. Rostek, C. Sonzogni, et al. (1997), Interhemispheric synchrony of the last deglaciation inferred from alkenone palaeothermometry, *Nature*, 385(6618), 707–710.
- Barnett, T., L. Dümenil, U. Schlese, and E. Roeckner (1988), The effect of eurasian snow cover on global climate, *Science*, 239(4839), 504–507.
- Barnett, T., L. Dümenil, U. Schlese, E. Roeckner, and M. Latif (1989), The effect

- of eurasian snow cover on regional and global climate variations, *Journal of the Atmospheric Sciences*, 46(5), 661–686.
- Belshaw, N., P. Freedman, R. O’nions, M. Frank, and Y. Guo (1998), A new variable dispersion double-focusing plasma mass spectrometer with performance illustrated for pb isotopes, *International Journal of Mass Spectrometry*, 181(1), 51–58.
- Bender, M. M. (1968), Mass spectrometric studies of carbon 13 variations in corn and other grasses., *Radiocarbon*, 10(2), 468–472.
- Berger, A. (1978), Long-Term Variations of Daily Insolation and Quaternary Climatic Changes, *J. Atmos. Sci.*, 35(12), 2362–2367, doi:10.1175/1520-0469(1978)035<2362:LTVODI>2.0.CO;2.
- Berger A. and Loutre M.F. (1991), Insolation values for the climate of the last 10 million years., *Quat. Sci. Rev.*, 10(4), 297–317.
- Berkelhammer, M., A. Sinha, L. Stott, H. Cheng, F. Pausata, and K. Yoshimura (2012), An abrupt shift in the indian monsoon 4000 years ago, *Climates, landscapes, and civilizations*, pp. 75–88.
- Berner, R. (1975), The role of magnesium in the crystal growth of calcite and aragonite from sea water, *Geochimica et Cosmochimica Acta*, 39(4), 489–504.
- Bhattacharyya, A., R. R. Yadav, H. P. Borgaonkar, and G. B. Pant (1992), Growth-ring analysis of Indian tropical trees: dendroclimatic potential, *Curr. Sci.*, 62, 736–741.
- Bhattacharyya, A., D. Eckstein, S. K. Shah, and V. Chaudhary (2007), Analyses of climatic changes around parambikulam, south india, based on early wood mean vessel area of teak, *Current Science*, 93(8), 1159.
- Biospeleologist (2013), Inner view of dandak cave of chhattisgarh, wikipedia, [Online; accessed 23-July-2016].
- Bischoff, J. L. (1968), Kinetics of calcite nucleation: magnesium ion inhibition and ionic strength catalysis, *Journal of Geophysical Research*, 73(10), 3315–3322.
- Biswas, J. (2010), Kotumsar cave biodiversity: a review of cavernicoles and their troglobiotic traits, *Biodiversity and conservation*, 19(1), 275–289.
- Biswas, J., and S. Shrotriya (2011), Dandak: a mammalian dominated cave ecosystem of india, *Subterranean Biology*, 8, 1.

- Bond, G., W. Showers, M. Cheseby, R. Lotti, P. Almasi, P. Priore, H. Cullen, I. Hajdas, G. Bonani, et al. (1997), A pervasive millennial-scale cycle in north atlantic holocene and glacial climates, *science*, *278*(5341), 1257–1266.
- Bond, G., B. Kromer, J. Beer, R. Muscheler, M. N. Evans, W. Showers, S. Hoffmann, R. Lotti-Bond, I. Hajdas, and G. Bonani (2001), Persistent solar influence on North Atlantic climate during the Holocene., *Science*, *294*(5549), 2130–6, doi:10.1126/science.1065680.
- Bond, G. C., and R. Lotti (1995), Iceberg discharges into the north atlantic on millennial time scales during the last glaciation, *Science*, *267*(5200), 1005–1010.
- Borgaonkar, H. P., A. B. Sikder, S. Ram, and G. B. Pant (2010), El Nino and related monsoon drought signals in 523-year-long ring width records of teak (*Tectona grandis* L.F.) trees from south India, *Palaeogeogr. Palaeoclimatol. Palaeoecol.*, *285*, 74–84, doi:10.1016/j.palaeo.2009.10.026.
- Borsato, A., S. Frisia, I. J. Fairchild, A. Somogyi, and J. Susini (2007), Trace element distribution in annual stalagmite laminae mapped by micrometer-resolution x-ray fluorescence: implications for incorporation of environmentally significant species, *Geochimica et Cosmochimica Acta*, *71*(6), 1494–1512.
- Breitenbach, S. (2010), Changes in monsoonal precipitation and atmospheric circulation during the holocene reconstructed from stalagmites from northeastern india, *Tech. rep.*, Citeseer.
- Breitenbach, S., K. Rehfeld, B. Goswami, J. Baldini, H. Ridley, D. Kennett, K. Prufer, V. Aquino, Y. Asmerom, V. Polyak, et al. (2012), Constructing proxy records from age models (copra), *Climate of the Past*, *8*(5), 1765–1779.
- Broecker, W. S., and S. Hemming (2001), Climate swings come into focus, *Science*, *294*(5550), 2308–9.
- Broecker, W. S., E. A. Olson, and P. C. ORR (1960), Radiocarbon measurements and annual rings in cave formations.
- Buckley, B. M., K. Palakit, K. Duangsathaporn, P. Sanguantham, and P. Prasomsin (2007), Decadal scale droughts over northwestern thailand over the past 448 years: links to the tropical pacific and indian ocean sectors, *Climate Dynamics*, *29*(1), 63–71.
- Burns, S. J., D. Fleitmann, A. Matter, U. Neff, and A. Mangini (2001), Speleothem evidence from oman for continental pluvial events during interglacial periods, *Geology*, *29*(7), 623–626.

- Burns, S. J., D. Fleitmann, M. Mudelsee, U. Neff, A. Matter, and A. Mangini (2002), A 780-year annually resolved record of indian ocean monsoon precipitation from a speleothem from south oman, *Journal of Geophysical Research: Atmospheres*, *107*(D20).
- Cai, Y., I. Y. Fung, R. L. Edwards, Z. An, H. Cheng, J.-E. Lee, L. Tan, C.-C. Shen, X. Wang, J. A. Day, et al. (2015), Variability of stalagmite-inferred indian monsoon precipitation over the past 252,000 y, *Proceedings of the National Academy of Sciences*, *112*(10), 2954–2959.
- Carter, H., et al. (1999), Determination of uranium and thorium in geological materials using extraction chromatography, *Analyst*, *124*(3), 271–274.
- Cerling, T. E., and J. M. Harris (1999), Carbon isotope fractionation between diet and bioapatite in ungulate mammals and implications for ecological and paleoecological studies, *Oecologia*, *120*(3), 347–363.
- Charles, C. D., J. Lynch-Stieglitz, U. S. Ninnemann, and R. G. Fairbanks (1996), Climate connections between the hemisphere revealed by deep sea sediment core/ice core correlations, *Earth and Planetary Science Letters*, *142*(1), 19–27.
- Chauhan, O. S., E. Vogelsang, N. Basavaiah, and U. Kader (2010), Reconstruction of the variability of the southwest monsoon during the past 3 ka, from the continental margin of the southeastern arabian sea, *Journal of Quaternary Science*, *25*(5), 798–807.
- Cheng, H., R. L. Edwards, C.-C. Shen, V. J. Polyak, Y. Asmerom, J. Woodhead, J. Hellstrom, Y. Wang, X. Kong, C. Spötl, et al. (2013), Improvements in ^{230}Th dating, ^{230}Th and ^{234}U half-life values, and U – Th isotopic measurements by multi-collector inductively coupled plasma mass spectrometry, *Earth and Planetary Science Letters*, *371*, 82–91.
- Clark, I. D., and P. Fritz (1997), *Environmental isotopes in hydrogeology*, CRC press.
- Claussen, M., C. Kubatzki, V. Brovkin, A. Ganopolski, P. Hoelzmann, and H.-J. Pachur (1999), Simulation of an abrupt change in saharan vegetation in the mid-holocene, *Geophysical research letters*, *26*(14), 2037–2040.
- Clift, P. D., A. Carter, L. Giosan, J. Durcan, G. A. Duller, M. G. Macklin, A. Alizai, A. R. Tabrez, M. Danish, S. VanLaningham, et al. (2012), U–Pb zircon dating evidence for a pleistocene sarasvati river and capture of the yamuna river, *Geology*, *40*(3), 211–214.

- Colin, C., C. Kissel, D. Blamart, and L. Turpin (1998), Magnetic properties of sediments in the bay of bengal and the andaman sea: impact of rapid north atlantic ocean climatic events on the strength of the indian monsoon, *Earth and Planetary Science Letters*, 160(3), 623–635.
- Colin, C., L. Turpin, J. Bertaux, A. Desprairies, and C. Kissel (1999), Ero-sional history of the himalayan and burman ranges during the last two glacial–interglacial cycles, *Earth and Planetary Science Letters*, 171(4), 647–660.
- Coplen, T. B., C. Kendall, and J. Hopple (1983), Comparison of stable isotope reference samples.
- Craig, H. (1954), Carbon 13 in plants and the relationships between carbon 13 and carbon 14 variations in nature, *The journal of geology*, pp. 115–149.
- Craig, H. (1957), Isotopic standards for carbon and oxygen and correction factors for mass-spectrometric analysis of carbon dioxide, *Geochimica et cosmochimica acta*, 12(1), 133–149.
- Craig, H., and C. D. Keeling (1963), The effects of atmospheric no 2 on the mea-sured isotopic composition of atmospheric co 2, *Geochimica et Cosmochimica Acta*, 27(5), 549–551.
- Cross, M., D. McGee, W. S. Broecker, J. Quade, J. D. Shakun, H. Cheng, Y. Lu, and R. Edwards (2015), Great Basin hydrology, paleoclimate, and connections with the North Atlantic: A speleothem stable isotope and trace element record from Lehman Caves, NV, *Quat. Sci. Rev.*, (January), doi:10.1016/j.quascirev.2015.06.016.
- Dahl-Jensen, D., K. Mosegaard, N. Gundestrup, G. D. Clow, S. J. Johnsen, A. W. Hansen, and N. Balling (1998), Past temperatures directly from the greenland ice sheet, *Science*, 282(5387), 268–271.
- Dansgaard, W. (1964), Stable isotopes in precipitation, *Tellus*, 16(4), 436–468, doi:10.1111/j.2153-3490.1964.tb00181.x.
- Dansgaard, W., S. Johnsen, H. Clausen, D. Dahl-Jensen, N. Gundestrup, C. Ham-mer, C. Hvidberg, J. Steffensen, A. Sveinbjörnsdottir, J. Jouzel, et al. (1993), Evidence for general instability of past climate from a 250-kyr ice-core record, *Nature*, 364(6434), 218–220.
- D’Arrigo, R. D., G. C. Jacoby, and P. J. Krusic (1994), Progress in dendroclimatic studies in indonesia, *Terr. Atmos. Oceanic Sci*, 5, 349–363.
- Dawson, T. E., S. Mambelli, A. H. Plamboeck, P. H. Templer, and K. P. Tu

- (2002), Stable isotopes in plant ecology, *Annual review of ecology and systematics*, pp. 507–559.
- DeMenocal, P. B. (2001), Cultural responses to climate change during the late holocene., *Science (New York, NY)*, 292(5517), 667–673.
- Denniston, R. F., L. A. González, Y. Asmerom, R. H. Sharma, and M. K. Reagan (2000), Speleothem evidence for changes in indian summer monsoon precipitation over the last 2300 years, *Quaternary Research*, 53(2), 196–202.
- Deplazes, G., A. Lückge, L. C. Peterson, A. Timmermann, Y. Hamann, K. A. Hughen, U. Röhl, C. Laj, M. A. Cane, D. M. Sigman, et al. (2013), Links between tropical rainfall and north atlantic climate during the last glacial period, *Nature Geoscience*, 6(3), 213–217.
- Dhir, R., S. Tondan, S. Rajaguru, and R. Ramesh (1999), Calcretes their genesis and significance in palaeoclimatic reconstruction in arid rajasthan india, *Palaeoecology of Africa and surrounding Islands*, pp. 223–30.
- Dhir, R., S. Tandon, B. Sareen, R. Ramesh, T. Rao, A. J. Kailath, and N. Sharma (2004), Calcretes in the thar desert: genesis, chronology and palaeoenvironment, *Journal of Earth System Science*, 113(3), 473–515.
- Duplessy, J. C. (1982), Glacial to interglacial contrasts in the northern indian ocean.
- Dutt, S., A. K. Gupta, S. C. Clemens, H. Cheng, R. K. Singh, G. Kathayat, and R. L. Edwards (2015), Abrupt changes in Indian summer monsoon strength during 33,800 to 5500 years B.P., pp. 1–7, doi:10.1002/2015GL064015. Received.
- Dutta, K., R. Bhushan, and B. Somayajulu (2001), Delta r correction values for the northern indian ocean., *Radiocarbon*, 43(2A), 483–488.
- Dykoski, C. A., R. L. Edwards, H. Cheng, D. Yuan, Y. Cai, M. Zhang, Y. Lin, J. Qing, Z. An, and J. Revenaugh (2005), A high-resolution, absolute-dated holocene and deglacial asian monsoon record from dongge cave, china, *Earth and Planetary Science Letters*, 233(1), 71–86.
- Edwards, R. L., J. Chen, and G. Wasserburg (1987), 238 u 234 u 230 th 232 th systematics and the precise measurement of time over the past 500,000 years, *Earth and Planetary Science Letters*, 81(2), 175–192.
- Eggins, S., J. Woodhead, L. Kinsley, G. Mortimer, P. Sylvester, M. McCulloch, J. Hergt, and M. Handler (1997), A simple method for the precise determination of ≥ 40 trace elements in geological samples by icpms using enriched isotope

- internal standardisation, *Chemical Geology*, 134(4), 311–326.
- Elmer, P. (2001), The 30-minute guide to icp-ms, *Perkin Elmer, Shelton CT*.
- Emeis, K.-C., D. M. Anderson, H. Doose, D. Kroon, and D. Schulz-Bull (1995), Sea-surface temperatures and the history of monsoon upwelling in the north-west arabian sea during the last 500,000 years, *Quaternary Research*, 43(3), 355–361.
- Emiliani, C. (1955), Pleistocene temperatures, *The Journal of Geology*, pp. 538–578.
- Enzel, Y., L. Ely, S. Mishra, R. Ramesh, R. Amit, B. Lazar, S. Rajaguru, V. Baker, and A. Sandler (1999), High-resolution holocene environmental changes in the thar desert, northwestern india, *Science*, 284(5411), 125–128.
- Epstein, S., R. Buchsbaum, H. A. Lowenstam, and H. C. Urey (1953), Revised carbonate-water isotopic temperature scale, *Geological Society of America Bulletin*, 64(11), 1315–1326.
- Fairchild, I. J., and P. C. Treble (2009), Trace elements in speleothems as recorders of environmental change, *Quaternary Science Reviews*, 28(5), 449–468.
- Fairchild, I. J., A. Borsato, A. F. Tooth, S. Frisia, C. J. Hawkesworth, Y. Huang, F. McDermott, and B. Spiro (2000), Controls on trace element (sr–mg) compositions of carbonate cave waters: implications for speleothem climatic records, *Chemical Geology*, 166(3), 255–269.
- Fairchild, I. J., A. Baker, A. Borsato, S. Frisia, R. W. Hinton, F. McDERMOTT, and A. F. Tooth (2001), Annual to sub-annual resolution of multiple trace-element trends in speleothems, *Journal of the Geological Society*, 158(5), 831–841.
- Fairchild, I. J., C. L. Smith, A. Baker, L. Fuller, C. Spotl, D. Matthey, F. McDermott, et al. (2006), Modification and preservation of environmental signals in speleothems, *Earth-Science Reviews*, 75(1), 105–153.
- Farquhar, G. D., J. R. Ehleringer, and K. T. Hubick (1989), Carbon isotope discrimination and photosynthesis, *Annual review of plant biology*, 40(1), 503–537.
- Faure, G. (1977), Principles of isotope geology.
- Fleitmann, D., S. J. Burns, M. Mudelsee, U. Neff, J. Kramers, A. Mangini,

- and A. Matter (2003), Holocene forcing of the indian monsoon recorded in a stalagmite from southern oman, *Science*, *300*(5626), 1737–1739.
- Fleitmann, D., S. J. Burns, A. Mangini, M. Mudelsee, J. Kramers, I. Villa, U. Neff, A. A. Al-Subbary, A. Buettner, D. Hippler, et al. (2007), Holocene itcz and indian monsoon dynamics recorded in stalagmites from oman and yemen (socotra), *Quaternary Science Reviews*, *26*(1), 170–188.
- Foley, J. A., J. E. Kutzbach, M. T. Coe, and S. Levis (1994), Feedbacks between climate and boreal forests during the holocene epoch.
- Frisia, S., A. Borsato, I. J. Fairchild, F. McDermott, and E. M. Selmo (2002), Aragonite-calcite relationships in speleothems (grotte de clamouse, france): environment, fabrics, and carbonate geochemistry, *Journal of Sedimentary Research*, *72*(5), 687–699.
- Fritts, H. (1976), Tree rings and climate (academic, new york).
- Gabitov, R., and E. Watson (2006), Partitioning of strontium between calcite and fluid, *Geochemistry, Geophysics, Geosystems*, *7*(11).
- Gadgil, S. (2003), The Indian Monsoon and Its Variability, *Annu. Rev. Earth Planet. Sci.*, *31*(1), 429–467, doi:10.1146/annurev.earth.31.100901.141251.
- Gascoyne, M. (1983), Trace-element partition coefficients in the calcite-water system and their paleoclimatic significance in cave studies, *Journal of Hydrology*, *61*(1), 213–222.
- Gascoyne, M. (1992), Palaeoclimate determination from cave calcite deposits, *Quaternary Science Reviews*, *11*(6), 609–632.
- Gasse, F., and E. Van Campo (1994), Abrupt post-glacial climate events in west asia and north africa monsoon domains, *Earth and Planetary Science Letters*, *126*(4), 435–456.
- Gibling, M., S. Tandon, R. Sinha, and M. Jain (2005), Discontinuity-bounded alluvial sequences of the southern gangetic plains, india: aggradation and degradation in response to monsoonal strength, *Journal of Sedimentary Research*, *75*(3), 369–385.
- Gibling, M., R. Sinha, N. Roy, S. Tandon, and M. Jain (2008), Quaternary fluvial and eolian deposits on the belan river, india: paleoclimatic setting of paleolithic to neolithic archeological sites over the past 85,000 years, *Quaternary Science Reviews*, *27*(3), 391–410.

- Giosan, L., P. D. Clift, M. G. Macklin, D. Q. Fuller, S. Constantinescu, J. A. Durcan, T. Stevens, G. A. Duller, A. R. Tabrez, K. Gangal, et al. (2012), Fluvial landscapes of the harappan civilization, *Proceedings of the National Academy of Sciences*, *109*(26), E1688–E1694.
- Gonfiantini, R. (1978), Standards for stable isotope measurements in natural compounds.
- Gonfiantini, R., W. Stichler, and K. Rozanski (1995), Standards and intercomparison materials distributed by the international atomic energy agency for stable isotope measurements.
- Goodbred, S. L. (2003), Response of the ganges dispersal system to climate change: a source-to-sink view since the last interstade, *Sedimentary Geology*, *162*(1), 83–104.
- Goodbred, S. L., and S. A. Kuehl (2000), Enormous ganges-brahmaputra sediment discharge during strengthened early holocene monsoon, *Geology*, *28*(12), 1083–1086.
- Govil, P., and P. D. Naidu (2010), Evaporation-precipitation changes in the eastern Arabian Sea for the last 68 ka: Implications on monsoon variability, *Paleoceanography*, *25*, 1–11, doi:10.1029/2008PA001687.
- Govil, P., and P. D. Naidu (2011), Variations of indian monsoon precipitation during the last 32kyr reflected in the surface hydrography of the western bay of bengal, *Quaternary Science Reviews*, *30*(27), 3871–3879.
- Grootes, P. M., and M. Stuiver (1997), Oxygen 18/16 variability in Greenland snow and ice with 10⁻³ - to 10⁵ -year time resolution, *J. Geophys. Res. Ocean.*, *102*(C12), 26,455–26,470, doi:10.1029/97JC00880.
- Grootes, P. M., M. Stuiver, J. W. C. White, S. Johnsen, and J. Jouzel (1993), Comparison of oxygen isotope records from the GISP2 and GRIP Greenland ice cores, *Nature*, *366*(6455), 552–554, doi:10.1038/366552a0.
- Gupta, A. K., D. M. Anderson, and J. T. Overpeck (2003), Abrupt changes in the asian southwest monsoon during the holocene and their links to the north atlantic ocean, *Nature*, *421*(6921), 354–357.
- Gupta, A. K., M. Das, and D. M. Anderson (2005), Solar influence on the Indian summer monsoon during the Holocene, *Geophys. Res. Lett.*, *32*(17), L17,703, doi:10.1029/2005GL022685.
- Gupta, S., and H. Polach (1985), *Radiocarbon Dating Practices at ANU*, 113–114,

173 pp.

- Haug, G. H., K. A. Hughen, D. M. Sigman, L. C. Peterson, and U. Röhl (2001), Southward migration of the intertropical convergence zone through the holocene, *Science*, *293*(5533), 1304–1308.
- Hellstrom, J. (2006), U–th dating of speleothems with high initial 230 th using stratigraphical constraint, *Quaternary Geochronology*, *1*(4), 289–295.
- Henderson, G. M. (2006), Caving in to new chronologies, *Science*, *313*(5787), 620–622.
- Hendy, C. (1971), The isotopic geochemistry of speleothems—I. The calculation of the effects of different modes of formation on the isotopic composition of speleothems and their applicability as palaeoclimatic indicators, *Geochim. Cosmochim. Acta*, *35*(8), 801–824, doi:10.1016/0016-7037(71)90127-X.
- Hendy, C., and A. Wilson (1968), Palaeoclimatic data from speleothems.
- Holland, H. D., T. V. Kirsipu, J. S. Huebner, and U. M. Oxburgh (1964), On some aspects of the chemical evolution of cave waters, *The Journal of Geology*, pp. 36–67.
- Horwitz, E. P., M. L. Dietz, R. Chiarizia, H. Diamond, A. M. Essling, and D. Graczyk (1992), Separation and preconcentration of uranium from acidic media by extraction chromatography, *Analytica Chimica Acta*, *266*(1), 25–37.
- Huang, Y., I. J. Fairchild, A. Borsato, S. Frisia, N. J. Cassidy, F. McDermott, and C. J. Hawkesworth (2001), Seasonal variations in sr, mg and p in modern speleothems (grotta di ernesto, italy), *Chemical Geology*, *175*(3), 429–448.
- Imbrie, J., and K. P. Imbrie (1986), *Ice ages: solving the mystery*, Harvard University Press.
- Ivanochko, T. S., R. S. Ganeshram, G.-J. A. Brummer, G. Ganssen, S. J. Jung, S. G. Moreton, and D. Kroon (2005), Variations in tropical convection as an amplifier of global climate change at the millennial scale, *Earth and Planetary Science Letters*, *235*(1), 302–314.
- Jacoby Jr, G., R. D'Arrigo, et al. (1990), Teak (*tectona grandis* lf), a tropical species of large-scale dendroclimatic potential., *Dendrochronologia*, *8*, 83–98.
- Jain, M., S. Tandon, A. Singhvi, S. Mishra, and S. Bhatt (2005), Quaternary alluvial stratigraphical development in a desert setting: a case study from the luni river basin, thar desert of western india, *Fluvial Sedimentology VII*,

- International Association of Sedimentologists. Special Publication, 35*, 349–371.
- Johnsen, S. J., D. Dahl-Jensen, N. Gundestrup, J. P. Steffensen, H. B. Clausen, H. Miller, V. Masson-Delmotte, A. E. Sveinbjörnsdottir, and J. White (2001), Oxygen isotope and palaeotemperature records from six greenland ice-core stations: Camp century, dye-3, grip, gisp2, renland northgrip, *Journal of Quaternary Science*, *16*(4), 299–307.
- Johnson, K. R. (2011), Long-distance relationship, *Nature Geoscience*, *4*, 426–427.
- Johnson, K. R., C. Hu, N. S. Belshaw, and G. M. Henderson (2006), Seasonal trace-element and stable-isotope variations in a chinese speleothem: the potential for high-resolution paleomonsoon reconstruction, *Earth and Planetary Science Letters*, *244*(1), 394–407.
- Jones, P. D. (1995), *Climate since AD 1500*, Psychology Press.
- Jung, S. J., D. Kroon, G. Ganssen, F. Peeters, and R. Ganeshram (2009), Enhanced arabian sea intermediate water flow during glacial north atlantic cold phases, *Earth and Planetary Science Letters*, *280*(1), 220–228.
- Juyal, N., L. Chamyal, S. Bhandari, R. Bhushan, and A. Singhvi (2006), Continental record of the southwest monsoon during the last 130ka: evidence from the southern margin of the thar desert, india, *Quaternary Science Reviews*, *25*(19), 2632–2650.
- Kalnay, E., M. Kanamitsu, R. Kistler, W. Collins, D. Deaven, L. Gandin, M. Iredell, S. Saha, G. White, J. Woollen, et al. (1996), The ncep/ncar 40-year reanalysis project, *Bulletin of the American meteorological Society*, *77*(3), 437–471.
- Kanamitsu, M., W. Ebisuzaki, J. Woollen, S.-K. Yang, J. J. Hnilo, M. Fiorino, and G. L. Potter (2002), NCEP–DOE AMIP-II Reanalysis (R-2), *Bull. Am. Meteorol. Soc.*, *83*(11), 1631–1643, doi:10.1175/BAMS-83-11-1631.
- Kar, A., A. Singhvi, S. Rajaguru, N. Juyal, J. Thomas, D. Banerjee, and R. Dhir (2001), Reconstruction of the late quaternary environment of the lower luni plains, thar desert, india, *Journal of Quaternary Science*, *16*(1), 61–68.
- Kay, G. F. (1931), Classification and duration of the pleistocene period, *Geological Society of America Bulletin*, *42*(1), 425–466.
- Kenoyer, J. M. (1998), *Ancient cities of the Indus valley civilization*, Oxford University Press; American Institute of Pakistan Studies.

- Kessarkar, P. M., V. Purnachadra Rao, S. W. A. Naqvi, and S. G. Karapurkar (2013), Variation in the Indian summer monsoon intensity during the Bølling-Ållerød and Holocene, *Paleoceanography*, *28*(3), 413–425, doi:10.1002/palo.20040.
- Khadkikar, A. S., L. Chamyal, and R. Ramesh (2000), The character and genesis of calcrete in late quaternary alluvial deposits, gujarat, western india, and its bearing on the interpretation of ancient climates, *Palaeogeography, Palaeoclimatology, Palaeoecology*, *162*(3), 239–261.
- Klimchouk, A. (2000), The formation of epikarst and its role in vadose speleogenesis, *Speleogenesis: Evolution of Karst Aquifers, National Speleological Society: Huntsville*, pp. 91–99.
- Kotlia, B. S., A. K. Singh, L. M. Joshi, and B. S. Dhaila (2014), Precipitation variability in the Indian Central Himalaya during last ca. 4,000 years inferred from a speleothem record: Impact of Indian Summer Monsoon (ISM) and Westerlies, *Quat. Int.*, doi:10.1016/j.quaint.2014.10.066.
- Kress, A., M. Saurer, U. Büntgen, K. S. Treydte, H. Bugmann, and R. T. Siegwolf (2009), Summer temperature dependency of larch budmoth outbreaks revealed by alpine tree-ring isotope chronologies, *Oecologia*, *160*(2), 353–365.
- Krishnan, R., K. Ramesh, B. Samala, G. Meyers, J. Slingo, and M. Fennessy (2006), Indian ocean-monsoon coupled interactions and impending monsoon droughts, *Geophysical research letters*, *33*(8).
- Kudrass, H., A. Hofmann, H. Doose, K. Emeis, and H. Erlenkeuser (2001), Modulation and amplification of climatic changes in the northern hemisphere by the indian summer monsoon during the past 80 ky, *Geology*, *29*(1), 63–66.
- Kumar, K. K., B. Rajagopalan, and M. A. Cane (1999), On the weakening relationship between the indian monsoon and enso, *Science*, *284*(5423), 2156–2159.
- Lachniet, M. S. (2009), Climatic and environmental controls on speleothem oxygen-isotope values, *Quat. Sci. Rev.*, *28*(5-6), 412–432, doi:10.1016/j.quascirev.2008.10.021.
- Laskar, A. H., S. Raghav, M. G. Yadava, R. A. Jani, A. C. Narayana, and R. Ramesh (2011), Potential of Stable Carbon and Oxygen Isotope Variations of Speleothems from Andaman Islands, India, for Paleomonsoon Reconstruction, *J. Geol. Res.*, *2011*, 1–7, doi:10.1155/2011/272971.
- Laskar, A. H., M. G. Yadava, R. Ramesh, V. J. Polyak, and Y. Asmerom (2013),

- A 4 kyr stalagmite oxygen isotopic record of the past Indian Summer Monsoon in the Andaman Islands, *Geochemistry, Geophys. Geosystems*, 14(9), 3555–3566, doi:10.1002/ggge.20203.
- Lauritzen, S.-E. (1995), High-resolution paleotemperature proxy record for the last interglaciation based on norwegian speleothems, *Quaternary Research*, 43(2), 133–146.
- Lauritzen, S.-E., and J. Lundberg (1999), Calibration of the speleothem delta function: an absolute temperature record for the holocene in northern norway, *The Holocene*, 9(6), 659–669.
- Lekshmy, P. R. (2015), Stable isotopic studies on monsoon vapour/clouds and precipitation over kerala, *Thesis submitted to MOHANLAL SUKHADIA UNIVERSITY*, p. 133.
- Leuschner, D. C., and F. Sirocko (2000), The low-latitude monsoon climate during dansgaard–oeschger cycles and heinrich events, *Quaternary Science Reviews*, 19(1), 243–254.
- Lisiecki, L. E., and M. E. Raymo (2005), A pliocene-pleistocene stack of 57 globally distributed benthic $\delta^{18}O$ records, *Paleoceanography*, 20(1).
- Lone, M. A., S. M. Ahmad, N. C. Dung, C. C. Shen, W. Raza, and A. Kumar (2014), Speleothem based 1000-year high resolution record of Indian monsoon variability during the last deglaciation, *Palaeogeogr. Palaeoclimatol. Palaeoecol.*, 395, 1–8, doi:10.1016/j.palaeo.2013.12.010.
- Ludwig, K. (2003), Mathematical–statistical treatment of data and errors for 230th/u geochronology, *Reviews in Mineralogy and Geochemistry*, 52(1), 631–656.
- Lutgens, F., and E. Tarbuck (2000), vol. 8th edition.
- Maharashtra-Government (1973), Report of the fact finding committee for survey of scarcity areas maharashtra state, *Mumbai, India*, p. 310.
- Maharatna, A. (1996), The demography of famines: an indian historical perspective.
- Maheshwari, A., A. Sial, R. Guhey, and V. Ferreira (2005), C-isotope composition of carbonates from indravati basin, india: Implications for regional stratigraphic correlation, *Gondwana Research*, 8(4), 603–610.
- Managave, S., and R. Ramesh (2012), Isotope dendroclimatology: A review with

- a special emphasis on tropics, in *Handbook of Environmental Isotope Geochemistry*, pp. 811–833, Springer.
- Managave, S., M. Sheshshayee, R. Ramesh, H. Borgaonkar, S. Shah, and A. Bhattacharyya (2011a), Response of cellulose oxygen isotope values of teak trees in differing monsoon environments to monsoon rainfall, *Dendrochronologia*, *29*(2), 89–97.
- Managave, S. R., M. S. Sheshshayee, H. P. Borgaonkar, and R. Ramesh (2010), Past break-monsoon conditions detectable by high resolution intra-annual $\delta^{18}\text{O}$ analysis of teak rings, *Geophys. Res. Lett.*, *37*(5), doi:10.1029/2009GL041172.
- Managave, S. R., M. S. Sheshshayee, A. Bhattacharyya, and R. Ramesh (2011b), Intra-annual variations of teak cellulose $\delta^{18}\text{O}$ in Kerala, India: Implications to the reconstruction of past summer and winter monsoon rains, *Clim. Dyn.*, *37*, 555–567, doi:10.1007/s00382-010-0917-9.
- Mann, M. E., R. S. Bradley, and M. K. Hughes (1999), Northern hemisphere temperatures during the past millennium: inferences, uncertainties, and limitations, *Geophysical research letters*, *26*(6), 759–762.
- Mason, A. J., and G. M. Henderson (2010), Correction of multi-collector-icp-ms instrumental biases in high-precision uranium–thorium chronology, *International Journal of Mass Spectrometry*, *295*(1), 26–35.
- Mattinson, J. (2000), Revising the “gold standard”—the uranium decay constants of jaffey et al., 1971, *EOS, Transactions of the American Geophysical Union*, *81*, S444.
- Mayewski, P. A., E. E. Rohling, J. C. Stager, W. Karlén, K. A. Maasch, L. D. Meeker, E. A. Meyerson, F. Gasse, S. van Kreveld, K. Holmgren, et al. (2004), Holocene climate variability, *Quaternary research*, *62*(3), 243–255.
- McCarroll, D., and N. J. Loader (2004), Stable isotopes in tree rings, *Quaternary Science Reviews*, *23*(7), 771–801.
- McClure, H. (1976), Radiocarbon chronology of late quaternary lakes in the arabian desert.
- McDermott, F., H. Schwarcz, and P. J. Rowe (2006), *Isotopes in speleothems*, Springer.
- McDonald, J., R. Drysdale, D. Hill, R. Chisari, and H. Wong (2007), The hydrochemical response of cave drip waters to sub-annual and inter-annual climate

- variability, wombeyan caves, se australia, *Chemical Geology*, 244(3), 605–623.
- McMillan, E. A., I. J. Fairchild, S. Frisia, A. Borsato, and F. McDERMOTT (2005), Annual trace element cycles in calcite–aragonite speleothems: evidence of drought in the western mediterranean 1200–1100 yr bp, *Journal of Quaternary Science*, 20(5), 423–433.
- Meehl, G. A. (1994), Influence of the land surface in the asian summer monsoon: External conditions versus internal feedbacks, *Journal of climate*, 7(7), 1033–1049.
- Midhun, M., and R. Ramesh (2015), Validation of $\delta^{18}\text{O}$ as a proxy for past monsoon rain by multi-GCM simulations, *Clim. Dyn.*, doi:10.1007/s00382-015-2652-8.
- Midhun, M., P. Lekshmy, R. Ramesh, K. Yoshimura, K. Sandeep, S. Kumar, R. Sinha, Ashutosh Singh, and S. Srivastava (2016), The effect of monsoon circulation on the stable isotopic composition of rainfall, *J. Geophys. Res.*, p. under review.
- Mook, W. G. (2006), *Introduction to isotope hydrology*, Taylor & Francis.
- Moore, G. (1952), Speleothem—a new cave term, *National Speleological Society News*, 10(6), 2.
- Morrill, C., J. T. Overpeck, and J. E. Cole (2003), A synthesis of abrupt changes in the asian summer monsoon since the last deglaciation, *The Holocene*, 13(4), 465–476.
- Morse, J. W., and M. L. Bender (1990), Partition coefficients in calcite: Examination of factors influencing the validity of experimental results and their application to natural systems, *Chemical Geology*, 82, 265–277.
- Murphy, J., P. Whetton, and A. Ritsema (1989), A re-analysis of a tree ring chronology from java, *Proceedings of the Koninklijke Nederlandse Akademie van Wetenschappen. Series B. Palaeontology, geology, physics, chemistry, anthropology*, 92(3), 241–257.
- Murray, J. W. (1954), The deposition of calcite and aragonite in caves, *The Journal of Geology*, pp. 481–492.
- Naidu, P. D., and B. A. Malmgren (2005), Seasonal sea surface temperature contrast between the holocene and last glacial period in the western arabian sea (ocean drilling project site 723a): Modulated by monsoon upwelling, *Paleoceanography*, 20(1).

- Neff, U., S. Burns, A. Mangini, M. Mudelsee, D. Fleitmann, and A. Matter (2001), Strong coherence between solar variability and the monsoon in oman between 9 and 6 kyr ago, *Nature*, *411*(6835), 290–293.
- Newton, A., R. Thunell, and L. Stott (2006), Climate and hydrographic variability in the indo-pacific warm pool during the last millennium, *Geophysical Research Letters*, *33*(19).
- O’Brien, S., P. Mayewski, L. Meeker, D. Meese, M. Twickler, and S. Whitlow (1995), Complexity of holocene climate as reconstructed from a greenland ice core.
- O’Neil, J. R., R. N. Clayton, and T. K. Mayeda (1969), Oxygen isotope fractionation in divalent metal carbonates., *Tech. rep.*, Univ. of Chicago.
- Ortiz, J., T. Guilderson, M. Sarnthein, et al. (2000), Coherent high-and low-latitude climate variability during the holocene warm period, *Science*, *288*(5474), 2198–2202.
- Overpeck, J., D. Anderson, S. Trumbore, and W. Prell (1996), The southwest Indian Monsoon over the last 18 000 years, *Clim. Dyn.*, *12*(3), 213–225, doi: 10.1007/BF00211619.
- Paillard, D., L. Labeyrie, and P. Yiou (1996), Macintosh program performs time-series analysis, *Eos, Transactions American Geophysical Union*, *77*(39), 379–379.
- Panarello, H. O., M. C. Albero, and F. E. Angiolini (1983), Stable isotope fractionation during benzene synthesis for radiocarbon dating., *Radiocarbon*, *25*(2), 529–532.
- Pant, G., and H. Borgaonkar (1983), Growth rings of teak trees and regional climatology, *Environ. Manag. Ed. by L.R Singh, R.C.Tiwari R.P.Srivastav, Allahabad Geogr. Soc. India*, pp. 153–155.
- Pant, G., K. Rupa Kumar, N. Sontakke, and H. Borgaonkar (1993), Climate variability over india on century and longer time scales, *Tropical Meteorology. Tata McGraw-Hill, New Delhi, India*, pp. 149–158.
- Pausata, F. S., D. S. Battisti, K. H. Nisancioglu, and C. M. Bitz (2011), Chinese stalagmite [$\delta^{18}O$] controlled by changes in the indian monsoon during a simulated heinrich event, *Nature Geoscience*, *4*(7), 474–480.
- Perrette, Y., J.-J. Delannoy, H. Bolvin, M. Cordonnier, J.-L. Destombes, E. A. Zhilinskaya, and A. Aboukais (2000), Comparative study of a stalagmite sample

- by stratigraphy, laser induced fluorescence spectroscopy, epr spectrometry and reflectance imaging, *Chemical Geology*, 162(3), 221–243.
- Pokharia, A. K., J. S. Kharakwal, and A. Srivastava (2014), Archaeobotanical evidence of millets in the Indian subcontinent with some observations on their role in the Indus civilization, *J. Archaeol. Sci.*, 42, 442–455, doi:10.1016/j.jas.2013.11.029.
- Polach, H., J. Gower, I. Fraser, and T. Rafter (1972), Synthesis of high purity benzene for radiocarbon dating, *Tech. rep.*, Australian National Univ., Canberra; comp.
- Ponton, C. (2012), Aridification of the indian subcontinent during the holocene: implications for landscape evolution, sedimentation, carbon cycle, and human civilizations, Ph.D. thesis, Massachusetts Institute of Technology.
- Ponton, C., L. Giosan, T. I. Eglinton, D. Q. Fuller, J. E. Johnson, P. Kumar, and T. S. Collett (2012), Holocene aridification of india, *Geophysical Research Letters*, 39(3).
- Possehl, G. L. (2002), *The Indus civilization: A contemporary perspective*, Rowman Altamira.
- Potts, P. J. (2012), *A handbook of silicate rock analysis*, Springer Science & Business Media.
- Prabhu, C., R. Shankar, K. Anupama, M. Taieb, R. Bonnefille, L. Vidal, and S. Prasad (2004), A 200-ka pollen and oxygen-isotopic record from two sediment cores from the eastern Arabian Sea, *Palaeogeogr. Palaeoclimatol. Palaeoecol.*, 214(4), 309–321, doi:10.1016/j.palaeo.2004.07.027.
- Prasad, S., and Y. Enzel (2006), Holocene paleoclimates of india, *Quaternary Research*, 66(3), 442–453.
- Prell, W. L., and J. E. Kutzbach (1987), Monsoon variability over the past 150,000 years, *Journal of Geophysical Research: Atmospheres*, 92(D7), 8411–8425.
- Pumijumnong, N., D. Eckstein, and U. Sass (1995), Tree-ring research on tectona grandis in northern thailand, *Iawa Journal*, 16(4), 385–392.
- Railsback, L. B., G. A. Brook, J. Chen, R. Kalin, and C. J. Fleisher (1994), Environmental controls on the petrology of a late holocene speleothem from botswana with annual layers of aragonite and calcite, *Journal of Sedimentary Research*, 64(1).

- Rajeevan, M., S. Gadgil, and J. Bhate (2010), Active and break spells of the indian summer monsoon, *Journal of earth system science*, *119*(3), 229–247.
- Ramesh, R., S. Bhattacharya, and K. Gopalan (1986), Stable isotope systematics in tree cellulose as palaeoenvironmental indicators-a review, *Geological Society of India*, *27*(1), 154–167.
- Ramesh, R., S. Bhattacharya, and G. Pant (1989), Climatic significance of δd variations in a tropical tree species from india.
- Ramesh, R., M. Tiwari, S. Chakraborty, S. R. Managave, M. G. Yadava, and D. Sinha (2010), Retrieval of south Asian monsoon variation during the Holocene from natural climatic archives, *Curr. Sci.*, *99*(12), 1770–1786.
- Rao, V. P., P. M. Kessarkar, M. Thamban, and S. K. Patil (2010), Paleoclimatic and diagenetic history of the late quaternary sediments in a core from the Southeastern Arabian Sea: Geochemical and magnetic signals, *J. Oceanogr.*, *66*, 133–146, doi:10.1007/s10872-010-0011-2.
- Rashid, H., B. Flower, R. Poore, and T. Quinn (2007), A 25ka indian ocean monsoon variability record from the andaman sea, *Quaternary Science Reviews*, *26*(19), 2586–2597.
- Reichert, G. J., M. den Dulk, H. J. Visser, C. H. van der Weijden, and W. J. Zachariasse (1997), A 225 kyr record of dust supply, paleoproductivity and the oxygen minimum zone from the murray ridge (northern arabian sea), *Palaeogeography, Palaeoclimatology, Palaeoecology*, *134*(1), 149–169.
- Reimer, P. J., M. G. Baillie, E. Bard, A. Bayliss, J. W. Beck, P. G. Blackwell, R. C. Bronk, C. E. Buck, G. S. Burr, R. L. Edwards, et al. (2009), Intcal09 and marine09 radiocarbon age calibration curves, 0-50,000 years cal bp.
- Repinski, P., K. Holmgren, S. Lauritzen, and J. Lee-Thorp (1999), A late holocene climate record from a stalagmite, cold air cave, northern province, south africa, *Palaeogeography, Palaeoclimatology, Palaeoecology*, *150*(3), 269–277.
- Richards, D. A., and J. A. Dorale (2003), Uranium-series chronology and environmental applications of speleothems, *Reviews in Mineralogy and Geochemistry*, *52*(1), 407–460.
- Richter, D. K., T. Götte, S. Niggemann, and G. Wurth (2004), REE³⁺ and Mn²⁺ activated cathodoluminescence in lateglacial and Holocene stalagmites of central Europe: evidence for climatic processes?, *The Holocene*, *14*(5), 759–767, doi:10.1191/0959683604hl754rp.

- Risi, C., S. Bony, and F. Vimeux (2008), Influence of convective processes on the isotopic composition ($\delta^{18}\text{O}$ and δd) of precipitation and water vapor in the tropics: 2. physical interpretation of the amount effect, *Journal of Geophysical Research: Atmospheres*, 113(D19).
- Roy, N., R. Sinha, and M. Gibling (2012), Aggradation, incision and interfluvial flooding in the Ganga valley over the past 100,000 years: testing the influence of monsoonal precipitation, *Palaeogeography, Palaeoclimatology, Palaeoecology*, 356, 38–53.
- Rozanski, K., L. Araguás-Araguás, and R. Gonfiantini (1993), Isotopic patterns in modern global precipitation, *Climate change in continental isotopic records*, pp. 1–36.
- Rudge, J. F., B. C. Reynolds, and B. Bourdon (2009), The double spike toolbox, *Chemical Geology*, 265(3), 420–431.
- Sano, M., M. Sheshshayee, S. Managave, R. Ramesh, R. Sukumar, and T. Sweda (2010), Climatic potential of $\delta^{18}\text{O}$ of *Abies spectabilis* from the Nepal Himalaya, *Dendrochronologia*, 28(2), 93–98.
- Sanwal, J., B. S. Kotlia, C. Rajendran, S. M. Ahmad, K. Rajendran, and M. Sandiford (2013), Climatic variability in Central Indian Himalaya during the last ~1800 years: Evidence from a high resolution speleothem record, *Quat. Int.*, 304, 183–192, doi:10.1016/j.quaint.2013.03.029.
- Sanyal, P., and R. Sinha (2010), Evolution of the Indian summer monsoon: synthesis of continental records, *Geological Society, London, Special Publications*, 342(1), 153–183.
- Saraswat, R., D. W. Lea, R. Nigam, A. Mackensen, and D. K. Naik (2013), Deglaciation in the tropical Indian Ocean driven by interplay between the regional monsoon and global teleconnections, *Earth Planet. Sci. Lett.*, 375, 166–175, doi:10.1016/j.epsl.2013.05.022.
- Sarkar, A., R. Ramesh, S. Bhattacharya, and G. Rajagopalan (1990), Oxygen isotope evidence for a stronger winter monsoon current during the last glaciation, *Nature*, 343(6258), 549–551.
- Sarkar, A., R. Ramesh, B. L. K. Somayajulu, R. Agnihotri, A. J. T. Jull, and O. S. Burr (2000), High resolution Holocene monsoon record from the eastern Arabian Sea, *Earth Planet. Sci. Lett.*, 177, 209–218, doi:10.1016/S0012-821X(00)00053-4.

- Sarkar, S., S. Prasad, H. Wilkes, N. Riedel, M. Stebich, N. Basavaiah, and D. Sachse (2015), Monsoon source shifts during the drying mid-holocene: Biomarker isotope based evidence from the core 'monsoon zone'(cmz) of india, *Quaternary Science Reviews*, 123, 144–157.
- Sasowsky, I. D., and J. Mylroie (2007), *Studies of cave sediments: physical and chemical records of paleoclimate*, Springer Science & Business Media.
- Schmidt, G. A., A. N. LeGrande, and G. Hoffmann (2007), Water isotope expressions of intrinsic and forced variability in a coupled ocean-atmosphere model, *Journal of Geophysical Research: Atmospheres*, 112(D10).
- Scholz, D., and D. Hoffmann (2008), 230th/u-dating of fossil corals and speleothems, *Quat. Sci. J*, 57, 52.
- Scholz, D., D. L. Hoffmann, J. Hellstrom, and C. B. Ramsey (2012), A comparison of different methods for speleothem age modelling, *Quaternary Geochronology*, 14, 94–104.
- Schulz, H., U. von Rad, and H. Erlenkeuser (1998), Correlation between arabian sea and greenland climate oscillations of the past 110,000 years, *Nature*, 393(6680), 54–57.
- Schulz, H., K.-C. Emeis, H. Erlenkeuser, U. von Rad, and C. Rolf (2002), The Toba Volcanic Event and Interstadial/Stadial Climates at the Marine Isotopic Stage 5 to 4 Transition in the Northern Indian Ocean, *Quat. Res.*, 57(1), 22–31, doi:10.1006/qres.2001.2291.
- Schulz, M., and A. Paul (2002), Holocene climate variability on centennial-to-millennial time scales: 1. climate records from the north-atlantic realm, in *Climate development and history of the North Atlantic realm*, pp. 41–54, Springer.
- Schwarcz, H. (1986), Geochronology and isotopic geochemistry of speleothems, *Handbook of environmental isotope geochemistry*, 2, 271–303.
- Seth, B., M. F. Thirlwall, S. L. Houghton, and C.-A. Craig (2003), Accurate measurements of th–u isotope ratios for carbonate geochronology using mc-icp-ms, *Journal of Analytical Atomic Spectrometry*, 18(11), 1323–1330.
- Shackleton, N. (1987), Oxygen isotopes, ice volume and sea level, *Quaternary Science Reviews*, 6(3), 183–190.
- Shackleton, N., and N. Opdyke (1976), Oxygen-isotope and paleomagnetic stratigraphy of pacific core v28-239 late pliocene to latest pleistocene, *Geological Society of America Memoirs*, 145, 449–464.

- Shah, S. K., A. Bhattacharyya, and V. Chaudhary (2007), Reconstruction of June–September precipitation based on tree-ring data of teak (*Tectona grandis* L.) from Hoshangabad, Madhya Pradesh, India, *Dendrochronologia*, *25*(1), 57–64, doi:10.1016/j.dendro.2007.02.001.
- Sharma, S., M. Joachimski, M. Sharma, H. Tobschall, I. Singh, C. Sharma, M. Chauhan, and G. Morgenroth (2004), Lateglacial and holocene environmental changes in ganga plain, northern india, *Quaternary Science Reviews*, *23*(1), 145–159.
- Shen, C.-C., R. L. Edwards, H. Cheng, J. A. Dorale, R. B. Thomas, S. B. Moran, S. E. Weinstein, and H. N. Edmonds (2002), Uranium and thorium isotopic and concentration measurements by magnetic sector inductively coupled plasma mass spectrometry, *Chemical Geology*, *185*(3), 165–178.
- Sijinkumar, A., B. N. Nath, and M. Guptha (2010), Late quaternary record of pteropod preservation from the andaman sea, *Marine Geology*, *275*(1), 221–229.
- Sijinkumar, A., B. N. Nath, G. Possnert, and A. Aldahan (2011), Pulleniatina minimum events in the andaman sea (ne indian ocean): Implications for winter monsoon and thermocline changes, *Marine Micropaleontology*, *81*(3), 88–94.
- Sikka, D. R., and S. Gadgil (1980), On the Maximum Cloud Zone and the ITCZ over Indian, Longitudes during the Southwest Monsoon, doi:10.1175/1520-0493(1980)108<1840:OTMCZA>2.0.CO;2.
- Singh, A., D. Kroon, and R. Ganeshram (2006), Millennial scale variations in productivity and omz intensity in the eastern arabian sea, *JOURNAL-GEOLOGICAL SOCIETY OF INDIA*, *68*(3), 369.
- Singhvi, A., and A. Kar (2004), The aeolian sedimentation record of the thar desert, *Journal of Earth System Science*, *113*(3), 371–401.
- Sinha, A., K. G. Cannariato, L. D. Stott, H.-C. Li, C.-F. You, H. Cheng, R. L. Edwards, and I. B. Singh (2005), Variability of southwest indian summer monsoon precipitation during the bølling-ållerød, *Geology*, *33*(10), 813–816.
- Sinha, A., K. G. Cannariato, L. D. Stott, H. Cheng, R. L. Edwards, M. G. Yadava, R. Ramesh, and I. B. Singh (2007), A 900-year (600 to 1500 ad) record of the indian summer monsoon precipitation from the core monsoon zone of india, *Geophysical Research Letters*, *34*(16).
- Sinha, A., M. Berkelhammer, L. Stott, M. Mudelsee, H. Cheng, and J. Biswas

- (2011), The leading mode of indian summer monsoon precipitation variability during the last millennium, *Geophysical Research Letters*, 38(15).
- Sinha, S., and M. Naik (2004), Aquatic biodiversity as food chain link in kotumsar cave, *Abstr., XVII Int. Symp. Biospeleology, Raipur*, p. 61.
- Sirocko, F., M. Sarnthein, H. Erlenkeuser, H. Lange, M. Arnold, and J. C. Duplessy (1993), Century-scale events in monsoonal climate over the past 24,000 years.
- Sridhar, A., R. Bhushan, D. Balaji, S. Band, and L. Chamyal (2016), Geochemical and sr–nd isotopic variations in palaeoflood deposits at mainstem–tributary junction, western india: Implications on late holocene flood events, *CATENA*, 139, 32–43.
- Srivastava, P., A. Kumar, A. Mishra, N. K. Meena, J. K. Tripathi, Y. Sundriyal, R. Agnihotri, and A. K. Gupta (2013), Early holocene monsoonal fluctuations in the garhwal higher himalaya as inferred from multi-proxy data from the malari paleolake, *Quaternary Research*, 80(3), 447–458.
- Staubwasser, M., and H. Weiss (2006), Holocene climate and cultural evolution in late prehistoric–early historic west asia, *Quaternary Research*, 66(3), 372–387.
- Steig, E. J. (1999), Mid-holocene climate change, *Science*, 286(5444), 1485.
- Steig, E. J., C. P. Hart, J. W. White, W. L. Cunningham, M. D. Davis, and E. S. Saltzman (1998), Change in climate, ocean and ice-sheet conditions in the ross embayment, antarctica at 6 ka, *Ann. Glaciol.*, 27.
- Stein, A. F., R. R. Draxler, G. D. Rolph, B. J. B. Stunder, M. D. Cohen, and F. Ngan (2015), NOAA’s HYSPLIT Atmospheric Transport and Dispersion Modeling System, *Bull. Am. Meteorol. Soc.*, 96(12), 2059–2077, doi:10.1175/BAMS-D-14-00110.1.
- Stuiver, M., and P. J. Reimer (1993), Calib users guide rev. 3.0, *University of Washington, Quaternary Isotope Laboratory*.
- Suresh, N., T. N. Bagati, R. Kumar, and V. C. Thakur (2007), Evolution of quaternary alluvial fans and terraces in the intramontane pinjaur dun, sub-himalaya, nw india: Interaction between tectonics and climate change, *Sedimentology*, 54(4), 809–833.
- Tang, K., and X. Feng (2001), The effect of soil hydrology on the oxygen and hydrogen isotopic compositions of plants’ source water, *Earth and Planetary Science Letters*, 185(3), 355–367.

- Thompson, L. G., E. Mosley-Thompson, M. Davis, J. Bolzan, J. Dai, L. Klein, T. Yao, X. Wu, Z. Xie, and N. Gundestrup (1989), Holocene—late pleistocene climatic ice core records from qinghai-tibetan plateau, *Science*, *246*(4929), 474–477.
- Tiwari, M., A. K. Singh, and R. Ramesh (2011), High-resolution monsoon records since last glacial maximum: a comparison of marine and terrestrial paleoarchives from south asia, *Journal of Geological Research*, 2011.
- Tomas, R. A., and P. J. Webster (1997), The role of inertial instability in determining the location and strength of near-equatorial convection, *Quarterly Journal of the Royal Meteorological Society*, *123*(542), 1445–1482.
- Tooth, A. F., and I. J. Fairchild (2003), Soil and karst aquifer hydrological controls on the geochemical evolution of speleothem-forming drip waters, crag cave, southwest ireland, *Journal of Hydrology*, *273*(1), 51–68.
- Turney, C., M. Baillie, S. Clemens, D. Brown, J. Palmer, J. Pilcher, P. Reimer, and H. H. Leuschner (2005), Testing solar forcing of pervasive holocene climate cycles, *Journal of Quaternary Science*, *20*(6), 511–518.
- Urey, H. C. (1947), The thermodynamic properties of isotopic substances, *Journal of the Chemical Society (Resumed)*, pp. 562–581.
- Verheyden, S. (2004), Trace elements in speleothems. a short review of the state of the art, *International Journal of Speleology*, *33*(1), 9.
- Verheyden, S., E. Keppens, I. J. Fairchild, F. McDermott, and D. Weis (2000), Mg, sr and sr isotope geochemistry of a belgian holocene speleothem: implications for paleoclimate reconstructions, *Chemical Geology*, *169*(1), 131–144.
- von Rad, U., M. Schaaf, K. H. Michels, H. Schulz, W. H. Berger, and F. Sirocko (1999), A 5000-yr record of climate change in varved sediments from the oxygen minimum zone off pakistan, northeastern arabian sea, *Quaternary Research*, *51*(1), 39–53.
- Wachter, E. A., and J. Hayes (1985), Exchange of oxygen isotopes in carbon dioxide-phosphoric acid systems, *Chemical Geology: Isotope Geoscience Section*, *52*(3), 365–374.
- Wang, Y., H. Cheng, R. L. Edwards, Y. He, X. Kong, Z. An, J. Wu, M. J. Kelly, C. A. Dykoski, and X. Li (2005), The holocene asian monsoon: links to solar changes and north atlantic climate, *Science*, *308*(5723), 854–857.
- Wang, Y., H. Cheng, R. L. Edwards, X. Kong, X. Shao, S. Chen, J. Wu, X. Jiang,

- X. Wang, and Z. An (2008), Millennial-and orbital-scale changes in the east asian monsoon over the past 224,000 years, *Nature*, 451(7182), 1090–1093.
- Wanner, H., J. Beer, J. Bütikofer, T. J. Crowley, U. Cubasch, J. Flückiger, H. Goosse, M. Grosjean, F. Joos, J. O. Kaplan, et al. (2008), Mid-to late holocene climate change: an overview, *Quaternary Science Reviews*, 27(19), 1791–1828.
- Weber, S. A., and W. R. Belcher (2003), Indus ethnobiology, *New perspectives from the field*, pp. 251–326.
- Webster, P. J., L. Chou, and Lau Ka Ming (1977), Mechanics effecting the State, Evolution and Transition of the Planetary Scale Monsoon, 115, 1463–1489.
- Wedepohl, K. H. (1995), The composition of the continental crust, *Geochimica et cosmochimica Acta*, 59(7), 1217–1232.
- Wenxiang, W., and L. Tungsheng (2004), Possible role of the “holocene event 3” on the collapse of neolithic cultures around the central plain of china, *Quaternary International*, 117(1), 153–166.
- Wigley, T., L. Plummer, and F. Pearson (1978), Mass transfer and carbon isotope evolution in natural water systems, *Geochimica et Cosmochimica Acta*, 42(8), 1117–1139.
- Wikipedia (2016a), Kutumsar cave, c. p. r. environmental education centre, chennai, [Online; accessed 23-July-2016].
- Wikipedia (2016b), Banayan tree formation, belum cave.
- Williams, P. W. (2008), The role of the epikarst in karst and cave hydrogeology: a review, *International Journal of Speleology*, 37(1), 1.
- Wright, H. E. (1993), *Global climates since the last glacial maximum*, U of Minnesota Press.
- Yadava, M. (2002), Stable Isotope systematics in cave calcites : Implications to past climatic changes in tropical India, Ph.D. thesis, Devi Ahilya Vishwavidyalaya University, Indore, India.
- Yadava, M., and R. Ramesh (1999), Speleothems-Useful proxies for past monsoon rainfall, *J. Sci. Ind. Res. (India)*, 58, 339–348.
- Yadava, M., and R. Ramesh (2001), Past rainfall and trace element variations in a tropical speleothem from india, *Mausam*, 52(1), 307–316.

- Yadava, M., and R. Ramesh (2005), Monsoon reconstruction from radiocarbon dated tropical indian speleothems, *The Holocene*, *15*(1), 48–59.
- Yadava, M., and R. Ramesh (2006), Stable Oxygen and Carbon Isotope Variations as Monsoon Proxies : A Comparative Study of Speleothems from Four Different Locations in India, *J. Geol. Soc. India*, *68*(September), 461–475.
- Yadava, M., and R. Ramesh (2007), Significant longer-term periodicities in the proxy record of the Indian monsoon rainfall, *New Astron.*, *12*(7), 544–555, doi:10.1016/j.newast.2007.04.001.
- Yadava, M., R. Ramesh, and G. Pant (2004), Past monsoon rainfall variations in peninsular India recorded in a 331-year-old speleothem, *The Holocene*, *14*(4), 517–524, doi:10.1191/0959683604hl728rp.
- Yadava, M., K. Sarswat, I. Singh, and R. Ramesh (2007), Evidences of early human occupation in the limestone caves of bastar, chhattisgarh, *Current Science*, *92*(6).
- Yatagai, A., K. Kamiguchi, O. Arakawa, A. Hamada, N. Yasutomi, and A. Kitoh (2012), APHRODITE: Constructing a Long-Term Daily Gridded Precipitation Dataset for Asia Based on a Dense Network of Rain Gauges, *Bull. Am. Meteorol. Soc.*, *93*(9), 1401–1415, doi:10.1175/BAMS-D-11-00122.1.
- Ye, H., and Z. Bao (2001), Lagged teleconnections between snow depth in northern eurasia, rainfall in southeast asia and sea-surface temperatures over the tropical pacific ocean, *International Journal of Climatology*, *21*(13), 1607–1621.
- Yin, J. H., and D. S. Battisti (2001), The importance of tropical sea surface temperature patterns in simulations of last glacial maximum climate, *Journal of Climate*, *14*(4), 565–581.
- Yonge, C., D. Ford, J. Gray, and H. Schwarcz (1985), Stable isotope studies of cave seepage water, *Chemical Geology: Isotope Geoscience Section*, *58*(1), 97–105.
- Yonge, C. J., L. Goldenberg, and H. R. Krouse (1989), An isotope study of water bodies along a traverse of southwestern canada, *Journal of Hydrology*, *106*(3), 245–255.
- Yoshimura, K., M. Kanamitsu, D. Noone, and T. Oki (2008), Historical isotope simulation using Reanalysis atmospheric data, *J. Geophys. Res.*, *113*(D19), D19,108, doi:10.1029/2008JD010074.
- Yuan, D., H. Cheng, R. L. Edwards, C. a. Dykoski, M. J. Kelly, M. Zhang,

- J. Qing, Y. Lin, Y. Wang, J. Wu, J. a. Dorale, Z. An, and Y. Cai (2004), Timing, duration, and transitions of the last interglacial Asian monsoon., *Science*, *304*(5670), 575–8, doi:10.1126/science.1091220.
- Zhisheng, A., S. C. Clemens, J. Shen, X. Qiang, Z. Jin, Y. Sun, W. L. Prell, J. Luo, S. Wang, H. Xu, Y. Cai, W. Zhou, X. Liu, W. Liu, Z. Shi, L. Yan, X. Xiao, H. Chang, F. Wu, L. Ai, and F. Lu (2011), Glacial-Interglacial Indian Summer Monsoon Dynamics, *Science (80-.)*, *333*(6043), 719–723, doi:10.1126/science.1203752.
- Zhou, H., B. Chi, M. Lawrence, J. Zhao, J. Yan, A. Greig, and Y. Feng (2008), High-resolution and precisely dated record of weathering and hydrological dynamics recorded by manganese and rare-earth elements in a stalagmite from central china, *Quaternary Research*, *69*(3), 438–446.
- Zorzi, C., M. F. S. Goñi, K. Anupama, S. Prasad, V. Hanquiez, J. Johnson, and L. Giosan (2015), Indian monsoon variations during three contrasting climatic periods: The holocene, heinrich stadial 2 and the last interglacial–glacial transition, *Quaternary Science Reviews*, *125*, 50–60.